Light-Driven Modulation of Nanoparticle Surfaces Using Photo-Labile Protecting Groups and Bioluminescence

Dissertation to obtain the Degree of Doctor of Natural Sciences
(Dr. rer. nat.)
from the Faculty of Chemistry and Pharmacy
University of Regensburg

Presented by
Jan Birringer
from Trier
2026

Jan Birringer

Light-Driven Modulation of Nanoparticle Surfaces Using Photo-Labile Protecting Groups and Bioluminescence

This work was carried out from March 2022 until February 2026 at the Department of Pharmaceutical Technology at the University of Regensburg.

The dissertation was prepared under the supervision of Prof. Dr. Achim Goepferich.

Doctoral application submitted on: 28th April, 2026

Examination board:

Chair: Prof. Dr. Steffen Pockes
1st Expert: Prof. Dr. Achim Goepferich
2nd Expert: Prof. Dr. Miriam Breunig
3rd Expert: Prof. Dr. Joachim Wegener

"I was taught that the way of progress was neither swift nor easy."

Marie Curie

To my family and beloved friends.

Table of Contents

Chapter 1

Introduction

Nanoparticles have emerged as a versatile and powerful platform for modern drug delivery. They have been extensively exploited in recent years, owing to their tunable physicochemical properties, high drug-loading capacity and desirable stability [1, 2]. Besides the high biocompatibility of organic nanoparticles based on lipids or polymers, these particles also have the ability to cross biological barriers, and their nanoscale dimension enable passive accumulation in tumors via the enhanced permeability and retention (EPR) effect [3–5]. Furthermore, active targeting of diseased tissue and increased cellular uptake can be achieved through surface functionalization with biomolecular recognition elements, known as ligands [6]. Compared to conventional systemic drug administration, nanoparticle-mediated delivery offers several fundamental advantages. The encapsulation of active pharmaceutical ingredients (APIs) enables nanoparticles to counteract the unfavorable intrinsic properties of drugs by imparting carrier-defined physicochemical characteristics [7, 8]. This results in improved biodistribution and enhanced bioavailability. Furthermore, nanoparticles can protect sensitive therapeutic cargo from premature degradation and enhance circulation time [9].

Despite these advantages, nanoparticles encounter several biological barriers that limit efficient and selective delivery. These barriers include opsonization and rapid clearance by the mononuclear phagocyte system (MPS), which removes the majority of administered nanoparticles before they reach their target site [10]. Furthermore, protein corona formation upon administration can mask intended targeting functionalities, while the limited specificity of targeting ligands may further contribute to off-target delivery, particularly when their receptors are ubiquitously expressed throughout the body [11–13]. More than 90 % of administered nanoparticles fail to reach their intended targets, resulting in suboptimal therapeutic outcome and potential off-target toxicity [14]. This lack of precision emphasizes the need for more adaptive and controllable nanoparticle systems capable of refining biodistribution and enhancing tissue selectivity.

To address these limitations, the concept of stimuli-responsive nanoparticles has gained significant attention [15–17]. These nanoparticles respond to specific stimuli, which can be endogenous (pH, enzymes, redox) or exogenous (light, temperature, magnetism). Of particular interest are designs that undergo dynamic surface modifications in biological environments, inspired by the adaptive strategies employed by viruses [18]. Among these stimuli, light is an excellent external trigger because it is non-invasive and enables precise control with high spatiotemporal resolution. Moreover, it is orthogonal to the biochemical environment and, therefore, does not depend on pathological conditions such as acidic pH or disease-associated enzyme activity, that endogenous triggers rely on.

Photo-labile protecting groups (PPG) are typically required for generating photo-responsive nanoparticles. Those PPGs are small photo-sensitive molecules that can be linked to the moiety of interest and cleaved upon light irradiation. A lot of PPGs with different physicochemical characteristics are available and can be categorized by mechanism of photolysis. To date, research has focused on eight types of PPGs: 2-nitrobenzyl, *meso*-methyl boron dipyrromethene (BODIPY) derivates, coumarin-4-ylmethyl, arylmethyl and arylcarbonylmethyl groups, as well as xanthane, cyanine and ruthenium complexes (Figure 1.1). PPGs derived from coumarin-4-ylmethyl are among the most extensively investigated, owing to their high molar absorption coefficient and favorable photosensitivity [19]. Importantly, their photolysis byproducts are generally non-toxic under normal conditions, which supports their potential for clinical application [20]. For a more detailed discussion of the photolysis mechanisms and spectral properties of the aforementioned PPGs, the reader is referred to the literature [21–23].

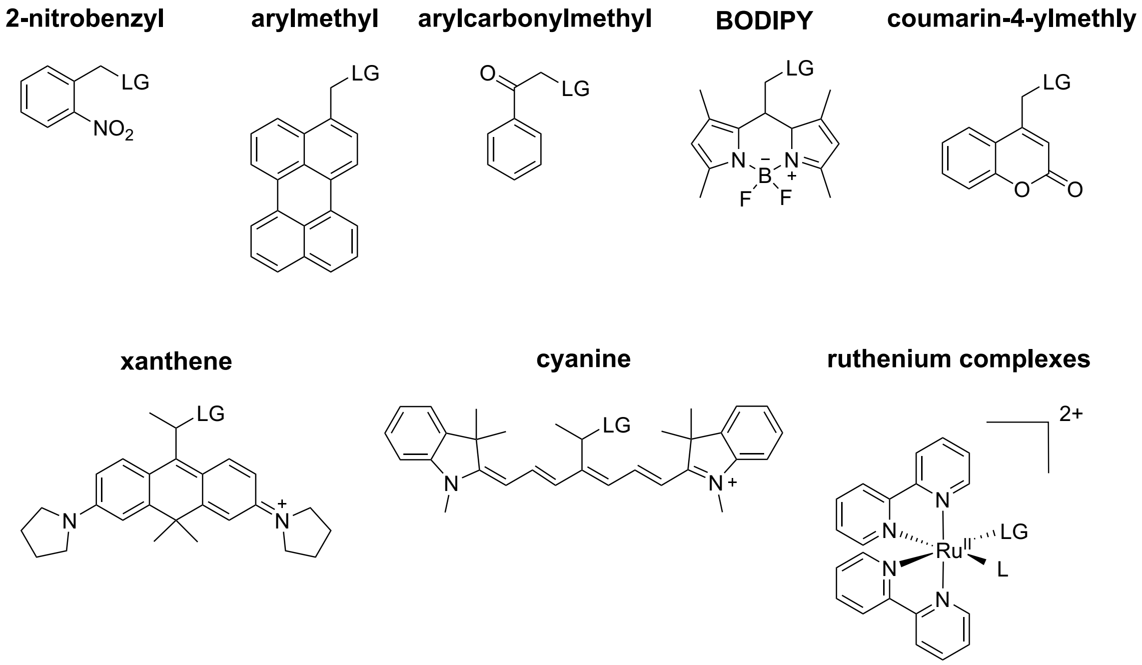

Figure 1.1: Common classes of photo-labile protecting groups. LG denotes a leaving group released upon photoactivation. L represents an ancillary ligand coordinated to the ruthenium center.

Light is commonly classified by wavelength into ultraviolet (UV, 200 – 400 nm), visible (400 – 700 nm), and near-infrared (NIR, 700 – 1000 nm) regions [24]. Short-wavelength lights such as UV and blue light possess higher energy but exhibit limited tissue penetration and can cause photo damage [25]. In biological tissues, wavelengths below 650 nm are strongly absorbed by tissue associated chromophores, including hemoglobin, oxy-hemoglobin and melanin, whereas wavelengths above 900 nm are predominantly absorbed by water [26, 27]. These optical constraints are particularly relevant for PPGs as their majority is activated by UV or visible light, resulting in poor penetration depth due to strong scattering and absorption in tissue [28, 29]. Consequently, red and NIR light with wavelengths $650 - 900\,\mathrm{nm}$, often referred to as "biological window", is preferred for biomedical applications because it can penetrate tissue more effectively and exhibits reduced phototoxicity [27, 30]. To address the limitations of poor tissue penetration, current strategies focus on red-shifting PPG absorption into NIR region and employing two-photon excitation. Further, upconverting nanoparticles, which convert low-energy photons into high-energy photons, and optical waveguides, which transport light deeper into tissue, are used. These approaches will be explained later.

Incorporation of PPGs into nanoparticles enable both photo-controlled drug release and drug targeting (Figure 1.2). Because photo-controlled drug release is not the focus of this work and has already been extensively discussed in the literature, it is only briefly outlined here [31, 32]. In drug-release applications, PPGs are covalently incorporated into prodrugs, rendering them biologically inactive until they reach the diseased site. Upon light irradiation, the PPG is cleaved, resulting in release of the active drug (Figure 1.2 a). Alternatively, PPGs can be integrated into nanocarriers, where light irradiation induces carrier dissociation and subsequent drug release. This can be achieved either through complete disintegration of the nanocarrier or by using the PPG as a cleavable linker between the drug and the carrier (Figure 1.2 b).

The focus of this work is photo-controlled targeting. Currently, three principal strategies are employed in this context: (1) direct modification of targeting ligands, (2) shielding ligands with detachable poly(ethylene glycol) (PEG) chains, and (3) anchoring ligands within the nanoparticles [20]. Importantly, all those concepts rely on an irreversible light response.

Direct Modification of Ligands with PPGs

Attaching PPGs to the functional sites of targeting ligands disable receptor binding by temporarily blocking the binding site on the ligand (Figure 1.2 c). This concept was first implemented by Dvir et al. in 2010 [33]. The amino acid sequence YIGSR in laminin, which adheres to the β_1 integrin on cell membrane, was rendered biologically inactive by attachment of 4,5-dimethoxy-2-nitrobenzyl (DMNB) to tyrosine. The photocaged YIGSR was coupled to the surface of polystyrene nanoparticles and adhesion of non-illuminated and illuminated ($\lambda = 365\,\mathrm{nm}$) nanoparticles to human umbilical vein endothelial cells (HUVEC) and mesenchymal stem cells were investigated. Illuminated particles exhibited a two-fold increase in adhesion relative to non-illuminated controls and particles modified with a non-adhering peptide, demonstrating effective photo-uncaging. Because β_1 integrin is ubiquitously

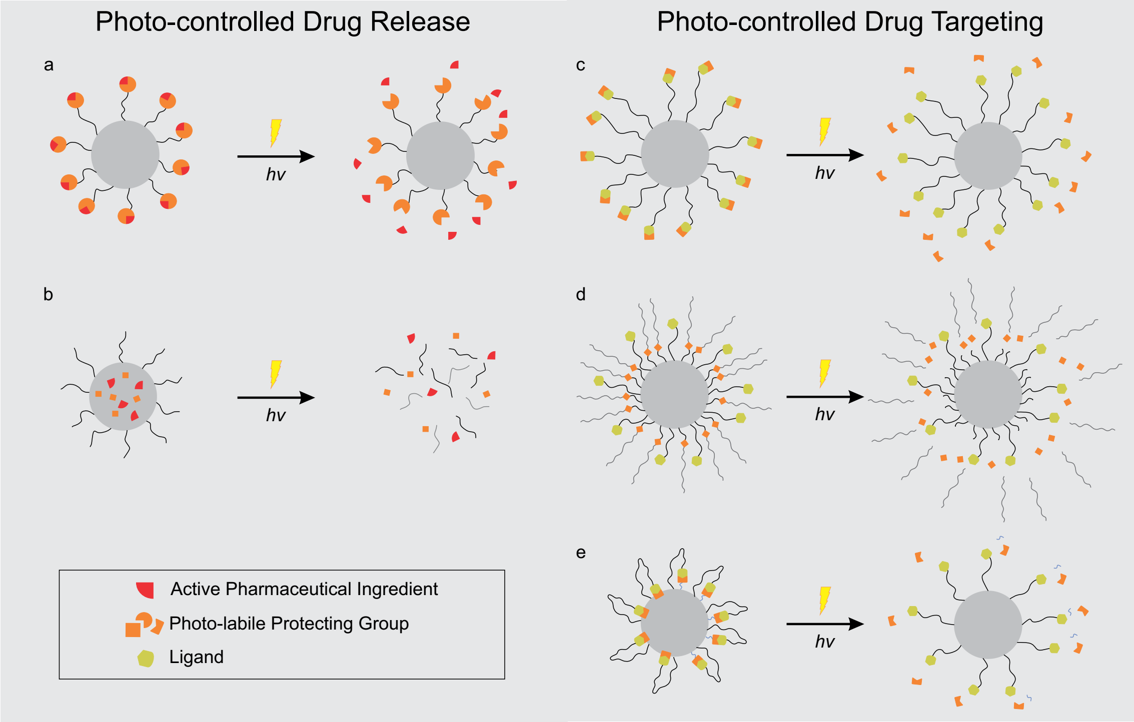

Figure 1.2: Schematic overview of photo-controlled drug release and drug targeting. Drug release approaches: **a** covalent attachment of photo-labile protecting groups (PPGs) to the active pharmaceutical ingredient to generate an inactive prodrug; **b** incorporation of PPGs within nanocarrier to induce light-triggered carrier dissociation. Drug targeting approaches: **c** direct caging of targeting ligands with PPGs to transiently suppress binding; **d** shielding ligands with photocleavable PEG chains, **e** anchoring ligands within nanoparticle core.

expressed throughout the body, targeting is restricted to the illuminated region and provides no inherent tissue selectivity by design. Fan et al. applied this photocaging concept to design tumor-specific nanoparticles by exploiting the high folate-receptor expression on cancer cells and incorporating photocaged folic acid on the nanoparticle surface [34]. In addition to blocking ligand-receptor interaction, PPGs can be used to neutralize charge of positively charged targeting ligands. The first photocaging of a positively charged cell-penetrating peptide (CPP) was reported by Shamay et al. in 2011 [35]. In this work, the penetrating-derived sequence RRMKWKK was photocaged by introducing three 6-nitroveratryloxycarbonyl (NVOC) groups into its lysine (K) residues. Upon UV irradiation ($\lambda = 365\,\text{nm}$), these groups were removed enabling rapid intracellular delivery of polymer-dye or polymer-drug conjugates into cancer cells. This caged CPP strategy was later transferred to nanostructured lipid carriers by Yang et al., allowing enhanced delivery of paclitaxel to human fibrosarcoma cells via unspecific uptake mechanism [36].

Shielding Ligands with Photocleavable PEG Chains

Functionalization of nanoparticles with PEG, often referred to as PEGylation, is a commonly used strategy to enhance nanoparticle stability in biological environments [37]. PEGylation improves colloidal stability by forming a hydrophilic shell that provides steric repulsion between particles [38]. In addition, PEG effectively reduces protein adsorption and limits recognition by the MPS, thereby prolonging circulation time [37]. However, PEGylation can also hinder the cellular uptake of nanoparticles and, therefore, limits effective drug delivery to targeting sites [39, 40]. This so called "PEG dilemma" can be exploited by using detachable PEG chains to temporarily shield targeting ligands. Subsequent removal of the PEG chains enables exposure of the ligands, a strategy which is often referred to as dePEGylation (Figure 1.2 d) [41, 42]. Zhou et al. investigated a light-triggered dePEGylation strategy based on an amphiphilic copolymer composed of poly(β-amino ester) (PAE) and PEG, with 2-nitrobenzyl (Nbz) incorporated at the block junction [43]. Micelles composed of the photo-labile copolymer PAE-Nbz-PEG and targeting PAE polymer functionalized with internalizing RGD peptide (iRDG), were loaded with upconverting nanoparticles. Upon NIR irradiation, the encapsulated upconverting nanoparticles emitted UV/visible light that cleaved the PEG chains, exposing the previously shielded iRGD ligand and resulting in enhanced cellular uptake via integrin receptor binding and micelle size shrinkage. The polymeric micelle platform demonstrated preferential doxorubicin delivery to tumor cells *in vivo* in tumor-bearing mice. Li et al. used the concept of ligand shielding by detachable PEG chains to install photo-responsive nanoparticles with nucleus-targeting for chlorambucil (Cb) delivery [44]. In the design, PKKKRKVR peptide serves as a nucleus localization sequence (NLS), which allows active transport of drug nanoparticles to the nucleus. The NLS peptide is linked to a short 1,2-disteroyl-*sn*-glcero-3-phosphoethanolamine-N-(PEG-2000)-(DSPE-PEG$_{2k}$), which is shielded by a long PEG-5000 (PEG$_{5k}$) chain on the photo-responsive prodrug, PEG$_{5k}$-[7-(diethylamino)coumarin-4-yl]methyl (DEACM)-Cb. DEACM was cleaved upon light irradiation at $\lambda = 420\,\text{nm}$ ($70\,\text{mW}\,\text{cm}^{-2}$ for 2 min), resulting in detachment of PEG$_{5k}$ from the nanoparticles. The photo-triggered dePEGylation process decreased the particle size and increased the surface charge, thereby improving cellular uptake and nucleus-targeting ability.

Anchoring Ligands within the Nanoparticle

Another strategy that can be employed to achieve photo-controlled targeting is to immobilize the ligands within the nanoparticle structure itself, using the PPG as a cleavable anchor. In this concept, PPGs may function directly as anchoring units, or their hydrophobicity can be increased through alkylation to improve their anchoring capability within the nanoparticle core (Figure 1.2 e). This latter approach was employed by Hansen et al., who modified a CPP at both termini with alkyl chains to form a surface-anchored loop on a PEGylated liposome [45]. One of the alkyl chains was conjugated to the peptide via a PEG-linked lipid, while the other was attached via a photo-labile nitrobenzyl linker. Within this anchored-loop design, the CPP was shielded by the outer PEG layer, but became exposed upon photolytic cleavage resulting in enhanced cellular uptake. PPGs with intrinsically hydrophobicity, such as (7-diethylaminocoumarin-4-yl)methyl (DEACM), can act as anchoring units without additional modification. Kohane and co-workers implemented such a concept in 2015 by masking cyclic RGD (cRGD), a ligand for integrin receptors, through incorporation of DEACM at its arginine (R) residue [46]. The caged cRGD was then linked to a poly(ethylene glycol)-*b*-poly(D,L-lactide)) (PEG-PLA) block copolymer. In the resulting self-assembled micelles, DEACM anchored the cRGD within the hydrophobic PLA core, alongside encapsulated photosensitizers and annihilators creating an upconversion system. The upconversion system enabled photocleavage of DEACM at irradiation with green light ($\lambda = 530\,\text{nm}$). The absorbed energy was converted to higher energy via triplet-triplet annihilation and transferred by fluorescence resonance energy transfer (FRET) to DEACM causing photolysis and presentation of cRGD. The *in vitro* experiments with HUVEC and human glioblastoma cells showed significant higher nanoparticle-cell interaction for the irradiated samples compared to non-irradiated controls. This phototargeting system further exhibited preferential accumulation of micelles in tumor tissues of tumor-bearing mice [47].

All three strategies enable precise targeting of diseased tissue, thereby reducing off-target drug delivery. Direct modification of ligands with PPGs requires complete blocking of the functional groups and therefore strongly depends on the chemical structures of both the PPG and the ligand. More versatile options are therefore provided by shielding or anchoring of ligands. However, all strategies share the inherent limitation of poor tissue penetration. Some of the examples discussed above illustrate how this challenge can be partially overcome, and in the following section we will outline additional approaches described in the literature to further address this problem.

Overcoming Limited Penetration of Light in Biological Tissue

The most intuitive solution is to shift PPG absorption into the "biological window", where tissue penetration is optimal. Several classes of long-wavelength PPGs have been developed for this purpose, including red- and NIR-absorbing coumarins, BODIPYs, cyanines, and xanthenes, all of which have been comprehensively reviewed in recent literature [19, 21, 48]. Because NIR photons carry lower energy, the energy gap between the ground state and excited state is smaller than in UV-activated systems. According to the gap law, non-radiative transition rates increase approximately exponentially as the energy gap decreases [49]. Thus, smaller energy gaps promote vibrational relaxation, making non-radiative decay pathways more competitive than productive photochemical cleavage. As a result, π-extended organic PPGs designed for NIR activation often display lower uncaging quantum yields (ϕ_u) [22]. However, their typically high molar absorption coefficients (ϵ) can partially compensate for low quantum yield, resulting in uncaging efficiencies ($\phi_u \epsilon$) sufficient for practical use [50].

Two-photon excitation offers an alternative to short-wavelength activation, as demonstrated by Olson et al., who cleaved the coumarin-derived photocage DEAC450 ($\lambda_{max} = 450\,\mathrm{nm}$) from glutamate using 900 nm irradiation [51]. The main limitation of two-photon excitation is the requirement for high-intensity laser system, which restricts widespread application.

The effective penetration depth can also be improved by using upconverting nanoparticles, which convert tissue-penetrating NIR photons into higher-energy photons. These upconverting nanoparticles typically consist of lanthanide-doped inorganic material, that absorb multiple low-energy NIR photons and emit a single higher-energy photon via anti-Stokes upconversion [52]. This process enables the activation of conventional UV or visible light-responsive PPGs within biological tissues while bypassing the penetration limitations of their native excitation wavelengths. Nevertheless, several limitations hinder clinical translation, including dose-dependent toxicological responses, incomplete knowledge of chronic exposure effects, and the lack of harmonized regulatory guidelines [53].

All aforementioned strategies rely on adapting the photo-responsive system itself, while a different approach to increasing light penetration is the use of optical waveguides. These waveguides are integrated directly into the tissue and fabricated from biocompatible and biodegradable polymers such as poly(D,L-lactide-*co*-glycolide (PLGA) or PLA, which possess a higher refractive index than the surrounding tissue. Therefore, they can guide and transport optical energy to inaccessible regions of conventional surface illumination. This approach opens up new possibilities for deeply distributed photo-sensitive interventions. However, its practical implementation is constrained by the requirement for surgical implantation of the waveguide material [54].

Despite significant advances in red-shifted PPGs, two-photon excitation and upconverting nanoparticles, as well as the implementation of waveguides, all approaches to overcome limitations in tissue penetration rely on external irradiation. Consequently, mechanisms capable of generating light within the biological environment have attracted increasing interest. Chemiluminescence describes the emission of light resulting from a chemical reaction. This phenomenon offers distinct advantages such as high sensitivity and an excellent signal-to-noise ratio, making it a powerful tool for biosensing and bioimaging [55]. Further, chemiluminescence systems can be integrated into nanocarriers for therapeutic applications such as photodynamic therapy (PDT) [56]. The work of Li et al. demonstrates the potential of chemiluminescent nanoparticles [57]. In their design, a conjugated polyfluorene vinylene (PFV) backbone is covalently functionalized with isoluminol moieties, which enables chemiluminescence in response to pathologically elevated levels of reactive oxygen species (ROS). Upon ROS exposure, PFV-Luminol not only emits chemiluminescence but also amplifies ROS production through chemiluminescence resonance energy transfer (CRET). By co-assembling PFV-Luminol with amphiphilic, folate-functionalized PEG-lipids, chemiluminescent nanoparticles are formed which enabled deep-tissue imaging and accumulation in tumor tissue with CRET-driven PDT without external irradiation.

Bioluminescence is a particular class of chemiluminescence in which visible photons are generated through enzyme-driven reactions, enabling light production without external excitation [58]. In addition to bioimaging and biosensing applications, bioluminescence systems have also been used in PDT [59–61]. In the work of Yang et al., polymeric nanoparticles were loaded with photosensitizer Rose Bengal, which is capable of generating ROS, and were additionally modified with firefly luciferase. The process of PDT was mediated by the bioluminescence resonance energy transfer (BRET) and the results of *in vivo* experiments displayed inhibition of tumor growth [61]. This BRET-mediated phototherapy conceptually demonstrates the potential for bioluminescence to be employed to stimulate photo-responsive nanoparticles within deep tissue. This potential is further supported by several recent studies showing that bioluminolysis can reliably drive PPG bond cleavage on small molecules via BRET [62–64]. In the study by Chang et al., coumarin-derived PPG, which exhibits absorption spectral matching to the emission of NanoLuc luciferase, was tethered to NanoLuc-HaloTag chimera [62]. This enabled highly efficient energy transfer from the NanoLuc to the PPG, resulting in rapid cleavage with kinetics comparable to those of conventional LED irradiation. The study demonstrated bioluminolysis in cellular systems, validated through coumarin uncaging in HeLa cells and functional release of a covalent kinase inhibitor (ibrutinib) in SKBR3 cancer cells.

In summary, a variety of strategies have been developed to achieve photo-controlled targeting, including ligand modification, ligand shielding with PEG chains, and anchoring ligands within the nanoparticles. This toolbox facilitates the precise spatiotemporal activation of nanoparticles, thereby enhancing tissue selectivity. The inherent limitations of light penetration in biological tissue have been a major driving force behind innovations in the field, ranging from the development of NIR-responsive PPGs and two-photon activation mechanisms to the introduction of upconverting nanoparticles and the implementation of optical waveguides. In addition to these approaches, bioluminescence has emerged as a conceptually distinct solution, providing endogenous photons for photocleavage independently of external irradiation. These developments collectively outline the technological and conceptual foundation upon which modern light-controlled targeting systems are being built.

References

[1] Safiul Islam et al. “Advances in nanoparticles in targeted drug delivery–A review”. In: *Results in Surfaces and Interfaces* 19 (2025), p. 100529. ISSN: 2666-8459. DOI: `10.1016/j.rsurfi.2025.100529`. URL: `https://www.sciencedirect.com/science/article/pii/S2666845925001163`.

[2] Shimaa Hosny et al. “Nanomaterials in biomedical applications: opportunities and challenges—a review”. In: *Chemical Papers* 79.5 (2025), pp. 2657–2678. ISSN: 0366-6352. DOI: `10.1007/s11696-025-03937-5`.

[3] Alanood S. Alfutaimani et al. “Exploring the landscape of Lipid Nanoparticles (LNPs): A comprehensive review of LNPs types and biological sources of lipids”. In: *International journal of pharmaceutics: X* 8 (2024), p. 100305. DOI: `10.1016/j.ijpx.2024.100305`.

[4] Ruixian Lian et al. “PLLA-PEG/mPEG Copolymer with Improved Hydrophilicity, Crystallinity, and Biocompatibility: An In-Depth Study on the Crystallization Kinetics”. In: *ACS applied materials & interfaces* 17.20 (2025), pp. 30067–30080. DOI: `10.1021/acsami.5c02818`.

[5] Hongmin Chen et al. “Rethinking cancer nanotheranostics”. In: *Nature reviews. Materials* 2 (2017). ISSN: 2058-8437. DOI: `10.1038/natrevmats.2017.24`.

[6] Amanda K. Pearce and Rachel K. O’Reilly. “Insights into Active Targeting of Nanoparticles in Drug Delivery: Advances in Clinical Studies and Design Considerations for Cancer Nanomedicine”. In: *Bioconjugate Chemistry* 30.9 (2019), pp. 2300–2311. DOI: `10.1021/acs.bioconjchem.9b00456`.

[7] Maximilian A. Beach et al. “Polymeric Nanoparticles for Drug Delivery”. In: *Chemical reviews* 124.9 (2024), pp. 5505–5616. DOI: `10.1021/acs.chemrev.3c00705`.

[8] Elvin Blanco, Haifa Shen, and Mauro Ferrari. “Principles of nanoparticle design for overcoming biological barriers to drug delivery”. In: *Nature biotechnology* 33.9 (2015), pp. 941–951. DOI: `10.1038/nbt.3330`.

[9] Nimeet Desai et al. “Nanoparticle Therapeutics in Clinical Perspective: Classification, Marketed Products, and Regulatory Landscape”. In: *Small (Weinheim an der Bergstrasse, Germany)* 21.29 (2025), e2502315. DOI: `10.1002/smll.202502315`.

[10] Zahid Hussain et al. “PEGylation: a promising strategy to overcome challenges to cancer-targeted nanomedicines: a review of challenges to clinical transition and promising resolution”. In: *Drug Delivery and Translational Research* 9.3 (2019), pp. 721–734. ISSN: 2190-3948. DOI: `10.1007/s13346-019-00631-4`.

[11] Sandra Ritz et al. “Protein corona of nanoparticles: distinct proteins regulate the cellular uptake”. In: *Biomacromolecules* 16.4 (2015), pp. 1311–1321. DOI: `10.1021/acs.biomac.5b00108`.

[12] Maria Marti-Solano et al. “Combinatorial expression of GPCR isoforms affects signalling and drug responses”. In: *Nature* 587.7835 (2020), pp. 650–656. DOI: `10.1038/s41586-020-2888-2`.

[13] Ying Shen et al. “Transferrin receptor 1 in cancer: a new sight for cancer therapy”. In: *American journal of cancer research* 8.6 (2018), pp. 916–931. ISSN: 2156-6976.

[14] Stefan Wilhelm et al. “Analysis of nanoparticle delivery to tumours”. In: *Nature Reviews Materials* 1.5 (2016). DOI: `10.1038/natrevmats.2016.14`.

[15] Nikolitsa Nomikou, Hamzah Masood, and Shiv Patel. “Stimulus-Responsive Nanoparticles for Drug Delivery”. In: *Fundamentals of Pharmaceutical Nanoscience*. Ed. by Ijeoma F. Uchegbu et al. Cham: Springer Nature Switzerland, 2024, pp. 389–422. ISBN: 978-3-031-59477-9. DOI: `10.1007/978-3-031-59478-6_15`.

[16] Alan Clavelland Ochioni, Italo Rennan Sousa Vieira, and Carlos Adam Conte-Junior. “Advances in stimuli-responsive nanoparticles for cancer therapy: Mechanisms, functional materials, and emerging technologies”. In: *Journal of Drug Delivery Science and Technology* 114 (2025), p. 107519. ISSN: 17732247. DOI: `10.1016/j.jddst.2025.107519`.

[17] Simona Mura, Julien Nicolas, and Patrick Couvreur. “Stimuli-responsive nanocarriers for drug delivery”. In: *Nature materials* 12.11 (2013), pp. 991–1003. DOI: `10.1038/nmat3776`.

[18] Zhihuan Liao et al. “Virus-inspired nanosystems for drug delivery”. In: *Nanoscale* 13.45 (2021), pp. 18912–18924. DOI: `10.1039/D1NR05872J`.

[19] Megan R. Clotworthy et al. “Coumarin-Derived Caging Groups in the Spotlight: Tailoring Physiochemical and Photophysical Properties”. In: *ChemPlusChem* 89.10 (2024), e202400377. DOI: `10.1002/cplu.202400377`.

[20] Jinzhao Liu, Weirong Kang, and Weiping Wang. “Photocleavage-based Photoresponsive Drug Delivery”. In: *Photochemistry and photobiology* 98.2 (2022), pp. 288–302. DOI: `10.1111/php.13570`.

[21] Pin-Han Lin et al. “Shining light on photo-responsive molecular tools: advances in visible-to-NIR activatable photolabile protecting groups”. In: *Organic & biomolecular chemistry* 23.43 (2025), pp. 9735–9751. DOI: `10.1039/d5ob00542f`.

[22] Roy Weinstain et al. “Visible-to-NIR-Light Activated Release: From Small Molecules to Nanomaterials”. In: *Chemical reviews* 120.24 (2020), pp. 13135–13272. DOI: `10.1021/acs.chemrev.0c00663`.

[23] Petr Klán et al. “Photoremovable protecting groups in chemistry and biology: reaction mechanisms and efficacy”. In: *Chemical reviews* 113.1 (2013), pp. 119–191. DOI: `10.1021/cr300177k`.

[24] Xueqi Lin et al. “Intellective and stimuli-responsive drug delivery systems in eyes”. In: *International journal of pharmaceutics* 602 (2021), p. 120591. DOI: `10.1016/j.ijpharm.2021.120591`.

[25] Karl P. Lawrence et al. “The UV/Visible Radiation Boundary Region (385-405 nm) Damages Skin Cells and Induces "dark" Cyclobutane Pyrimidine Dimers in Human Skin in vivo”. In: *Scientific reports* 8.1 (2018), p. 12722. DOI: `10.1038/s41598-018-30738-6`.

[26] Joana M. Silva, Eduardo Silva, and Rui L. Reis. “Light-triggered release of photocaged therapeutics - Where are we now?” In: *Journal of controlled release : official journal of the Controlled Release Society* 298 (2019), pp. 154–176. DOI: `10.1016/j.jconrel.2019.02.006`.

[27] Alina Y. Rwei, Weiping Wang, and Daniel S. Kohane. “Photoresponsive nanoparticles for drug delivery”. In: *Nano today* 10.4 (2015), pp. 451–467. ISSN: 1748-0132. DOI: `10.1016/j.nantod.2015.06.004`.

[28] Caerwyn Ash et al. “Effect of wavelength and beam width on penetration in light-tissue interaction using computational methods”. In: *Lasers in medical science* 32.8 (2017), pp. 1909–1918. DOI: `10.1007/s10103-017-2317-4`.

[29] Louise Finlayson et al. “Depth Penetration of Light into Skin as a Function of Wavelength from 200 to 1000 nm”. In: *Photochemistry and photobiology* 98.4 (2022), pp. 974–981. DOI: `10.1111/php.13550`.

[30] R. Weissleder. “A clearer vision for in vivo imaging”. In: *Nature biotechnology* 19.4 (2001), pp. 316–317. DOI: `10.1038/86684`. URL: `https://www.nature.com/articles/nbt0401_316`.

[31] Akshaya Bansal and Yong Zhang. “Photocontrolled nanoparticle delivery systems for biomedical applications”. In: *Accounts of chemical research* 47.10 (2014), pp. 3052–3060. DOI: `10.1021/ar500217w`.

[32] Yu Tao et al. “Light: A Magical Tool for Controlled Drug Delivery”. In: *Advanced functional materials* 30.49 (2020). ISSN: 1616-301X. DOI: `10.1002/adfm.202005029`.

[33] Tal Dvir et al. “Photo-targeted nanoparticles”. In: *Nano letters* 10.1 (2010), pp. 250–254. DOI: `10.1021/nl903411s`.

[34] Nien-Chu Fan et al. “Photocontrolled targeted drug delivery: photocaged biologically active folic acid as a light-responsive tumor-targeting molecule”. In: *Angewandte Chemie (International ed. in English)* 51.35 (2012), pp. 8806–8810. DOI: `10.1002/anie.201203339`.

[35] Yosi Shamay et al. “Light induced drug delivery into cancer cells”. In: *Biomaterials* 32.5 (2011), pp. 1377–1386. DOI: `10.1016/j.biomaterials.2010.10.029`.

[36] Yang Yang et al. “Preparation and characterization of photo-responsive cell-penetrating peptide-mediated nanostructured lipid carrier”. In: *Journal of drug targeting* 22.10 (2014), pp. 891–900. DOI: `10.3109/1061186X.2014.940589`.

[37] Jung Soo Suk et al. “PEGylation as a strategy for improving nanoparticle-based drug and gene delivery”. In: *Advanced drug delivery reviews* 99.Pt A (2016), pp. 28–51. DOI: `10.1016/j.addr.2015.09.012`.

[38] Donald E. Owens and Nicholas A. Peppas. “Opsonization, biodistribution, and pharmacokinetics of polymeric nanoparticles”. In: *International journal of pharmaceutics* 307.1 (2006), pp. 93–102. DOI: `10.1016/j.ijpharm.2005.10.010`.

[39] Shyh-Dar Li and Leaf Huang. “Stealth nanoparticles: high density but sheddable PEG is a key for tumor targeting”. In: *Journal of controlled release : official journal of the Controlled Release Society* 145.3 (2010), pp. 178–181. DOI: `10.1016/j.jconrel.2010.03.016`.

[40] Hiroto Hatakeyama, Hidetaka Akita, and Hideyoshi Harashima. “The polyethyleneglycol dilemma: advantage and disadvantage of PEGylation of liposomes for systemic genes and nucleic acids delivery to tumors”. In: *Biological & pharmaceutical bulletin* 36.6 (2013), pp. 892–899. DOI: `10.1248/bpb.b13-00059`.

[41] Li Kong et al. “Temporal Control of Membrane Fusion through Photolabile PEGylation of Liposome Membranes”. In: *Angewandte Chemie (International ed. in English)* 55.4 (2016), pp. 1396–1400. DOI: `10.1002/anie.201509673`.

[42] Li Kong, Frederick Campbell, and Alexander Kros. “DePEGylation strategies to increase cancer nanomedicine efficacy”. In: *Nanoscale horizons* 4.2 (2019), pp. 378–387. DOI: `10.1039/c8nh00417j`.

[43] Mengxue Zhou et al. “Light-Triggered PEGylation/dePEGylation of the Nanocarriers for Enhanced Tumor Penetration”. In: *Nano letters* 19.6 (2019), pp. 3671–3675. DOI: `10.1021/acs.nanolett.9b00737`.

[44] Yafei Li et al. “Photo-triggered nucleus targeting for cancer drug delivery”. In: *Nano Research* 14.8 (2021), pp. 2630–2636. ISSN: 1998-0124. DOI: `10.1007/s12274-020-3264-0`.

[45] Morten B. Hansen et al. “Constrained and UV-activatable cell-penetrating peptides for intracellular delivery of liposomes”. In: *Journal of controlled release : official journal of the Controlled Release Society* 164.1 (2012), pp. 87–94. DOI: `10.1016/j.jconrel.2012.10.008`.

[46] Weiping Wang et al. “Efficient Triplet-Triplet Annihilation-Based Upconversion for Nanoparticle Phototargeting”. In: *Nano letters* 15.10 (2015), pp. 6332–6338. DOI: `10.1021/acs.nanolett.5b01325`.

[47] Qian Liu et al. “Enhanced Precision of Nanoparticle Phototargeting in Vivo at a Safe Irradiance”. In: *Nano letters* 16.7 (2016), pp. 4516–4520. DOI: `10.1021/acs.nanolett.6b01730`.

[48] Shang Jia and Ellen M. Sletten. “Spatiotemporal Control of Biology: Synthetic Photochemistry Toolbox with Far-Red and Near-Infrared Light”. In: *ACS chemical biology* 17.12 (2022), pp. 3255–3269. DOI: `10.1021/acschembio.1c00518`.

[49] Ken Barat. *Laser Safety.* CRC Press, 2008. ISBN: 9780429147791. DOI: `10.1201/9781420068559`.

[50] Tomáš Šolomek, Jakob Wirz, and Petr Klán. “Searching for Improved Photoreleasing Abilities of Organic Molecules”. In: *Accounts of chemical research* 48.12 (2015), pp. 3064–3072. DOI: `10.1021/acs.accounts.5b00400`.

[51] Jeremy P. Olson et al. “Spectral evolution of a photochemical protecting group for orthogonal two-color uncaging with visible light”. In: *Journal of the American Chemical Society* 135.42 (2013), pp. 15948–15954. DOI: `10.1021/ja408225k`.

[52] Shivangi Sangwan et al. “A comprehensive review on upconversion nanoparticles: From synthesis strategies to multifunctional applications”. In: *Next Materials* 11 (2026), p. 101697. ISSN: 29498228. DOI: `10.1016/j.nxmate.2026.101697`.

[53] Aditi Joshi et al. ““Up-conversion nanoparticles: Toxicity and Pharmacokinetics””. In: *Journal of Molecular Structure* 1350 (2026), p. 143914. ISSN: 0022-2860. DOI: `10.1016/j.molstruc.2025.143914`. URL: `https://www.sciencedirect.com/science/article/pii/S002228602502561X`.

[54] Sedat Nizamoglu et al. “Bioabsorbable polymer optical waveguides for deep-tissue photomedicine”. In: *Nature communications* 7 (2016), p. 10374. DOI: `10.1038/ncomms10374`.

[55] Fang Zhao et al. “Recent Advances and Optimization Strategies in Chemiluminescence for Enhanced Bioimaging Performance †”. In: *Chinese Journal of Chemistry* 43.21 (2025), pp. 2810–2824. ISSN: 1001-604X. DOI: `10.1002/cjoc.70129`.

[56] Mingwang Yang et al. “Chemiluminescence for bioimaging and therapeutics: recent advances and challenges”. In: *Chemical Society reviews* 49.19 (2020), pp. 6800–6815. DOI: `10.1039/d0cs00348d`.

[57] Ling Li et al. “Chemiluminescent Conjugated Polymer Nanoparticles for Deep-Tissue Inflammation Imaging and Photodynamic Therapy of Cancer”. In: *Journal of the American Chemical Society* 146.9 (2024), pp. 5927–5939. DOI: `10.1021/jacs.3c12132`.

[58] Sung-Bae Kim and Tadaomi Furuta. “Bioluminescence from the bright and dark sides”. In: *Frontiers in Chemical Biology* 3 (2024). DOI: `10.3389/fchbi.2024.1459397`.

[59] Min-Kyung So et al. “Self-illuminating quantum dot conjugates for in vivo imaging”. In: *Nature Biotechnology* 24.3 (2006), pp. 339–343. ISSN: 1546-1696. DOI: `10.1038/nbt1188`.

[60] Yusuke Ikeda et al. “Design of luciferase-displaying protein nanoparticles for use as highly sensitive immunoassay detection probes”. In: *The Analyst* 141.24 (2016), pp. 6557–6563. DOI: `10.1039/c6an01253a`.

[61] Yingkun Yang et al. “Biodegradable Polymer Nanoparticles for Photodynamic Therapy by Bioluminescence Resonance Energy Transfer”. In: *Biomacromolecules* 19.1 (2018), pp. 201–208. DOI: `10.1021/acs.biomac.7b01469`.

[62] Dalu Chang et al. “Luciferase-Induced Photouncaging: Bioluminolysis”. In: *Angewandte Chemie (International ed. in English)* 58.45 (2019), pp. 16033–16037. DOI: `10.1002/anie.201907734`.

[63] Dalu Chang et al. “Luciferase Controlled Protein Interactions”. In: *Journal of the American Chemical Society* 143.10 (2021), pp. 3665–3670. DOI: `10.1021/jacs.0c11016`.

[64] Eric Lindberg et al. “Luciferase-induced photoreductive uncaging of small-molecule effectors”. In: *Nature communications* 9.1 (2018), p. 3539. DOI: `10.1038/s41467-018-05916-9`.

Chapter 2

Goals of the Thesis

Nanoparticles, owing to their high surface-to-volume ratio and their ability to penetrate tissues and cross membrane barriers, represent a promising platform for targeted and controlled drug delivery. They can encapsulate a plethora of therapeutic agents and extend their circulation time in vivo, thereby improving drug stability and bioavailability. Their size enables passive accumulation in tumor tissue via the enhanced permeability and retention (EPR) effect [1]. Furthermore, nanoparticle surfaces can be functionalized with biorecognition molecules, ligands, to actively target diseased tissues and enhance cellular uptake. Despite these advantages, unwanted off-target delivery remains a major limitation. More than 90 % of the applied nanoparticles do not reach the targeted tissues, thereby possibly harming healthy tissue or causing undesired side-effects [2]. Nanoparticles face several biological barriers, including opsonization and subsequent rapid cleance by the mononuclear phagocyte system, which removes most administered nanoparticles before they reach the target site [3]. In addition, off-target delivery can be exacerbated by the limited specificity of targeting ligands, particularly when their receptors are ubiquitously expressed throughout the body [4, 5]. To achieve enhanced control over the biodistribution of nanoparticles and to increase their tissue selectivity, the design of stimuli-responsive nanoparticles has recently gained significant attention [6, 7]. In particular, modification that occur dynamically after nanoparticle administration in biological environments are of high interest, as these dynamic surface modifications mirror adaptive strategies employed by viruses [8]. The engineering of such adaptable nanoparticles can be achieved by incorporating functional moieties into the nanoparticle design which respond to internal (pH, enzymes, redox) or external stimuli (light, magnetism, temperature) [9, 10]. Among these stimuli, light represents an especially promising external trigger as it is non-invasive and allows precise control with high spatiotemporal resolution [11]. However, the application of light as a trigger is not without limitations, primarily due to the phenomenon of tissue absorption, which significantly restricts the depth of penetration.

Chapter 1 addresses these challenges associated with light-based activation in biological environments, outlines the approaches developed to overcome them, and introduces the conceptual frameworks and mechanisms of light-controlled drug targeting.

Even if nanoparticles reach their target tissue, they typically still need to cross cellular membranes and escape the endosomal compartment to exert biological effects, processes that remain inherently challenging. Higher levels of positive charge enhance cellular uptake and may facilitate endosomal escape [12, 13]. However, increased positive charge is also associated with several drawbacks, including enhanced protein adsorption leading to premature clearance, stronger interactions with the extracellular matrix, and cytotoxic effects [14–16]. In contrast, nanoparticles bearing a negative surface charge exhibit reduced interactions with the extracellular matrix and lower degrees of opsonization.

Accordingly, the design of a nanoparticle system with switchable surface charge was investigated in **Chapter 3** (Figure 2.1). The core-shell nanoparticles consisted of poly(D,L-lactide-*co*-glycolide (PLGA) and a poly(ethylene glycol)-*b*-poly-(D,L-lactide) (PEG-PLA) block copolymer were modified with positively charged cell-penetrating peptide (CPP). CPPs are short peptide sequences that possess a high intrinsic capacity for cellular uptake and promotion of endosomal escape for intracellular cargo delivery but require temporary masking to avoid nonspecific interactions [17, 18]. To achieve switchable surface charge, a photo-labile protecting group (PPG) was incorporated into the nanoparticle design to transiently camouflage the CPP characteristics. In this chapter, an investigation is conducted into the physicochemical and biological characteristics of the photo-responsive nanoparticles, including their ability to mask CPP properties and undergo photocleavage.

Beyond externally activated systems, bioluminescent nanoparticles themselves have emerged as a unique class of functional nanomaterials with promising biomedical application including biosensing and bioimaging [19, 20]. Bioluminescent systems (BLS) rely on luciferase enzymes that autonomously generate light through the oxidation of their substrate, luciferin. This intrinsic light production offers several advantages over conventional fluorescence techniques by eliminating autofluorescence, photobleaching, and phototoxicity while providing high signal-to-noise ratios [21, 22]. Bioluminescent nanoparticles enable researchers to visualize biodistribution and accumulation in deep tissues where conventional fluorescence imaging is severely limited by absorption and scattering [22]. Many of the investigated bioluminescent nanomaterials are based on inorganic systems, in particular quantum dots or gold nanoparticles [23]. In contrast, polymeric nanoparticles have been explored far less, despite offering several important advantages. Their chemical versatility allows precise surface modification and encapsulation of drug molecules. Moreover, polymeric nanocarriers typically exhibit excellent biocompatibility and favorable degradation profiles, making them especially attractive for biomedical imaging and long-term in vivo studies [24].

In **Chapter 4** (Figure 2.1), a luciferase was introduced into our core-shell nanoparticle design. NanoLuc, a small luciferase originating from the deep-sea shrimp *Oplophorus gracilirostris*, was selected due to its highly favorable characteristics for a bioluminescent nanoparticle platform. Upon oxidation of its substrate furimazine, NanoLuc emits intense blue light with a high quantum yield and operates without the need for additional cofactors or coenzymes [25]. Moreover, it exhibits remarkable stability under acidic conditions and elevated temperatures, making it a robust and efficient source of bioluminescence within polymeric nanoparticle systems [26]. In this study, NanoLuc was further modified to potentially enhance its coupling compatibility and was subsequently analyzed for its luminescence activity before and after conjugation to nanoparticles.

Chapter 5 (Figure 2.1) aimed to combine the two implemented nanoparticle designs into bioluminescent-responsive nanoparticles. By harnessing endogenous, self-generated light, bioluminescent nanoparticles circumvent the scattering and absorption constraints that restrict conventional photoactivation. Specifically, the limited penetration depth of external light becomes irrelevant when the nanoparticle itself provides the energy required for PPG cleavage. Bioluminescence resonance energy transfer (BRET) is a non-radiative energy transfer process in which light emitted by a luciferase-substrate pair is directly transferred to the PPG. Efficient BRET depends on sufficient spectral overlap between donor (luciferase) and acceptor (PPG) as well as their proximity within the Foerster radius [27]. The photo-responsive nanoparticles from Chapter 3 exhibit deficient spectral alignment with NanoLuc, thereby limiting the probability of BRET-induced cleavage. Accordingly, this chapter investigates a red-shifted PPG that is compatible with NanoLuc emission as a new caging entity for CPP. Furthermore, the study focuses on determining whether sufficient BRET can be achieved within the nanoparticle system.

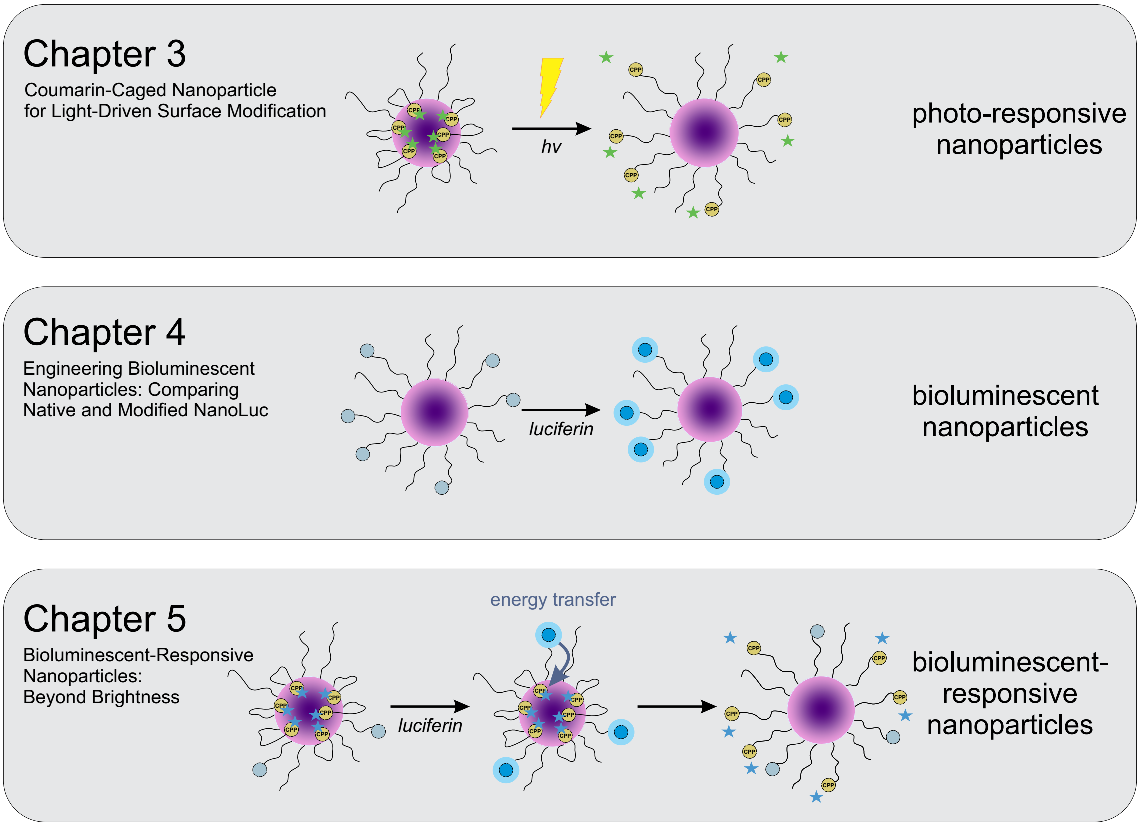

Figure 2.1: Schematic overview of the experimental thesis chapters. Chapter 3 describes the development of photo-responsive nanoparticles. Chapter 4 focuses on the design of bioluminescent nanoparticles by implementing NanoLuc variants into core-shell nanoparticles. Chapter 5 assesses whether NanoLuc-driven bioluminescence can effectively trigger photocleavage within the nanoparticle design.

References

[1] Alanood S. Alfutaimani et al. “Exploring the landscape of Lipid Nanoparticles (LNPs): A comprehensive review of LNPs types and biological sources of lipids”. In: *International journal of pharmaceutics: X* 8 (2024), p. 100305. DOI: `10.1016/j.ijpx.2024.100305`.

[2] Stefan Wilhelm et al. “Analysis of nanoparticle delivery to tumours”. In: *Nature Reviews Materials* 1.5 (2016). DOI: `10.1038/natrevmats.2016.14`.

[3] Zahid Hussain et al. “PEGylation: a promising strategy to overcome challenges to cancer-targeted nanomedicines: a review of challenges to clinical transition and promising resolution”. In: *Drug Delivery and Translational Research* 9.3 (2019), pp. 721–734. ISSN: 2190-3948. DOI: `10.1007/s13346-019-00631-4`.

[4] Maria Marti-Solano et al. “Combinatorial expression of GPCR isoforms affects signalling and drug responses”. In: *Nature* 587.7835 (2020), pp. 650–656. DOI: `10.1038/s41586-020-2888-2`.

[5] Ying Shen et al. “Transferrin receptor 1 in cancer: a new sight for cancer therapy”. In: *American journal of cancer research* 8.6 (2018), pp. 916–931. ISSN: 2156-6976.

[6] Alan Clavelland Ochioni, Italo Rennan Sousa Vieira, and Carlos Adam Conte-Junior. “Advances in stimuli-responsive nanoparticles for cancer therapy: Mechanisms, functional materials, and emerging technologies”. In: *Journal of Drug Delivery Science and Technology* 114 (2025), p. 107519. ISSN: 17732247. DOI: `10.1016/j.jddst.2025.107519`.

[7] Nikolitsa Nomikou, Hamzah Masood, and Shiv Patel. “Stimulus-Responsive Nanoparticles for Drug Delivery”. In: *Fundamentals of Pharmaceutical Nanoscience*. Ed. by Ijeoma F. Uchegbu et al. Cham: Springer Nature Switzerland, 2024, pp. 389–422. ISBN: 978-3-031-59477-9. DOI: `10.1007/978-3-031-59478-6_15`.

[8] Zhihuan Liao et al. “Virus-inspired nanosystems for drug delivery”. In: *Nanoscale* 13.45 (2021), pp. 18912–18924. DOI: `10.1039/D1NR05872J`.

[9] Eun Seong Lee et al. “Super pH-sensitive multifunctional polymeric micelle for tumor pH(e) specific TAT exposure and multidrug resistance”. In: *Journal of controlled release : official journal of the Controlled Release Society* 129.3 (2008), pp. 228–236. DOI: `10.1016/j.jconrel.2008.04.024`.

[10] Nien-Chu Fan et al. “Photocontrolled targeted drug delivery: photocaged biologically active folic acid as a light-responsive tumor-targeting molecule”. In: *Angewandte Chemie (International ed. in English)* 51.35 (2012), pp. 8806–8810. DOI: `10.1002/anie.201203339`.

[11] Mahdi Karimi et al. “Smart Nanostructures for Cargo Delivery: Uncaging and Activating by Light”. In: *Journal of the American Chemical Society* 139.13 (2017), pp. 4584–4610. DOI: `10.1021/jacs.6b08313`.

[12] Slavko Kralj et al. “Effect of surface charge on the cellular uptake of fluorescent magnetic nanoparticles”. In: *Journal of Nanoparticle Research* 14.10 (2012). ISSN: 1388-0764. DOI: `10.1007/s11051-012-1151-7`.

[13] Dehua Pei and Marina Buyanova. “Overcoming Endosomal Entrapment in Drug Delivery”. In: *Bioconjugate Chemistry* 30.2 (2019), pp. 273–283. DOI: `10.1021/acs.bioconjchem.8b00778`.

[14] Qiuju Dai et al. “Enzyme-Responsive Modular Peptides Enhance Tumor Penetration of Quantum Dots via Charge Reversal Strategy”. In: *ACS applied materials & interfaces* 16.5 (2024), pp. 6208–6220. DOI: `10.1021/acsami.3c11500`.

[15] Hana Cho et al. “Beyond Nanoparticle-Based Intracellular Drug Delivery: Cytosol/Organelle-Targeted Drug Release and Therapeutic Synergism”. In: *Macromolecular bioscience* 24.7 (2024), e2300590. DOI: `10.1002/mabi.202300590`.

[16] Xiao-Ru Shao et al. “Independent effect of polymeric nanoparticle zeta potential/surface charge, on their cytotoxicity and affinity to cells”. In: *Cell proliferation* 48.4 (2015), pp. 465–474. DOI: `10.1111/cpr.12192`.

[17] Alessandro Gori et al. “Cell Penetrating Peptides: Classification, Mechanisms, Methods of Study, and Applications”. In: *ChemMedChem* 18.17 (2023), e202300236. DOI: `10.1002/cmdc.202300236`.

[18] Ashweta Sahni, Ziqing Qian, and Dehua Pei. “Cell-Penetrating Peptides Escape the Endosome by Inducing Vesicle Budding and Collapse”. In: *ACS chemical biology* 15.9 (2020), pp. 2485–2492. DOI: `10.1021/acschembio.0c00478`.

[19] Min-Kyung So et al. “Self-illuminating quantum dot conjugates for in vivo imaging”. In: *Nature Biotechnology* 24.3 (2006), pp. 339–343. ISSN: 1546-1696. DOI: `10.1038/nbt1188`.

[20] Yusuke Ikeda et al. “Design of luciferase-displaying protein nanoparticles for use as highly sensitive immunoassay detection probes”. In: *The Analyst* 141.24 (2016), pp. 6557–6563. DOI: `10.1039/c6an01253a`.

[21] Anna C. Love and Jennifer A. Prescher. “Seeing (and Using) the Light: Recent Developments in Bioluminescence Technology”. In: *Cell chemical biology* 27.8 (2020), pp. 904–920. DOI: `10.1016/j.chembiol.2020.07.022`.

[22] Enya Li et al. “Macromolecular assembly of bioluminescent protein nanoparticles for enhanced imaging”. In: *Materials today. Bio* 17 (2022), p. 100455. DOI: `10.1016/j.mtbio.2022.100455`.

[23] Polina M. Ivantcova et al. “Exploring the synergy between bioluminescence and nanomaterials: Innovations in analytical and therapeutic applications”. In: *Colloids and surfaces. B, Biointerfaces* 251 (2025), p. 114631. DOI: `10.1016/j.colsurfb.2025.114631`.

[24] Małgorzata Geszke-Moritz and Michał Moritz. “Biodegradable Polymeric Nanoparticle-Based Drug Delivery Systems: Comprehensive Overview, Perspectives and Challenges”. In: *Polymers* 16.17 (2024). DOI: `10.3390/polym16172536`.

[25] Christopher G. England, Emily B. Ehlerding, and Weibo Cai. “NanoLuc: A Small Luciferase Is Brightening Up the Field of Bioluminescence”. In: *Bioconjugate Chemistry* 27.5 (2016), pp. 1175–1187. DOI: `10.1021/acs.bioconjchem.6b00112`.

[26] Mary P. Hall et al. “Engineered luciferase reporter from a deep sea shrimp utilizing a novel imidazopyrazinone substrate”. In: *ACS chemical biology* 7.11 (2012), pp. 1848–1857. DOI: `10.1021/cb3002478`.

[27] Th. Förster. “Zwischenmolekulare Energiewanderung und Fluoreszenz”. In: *Annalen der Physik* 437.1-2 (1948), pp. 55–75. ISSN: 0003-3804. DOI: `10.1002/andp.19484370105`.

Chapter 3

Coumarin-Caged Nanoparticle for Light-Driven Surface Modification

Published in ChemMedChem

This chapter was published as: Birringer, J., Konrad, J., Melchner, S., Remmert, M., & Goepferich, A. (2025). Coumarin-Caged Nanoparticle for Light-Driven Surface Modification. *ChemMedChem*, *20*(22), e202500636.

Abstract

Photo-labile protecting groups (PPGs) allow for the selective activation of an originally caged moiety by light exposure at a specific wavelength. Incorporation of PPG in nanoparticles (NPs) enables precise spatiotemporal control over NPs surface properties. Thus, physicochemical and biological properties of NPs can be modified even after administration in a biological environment. In this study, this mechanism is used to control the cell uptake of NPs. To this end, polymeric core-shell NPs are used composed of poly(D,L-lactide-*co*-glycolide) and a poly(ethylene glycol)-*b*-poly(D,L-lactide) block copolymer modified with positively charged cell-penetrating peptide (CPP). Surface charge of CPP-NPs (+23.50 mV), measured as zetapotential, is effectively diminished by the attachment of coumarin-derived PPG to CPP (+12.50 mV) resulting in reduced cell uptake. Upon light irradiation with light-emitting diode ($\lambda = 365\,\text{nm}$) the PPG is cleaved, restoring the zetapotential (+24.67 mV) and triggering an enhanced cell uptake. This opens the door to trigger the cellular uptake of NPs that are intended to transport drugs to their target cells in the future.

Graphical Abstract

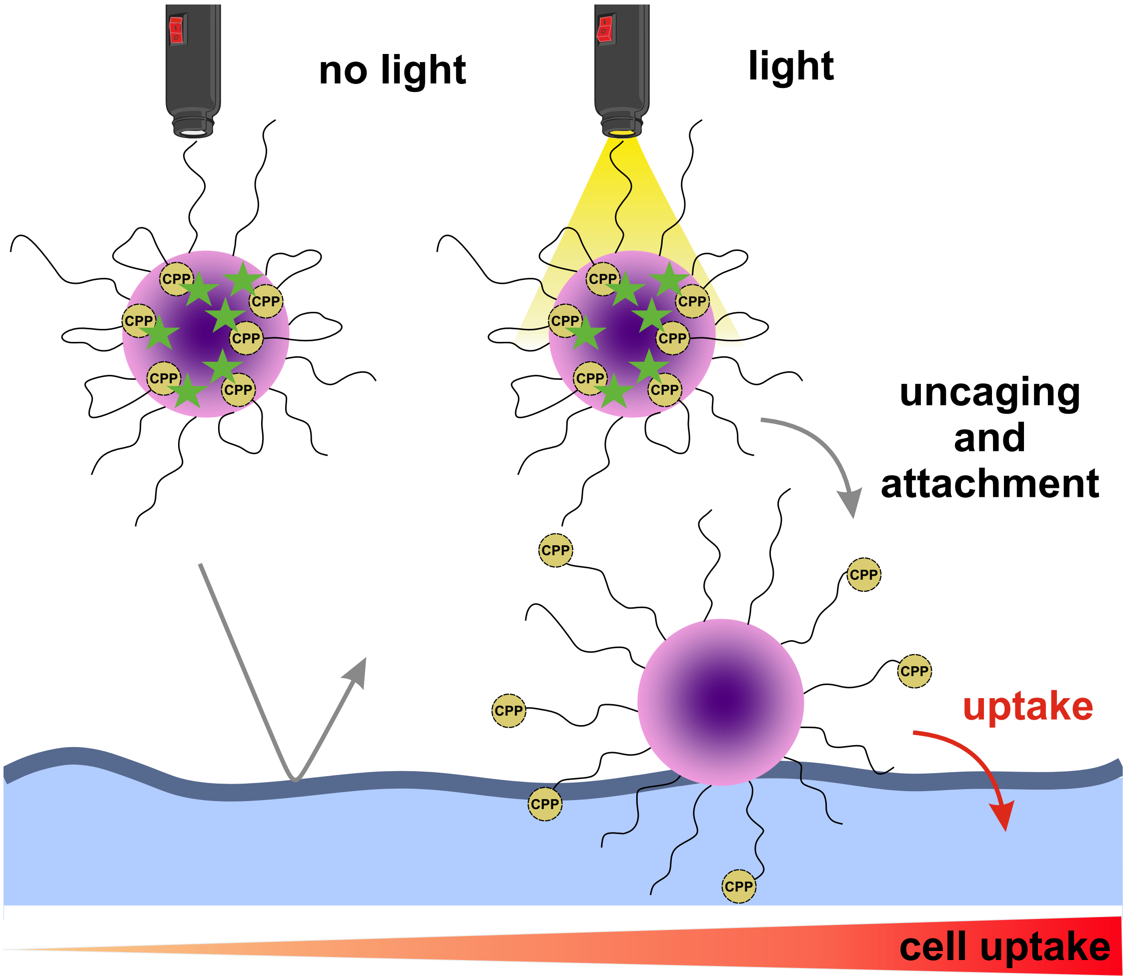

Photo-responsive nanoparticles (NPs) enable spatiotemporal control over drug delivery. Attachment of a photo-labile protecting group (PPG) to cell-penetrating peptide (CPP) effectively camouflages the positive charge of NPs. Light irradiation cleaves the PPG, exposing the CPP on the NP surface and thereby enhancing cellular uptake.

3.1 Introduction

Polymeric nanoparticles (NPs) are regarded as a promising platform for targeted drug delivery and controlled drug release to cells. However, despite active targeting concepts, NPs reach the targeted tissue only in a single-digit percentage range. Consequently, more than 90 % of the applied NPs can cause undesired effects at off-target sites [1]. To achieve enhanced control over the NPs' biodistribution and to increase their tissue selectivity, the design of modular physicochemical properties has recently attracted more attention [2, 3]. Especially, modification of properties after NP administration in a biological environment are of high interest as these dynamic surface modifications mirror adaptive strategies employed by viruses [4, 5]. To obtain adaptable NPs, moieties responding to either internal (pH, enzymes, redox) or external (light, magnetism, temperature) stimuli can be implemented [6, 7]. Light is an excellent external trigger as it is non-invasive and offers high spatial and temporal resolution and control [8]. However, light penetration in tissues remains challenging. Especially in the visible and ultraviolet region, tissue scatters and significantly absorbs light. Thus, light suffers from a rather limited penetration depth and is only reasonably applicable to tissues that can be directly penetrated, such as the vitreous of the eyes [9–12]. Despite this limitation, innovative strategies to use light for photo-controlled drug release or drug delivery [13–15] have been developed as it is independent of the biological environment.

In terms of photo-controlled drug delivery, photo-labile protecting groups (PPG), also referred to as "photocage", are commonly used. PPG can, thereby, mask the biological function of a moiety, such as cell-penetrating peptides (CPP), providing spatiotemporal control over their visibility [16]. CPPs have the ability to penetrate cell membranes and facilitate the intracellular delivery of associated cargos [17, 18]. Furthermore, it is hypothesized that CPPs promote endosomal escape [19–21]. Consequently, CPPs are considered a precious tool for NP surface functionalization, improving intracellular drug delivery. The transactivator of transcription (TAT) protein from human immunodeficiency virus (HIV), one of the most studied CPPs, is rich in basic amino acids (2 lysine and 6 arginine) causing a highly positive net charge [22]. Functionalizing NPs with TAT alters their surface charge and increases NP uptake [23]. The incorporation of coumarin-derived PPG (DEAC) into the TAT sequence masks some of the positive charges that mediate cell uptake and cause the hiding of the sequence inside the NP corona (Figure 3.1 A, C) [12, 24]. Upon light irradiation the PPG is cleaved, presenting TAT on the NP surface restoring the CPP's penetration enhancing properties.

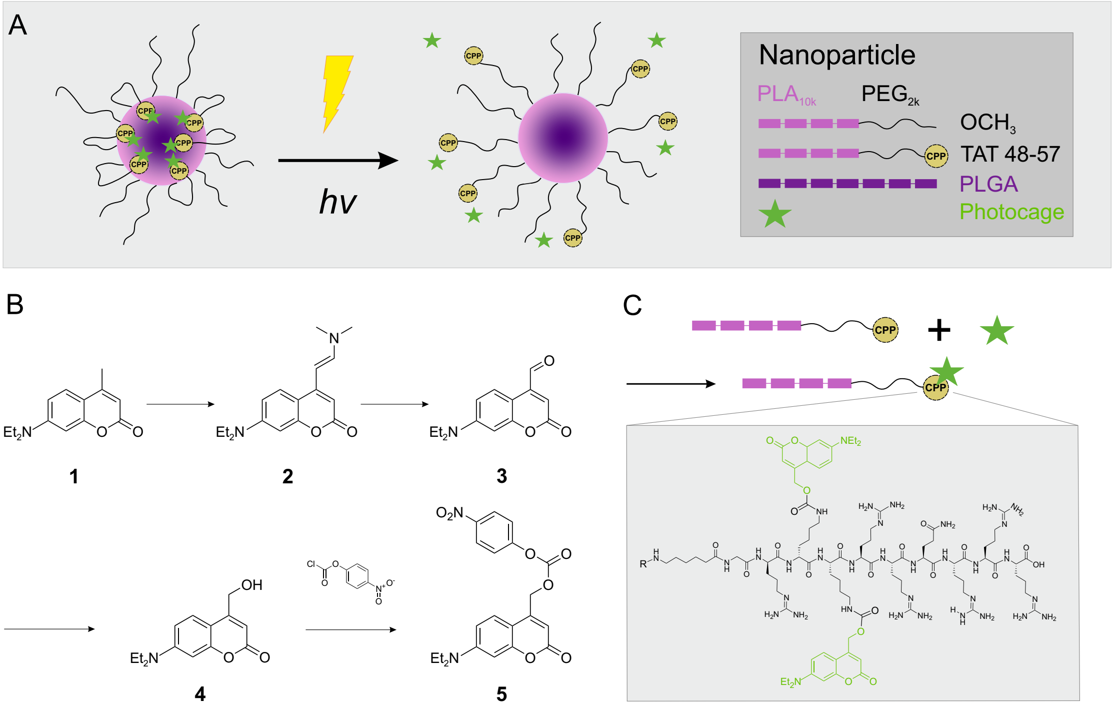

Figure 3.1: Schematic representation of photo-responsive NPs and synthesis of photo-labile protecting group (PPG). **A** Photo-responsive core-shell nanoparticle composed of PLGA and PEG-PLA block copolymer, with its surface functionalized by photocaged CPP. **B** Synthesis scheme of coumarin-derived PPG. **C** Schematic synthesis of photocaged TAT-polymer. The amino acid sequence of TAT 48-57 (CPP) is depicted in the grey box. Coumarin-derived PPG (green) is attached to the lysine residues of TAT 48-57.

In the work of Wang et al., this caging concept was already established using polymeric micelles consisting of poly(ethylene glycol)-*b*-poly(D,L-lactide) (PEG-PLA) block copolymer, which are relatively stable in vitro [12, 25]. However, in vivo stability of block copolymer micelles is poor with a dissociation time of less than 10 min [26]. However, long circulation times of NPs in blood are crucial for their use in chronic disease treatment as otherwise repeated dosing in brief intervals is necessary. In contrast to polymeric micelles, NPs have better stability in vivo. Core-shell NPs consisting of poly(D,L-lactide-*co*-glycolide) (PLGA) and PEG-PLA block copolymer for example are stable for at least 10 days [27].

Stability of drug delivery system is intrinsically linked with the release of the incorporated drug. Thus, poor stability of micelles can lead to premature drug release causing undesirable side effects or even worse, decreasing the therapeutic efficacy [26, 28, 29]. Reports in the literature have demonstrated that NPs composed of a core material with high molecular weight retain hydrophobic drugs better than micelles and have an increased circulation time in the blood [30].

In addition to enhanced stability, NPs offer significant advantages in ligand presentation and molecular engineering. Like liposomes, which are known for their membrane fluidity, copolymeric micelles exhibit characteristic single-chain exchange [31, 32]. Dynamic rearrangement of polymer chains might cause functional loss of hydrophobic ligands as these moieties can become embedded in micellar core [33]. In core-shell NP design, the mobility of block copolymer is reduced due to their anchoring within the hydrophobic core. However, this assembly preserves flexibility allowing ligand mobility and enhanced avidity [34]. Moreover, the use of solid core NPs facilitates stable surface engineering [35].

Therefore, our goal was to scrutinize whether the concept of camouflaging CPPs with PPGs could also be used for NPs. The specific aim of this study was to design a NP system, that offers spatiotemporal control over NP uptake by target cells.

3.2 Material and Methods

3.2.1 Materials

Ultrapure water was obtained from a Milli-Q water purification system (Millipore, Schwalbach, Germany). Unless otherwise stated, all chemicals and reagents were obtained from Sigma-Aldrich (Taufkirchen, Germany) in analytical grade. Heterobifunctional poly(ethylene glycol)carboxylic acid with a molecular mass of $2000\,\mathrm{g\,mol^{-1}}$ (COOH-PEG$_{2k}$-OH) was purchased from Jenkem Technology USA, Inc. (Allen, TX, USA). Poly(ethylene glycol) methyl ether with a molecular mass of $2000\,\mathrm{g\,mol^{-1}}$ (mPEG$_{2k}$-OH) as well as Resomer RG 502 H, poly(D,L-lactide-*co*-glycolide) (lactide:glycolide 50:50, acid terminated, M$_w$ 7000-17 000 Da) (PLGA) were obtained from Sigma-Aldrich (Taufkirchen, Germany). 1-Ethyl-3-(3-dimethylaminopropyl)carbodiimide (EDC) and 7-(diethylamino)-4-(hydroxymethyl)coumarin (DEAC) were sourced from TCI (Eschborn, Germany). N-Hydroxysuccinimide (NHS) was purchased from Carl Roth (Karlsruhe, Germany). 1-[Bis(dimethylamino)-methylene]-1H-1,2,3-triazolo[4,5-b]pyridinium 3-oxide hexafluorophosphate (HATU) was obtained from Fluorochem (Gadfield, United Kingdom). The fluorescent dye Cy5 was purchased from Lumiprobe (Hannover, Germany). 7-(Diethylamino)-4-methyl-coumarin, N,N-dimethylformaidedimethylacetal (DMF-DMA), 4-nitrophenyl-chloroformate, and protected amino acids Fmoc-Arg(Pbf)-OH, Fmoc-Gln(Trt)-OH, Fmoc-D-Lys(Boc)-OH, Fmoc-Gly-OH and Fmoc-6-AHx-OH were obtained from BLD-pharm (Karlsruhe, Germany). While Fmoc-Tyr(tBu)-OH was purchased from Iris Biotech (Marktredwitz, Germany). 2-Chlorotrityl chloride resin was sourced from Carbolution Chemicals (St. Ingbert, Germany). Sodium metaperiodate ($NaIO_4$) was purchased from VWR International GmbH (Darmstadt, Germany). The cellulose dialysis membranes had a molecular weight cut-off (MWCO) of 6-8 kDa and were obtained from Spectrum Laboratories, Inc. (Rancho Domingues, CA, USA). The frits had a pore size of 35 µm and were sourced from Roland Vetter Laborbedarf (Ammerbuch, Germany). The infrared lamp was obtained from Medisana (Neuss, Germany), with a thermostat from PEARL GmbH (Buggingen, Germany). Syringes were purchased from Braun (Melsungen, Germany). Nuclear magnetic resonance (NMR) spectra were recorded on a Bruker Avance-400 or Avance-500 NMR spectrometer (Bruker, Billerica, MA, USA). High-resolution mass spectrometry (HRMS) was performed on a Q-TOF 6540 ultrahigh definition(UHD) liquid chromatography/mass spectrometry (LC/MS) system (Agilent Technologies, Santa Clara, CA, USA) using an electrospray ionization (ESI) source. High-performance liquid chromatography (HPLC) analysis was performed with 1260 Infinity II from Agilent Technologies (Santa Clara, CA, USA) using a Kinetex EVO C18 column (100 Å, 2.6 µm, 150 mm x 4.6 mm, Phenomenex Ltd., Germany). Preparative HPLC analysis was performed with Prep 150 LC system from Waters (Eschborn, Germany) consisting of a 2545 binary gradient module, a 2489 UV/visible detector and a Waters Fraction Collector III. A Gemini-NX C18 column (110 Å, 5 µm, 250 mm × 21 mm, Phenomenex Ltd., Germany) was used. Flash chromatography was performed with puriFlash® XS520Plus (Advion Interchim scientific, Ithaka, NY, USA) using pre-packed silica cartridges. HeLa (CCL-2) cells were purchased from ATCC (Manassas, VA, USA). For all microscopic experiments, the cells were seeded in 8-well microscopy slides from Ibidi (Graefelfing, Germany). Dako Faramount Mounting Medium was obtained from Agilent Technologies (Santa Clara, CA, USA). CellMask™ Green was purchased from Invitrogen, Life Technologies GmbH (Darmstadt, Germany). Dulbecco's phosphate-buffered saline (DPBS) was prepared inhouse according to the standard formulation, filtrated and autoclaved before use.

3.2.2 Synthesis of Cell-Penetrating Peptide

The TAT sequence was synthesized by manual solid-phase peptide synthesis using a standard Fmoc strategy following the procedure of Bresinsky et al. [36]. The 2-chlorotrityl chloride resin (300 mg, 1.182 mmol g^{-1}, 0.355 mmol, 1.00 equiv) was weighed into a fritted 20 mL syringe. 15 mL of dichloromethane (DCM) was added to swell the resin at room temperature (RT) for 30 min. Subsequently, DCM was then aspirated with a vacuum flask. The first amino acid (2.50 equiv) was dissolved in the smallest possible volume of DCM. If this was not feasible, small quantities of dimethylformamide (DMF) were added gradually until complete dissolution was achieved. 2.50 equiv of 2,4,6 collidine was added and the solution was transferred into the syringe and shaken for 3 h at RT. Subsequent to the aspiration of the solvent, the resin containing the bound amino acid was rinsed three times with 15 mL DCM. A total of 15 mL of piperidine 20 % (V/V) in DMF was drawn into a syringe and agitated on an orbital shaker at 35 °C for 15 min to remove the N-terminal Fmoc-protecting group. The shaker was covered with a box insulated with aluminium foil and the temperature was adjusted with an infrared lamp. Temperature was controlled by a thermostat. After deprotection, the residual resin was washed with 15 mL DMF. For the subsequent coupling steps, the respective amino acid (2.50 equiv) and HATU (2.50 equiv) were weighed in separately. Both were dissolved in 7 mL respectively 5 mL DCM and collidine (2.50 equiv) were added to the solution of HATU. Afterwards, both solutions were transferred into the syringe and agitated for 1 h at RT. The deprotecting and coupling steps were repeated until the TAT sequence was built up. Finally, the resin was rinsed with methanol, DCM, diethyl ether, each (2 x 15 mL), using a vacuum flask. For peptide detachment from resin, the dried resin was transferred into a round-bottom flask and a solution of hexafluoroisopropanol

20 % (HFIP) in DMF was added dropwise. After stirring for 2 h, the solution was filtrated, and the filtrate was evaporated. Then, the sidechain protected peptide was analyzed via HPLC and mass spectrometry. For further detail see Supporting Information (Table S3.1).

3.2.3 Polymer Synthesis

COOH-PEG$_{2k}$-PLA$_{10k}$ and mPEG$_{2k}$-PLA$_{10k}$ block copolymers were synthesized according to Qian et al. with modifications as previously described by our group [37, 38]. In brief, the heterobifunctional PEG polymer (1 equiv.), COOH-PEG$_{2k}$ respectively mPEG$_{2k}$, served as macroinitiator for the reaction with cyclic lactide (3,6-dimethyl-1,4-dioxane-2,5-dione) (70 equiv.). Both were dissolved in anhydrous DCM and mixed with 1,8-diazabicyclo[5.4.0]undec-7-ene (DBU) (3 equiv.). The mixture was stirred for precisely 1 h at RT. Subsequently, the polymerization reaction was quenched with benzoic acid (10 equiv.). The reaction product was precipitated in 20-fold amount of ice-cold diethyl ether and dried under nitrogen flow overnight at RT. The resulting polymers were characterized via ^{1}H-NMR.

3.2.4 Fluorescence Labeling of PLGA

To detect NPs in cells, the core forming PLGA was covalently linked to a fluorescent dye as previously described by our group [39]. In brief, carboxylic acid-terminated PLGA (Resomer RG 502 H) (1 equiv.) and cyanine-5-amine (0.1 equiv.) were dissolved in anhydrous DMF. For activation of the carboxylic acid 2-(1H-benzotriazol-1-yl)-1,1,3,3-tetramethyluronium-hexafluorophosphat (HBTU) (2 equiv.) was added to the reaction mixture. Subsequently, N-ethyl-N-(propan-2-yl)propan-2-amine (DIPEA) (4 equiv.) was added and the reaction mixture was stirred overnight at RT under light exclusion. The excess of free fluorescent dye was removed by precipitation in 20-fold amount of ice-cold diethyl ether and dried under nitrogen. The polymer was dissolved in ACN and precipitated again. This step was repeated until the supernatant was no longer blue. The product was dried under nitrogen flow at RT.

3.2.5 Synthesis of 7-Diethylamino-4-Hydroxymethylcoumarin (DEAC)

The PPG 7-diethylamino-4-hydroxymethylcoumarin (DEAC) was synthesized as previously described by Weinrich et al. with small modifications [40]. Synthesis scheme is depicted in Figure 3.1 B. For detailed synthesis see Supporting Information.

3.2.6 Activation of DEAC

For synthesis of caged TAT ([TAT]) the photocage DEAC needed to be activated. Therefore, the hydroxy function was transformed into a reactive carbonate. A solution of DEAC **4** (234 mg, 946 µmol, 1.00 equiv.) and 4-nitrophenylchloroformate (1.91 g, 9.47 mmol, 10.0 equiv.) in anhydrous DCM (25 mL) was cooled to 0 °C. DIPEA (1.65 mL, 9.47 mmol, 10.0 equiv.) was added dropwise and stirred for 15 min. The reaction solution was then stirred for 6 h at RT. Subsequently, the mixture was washed twice with 0.01 N HCl (100 mL). Organic layer was removed under reduced pressure. Purification of synthesis product was performed by preparative HPLC. The mobile phase consisted of solvent A (Millipore water with 0.1 % trifluoroacetic acid, TFA) and solvent B (acetonitrile). The separation was initiated with an isocratic hold at 20 % B for 1 min, followed by a linear gradient from 20 % to 95 % B over 19 min at a flow rate of 20 mL/min. Detection was performed at 220 nm. Fractions containing the desired product were collected, pooled, and lyophilized to yield the purified compound. The compound was analyzed by MS, NMR and HPLC.

3.2.7 TAT 48-57 Coupling to Polymer

For activation of block copolymer, COOH-PEG$_{2k}$-PLA$_{10k}$ was dissolved in anhydrous DMF. EDC and NHS (each 25 equiv.) were added as powder. The mixture was stirred for 1 h at RT. β-mercaptoethanol (35 equiv.) were added for 15 min at RT to quench the excess of EDC. The protected TAT 48-57 was dissolved in 1 mL DMF and added to the reaction mixture. DIPEA (10 equiv.) was added, and the reaction was stirred for 24 h at RT. Subsequently, the reaction product was precipitated in 20-fold amount of ice-cold diethyl ether and dried under nitrogen flow overnight at RT. Deprotection of all sidechains of the TAT 48-57 was performed after the coupling reaction to enable a specific N-terminus coupling to the polymer. The modified polymer was dissolved in a mixture of 3 mL trifluoroacetic acid, phenol, water, triisopropyl silane (88/5/5/2 [%]) and stirred for 1 h at RT. Afterwards, the reaction product was precipitated in 20-fold amount of ice-cold diethyl ether and dried under vacuum overnight. The reaction product was dissolved in as little acetonitrile (ACN) as possible. Small quantities of dimethyl sulfoxide were used as solubilizer. Polymeric micelles were produced by dropwise addition of polymer solution into a 10-fold excess of vigorously stirring Millipore water. The solution was stirred for 3 h under a fume hood to evaporate the organic solvent. The excess of TAT48-57 and regents were removed by dialysis. Polymeric micelles were transferred into a dialysis tube with a MWCO of 6-8 kDa and were dialyzed against 4 L of Millipore water with medium change after 30 min, 2 h and 14 h; 19 h total. The polymeric micelles were lyophilized to obtain TAT48-57-PEG$_{2k}$-PLA$_{10k}$ (TAT-PEG$_{2k}$-PLA$_{10k}$).

The coupling efficiency (CE) was determined by Fluram assay.

3.2.8 Fluram Assay

Initially, the amount of lysine hydrochloride corresponding to 100 % CE was calculated (Supporting Information, Equation (3.7)). A calibration line was recorded in order to verify the linear relationship between free primary amine and fluorescence signal. Therefore, lysine hydrochloride stock solution (2 mg mL^{-1} in Millipore water) was diluted to reach a concentration range of 5-40 µg mL^{-1}. Micelles of TAT-PEG$_{2k}$-PLA$_{10k}$ were formed by nanoprecipitation. TAT-PEG$_{2k}$-PLA$_{10k}$ stock solution was diluted to a concentration of 10 mg mL^{-1} and dropwise added into 10-fold amount of Millipore water with vigorous stirring. The solution was stirred for 3 h under a fume hood to evaporate the organic solvent. Fluorescamine reagent was freshly prepared by dissolving fluorescamine in acetone to reach a final concentration of 0.3 mg mL^{-1}. The assay was performed by pipetting 170 µL borate buffer (pH 8.5) into a white 96-well plate. Subsequently, 10 µL of micelles or lysine hydrochloride was added on top and the well plate was shaken for 5 min at 150 rpm. The pH was checked to be at 8.5. Afterwards, 20 µL fluorescamine reagent was added to the mixture and incubated at RT for 1 min while shaking at 150 rpm. The fluorescence was measured at $\lambda_{em} = 485$ nm ($\lambda_{ex} = 380$ nm) on a FLUOstar Omega plate reader (BMG Labtech, Ortenberg, Germany). The CE was determined by setting the measured value of TAT micelles in relation to the amount of lysine hydrochloride which corresponds to 100 % CE.

3.2.9 Synthesis of Caged Polymer [TAT]-PEG$_{2k}$-PLA$_{10k}$

TAT-PEG$_{2k}$-PLA$_{10k}$ (80 mg, 5.91 µmol, 1.00 equiv.) was dissolved in the smallest possible amount of DMF. Subsequently, DIPEA (15.3 µL, 87.8 µmol, 14.8 equiv.) and activated DEAC (18.14 mg, 44.03 µmol, 7.44 equiv.) were added to the solution and stirred for 6 days at RT. Subsequently, the reaction product was precipitated in 20-fold amount of ice-cold diethyl ether and dried under nitrogen flow overnight at RT.

3.2.10 Quantification of Caged Polymer

DEAC (10 mg mL^{-1}) and [TAT]-PEG$_{2k}$-PLA$_{10k}$ (40 mg mL^{-1}) were dissolved in ACN. DEAC was diluted to achieve a concentration range of 2.5-20 µg mL^{-1} for construction of a calibration line. [TAT]-PEG$_{2k}$-PLA$_{10k}$ was diluted to 400 µg mL^{-1}. Absorption spectra were recorded, and absorbance was measured at $\lambda_{ex} = 377$ nm on a FLUOstar Omega plate reader. The absorption was used to calculate CE of DEAC to TAT polymer (Supporting Information, Equation (3.11)).

3.2.11 Spectral Characterization of DEAC and DEAC Conjugates

Absorption measurements were performed using a FLUOstar Omega plate reader. Therefore, 200 µL samples were transferred into quartz 96 well plate (Hellma GmbH & Co. KG, Müllheim, Germany). Fluorescence spectra were obtained by Cary Eclipse or BioTek Synergy Neo2 (Agilent Technologies, Santa Clara, CA, USA) using a quartz cuvette or black well plate.

3.2.12 Photocleavage of DEAC

For all uncaging experiments a light-emitting diode (LED, LED-TECH.DE optoelectronics GmbH, Moers, Germany) with $\lambda_{em} = 365\,\text{nm}$ and lens SM2F (Thorlabs Inc., NJ, USA) were used (Supporting Information, Figure S3.17 A). The LED irradiance power was measured with FieldMax II Top laser power and energy meter (Coherent, Saxonburg, PA, USA). The sample was transferred into a micro-UV-transparent cuvette (Brand GmbH+Co KG, Wertheim, Germany) and irradiated with different powers and over different times.

Cleavage of DEAC-NH-PEG$_{2k}$-PLA$_{10k}$

In order to determine irradiation time and energy required for photocleavage of DEAC, DEAC-NH-PEG$_{2k}$-PLA$_{10k}$ was irradiated under various conditions. The uncaging was monitored via HPLC. The mobile phase consisted of solvent A (Millipore water with 0.05 % TFA) and solvent B (acetonitrile with 0.05 % TFA). The flow rate was maintained at 1 mL/min The chromatographic method initiated with an isocratic hold at 95 % A / 5 % B for 1 min, followed by a linear gradient to 5 % A / 95 % B over 15 min. The high-organic phase was maintained for 4 min, after which the system was returned to the initial conditions (95 % A / 5 % B) for column re-equilibration. Detection was carried out with a fluorescence detector with excitation at 375 nm and emission monitored at 480 nm.

Uncaging of [TAT]-Nanoparticles

The cleavage of DEAC from [TAT]-NP was studied by zetapotential measurements. First, NPs were irradiated for 1 min, 2 min and 5 min with a LED power of 100 mW. Subsequently, NPs were diluted 1:20 in 2 mM $NaCl_2$ and then zetapotential was measured with Malvern Zetasizer Nano ZS (Malvern, United Kingdom).

3.3 Photobleaching of Cy5

Photobleaching of Cy5 was observed during uncaging experiments. Therefore, further investigations on quantification of photobleaching were performed. Carboxy-terminated NP (COOH-NP) as well as [TAT]-NP [TAT]-NP were irradiated for various time points with a LED power of 100 mW. Afterwards, NPs were diluted 1:4 with Millipore water and fluorescence intensity of Cy5 ($\lambda_{ex} = 640\,\text{nm}$, $\lambda_{em} = 681\,\text{nm}$) was measured. A photobleaching correlation factor (k) was calculated (eq. (3.1)).

$$k = \frac{RFU_{no\ irradiation}}{RFU_{60\,\text{s}}} \tag{3.1}$$

RFU is defined as relative fluorescence units.

3.3.1 Nanoparticle Preparation and Characterization

Core-shell NPs were manufactured by nanoprecipitation. PLGA and the corresponding PLA-PEG copolymer were dissolved at a ratio of 30/70 (m/m) in ACN reaching a final concentration of $10\,\text{mg}\,\text{mL}^{-1}$. The organic phase was added dropwise into the 10-fold excess of stirring (900 rpm) 10 % Dulbecco's phosphate-buffered saline (DPBS). The mixture was stirred for 3 h at RT to remove the organic solvent. NP with methoxy-terminated polymer chains (mPEG$_{2k}$-PLA$_{10k}$) served as a negative control, whereas NP consisting of 50 % TAT-PEG$_{2k}$-PLA$_{10k}$ and 50 % mPEG$_{2k}$-PLA$_{10k}$ served as a positive control.

NP tracking analysis (NTA) (NanoSight NS300, Malvern, United Kingdom) was used to determinate NP size (hydrodynamic diameter, d_h) and concentration. For NTA measurements the NPs were diluted with Millipore water to reach a particle concentration of 20-100 particles per frame. The polydispersity index (PDI) was calculated with the following equation.

$$PDI = (\frac{\sigma}{\mu})^2 \tag{3.2}$$

μ is defined by the mean particle size and σ is representing the standard deviation.

Zetapotential measurements were performed with Malvern Zetasizer Nano ZS (Malvern, United Kingdom). Therefore, NP were diluted with 2 mM NaCl$_2$ by a factor of 20.

3.3.2 Cell Culture

HeLa cells were cultivated in Eagle's minimum essential medium (EMEM) and with 10 % fetal bovine serum (FBS) (PAN-biotech GmbH, Aidenbach, Germany).

3.3.3 Flow Cytometry

HeLa cells were seeded into 24-well plates at a concentration of 80 000 cells/well and incubated for 24 h at 37 °C and 5 % CO_2. NPs containing Cy5-PLGA were prepared and characterized. [TAT]-NP were uncaged by irradiation with LED for 1 min at 100 mW and zetapotential was measured as described before. Leibovitz medium (LM) was used to adjust the NP concentration to 100 pM. The cell medium was discarded and 200 µL of NP formulation was added to each well. LM was used as cell blank. After incubation for 60 min at 37 °C, 5 % CO_2, the particle solution was discarded, washed with 500 µL warm DPBS and the cells were harvested using 300 µL of 0.05 % typsin/0.02 % EDTA solution. All subsequent work was done on ice. After complete cell detachment, typsin was quenched by the addition of 400 µL EMEM + 10 % FBS and the cell suspension of each well was transferred into Eppendorf Tubes®. After centrifugation for 5 min at 200 rcf at 4 °C, the supernatant was aspirated and the cell pellets were washed with 500 µL cold DPBS. Centrifugation step was repeated and the cell pellets were resuspended in 300 µL cold n DPBS and stored on ice. Directly before the flow cytometry measurement, the cell suspension was transferred into flow cytometry tubes. The samples were analyzed using a FACS Canto II (Becton Dickinson, Franklin Lakes, NJ). NPs were excited at 633 nm, and the emission was recorded using a 661/16 nm bandpass filter. Flow cytometry data was analyzed using Flowing software 2.5.1 (Turku Centre for Biotechnology, Turku, Finland, with the support of Biocenter Finland). To take photobleaching of Cy5 into account, the results from [TAT]-NP were multiplied by an experimentally determined correlation factor κ.

3.3.4 Confocal Laser Scanning Microscopy (CLSM)

For a detailed analysis of NP-cell interaction, HeLa cells were seeded into 8-well Ibidi slide at a concentration of 20 000 or 10 000 cells/well and cultured for 24 h, respectively 48 h at 37 °C, 5 % CO_2. NP concentration was adjusted to 100 pM by dilution with LM. The cell medium in the wells was then replaced by 200 µL of NP formulation. LM was used as cell blank. After incubation for 60 min at 37 °C, 5 % CO_2, the particle solution was aspirated and cells were washed with 300 µL prewarmed sterile DPBS. Then, 300 µL medium was added and the cells were incubated for further 24 h, respectively 1 h. Afterwards, the medium was aspirated and the cells were incubated with 180 µL Cell Mask Green staining solution (5 µg mL^{-1} in LM) for 10 min at 37 °C, 5 % CO_2 for membrane and cytosol staining. The cells were washed twice with 300 µL prewarmed DPBS. Then, fixation of the cells was conducted by adding 250 µL of 4 % paraformaldehyde (PFA) solution in DPBS. The cells were incubated for 15 min at RT and then washed with 300 µL prewarmed DPBS. Subsequently, the cell nuclei were stained by incubating 4′,6′-diamidine-2′-phenylindole dihydrochloride (DAPI) staining solution ($1\,\mu g\,mL^{-1}$ in DPBS) for 10 min at RT. Following an additional washing step, the cells were mounted using Dako Farmount Mounting Medium and stored at 37 °C in the dark until measurement. The cells and NPs were imaged using Zeiss LSM 710 confocal microscope (Carl Zeiss microscopy GmbH, Jena, Germany). Fluorescence signals were acquired in separate channels using dye-specific excitation lasers: 405 nm for DAPI, 488 nm for CellMask Green, and 633 nm for Cy5. These individual channels were subsequently combined to merged images. Furthermore, images were taken at different focal planes to create a Z-stack and obtain three-dimensional information of the sample. Images were analyzed using Zeiss Zen software 3.8.

3.3.5 Transmission Electron Microscopy

For imaging of mPEG-, TAT- and [TAT]-NP, particles were prepared as outlined above. Subsequently, 5 µL of nanoparticles were transferred on a 9 nm carbon film, which had been floated onto a 3.05 mm Cu-TEM grid (400 mesh) for 5 s at RT. The sample was removed with tissue paper and applied 3 more time in case of mPEG-NP and then washed with bi-distilled water. Uranyl acetate (1 % in demineralized water, 5 µL, 30 s at RT) was used for staining. Images were captured at a magnification of 20,0000-fold on a JEM2100F instrument (JEOL, Freising, Germany) using SerialEM software. For analysis Fiji software was used [41]. Visualization of data was performed with R software 4.3.2 (R Core Team (2022). R: A language and environment for statistical computing. R Foundation for Statistical Computing, Vienna, Austria. URL https://www.R-project.org/).

3.3.6 Statistics

One-way ANOVA was used to assess group differences. Brown-Forsythe test was applied to verify homogeneity of variances. If ANOVA indicated significance ($p < 0.05$), Tukey's post hoc test was used for pairwise comparisons. Analyses were performed using Origin 2002b (OriginLab Corporation, Northampton, MA, USA) software, with a significance set at $p < 0.05$.

3.4 Results and Discussion

3.4.1 Synthesis and Characterization of Photo-Responsive Nanoparticles

For investigation of light-controlled uptake of NPs into cells, the components of core-shell NPs were modified. To study uptake behavior in vitro, fluorescence dye Cyanine5 (Cy5) was tethered to PLGA enabling NP visualization in flow cytometry and confocal microscopy. PLA-PEG was functionalized with CPP TAT protected by a coumarin-derived PPG [TAT] and TAT without any modification. Therefore, TAT was synthesized with a purity of 89 % and coupled to COOH-PEG$_{2k}$-PLA$_{10k}$ with a coupling efficiency (CE) of greater than 90 %. The coumarin-derived PPG (7-(diethylamino)-4-(hydroxymethyl)-coumarin, DEAC) was synthesized with a purity of greater than 90 % and subsequently coupled to TAT-PEG$_{2k}$-PLA$_{10k}$ with an efficiency of 56 % ([TAT]-PEG$_{2k}$-PLA$_{10k}$). In a previous study, it was shown that TAT-NP with a degree of 50 % functionalization (DOF) resulted in a positive surface charge, measured as particle zetapotential [23]. Therefore, the same DOF for TAT-NP as well as [TAT]-NP was used in the present study. Methoxy-terminated polymer chain-derived NP (mPEG-NP) served as control. All NPs were characterized in terms of size, size distribution and surface charge (Figure 3.2).

The control NP were smaller in size (90.2 ± 4.16 nm) than TAT-functionalized NP (139.73 ± 1.36 nm) and photocaged [TAT]-NP (157.93 ± 1.74 nm) (Figure 3.2 A). However, the functionalized NPs showed higher conformity as reflected by lower polydispersity index (PDI) value (mPEG-NP: PDI = 0.266; TAT-NP: PDI = 0.136; [TAT]-NP: PDI = 0.153; Figure 3.2 A). The larger size of functionalized NPs can be explained by their composition. TAT is rich in positively charged amino acids, which are extensively solvated and thus resulting in larger hydrodynamic diameter (d_h). Size increase of [TAT]-NP in comparison to TAT-NP can be explained by the orientation of DEAC towards the NP core, which results in combinations with the higher molecular mass to a larger size. Huge difference in d_h of functionalized NPs in comparison to control NP raised the question of comparability in uptake experiments. Therefore, the actual size of core-shell NPs was determined via transmission electron microscopy (TEM). The violin plot (Figure 3.2 C) depicts the unimodal distribution of NP sizes within the analyzed sample, highlighting both the median and mean values, as well as the variability in size. Comparison of the mean sizes revealed that mPEG-NP still exhibited the smallest in diameter (30.67 ± 8.36 nm), followed by TAT-NP (36.16 ± 12.62 nm) while [TAT]-NP displayed the largest size of 43.52 ± 16.57 nm). In Figure 3.2 D the density plot of size distribution of studied NPs is shown. The shaded regions indicate areas of overlap between NP types, highlighting similarities in their size distributions. The overlap value (value: 1 = complete overlap) was calculated for each NP pairing. The ratios (mPEG-NP - TAT-NP: 0.766; mPEG-NP - [TAT]-NP: 0.555; TAT-NP - [TAT]-NP: 0.782) indicate that NPs are more alike than NP tracking analysis (NTA) measurements and mean size values suggest. Functionalized NPs exceeded the desired size of $< 100\,\mathrm{nm}$ for in vivo experiments. However, for this proof of concept study we were not concerned and for future experiments, the size of functionalized NPs could be reduced by using a microfluidic synthesis that would provide us with smaller and uniformer NPs [38].

As the charge of CPPs plays a crucial role in their ability to facilitate cellular uptake, the zetapotential of NP was of high interest. Zetapotentials of mPEG and functionalized NPs are depicted in Figure 3.2 B. Control NPs had a negative zetapotential of $-22.27\,\mathrm{mV}$. As expected, functionalization of NP led to a change in surface charge. TAT-NP had a positive surface charge of $+\,23.50\,\mathrm{mV}$. By incorporation of DEAC into the TAT sequence we aimed to mask the NP's positive charge. The positive charge was partially masked and the photocaged NP had a diminished positive zetapotential of $+12.50\,\mathrm{mV}$. Irradiation of [TAT]-NP with light for 1 min ([TAT]-NP + hv 1 min) led to a positive surface charge of $+\,24.67\,\mathrm{mV}$. The zetapotential reduction of [TAT]-NP to approximately half of the zetapotential value of TAT-NP, can be explained by incomplete linkage of DEAC to TAT. As CE of DEAC to TAT-PEG$_{2k}$-PLA$_{10k}$ was 56 %, [TAT]-NP actually consisted of [TAT]-PEG$_{2k}$-PLA$_{10k}$ as well as TAT-PEG$_{2k}$-PLA$_{10k}$ polymer.

3.4.2 Photocleavage of DEAC

To confirm sufficient uncaging potential and gain information about the stability of DEAC caged polymer, uncaging experiments with a model polymer were conducted. DEAC was coupled via an amide bond to amino-terminated PEG-PLA (DEAC-NH-PEG$_{2k}$-PLA$_{10k}$) representing the linkage of DEAC to ϵ-amino group of lysine in the [TAT]-polymer conjugate. Photocleavage of DEAC from the polymer led to a decrease in the integrated fluorescence signal of DEAC-NH-PEG$_{2k}$-PLA$_{10k}$. We found that the DEAC modified model polymer is stable for at least 1 h under ambient light as no change in signal intensity was detected (Figure 3.3 A). This is important as all experiments, especially cell culture experiments, would not to be performed under light exclusion. The longer the irradiation time, respectively the higher the light-emitting diode (LED) power, the higher was the uncaging yield (Figure 3.3 A). More important than the investigation of the uncaging efficiency of the model polymer under light irradiation, was the reconstitution of characteristics of TAT-NP. Therefore, uncaging experiments with zetapotential readout were performed. TAT-NP had a zetapotential of $+\,24.67\,\mathrm{mV}$ that dropped after the incor-

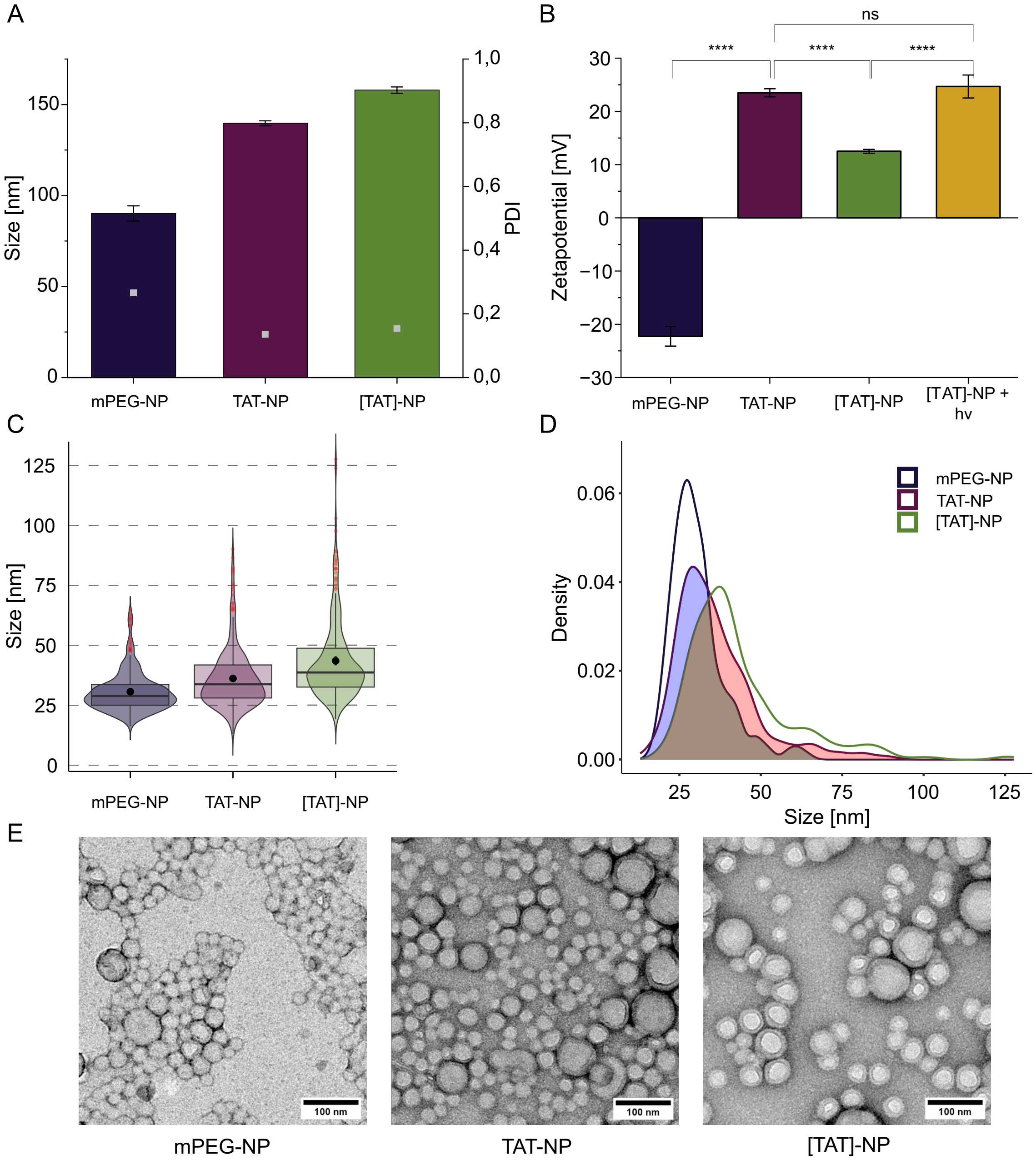

Figure 3.2: Characterization of NPs. **A** Size as mean hydrodynamic diameter (d_h) and PDI. **B** Zetapotentials. Data represent mean ± SD (n=3, level of statistical significance is indicated as * $p \leq 0.05$, ** $p \leq 0.01$, *** $p \leq 0.001$, **** $p \leq 0.0001$). **C** Violin plot represents size distribution of diameters measured from TEM images. The median NP size is shown as horizontal line within the box, whose lower and upper edges represent the first (Q1) and third (Q3) quartiles, respectively. Whiskers indicate the most extreme data points within 1.5 times the interquartile range from the lower and upper quartiles. Points beyond this range are shown individually as outliers and are displayed as individual points in red. 95 % confidence interval for the mean is represent by black dot with bars. Mean size of NPs differed significantly (Welch-Test, see Figure S3.18). A total of 300 NPs were measured. **D** Density curve of NP size distribution and overlap. The density curves illustrate the smoothed distribution of sizes for each NP. Overlap between size distributions of NP types are indicated as shaded areas. A total of 300 NPs were measured. **E** Representative TEM micrographs of each NP formulation. Scale bars are indicated in each panel.

poration of DEAC into the TAT sequence to + 10.32 mV. Irradiation with 100 mW for 1 min was sufficient to uncage the NPs since their zetapotential (+ 19.60 mV) was in the same range as that of the TAT-NP (Figure 3.3 B). Increasing irradiation time to 2 min resulted in a greater zetapotential (+ 22.03 mV), but the differences in zetapotential for all irradiated samples were not statistically significant. Therefore, the irradiation time was set to 1 min for the cell experiments. Performing uncaging experiments with [TAT]-NP resulted in a loss of color of respective aqueous NP solutions (Figure S3.17 B). Consequently, photobleaching of Cy5 incorporated into the NPs was investigated.

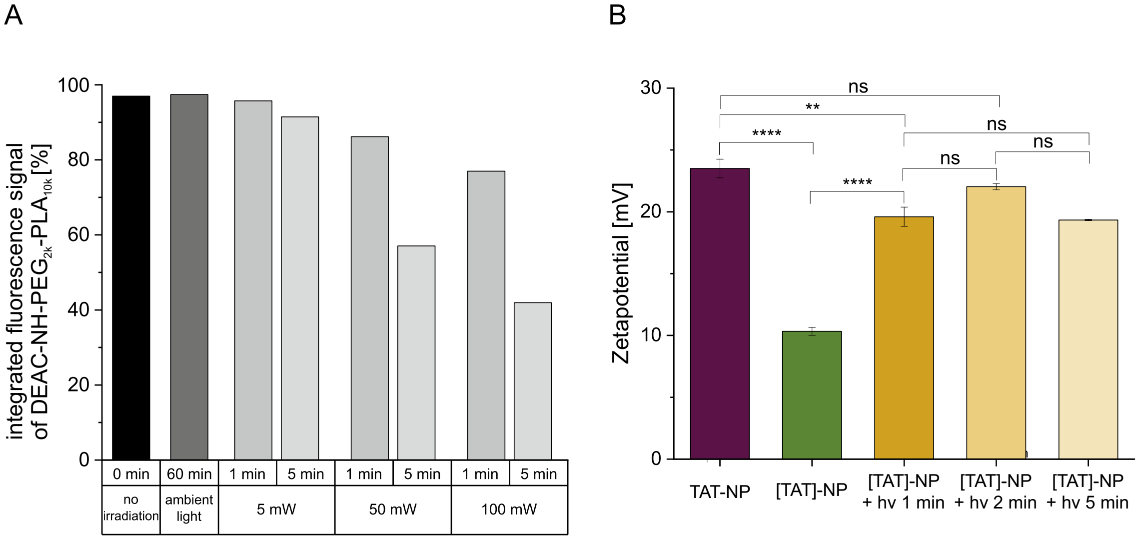

Figure 3.3: Photocleavage of DEAC from polymer. **A** The integral of fluorescence detector (FLD) signal $\lambda_{ex} = 375\ nm$, $\lambda_{em} = 480\ nm$ at the retention time of DEAC-NH-PEG$_{2k}$-PLA$_{10k}$ as a function of different irradiation times and LED powers. Irradiation experiments were performed using a LED with an emission wavelength λ_{em} = 365 nm **B** Zetapotential of TAT-NP and [TAT]-NP without and with LED irradiation. For irradiated samples no significant difference in zetapotential were measured. The LED power was set to 100 mW, λ_{em} = 365 nm. Data represent mean ± SD (n=3, level of statistical significance is indicated as * $p \leq 0.05$, ** $p \leq 0.01$, *** $p \leq 0.001$, **** $p \leq 0.0001$).

3.4.3 Spectral Properties of DEAC and Conjugates

Besides quantification of reaction yields, photophysical properties of synthesized photocage DEAC, caged polymer and fluorescent NPs were measured to characterize our NP design. We hypothesized that the hydrophobicity of DEAC would cause an orientation of [TAT] towards the hydrophobic PLGA core of [TAT]-NP and thus, mask to some extent the positive charge of TAT. This hypothesis was based on two previous studies [12, 24]. To support our hypothesis, spectral measurements were performed. The absorption spectra of DEAC and conjugates in acetonitrile (ACN) and aqueous solution (Figure 3.4 A) are similar in shape and differ only slightly in their maxima due to solvent polarity and different linkage. In comparison to absorption, the polarity of the solvent has a strong impact on the fluorescence spectrum of the coumarin-derived PPG [42]. Thus, fluorescence was used to characterize the core-shell NPs. In ACN, a hydrophobic surrounding, the fluorescence spectrum of DEAC was found to be blue shifted ($\lambda_{em} = 457\ nm$) in comparison to an aqueous solution ($\lambda_{em} = 493\ nm$) (Figure 3.4 B). Since the fluorescence spectrum of [TAT]-NP ($\lambda_{em} = 463\ nm$) resembled that to DEAC in ACN and was blue shifted relactive to DEAC in aqueous solution, we concluded that DEAC is located in a hydrophobic environment. This suggests that DEAC is orientated towards the core. After irradiation of [TAT]-NP with light at $\lambda_{em,max} = 365\ nm$ for 1 min, the fluorescence spectrum of DEAC was red-shifted. The emission shift indicates a structural change of NP and that DEAC is in a more hydrophilic environment (Figure 3.4 B,C). The lower fluorescence signal can be explained by photobleaching. Excitation of [TAT]-NP at $\lambda_{ex} = 380\ nm$ led to an additional emission peak with $\lambda_{em,max} = 668\ nm$. This spectrum belongs to the fluorescent dye, Cy5, incorporated in the PLGA core, which is normally not excited at that wavelength (Figure 3.4 B)). The energy for Cy5 excitation is provided by Foerster resonance energy transfer (FRET), proofing proximity of DEAC and Cy5.

Calculation of the Foerster radius (R_0) of this pair of dyes resulted in 3.26 nm (Supporting Information, Equation (5.5)). At the distance of R_0 the energy transfer efficiency between a donor and acceptor is 50 %. At longer distances, the efficiency declines at a rate proportional to the sixth power, thereby reducing the probability of FRET [43]. The PEG layer of core-shell NPs had a thickness of 8.28 nm (Supporting Information, eq. (3.17)). Consequently, the distance between DEAC and Cy5 would be greater than twice R_0 if DEAC would be located on the surface of the NP, rendering FRET highly unlikely. Thus, the appearance of FRET supports the hypothesis that DEAC anchored TAT within the NP.

As the extent of NP uptake into HeLa cells is quantified by fluorescence readout of Cy5, photobleaching of Cy5 could have a tremendous impact on the outcome of flow cytometry experiments. Therefore, a bleaching factor κ was determined to take the reduced fluorescence of irradiated sample into account. In Figure 3.4 D, the fluorescence signal of Cy5 is plotted against different irradiation times. [TAT]-NPs shown a strong decrease in fluorescence signal of Cy5 with increasing irradiation time. Carboxy-terminated NPs, as a control, exhibited no decrease in Cy5 fluorescence (Supporting Information, Figure S3.17 C).

The photobleaching of [TAT]-NP can be explained by FRET. The emission spectrum of DEAC is slightly overlapping with the excitation spectrum of Cy5 (Figure 3.4 C). Thus, the energy provided for DEAC excitation is transferred to Cy5, resulting in excitation and gradually causing photobleaching. The calculated photobleaching factor κ for an irradiation time of 1 min has a value of 1.496.

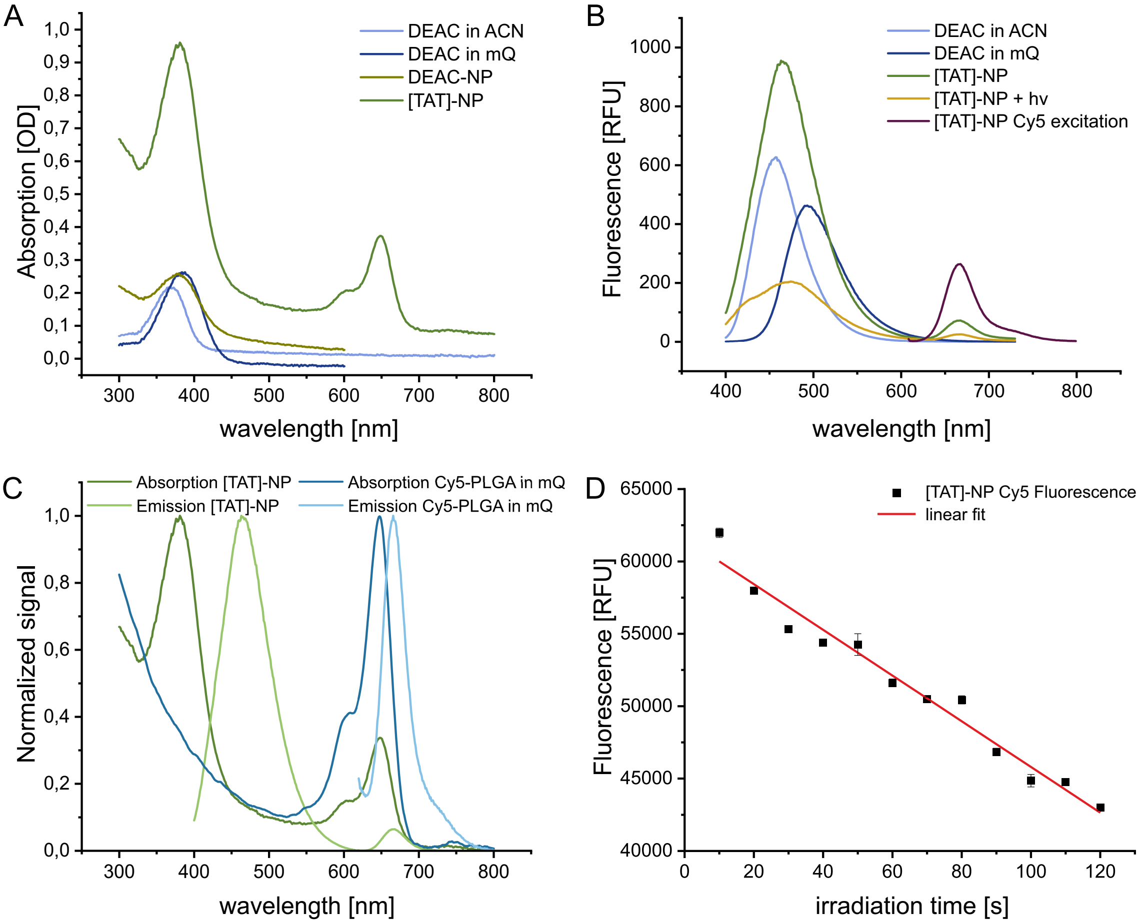

Figure 3.4: Spectral properties of DEAC and photo-responsive NPs. **A** Absorption spectrum of DEAC in ACN (λ_{max} = 368 nm), DEAC in Millipore water (mQ) (λ_{max} = 384 nm), DEAC-NP (made of DEAC-NH-PEG$_{2k}$-PLA$_{10k}$) (λ_{max} = 377 nm), and [TAT]-NP (λ_{max} = 381 nm, λ_{max} = 648 nm). The first peak ($\lambda \approx 380$ nm) is related to DEAC, whereas second peak ($\lambda_{max} = 648\,nm$) is caused by Cy5 in the NP core. **B** Fluorescence emission spectra of DEAC in ACN ($\lambda_{em,max} = 457\,nm$) and mQ ($\lambda_{em,max} = 493\,nm$), [TAT]-NP ($\lambda_{em,max} = 463\,nm$), [TAT]-NP irradiated for 1 min (100 mW, $\lambda_{em,max} = 474\,nm$) at an excitation wavelength of λ_{ex} = 380 nm. Upon excitation at λ_{ex} = 600 nm, Cy5 exhibited a fluorescence emission spectrum with a maximum at $\lambda_{em,max} = 668$ nm (referred to as [TAT]-NP Cy5 excitation). **C** Absorption and fluorescence emission spectra of [TAT]-NP, and Cy5-PLGA. Individual peaks were normalized to their highest peak intensity to enable comparison between spectra. [TAT]-NP $\lambda_{abs,max_1} = 381\,nm$, $\lambda_{abs,max_2} = 648\,nm$, $\lambda_{em,max_1} = 463\,nm$, $\lambda_{em,max_2} = 668$ nm. Cy5-PLGA $\lambda_{abs,max} = 647\,nm$, $\lambda_{em,max} = 666\,nm$. **D** Photobleaching of Cy5 after LED irradiation of [TAT]-NP at $\lambda = 365$ nm; LED power: 100 mW. Fluorescence of Cy5 (RFU, relative fluorescence units) is plotted against irradiation time of NPs.

3.4.4 In Vitro Performance of NPs

The uptake respectively attachment of mPEG-, TAT-, [TAT]- and irradiated [TAT]-NP to HeLa cells were studied by flow cytometry (Figure 3.5 A). Comparing the cell-associated fluorescence of non-functionalized and TAT functionalized NP, functionalized NP showed higher signals. Positively charged TAT-NP showed a 35-fold higher uptake in HeLa cells than those exposed to TAT-free mPEG-NP. HeLa cells incubated with [TAT]-NP exhibited less cell-associated fluorescence in comparison to TAT-NP, suggesting that the caging strategy prevented CPP-mediated NP-cell interaction. Measured data of previously irradiated [TAT]-NP ([TAT]-NP + hv) was multiplied by photobleaching factor κ. The cell-associated fluorescence of [TAT]-NP + hv was greater than the non-irradiated sample ([TAT]-NP), but less than photocage-free TAT-NP. Despite complete reconstitution of zetapotential of masked NP after light irradiation, uptake potential of TAT-NP could not be completely restored. The incorporation of DEAC into NP design reduced cell-associated fluorescence by half, which can also be explained by 56 % CE of DEAC to TAT-PEG$_{2k}$-PLA$_{10k}$. In addition to non-caged lysine residues, the presence of non-caged arginine residues may contribute to the increased cellular uptake in comparison to blank NP. Theoretically, poly-lysine peptides might offer an alternative approach to obtain better camouflaged NP. However, their comparatively limited membrane binding and penetrating capabilities reduce their suitability for practical applications [44].

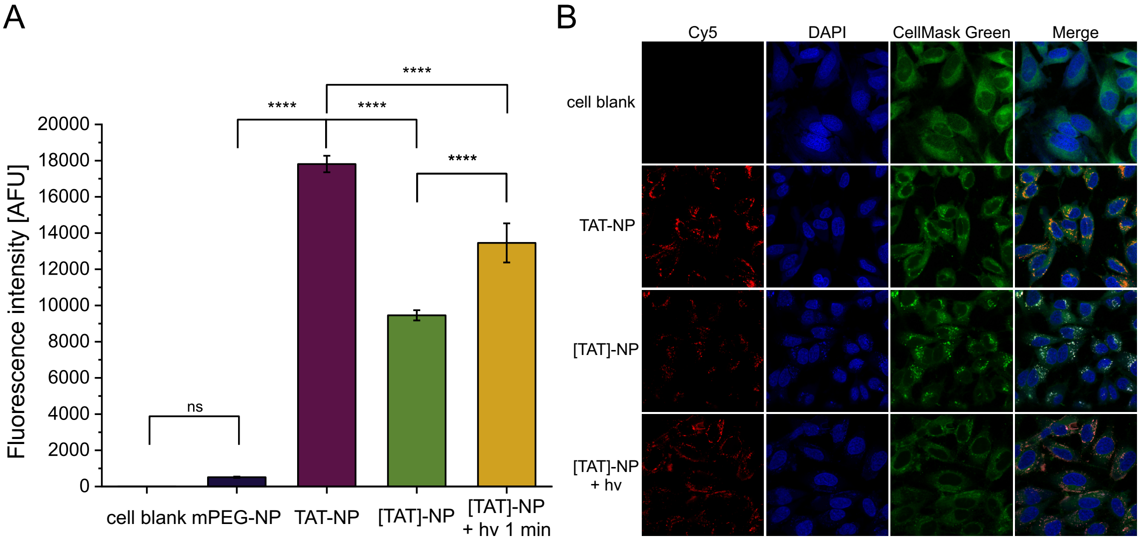

Figure 3.5: Flow cytometric and CLSM analysis of photo-responsive NPs. **A** Results from flow cytometry experiment. Fluorescence intensity of 1 min irradiated [TAT]-NP ([TAT]-NP + hv) was multiplied by photobleaching factor κ. Data represent mean ± SD ($n = 3$, level of statistical significance is indicated as * $p \leq 0.05$, ** $p \leq 0.01$, *** $p \leq 0.001$, **** $p \leq 0.0001$), (AFU, arbitrary fluorescence units). **B** CLSM images showing of the cellular uptake of Cy5-labeled NP (red) in HeLa cells at 24 h post-incubation time. Cell nuclei were labeled with DAPI (blue). CellMask Green (green) was used for staining cell membrane and cytosol.

To obtain detailed information at the single-cell level, confocal microscopy was used. Figure 3.5 B shows the confocal images of treated HeLa cells at 24 h postincubation time. In the merged fluorescence images [TAT]-NP appeared white. This is caused by the overlap of all three colors as DEAC was excited by laser at 405 nm and 488 nm while Cy5 was excited 633 nm. Irradiated [TAT]-NP appear red in the merged channel confirming the absence of DEAC and thus sufficient uncaging. All in all, the findings from flow cytometry were confirmed. To differentiate between cell uptake and adsorption of NP to the cell membrane, cells were investigated after two post-incubation times (Figure 3.6 A). Z-stack images taken at 1 h post-incubation time show that NPs are attached to cell surface, whereas NP had been taken up by cells 24 h post-incubation (Figure 3.6 B).

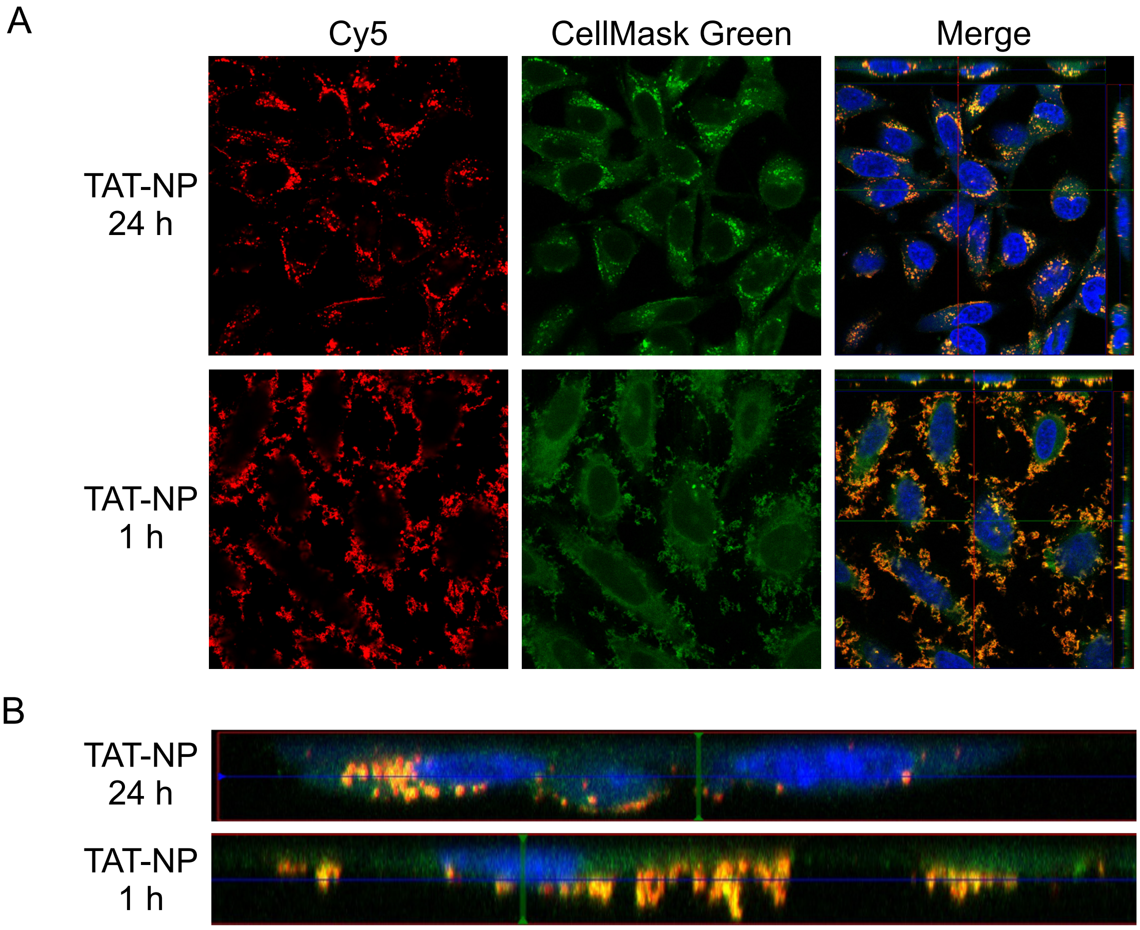

Figure 3.6: Characterization of interaction between TAT-NP and HeLa cells. **A** CLSM images showing the cellular interaction of TAT-NP (red) at 24 h and 1 h post-incubation time. **B** Orthogonal projections of CLSM Z-stack images enable distinction between surface-bound and internalized TAT-NP (red) after different post-incubation times. Cell nuclei were labeled with DAPI (blue). Cell membrane and cytosol were stained with CellMask Green (green).

3.5 Conclusion

We were able to incorporate a PPG into our NP design changing its physicochemical as well as biological properties. While the particles carrying the CPP are genuinely internalized by cells, conjugation of DEAC effectively camouflaged them, thus significantly reducing cell uptake. Upon light irradiation, the CPP‘s penetration enhancing properties were restored. This new NP design offers the possibility to obtain greater spatial and temporal control over NP uptake once they encounter the target cell in a tissue of interest. Due to the absorption properties of the selected coumarin-derived photocage, which requires activation by light of short-wavelength with limited tissue penetration, the practical application is limited to tissues that can be directly exposed to light, such as ocular tissues. Recent research from Nizamoglu et al. on optical waveguides for deep-tissue photomedicine suggests potential for extending applications to surface-near tissues as well [45]. In the future, such NPs could enable better spatiotemporal targeting of cells in a diseased tissue. Furthermore, they could be used to allow for spatiotemporal drug transfer into target cells.

References

[1] Stefan Wilhelm et al. “Analysis of nanoparticle delivery to tumours”. In: *Nature Reviews Materials* 1.5 (2016). DOI: `10.1038/natrevmats.2016.14`.

[2] Qiankun Ni et al. “Nanomaterials with changeable physicochemical property for boosting cancer immunotherapy”. In: *Journal of controlled release : official journal of the Controlled Release Society* 342 (2022), pp. 210–227. DOI: `10.1016/j.jconrel.2022.01.003`.

[3] Qianqian Lu et al. “Nanoparticles with transformable physicochemical properties for overcoming biological barriers”. In: *Nanoscale* 15.32 (2023), pp. 13202–13223. DOI: `10.1039/D3NR01332D`.

[4] Ki Young Choi et al. “Hyaluronic Acid-Based Activatable Nanomaterials for Stimuli-Responsive Imaging and Therapeutics: Beyond CD44-Mediated Drug Delivery”. In: *Advanced materials (Deerfield Beach, Fla.)* 31.34 (2019), e1803549. DOI: `10.1002/adma.201803549`.

[5] Zhihuan Liao et al. “Virus-inspired nanosystems for drug delivery”. In: *Nanoscale* 13.45 (2021), pp. 18912–18924. DOI: `10.1039/D1NR05872J`.

[6] Eun Seong Lee et al. “Super pH-sensitive multifunctional polymeric micelle for tumor pH(e) specific TAT exposure and multidrug resistance”. In: *Journal of controlled release : official journal of the Controlled Release Society* 129.3 (2008), pp. 228–236. DOI: `10.1016/j.jconrel.2008.04.024`.

[7] Nien-Chu Fan et al. “Photocontrolled targeted drug delivery: photocaged biologically active folic acid as a light-responsive tumor-targeting molecule”. In: *Angewandte Chemie (International ed. in English)* 51.35 (2012), pp. 8806–8810. DOI: `10.1002/anie.201203339`.

[8] Mahdi Karimi et al. “Smart Nanostructures for Cargo Delivery: Uncaging and Activating by Light”. In: *Journal of the American Chemical Society* 139.13 (2017), pp. 4584–4610. DOI: `10.1021/jacs.6b08313`.

[9] Caerwyn Ash et al. “Effect of wavelength and beam width on penetration in light-tissue interaction using computational methods”. In: *Lasers in medical science* 32.8 (2017), pp. 1909–1918. DOI: `10.1007/s10103-017-2317-4`.

[10] Louise Finlayson et al. “Depth Penetration of Light into Skin as a Function of Wavelength from 200 to 1000 nm”. In: *Photochemistry and photobiology* 98.4 (2022), pp. 974–981. DOI: `10.1111/php.13550`.

[11] Lorenzo Guidi, Maria Grazia Cascone, and Elisabetta Rosellini. “Light-responsive polymeric nanoparticles for retinal drug delivery: design cues, challenges and future perspectives”. In: *2405-8440* 10.5 (), e26616. ISSN: 2405-8440. DOI: `10.1016/j.heliyon.2024.e26616`.

[12] Yanfei Wang et al. “Intravenous treatment of choroidal neovascularization by photo-targeted nanoparticles”. In: *Nature communications* 10.1 (2019), p. 804. DOI: `10.1038/s41467-019-08690-4`.

[13] Congcong Xu et al. “Photo-controlled release of paclitaxel and model drugs from RNA pyramids”. In: *Nano Research* 12.1 (2019), pp. 41–48. ISSN: 1998-0124. DOI: `10.1007/s12274-018-2174-x`.

[14] Yang Yang et al. “Photoresponsive Drug Delivery Systems: Challenges and Progress”. In: *Advanced functional materials* 34.38 (2024). ISSN: 1616-301X. DOI: `10.1002/adfm.202402975`.

[15] Jinzhao Liu, Weirong Kang, and Weiping Wang. “Photocleavage-based Photoresponsive Drug Delivery”. In: *Photochemistry and photobiology* 98.2 (2022), pp. 288–302. DOI: `10.1111/php.13570`.

[16] Günter Mayer and Alexander Heckel. “Biologically active molecules with a "light switch"”. In: *Angewandte Chemie (International ed. in English)* 45.30 (2006), pp. 4900–4921. DOI: `10.1002/anie.200600387`.

[17] Alessandro Gori et al. “Cell Penetrating Peptides: Classification, Mechanisms, Methods of Study, and Applications”. In: *ChemMedChem* 18.17 (2023), e202300236. DOI: `10.1002/cmdc.202300236`.

[18] Sara Silva, António J. Almeida, and Nuno Vale. “Combination of Cell-Penetrating Peptides with Nanoparticles for Therapeutic Application: A Review”. In: *Biomolecules* 9.1 (2019). DOI: `10.3390/biom9010022`.

[19] Dakota J. Brock et al. “Efficient cell delivery mediated by lipid-specific endosomal escape of supercharged branched peptides”. In: *Traffic (Copenhagen, Denmark)* 19.6 (2018), pp. 421–435. DOI: `10.1111/tra.12566`.

[20] Dehua Pei and Marina Buyanova. “Overcoming Endosomal Entrapment in Drug Delivery”. In: *Bioconjugate Chemistry* 30.2 (2019), pp. 273–283. DOI: `10.1021/acs.bioconjchem.8b00778`.

[21] Ashweta Sahni, Ziqing Qian, and Dehua Pei. “Cell-Penetrating Peptides Escape the Endosome by Inducing Vesicle Budding and Collapse”. In: *ACS chemical biology* 15.9 (2020), pp. 2485–2492. DOI: `10.1021/acschembio.0c00478`.

[22] Mafalda Rizzuti et al. “Therapeutic applications of the cell-penetrating HIV-1 Tat peptide”. In: *Drug discovery today* 20.1 (2015), pp. 76–85. DOI: `10.1016/j.drudis.2014.09.017`.

[23] Melanie Walter et al. “Long-term residence and efficacy of adenovirus-mimetic nanoparticles in renal target tissue”. In: *Journal of drug targeting* 32.10 (2024), pp. 1320–1332. DOI: `10.1080/1061186X.2024.2390628`.

[24] Weiping Wang et al. “Efficient Triplet-Triplet Annihilation-Based Upconversion for Nanoparticle Phototargeting”. In: *Nano letters* 15.10 (2015), pp. 6332–6338. DOI: `10.1021/acs.nanolett.5b01325`.

[25] Tobias Miller et al. “Comparative Investigations on In Vitro Serum Stability of Polymeric Micelle Formulations”. In: *1573-904X* 29.2 (), pp. 448–459. ISSN: 1573-904X. DOI: `10.1007/s11095-011-0555-x`. (Visited on 04/09/2025).

[26] Tobias Miller et al. “Premature drug release of polymeric micelles and its effects on tumor targeting”. In: *International journal of pharmaceutics* 445.1-2 (2013), pp. 117–124. DOI: `10.1016/j.ijpharm.2013.01.059`.

[27] Melanie Walter et al. “Conditional Cell-Penetrating Peptide Exposure as Selective Nanoparticle Uptake Signal”. In: *ACS applied materials & interfaces* 16.29 (2024), pp. 37734–37747. DOI: `10.1021/acsami.4c07821`.

[28] Xianglong Hu et al. “Thiol and pH dual-responsive dynamic covalent shell cross-linked micelles for triggered release of chemotherapeutic drugs”. In: *Polym. Chem.* 4.3 (2013), pp. 695–706. ISSN: 1759-9954. DOI: `10.1039/C2PY20701J`.

[29] Helen M. Burt et al. “Development of copolymers of poly(d,l-lactide) and methoxypolyethylene glycol as micellar carriers of paclitaxel”. In: *Colloids and Surfaces B: Biointerfaces* 16.1-4 (1999), pp. 161–171. ISSN: 09277765. DOI: `10.1016/S0927-7765(99)00067-3`.

[30] Kevin Letchford and Helen M. Burt. “Copolymer micelles and nanospheres with different in vitro stability demonstrate similar paclitaxel pharmacokinetics”. In: *Molecular pharmaceutics* 9.2 (2012), pp. 248–260. DOI: `10.1021/mp2002939`.

[31] Jing Zhao and Shirui Mao. “Tuning the membrane fluidity of liposomes for desirable in vivo fate with enhanced drug delivery”. In: vol. 34. Advances in Biomembranes and Lipid Self-Assembly. Elsevier, 2021, pp. 67–106. ISBN: 9780323914994. DOI: `10.1016/bs.abl.2021.11.003`.

[32] Zhenlong Li and Elena E. Dormidontova. “Equilibrium chain exchange kinetics in block copolymer micelle solutions by dissipative particle dynamics simulations”. In: *Soft Matter* 7.9 (2011), p. 4179. ISSN: 1744-683X. DOI: `10.1039/C0SM01443E`.

[33] Jing Wang, Michael Dzuricky, and Ashutosh Chilkoti. “The Weak Link: Optimization of the Ligand-Nanoparticle Interface To Enhance Cancer Cell Targeting by Polymer Micelles”. In: *Nano letters* 17.10 (2017), pp. 5995–6005. DOI: `10.1021/acs.nanolett.7b02225`.

[34] Sara Maslanka Figueroa et al. “The Effect of Ligand Mobility on the Cellular Interaction of Multivalent Nanoparticles”. In: *Macromolecular bioscience* 20.4 (2020), e1900427. DOI: `10.1002/mabi.201900427`.

[35] Maximilian A. Beach et al. “Polymeric Nanoparticles for Drug Delivery”. In: *Chemical reviews* 124.9 (2024), pp. 5505–5616. DOI: `10.1021/acs.chemrev.3c00705`.

[36] Merlin Bresinsky et al. “Characterization of caspase-2 inhibitors based on specific sites of caspase-2-mediated proteolysis”. In: *Archiv der Pharmazie* 355.9 (2022), e2200095. DOI: `10.1002/ardp.202200095`.

[37] Haitao Qian et al. “A Strategy for Control of "Random" Copolymerization of Lactide and Glycolide: Application to Synthesis of PEG-b-PLGA Block Polymers Having Narrow Dispersity”. In: *Macromolecules* 44.18 (2011), pp. 7132–7140. ISSN: 0024-9297. DOI: `10.1021/ma201169z`.

[38] Kathrin Abstiens and Achim M. Goepferich. “Microfluidic manufacturing improves polydispersity of multicomponent polymeric nanoparticles”. In: *Journal of Drug Delivery Science and Technology* 49 (2019), pp. 433–439. ISSN: 17732247. DOI: `10.1016/j.jddst.2018.12.009`.

[39] Kathrin Schorr et al. “The quantity of ligand-receptor interactions between nanoparticles and target cells”. In: *Nanoscale horizons* 10.4 (2025), pp. 803–823. DOI: `10.1039/D4NH00645C`.

[40] Timo Weinrich et al. “Synthesis of a Cytidine Phosphoramidite with Protected Nitroxide Spin Label for EPR Experiments with RNA”. In: *European Journal of Organic Chemistry* 2017.3 (2017), pp. 491–496. ISSN: 1434-193X. DOI: `10.1002/ejoc.201601174`.

[41] Johannes Schindelin et al. “Fiji: an open-source platform for biological-image analysis”. In: *Nature methods* 9.7 (2012), pp. 676–682. ISSN: 1548-7091. DOI: `10.1038/nmeth.2019`.

[42] B. Shivaleela et al. “Effect of solvent on fluorescence and absorption spectra of fluorescent coumarin derivative: Estimation of ground and excited state dipole moments”. In: *Materials Today: Proceedings* 68 (2022), pp. 564–572. ISSN: 22147853. DOI: `10.1016/j.matpr.2022.08.248`.

[43] Martin Pelosse et al. “Genetically Encoded Fluorescent Biosensors to Explore AMPK Signaling and Energy Metabolism”. In: *Experientia supplementum (2012)* 107 (2016), pp. 491–523. ISSN: 1664-431X. DOI: `10.1007/978-3-319-43589-3_20`.

[44] Sunil S. Shah et al. “Polyamide Backbone Modified Cell Targeting and Penetrating Peptides in Cancer Detection and Treatment”. In: *Frontiers in chemistry* 8 (2020), p. 218. ISSN: 2296-2646. DOI: `10.3389/fchem.2020.00218`.

[45] Sedat Nizamoglu et al. “Bioabsorbable polymer optical waveguides for deep-tissue photomedicine”. In: *Nature communications* 7 (2016), p. 10374. DOI: `10.1038/ncomms10374`.

Supporting Information
Chapter 3

S3.1 Synthesis and Characterization

S3.1.1 Polymer Synthesis

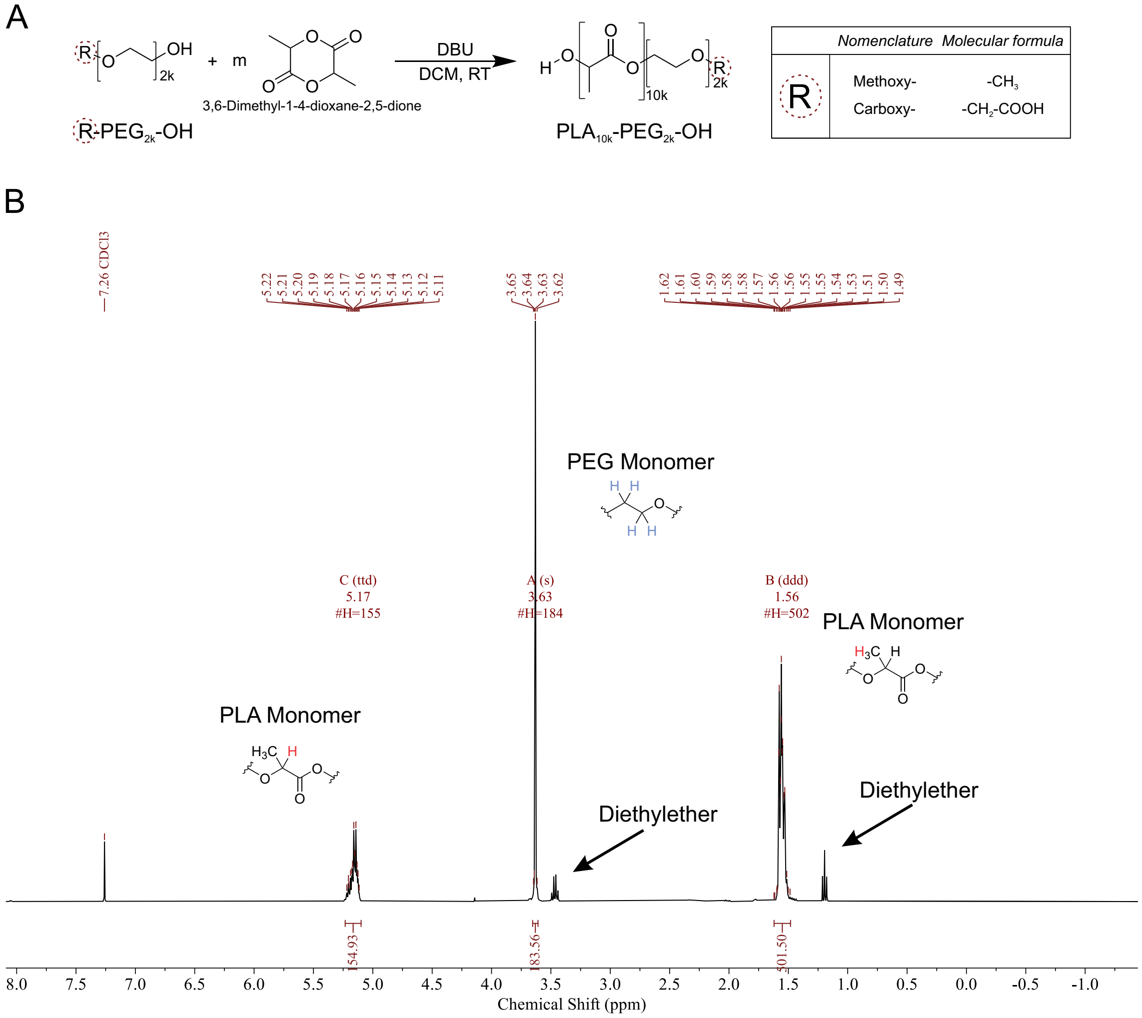

Figure S3.1: Block copolymer synthesis and characterization. **A** Chemical equation for the synthesis of PLA-PEG block copolymer. The block copolymers were synthesized with different end groups (R). **B** Exemplary ^{1}H-NMR spectrum (400 MHz, $CDCl_3$) of COOH-PEG$_{2k}$-PLA$_{10k}$ block copolymer.

S3.1.2 Synthesis of protected TAT 48-57$_{prot.}$

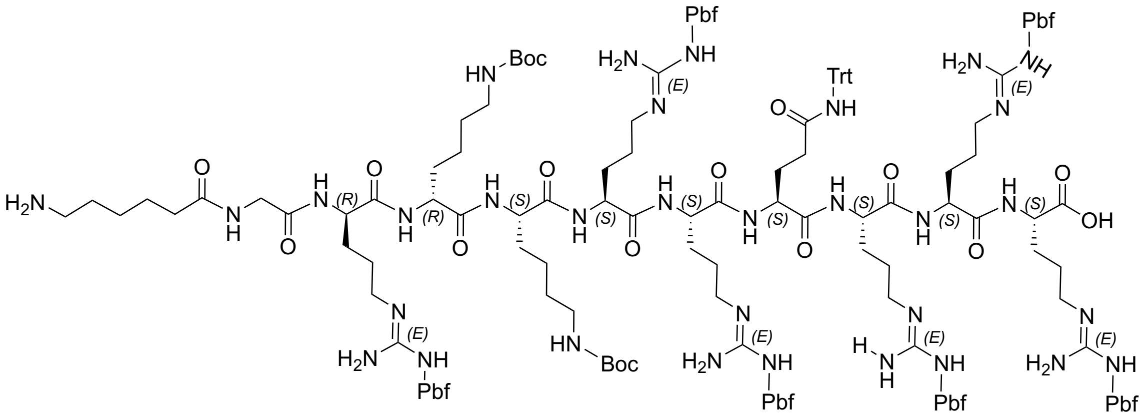

Chemical Formula: $C_{168}H_{246}N_{32}O_{35}S_6$

Exact Mass: 3463.68

Molecular Weight: 3466.37

Figure S3.2: Structure of TAT 48-57$_{\mathrm{prot.}}$.

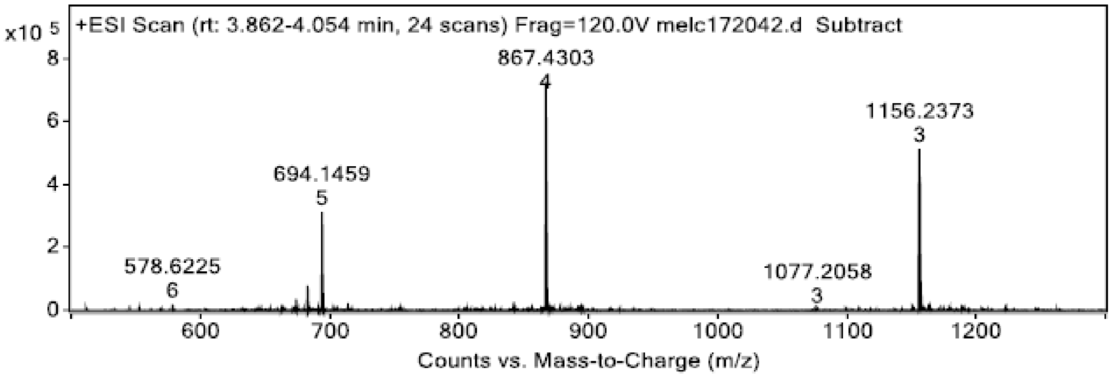

Figure S3.3: Mass spectrum of TAT 48-57$_{\mathrm{prot.}}$.

HRMS (ESI) m/z calculated for $C_{168}H_{246}N_{32}O_{35}S_6 + 4H^+$: 867.4279, found: 867.4303.

Table S3.1: HPLC method for analysis of TAT 48-57$_{\text{prot.}}$. Flow rate: 1 mL

Time [min]	H_2O + 0.05 %TFA	ACN + 0.05 %TFA
0	95	5
1	95	5
16	5	95
22	5	95
22.30	95	5
30	95	5

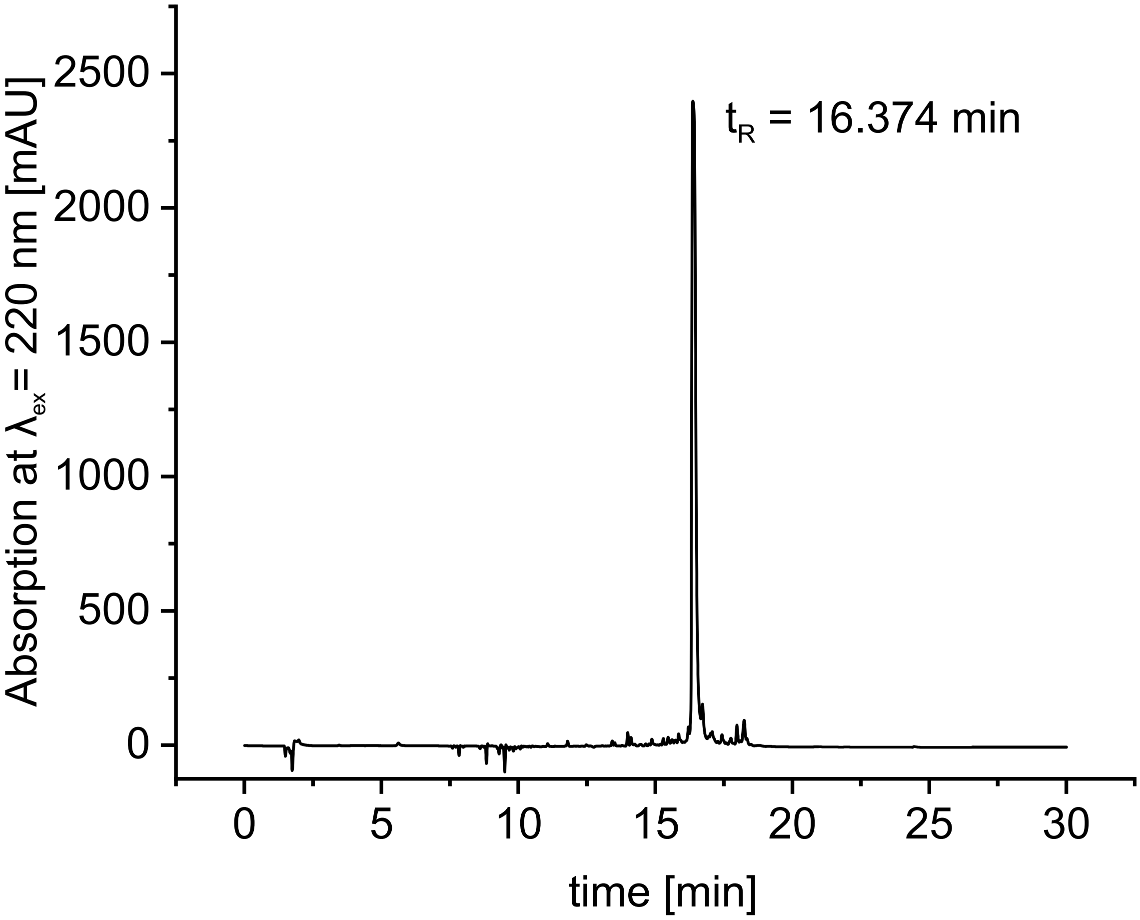

Figure S3.4: RP-HPLC analysis of TAT 48-57$_{\text{prot.}}$. Retention time t_R of TAT 48-57$_{\text{prot.}}$: 16.374 min. milli Absorbance Units, mAU.

S3.1.3 Synthesis of 7-diethylamino-4-hydroxymethylcoumarin (DEAC)

7-(diethylamino)-4-(2-dimethylamino)vinylcoumarin (2)

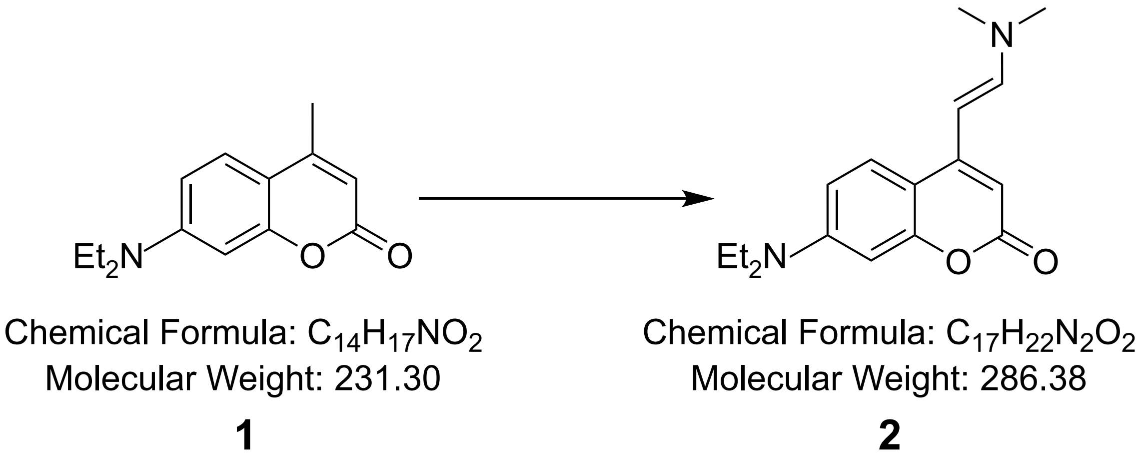

Scheme S3.1: Reaction equation for synthesis of 7-(diethylamino)-4-(2-dimethylamino)vinylcoumarin (**2**)

To a solution of 7-(diethylamino)-4-methyl-coumarin **1** (24.2 g, 105 mmol, 1.00 equiv.) in DMF (100 mL) DMF-DMA (25 mL, 210 mmol, 2.00 equiv.) was added. The reaction mixture was heated to reflux for 22 h. Reaction was cooled to RT and subsequently conc. $NaHCO_3$ solution and CH_2Cl_2 were added. The organic layer was separated and the aqueous layer was extracted with CH_2Cl_2. Organic layers were combined and solvent was removed under reduced pressure. Purification of synthesis product by flash chromatography gave title compound (**2**) as a goldish solid. Mobile phase: linear gradient, 0-10 min: petrol ether/ethyl acetate 80:20-40:60, 10-15 min: 40:60 (isocratic), 15-19:30 min: 40:60-20:80, 19:30-25 min: 20:80-0:100, 25-70 min: 0:100 (isocratic). Flow: 50 mL/min. Detection was performed at 366 nm.

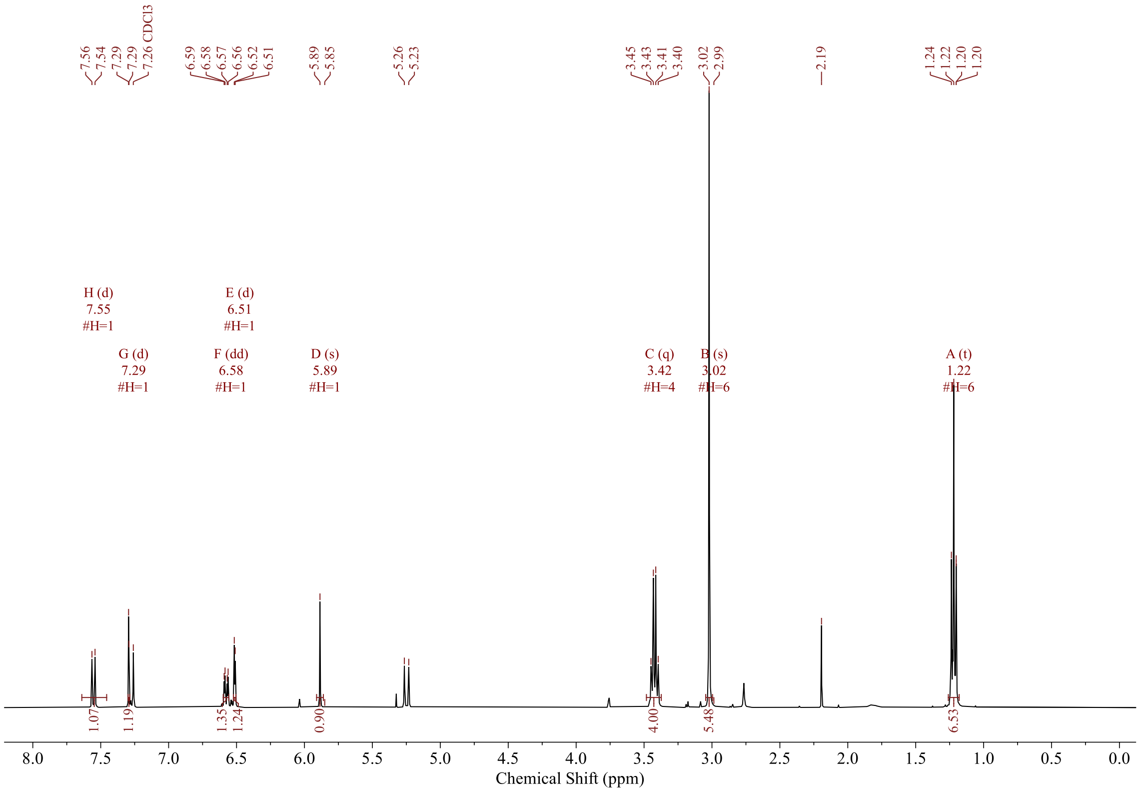

Figure S3.5: ^{1}H-NMR spectrum of 7-(diethylamino)-4-(2-dimethylamino)-vinylcoumarin. ^{1}H-NMR (400 MHz, $CDCl_3$) δ(ppm) 7.55 (d, J = 9.1 Hz, 1H), 7.29 (d, 1H), 6.58 (dd, J = 9.0, 2.6 Hz, 1H), 6.51 (d, J = 2.6 Hz, 1H), 5.89 (s, 1H), 3.42 (q, J = 7.1 Hz, 4H), 3.02 (s, 6H), 1.22 (t, J = 7.0 Hz, 6H).

7-diethylamino-4-formylcoumarin (3)

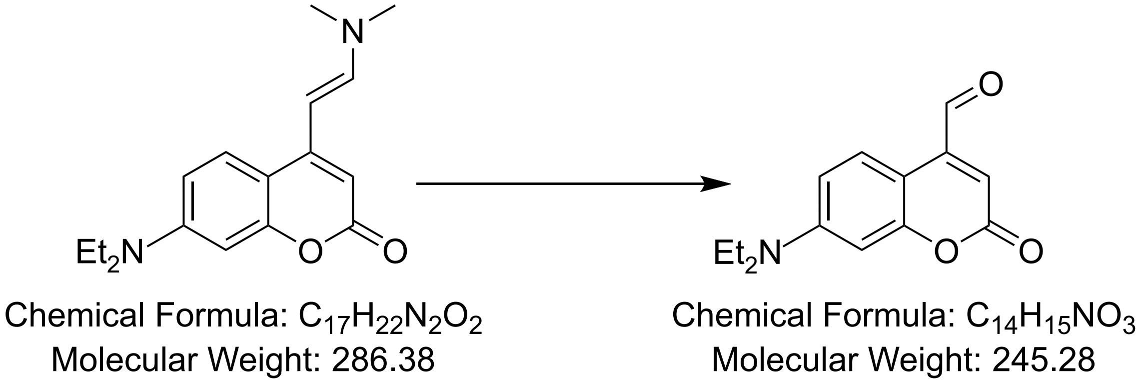

2 **3**

Scheme S3.2: Reaction equation for synthesis of 7-diethylamino-4-formylcoumarin (**3**)

The enamine **2** (3.74 g, 13.1 mmol, 1.00 equiv.) was suspended in a mixture of THF/DCM (110 mL 11:1). A solution of $NaIO_4$ (8.40 g, 39.2 mmol, 3.00 equiv.) in water was added and the resulting mixture was stirred at RT for 2 h. The mixture was filtered on Celite and washed with ethyl acetate. Half of the solvent was removed under reduced pressure and conc. $NaHCO_3$ solution was added. The organic layer was separated and the aqueous layer was extracted with CH_2Cl_2. The combined organic layers were dried with $MgSO_4$ and the solvent was removed under reduced pressure. Purification by silica gel chromatography (ethyl acetate/petrol ether, 1:1) gave title compound **(3)** (2.73 g, 85.0 %) as a redish solid.

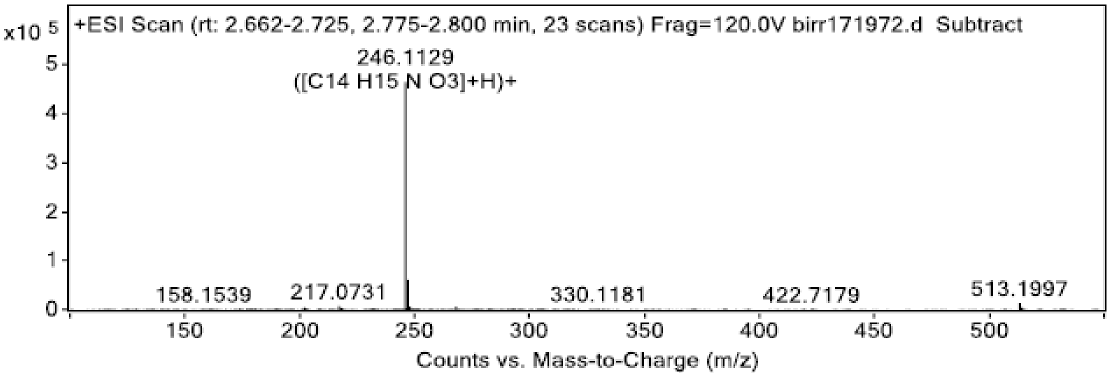

Figure S3.6: Mass spectrum of 7-diethylamino-4-formylcoumarin$_{\text{prot.}}$.
MS (ESI) m/z calculated for $C_{14}H_{15}NO_3 + H^+$: 246.11, found: 246.1129.

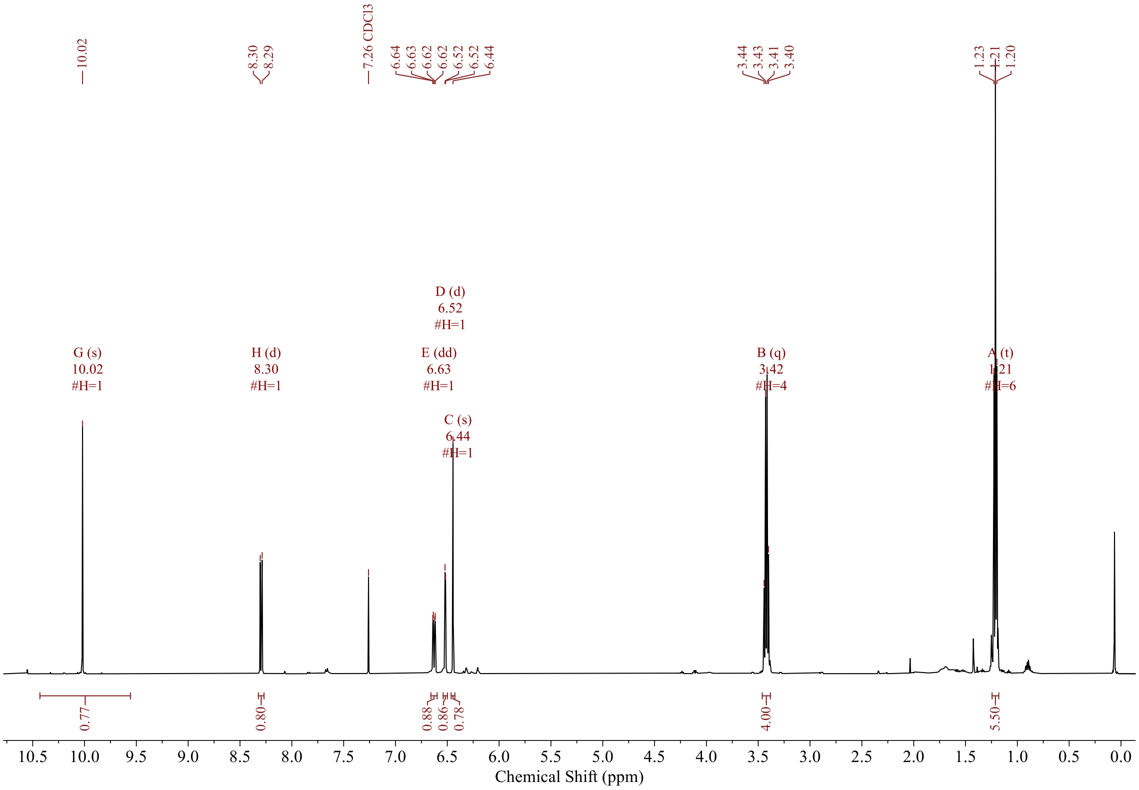

Figure S3.7: ^{1}H-NMR spectrum of 7-diethylamino-4-formylcoumarin. ^{1}H-NMR (500 MHz, $CDCl_3$) δ(ppm) 10.02 (s, 1H), 8.30 (d, J = 9.2 Hz, 1H), 6.63 (dd, J = 9.2, 2.6 Hz, 1H), 6.52 (d, J = 2.6 Hz, 1H), 6.44 (s, 1H), 3.42 (q, J = 7.1 Hz, 4H), 1.21 (t, J = 7.1 Hz, 6H).

7-diethylamino-4-hydroxymethylcoumarin (4)

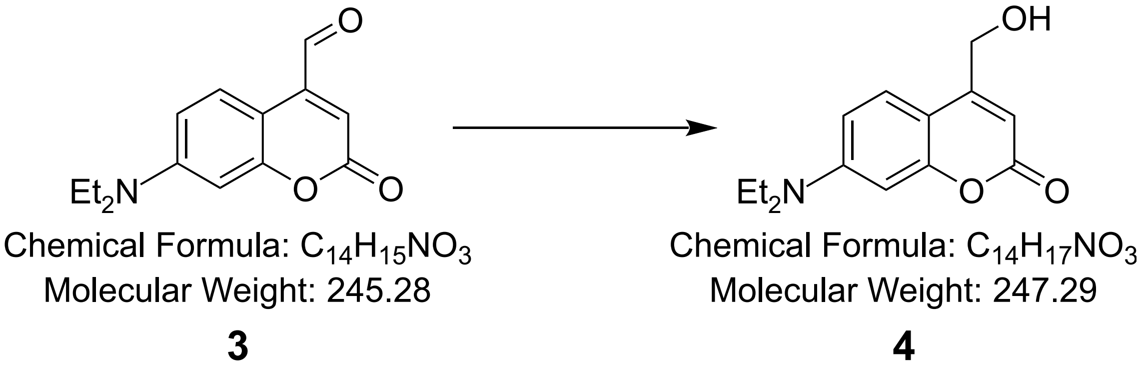

Scheme S3.3: Reaction equation for synthesis of 7-diethylamino-4-hydroxymethylcoumarin (**4**)

A solution of aldehyde **3** (2.63 g, 10.7 mmol, 1.00 equiv.) in THF (50 mL) was cooled to 0 °C. $NaBH_4$ (984 mg, 21.4 mmol, 2.43 equiv.) was added and the mixture was stirred for 5 h at RT. Subsequently conc. $NaHCO_3$ solution was added, the organic layer was separated and the aqueous layer was extracted with CH_2Cl_2. Title compound **4** (2.46 g, 92.7 %) was isolated as a yellow solid.

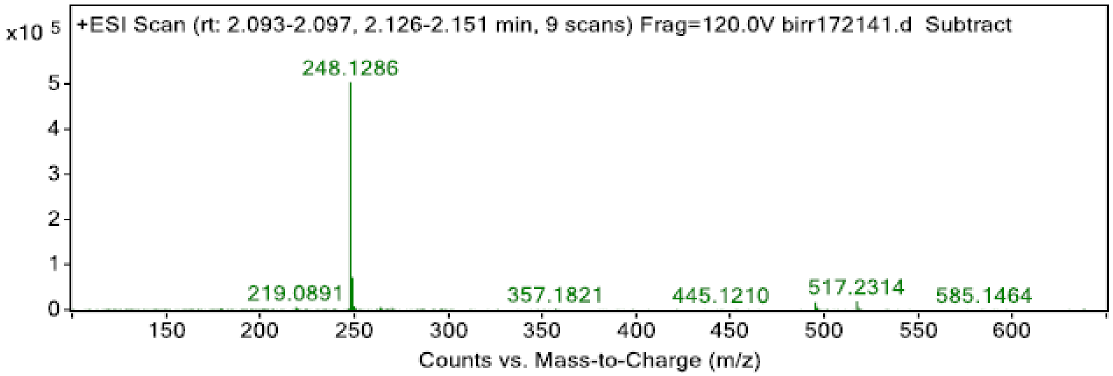

Figure S3.8: Mass spectrum of 7-diethylamino-4-hydroxymethylcoumarin$_{\text{prot.}}$. MS (ESI) m/z calculated for $C_{14}H_{17}NO_3 + H^+$: 248.12, found: 248.1286.

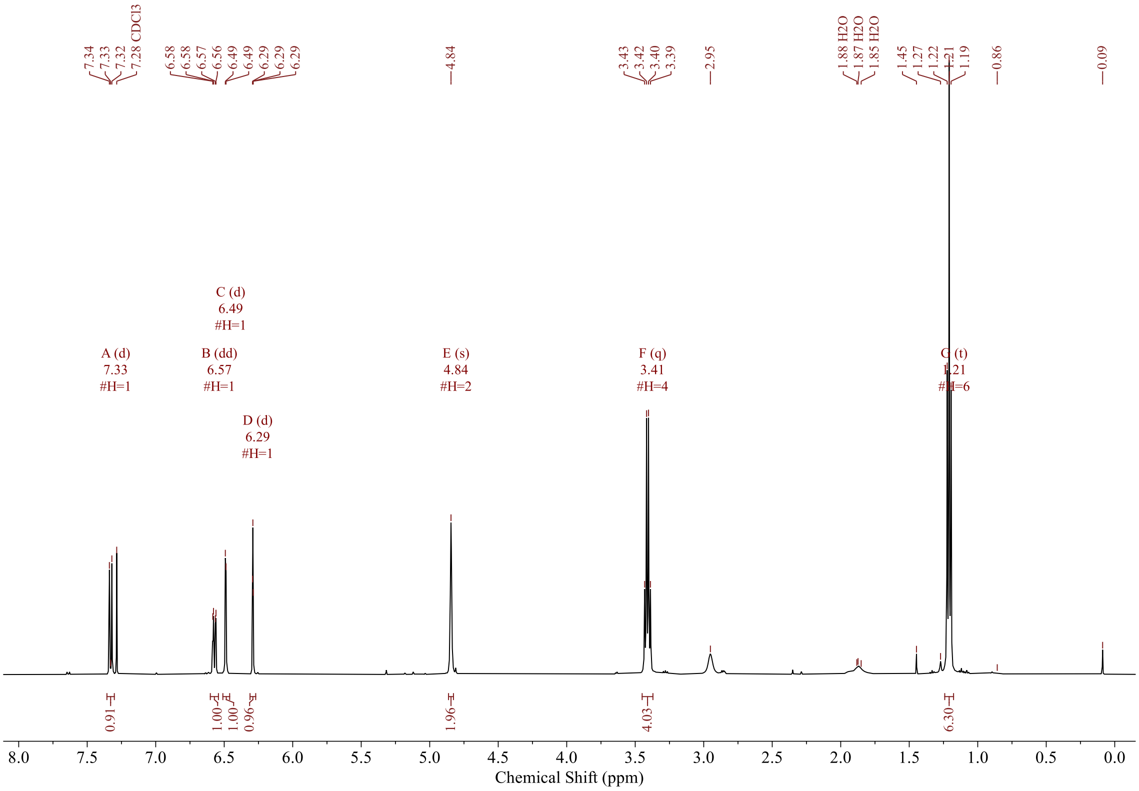

Figure S3.9: ^{1}H-NMR spectrum of 7-diethylamino-4-hydroxymethylcoumarin. ^{1}H-NMR (500 MHz, $CDCl_3$) δ(ppm) 7.33 (d, J = 9.0 Hz, 1H), 6.57 (dd, J = 9.0, 2.6 Hz, 1H), 6.49 (d, J = 2.6 Hz, 1H), 6.29 (d, J = 1.4 Hz, 1H), 4.84 (s, 2H), 3.41 (q, J = 7.1 Hz, 4H), 1.21 (t, J = 7.1 Hz, 6H).

Table S3.2: HPLC method for analysis of 7-diethylamino-4-hydroxymethylcoumarin. Flow rate: 1 mL

Time [min]	H_2O + 0.05 %TFA	ACN + 0.05 %TFA
0	75	25
1	75	25
21	40	60
21.1	5	95
25	5	95
25.1	75	25
30	75	25

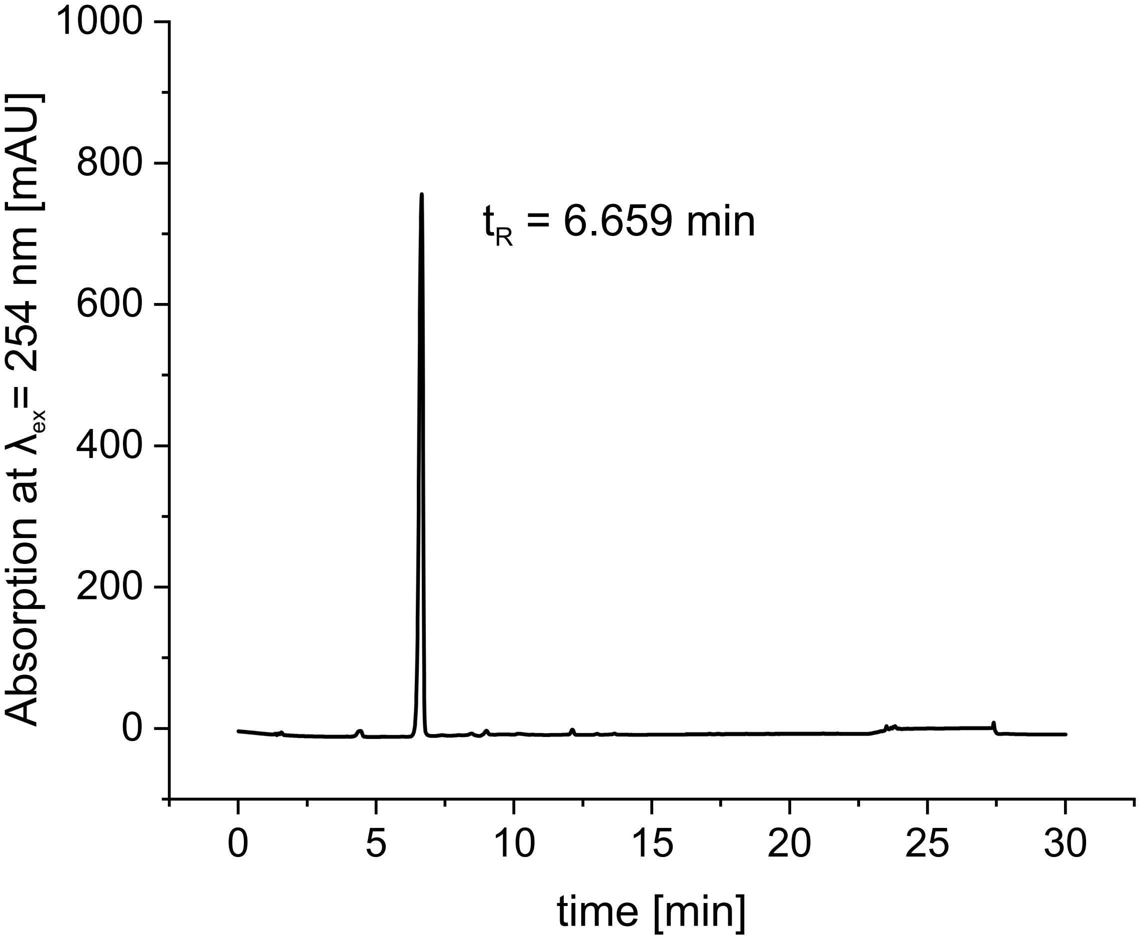

Figure S3.10: RP-HPLC analysis of 7-diethylamino-4-hydroxymethylcoumarin. Retention time t_R : 6.659 min. Purity of 91.99 %. milli Absorbance Units, mAU.

S3.1.4 Activation of DEAC

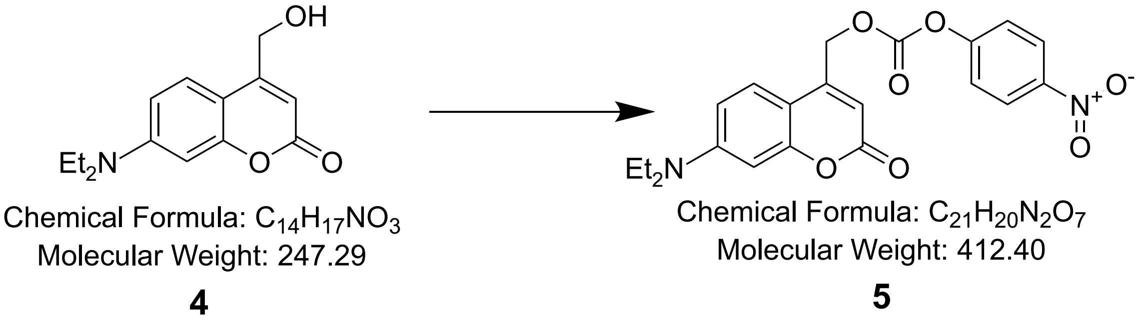

Scheme S3.4: Reaction equation for synthesis of 7-(diethylamino)-2-oxo-2H-chromen-4-yl)methyl (4-nitrophenyl) carbonate (**5**)

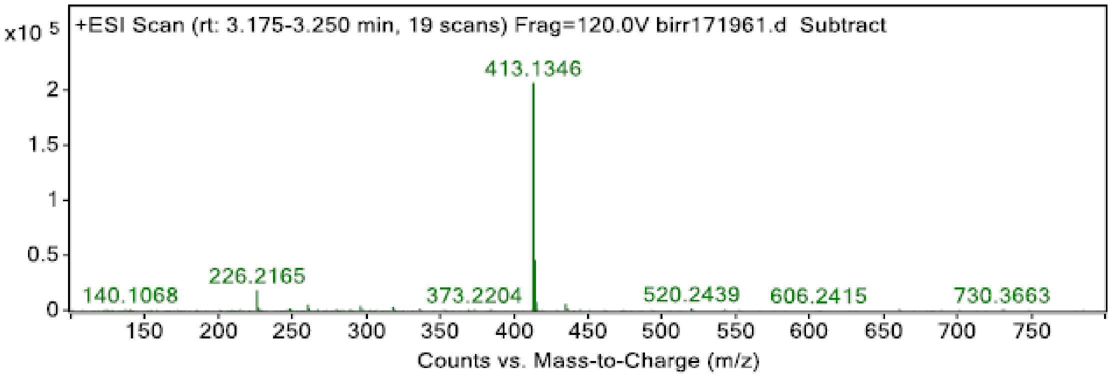

Figure S3.11: Mass spectrum of 7-(diethylamino)-2-oxo-2H-chromen-4-yl)methyl (4-nitrophenyl) carbonate$_{\text{prot.}}$.
MS (ESI) m/z calculated for $C_{21}H_{20}N_2O_7 + H^+$: 413.13 found: 413.1346.

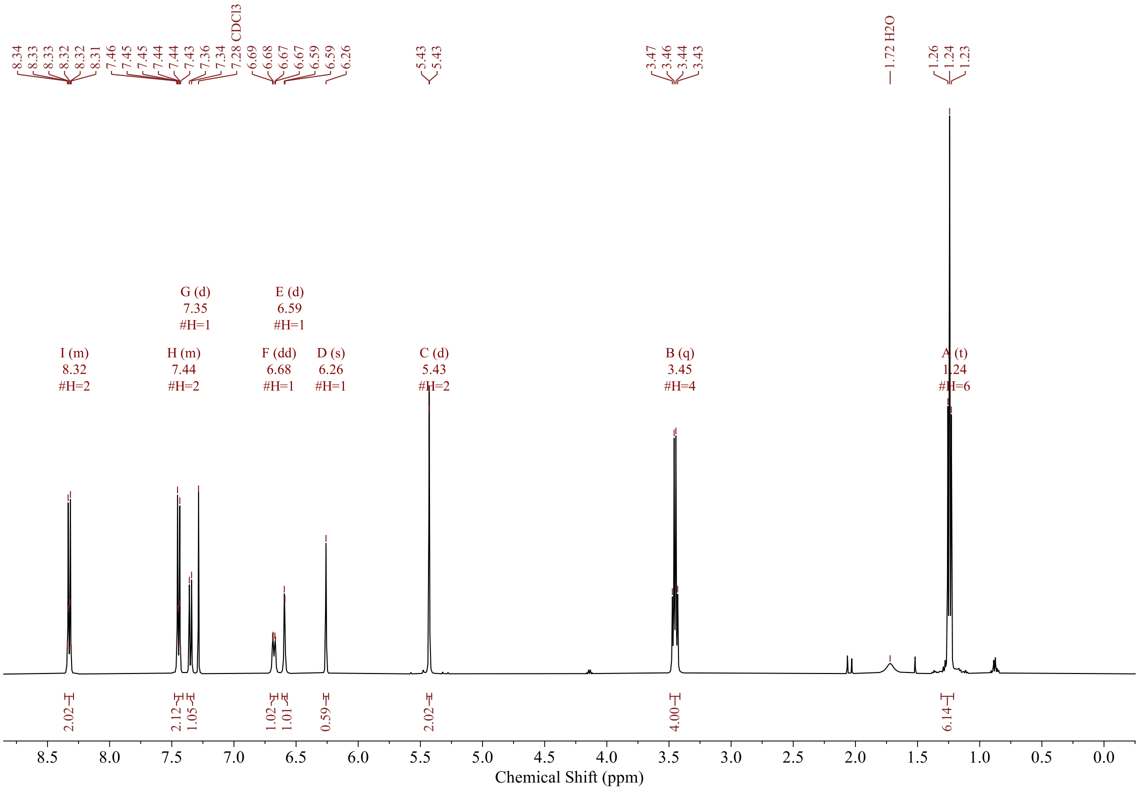

Figure S3.12: ^{1}H-NMR spectrum of 7-(diethylamino)-2-oxo-2H-chromen-4-yl)methyl (4-nitrophenyl) carbonate. ^{1}H-NMR (500 MHz, $CDCl_3$) δ(ppm) 8.36 - 8.29 (m, 2H), 7.48 - 7.41 (m, 2H), 7.35 (d, J = 9.0 Hz, 1H), 6.68 (dd, J = 9.3, 2.5 Hz, 1H), 6.59 (d, J = 2.6 Hz, 1H), 6.26 (s, 1H), 5.43 (d, J = 1.3 Hz, 2H), 3.45 (q, J = 7.1 Hz, 4H), 1.24 (t, J = 7.1 Hz, 6H).

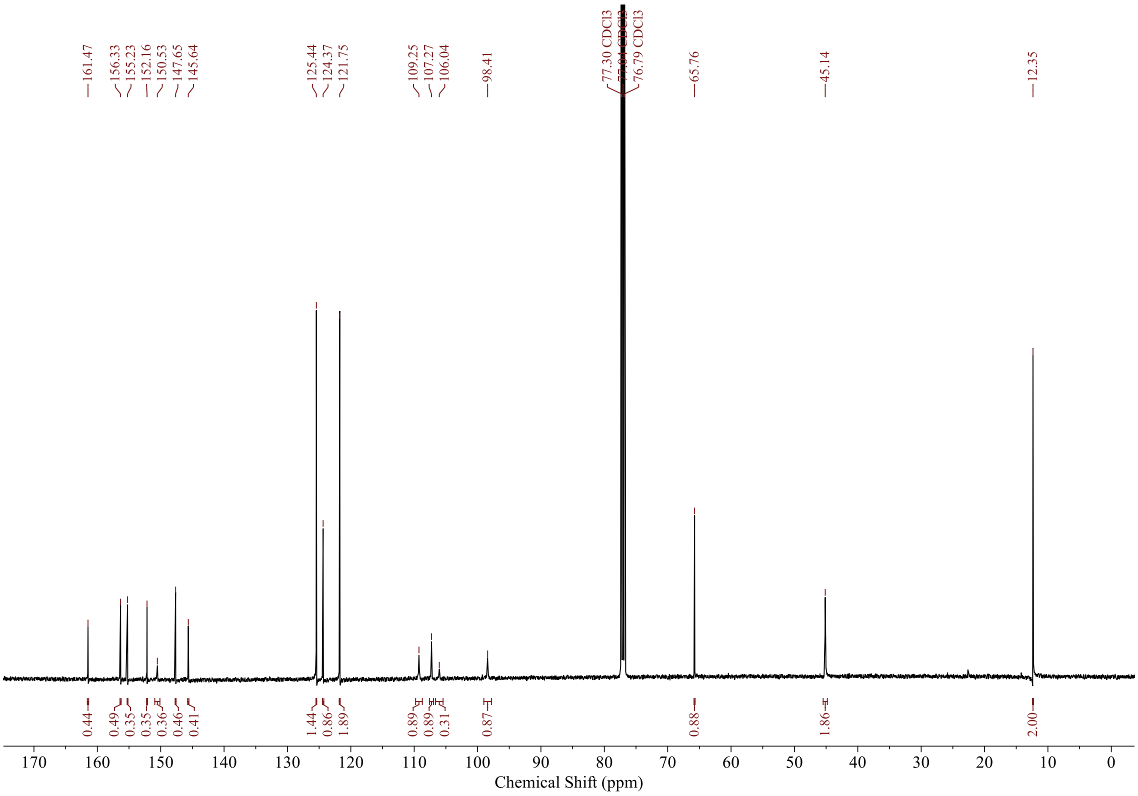

Figure S3.13: ^{13}C-NMR spectrum of 7-(diethylamino)-2-oxo-2H-chromen-4-yl)methyl (4-nitrophenyl) carbonate. ^{13}C-NMR (126 MHz, $CDCl_3$) δ(ppm) 161.47, 156.33, 155.23, 152.16, 150.53, 147.65, 145.64, 125.44, 124.37, 121.75, 109.25, 107.27, 106.04, 98.41, 65.76, 45.14, 12.35.

Table S3.3: HPLC method for analysis of 7-(diethylamino)-2-oxo-2H-chromen-4-yl)methyl (4-nitrophenyl) carbonate. Flow rate: 1 mL

Time [min]	H_2O + 0.05 %TFA	ACN + 0.05 %TFA
0	95	5
1	95	5
16	5	95
20	5	95
20.3	95	5
25	95	5

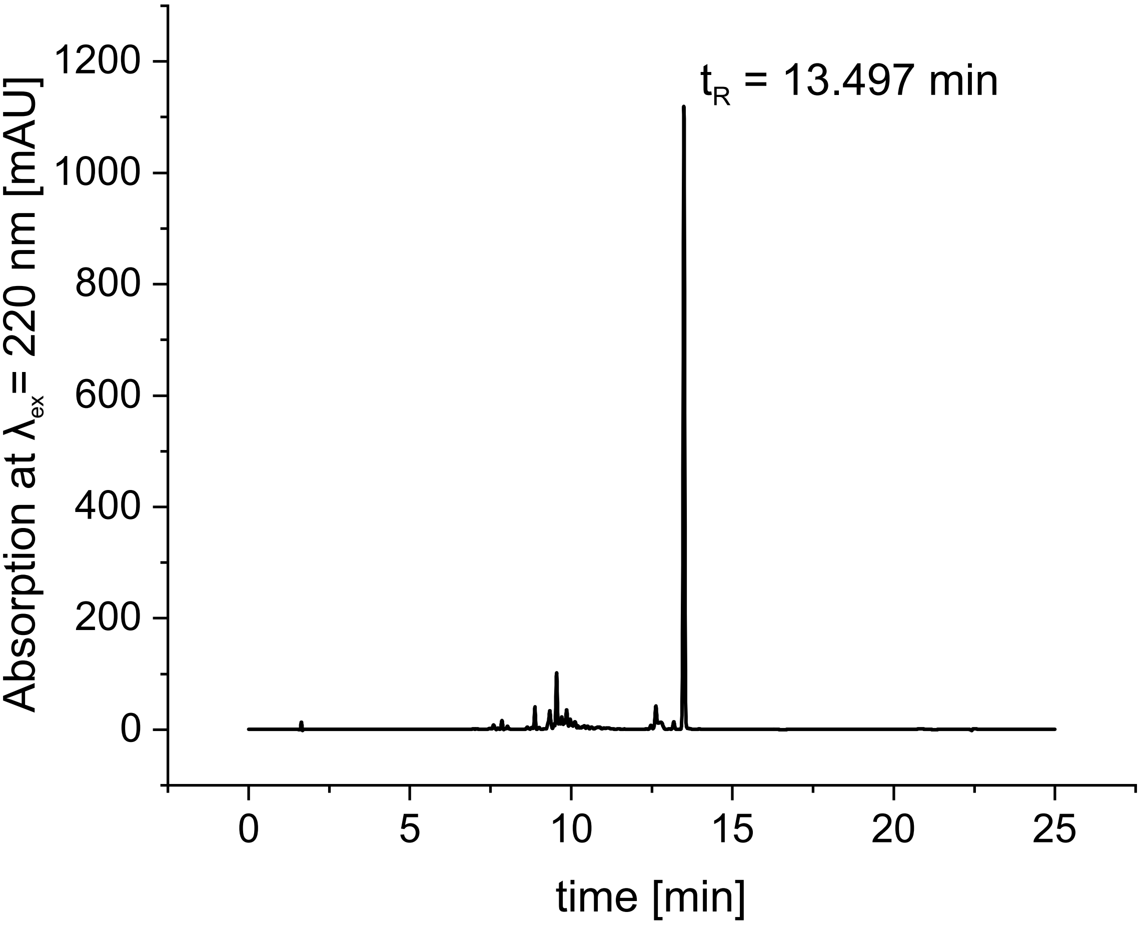

Figure S3.14: RP-HPLC analysis of 7-(diethylamino)-2-oxo-2H-chromen-4-yl)-methyl (4-nitrophenyl) carbonate. Retention time t_R : 13.497 min. Purity of 69.84 %. milli Absorbance Units, mAU.

S3.1.5 TAT 48-57 Coupling to Polymer

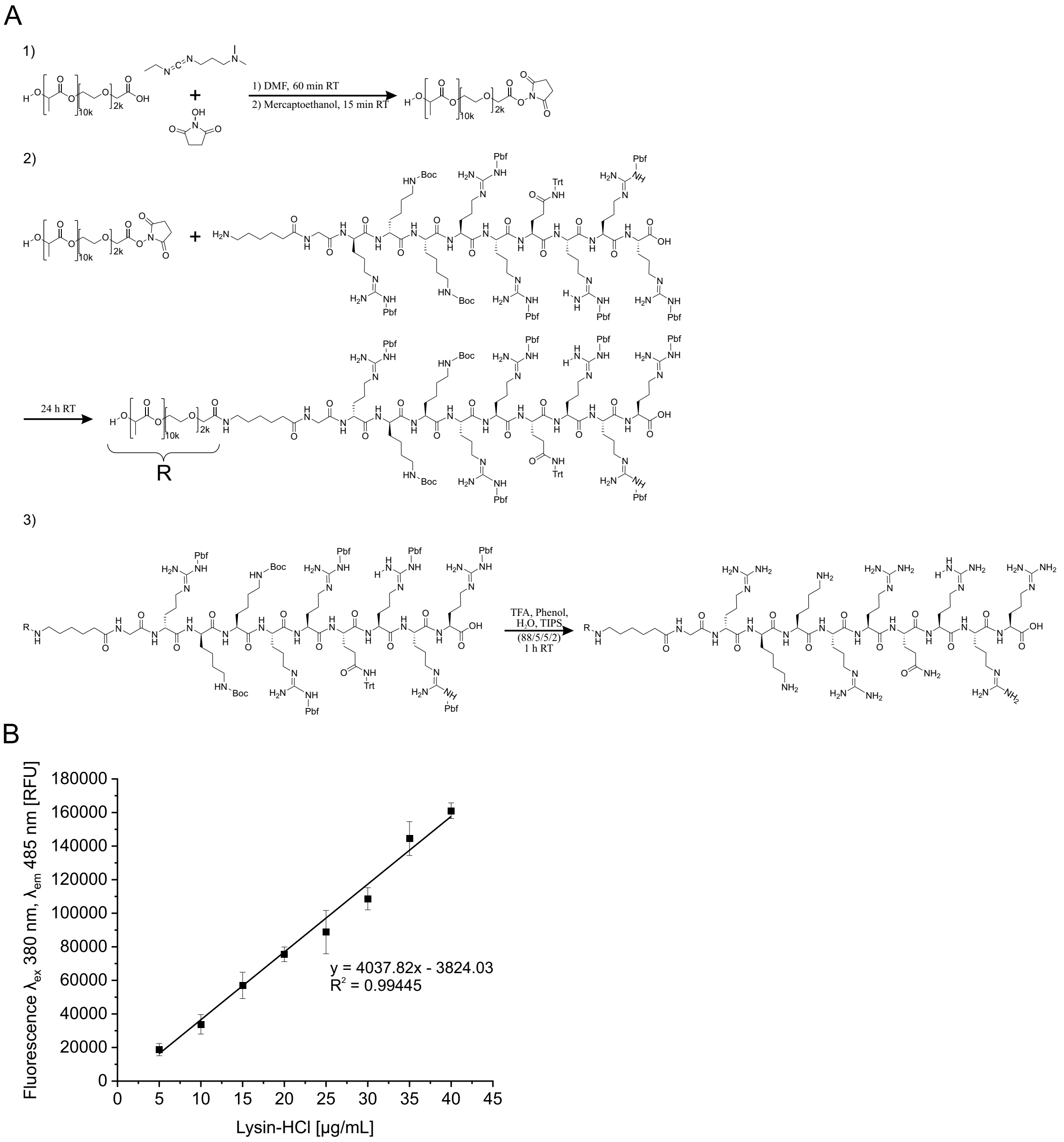

Figure S3.15: Functionalization of block copolymer and coupling efficiency. **A** 1) and 2) Reaction equation for the coupling of TAT 48-57 to the polymer via EDC/NHS chemistry. 3) Chemical equation for deprotection of sidechain protected TAT 48-57. **B** Plotting a calibration line for proofing linearity of Fluram assay by measuring the fluorescence of defined concentration of lysine hydrochloride after the addition of fluorescamine.

Calculation of lysine hydrochloride amount, which corresponds to 100 % coupling efficiency (CE).

$$\mathrm{m_{TAT-Polymer}} = \frac{\mathrm{conc_{micelles}}}{\mathrm{V_{sample}}} \tag{3.3}$$

$$\mathrm{n_{Lysine\ in\ TAT\ 48-57}} = \frac{\mathrm{m_{TAT-Polymer}}}{\mathrm{M_{TAT-Polymer}}} * 2 \tag{3.4}$$

$M_{\mathrm{COOH-PEG_{2k}-PLA_{10k}}}$ determined by ^{1}H-NMR and $M_{\mathrm{TAT\ 48-57}}$ was used to calculate $M_{\mathrm{TAT-Polymer}}$ [1].

$$M_{\mathrm{TAT-Polymer}} = M_{\mathrm{COOH-PEG_{2k}-PLA_{10k}}} + M_{\mathrm{TAT48-57}} \tag{3.5}$$

$$m_{\mathrm{Lysine-HCL(100\,\%)}} = n_{\mathrm{Lysine\ in\ TAT\ 48-57}} * M_{\mathrm{Lysine-HCl}} \tag{3.6}$$

CE of TAT-Polymer was calculated with the following equation:

$$CE_{\mathrm{TAT-Polymer}}[\%] = \frac{RFU_{\mathrm{TAT-Polymer}}}{RFU_{\mathrm{Lysine-HCl\ (100\,\%)}}} * 100 \tag{3.7}$$

The CE of TAT-Polymer reaction was 93.68 % ± 3.79 % (N=3).

S3.1.6 Quantification of DEAC Coupling to TAT-Polymer

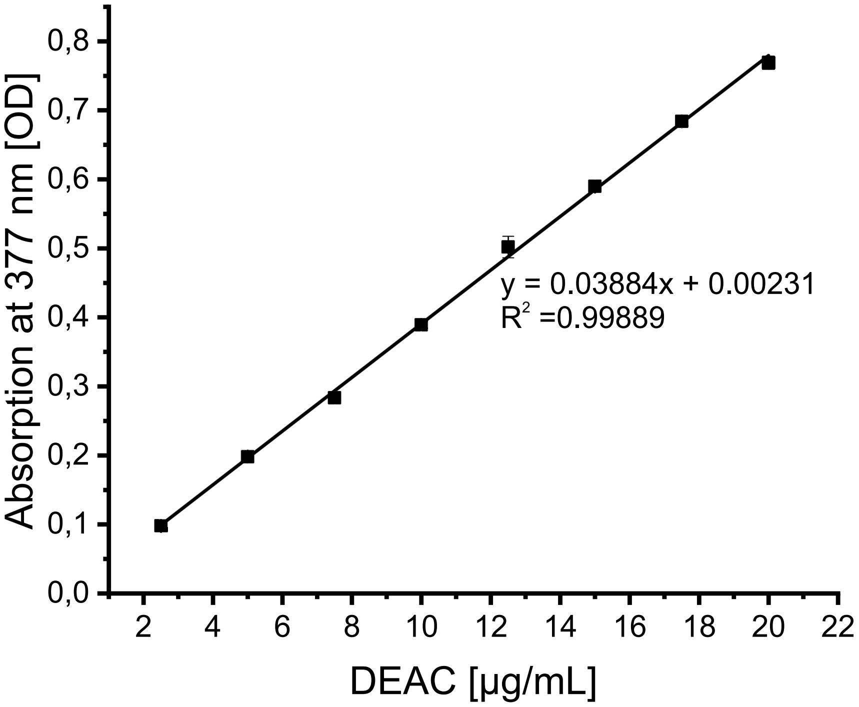

Figure S3.16: Coupling efficiency of DEAC to TAT-polymer. Plotting a calibration line for quantification of DEAC coupling to TAT-Polymer. Absorption is plotted against DEAC concentration.

Assuming a complete reaction, two DEAC molecules couple to TAT-polymer. The efficiency is calculated:

$$\mathrm{c_{DEAC}} = \frac{\beta_{\mathrm{DEAC}}}{\mathrm{M_{DEAC}}} \tag{3.8}$$

$\beta_{\mathrm{[TAT]-PEG_{2k}-PLA_{10k}Polymer}}$ is the mass concentration of DEAC coupled to TAT-PEG_{2k}-PLA_{10k} determined by absorption measurement.

$$\mathrm{c_{[TAT]-PEG_{2k}-PLA_{10k}Polymer}} = \frac{\beta_{\mathrm{[TAT]-PEG_{2k}-PLA_{10k}Polymer}}}{\mathrm{M_{[TAT]-PEG_{2k}-PLA_{10k}Polymer}}} \tag{3.9}$$

$\mathrm{M_{[TAT]-PEG_{2k}-PLA_{10k}Polymer}}$ was calculated as followed:

$$\mathrm{M_{[TAT]-PEG_{2k}-PLA_{10k}Polymer}} = \mathrm{M_{TAT-PEG_{2k}-PLA_{10k}Polymer}} + (2 * \mathrm{M_{DEAC}} - 2) \tag{3.10}$$

$$\mathrm{CE_{[TAT]-PEG_{2k}-PLA_{10k}Polymer}}[\%] = \frac{\frac{\mathrm{c_{DEAC}}}{\mathrm{c_{[TAT]-PEG_{2k}-PLA_{10k}Polymer}}}}{2} * 100 \tag{3.11}$$

S3.1.7 PLGA Labeling

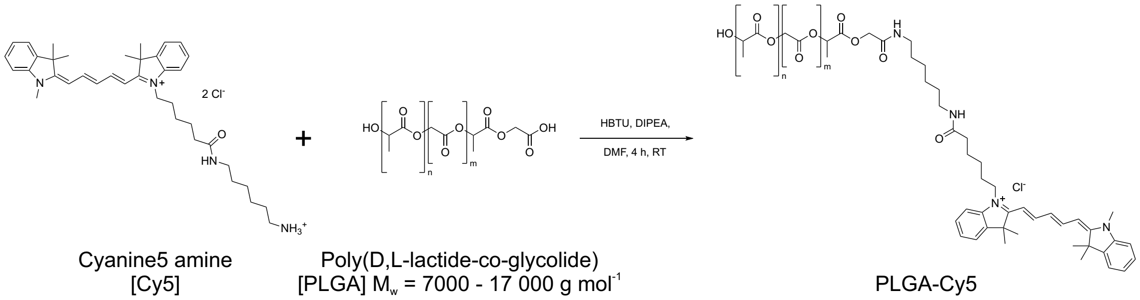

Scheme S3.5: Chemical equation for synthesis of Cy5 coupling to PLGA.

S3.2 Calculation on Foerster Radius and Characterization of PEG Conformation

The Foerster Radius (R_0) was calculated with Equation (3.12)

$$R_0 = 0.211 * \sqrt[6]{\kappa^2 n^{-4} Q_D J(\lambda)} \tag{3.12}$$

where κ^2 is the orientation factor, n is the refractive index, Q_D is the quantum yield of the donor and $J(\lambda)$ is the overlap integral calculated separately by Equation (3.13) [2].

$$J(\lambda) = \frac{\int\limits_0^\infty F_D(\lambda)\varepsilon_A(\lambda)\lambda^4\, d\lambda}{\int\limits_0^\infty F_D(\lambda)\, d\lambda} \tag{3.13}$$

$\varepsilon_A(\lambda)$ is the extinction coefficient of the acceptor fluorophore at a defined wavelength, F_D is the fluorescence spectrum of the donor. For the calculation of Foerster radius for the FRET pair DEAC-Cy5, κ^2 was assumed 2/3 and Q_D was obtained from literature with a value of 0.079 [3]. R_0 was calculated to be 32.6 Å or 3.26 nm respectively.

The PEG chains in core-shell NP design can arrange either as a mushroom or a brush conformation. The conformation is described by the quotients of Flory Radius (R_F) and grafting distance (D) of PEG chains which was previously described by our group and others [1, 4]. A value of $R_F/D < 1$ is linked to mushroom conformation and $R_F/D > 1$ is referred as brush conformation, which can be further characterized as dense brush with a $R_F/D > 2.8$ [4]. R_F is defined by Equation (3.14), where α is the length of a PEG monomer (0.35 nm) and N is the number of monomers in PEG chain calculated by dividing the molecular weight of the PEG chain (2000 g mol^{-1}) by the monomer molecular weight (44 g mol^{-1}).

$$R_F = \alpha * N^{\frac{3}{5}} \tag{3.14}$$

For the PEG$_{2k}$-PLA$_{10k}$ block copolymer used in our NP design R_F has a value of 3.46 nm. The grafting distance (D) between two polymer chains on a particle surface is calculated by Equation (3.15), where S corresponds to the surface occupied by a single PEG chain [5].

$$D = 2 * \sqrt[2]{\frac{S}{\pi}} \tag{3.15}$$

S is given by:

$$S = \frac{6 * M_{PEG}}{d_h * N_A * f * \rho_{NP}} \tag{3.16}$$

where, M_{PEG} is the molecular weight of the PEG chain, d_h is the hydrodynamic diameter of the NP, N_A is the Avogadro number, f is the mass fraction of PEG in the blends of the PEG$_{2k}$-PLA$_{10k}$ block copolymer and ρ_{NP} is the density of the NP. The density of 1.25 g cm^{-2} for NP was estimated corresponding to the density of NP composed of PLA-g-PEG blends [6]. D was calculated to be 0.99 nm, resulting in a value for $R_F/D = 3.58$. The thickness of the PEG layer was calculated by Equation (3.17) had a value of 8.28 nm [4].

$$L = \frac{N * \alpha^{5/3}}{D^{2/3}} \tag{3.17}$$

Thus, it could be assumed that the polymer chains arrange in a brush conformation.

S3.3 Photobleaching

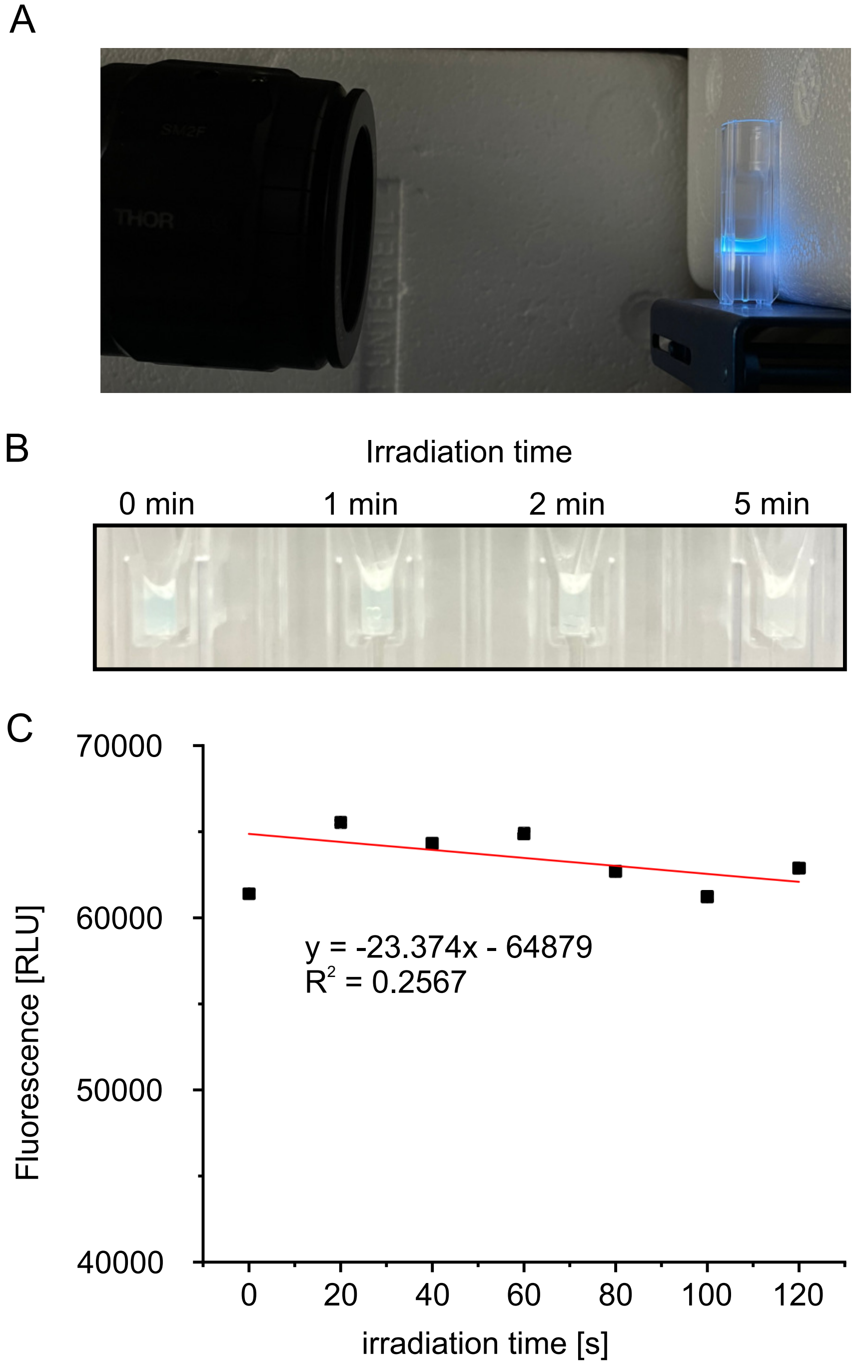

Figure S3.17: Photobleaching of NPs. **A** Irradiation setup. **B** Image of [TAT]-NP before and after different irradiation times. **C** Fluorescence of Cy5 of COOH-NP is plotted against irradiation time of NPs with LED at $\lambda = 365\,\text{nm}$.

S3.4 Nanoparticle Characterization

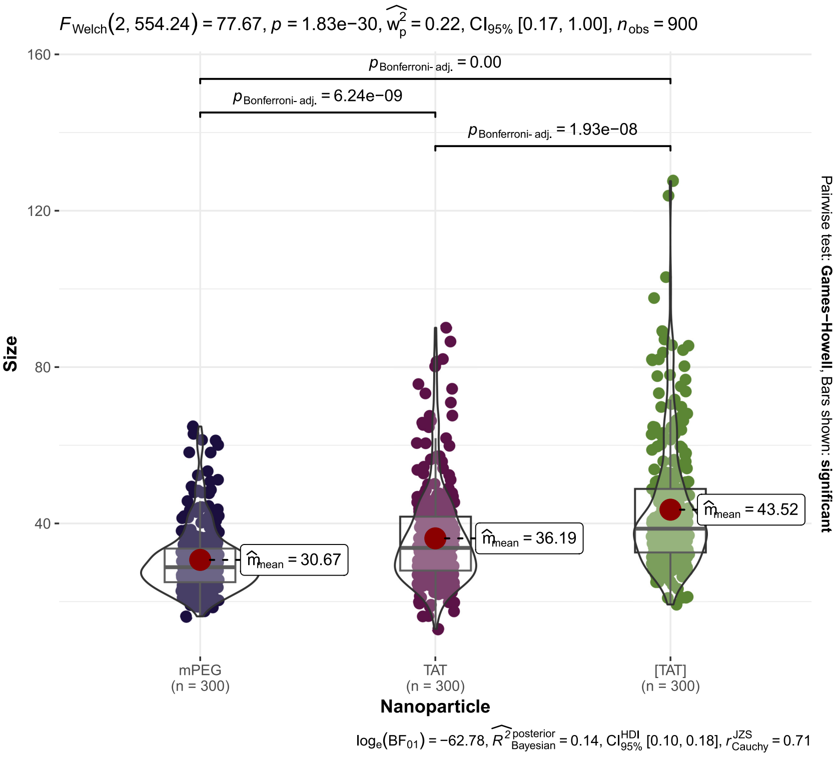

Figure S3.18: Size distribution and statistics of TEM dataset. Violin plots of NP size distributions depicting the full kernel density of measured sizes. The median NP size is shown as horizontal line within the box, whose lower and upper edges represent the first (Q1) and third (Q3) quartiles, respectively. Whiskers indicate the most extreme data points within 1.5 times the interquartile range from the lower and upper quartiles. Red dots indicate mean sizes. A one-way Welch's ANOVA with p-values < 0.001 (adjusted using Bonferroni method) showed significant differences in NP mean size.

References

[1] Kathrin Schorr et al. "The quantity of ligand-receptor interactions between nanoparticles and target cells". In: *Nanoscale horizons* 10.4 (2025), pp. 803–823. DOI: `10.1039/D4NH00645C`.

[2] P. Wu and L. Brand. "Resonance energy transfer: methods and applications". In: *Analytical biochemistry* 218.1 (1994), pp. 1–13. ISSN: 0003-2697. DOI: `10.1006/abio.1994.1134`.

[3] André Vidal Pinheiro et al. "pH effect on the photochemistry of 4-methylcoumarin phosphate esters: caged-phosphate case study". In: *The journal of physical chemistry. A* 114.49 (2010), pp. 12795–12803. DOI: `10.1021/jp103045u`.

[4] Qi Yang and Samuel K. Lai. "Engineering Well-Characterized PEG-Coated Nanoparticles for Elucidating Biological Barriers to Drug Delivery". In: *Methods in molecular biology (Clifton, N.J.)* 1530 (2017), pp. 125–137. DOI: `10.1007/978-1-4939-6646-2_8`.

[5] R. Gref et al. "'Stealth' corona-core nanoparticles surface modified by polyethylene glycol (PEG): influences of the corona (PEG chain length and surface density) and of the core composition on phagocytic uptake and plasma protein adsorption". In: *Colloids and Surfaces B: Biointerfaces* 18.3-4 (2000), pp. 301–313. ISSN: 09277765. DOI: `10.1016/S0927-7765(99)00156-3`.

[6] Jean-Michel Rabanel et al. "Effect of the Polymer Architecture on the Structural and Biophysical Properties of PEG-PLA Nanoparticles". In: *ACS applied materials & interfaces* 7.19 (2015), pp. 10374–10385. DOI: `10.1021/acsami.5b01423`.

Chapter 4

Engineering Bioluminescent Nanoparticles: Comparing Native and Modified NanoLuc

Abstract

Bioluminescent nanoparticles (NPs) represent a promising platform in bioimaging and biosensor applications. In this study, we report for the first time, the successful incorporation of NanoLuc, a small and bright luciferase, in polymeric core-shell NPs. To this end, we used NPs composed of poly(D,L-lactide-*co*-glycolide) and a poly(ethylene glycol)-*b*-poly(D,L-lactide) block copolymer functionalized with maleimide. This functionalization allows covalent immobilization of NanoLuc within the NP shell via its native cysteine residue. An additional cysteine residue was incorporated into the sequence following the NanoLuc open reading frame. This modification significantly improved coupling efficiency, enabling immobilization of a greater amount of protein. Furthermore, the modified NanoLuc variant retained its enzymatic activity after immobilization, whereas native NanoLuc lost approximately 90 % of its activity.

4.1 Introduction

Bioluminescence refers to the generation of light through enzyme-mediated oxidation reactions, typically involving a substrate, luciferin, catalyzed by the enzyme luciferase. This phenomenon does not require external excitation and offers distinct advantages such as high sensitivity, high quantum yield and an excellent signal-to-noise ratio, making it a powerful tool for real-time imaging of molecular and cellular processes [1]. These unique properties have led to the implementation of bioluminescent system (BLS) in biotechnology as biosensors and bioimaging tools [2, 3]. The convergence of luciferase-based BLS and nanoparticles (NPs) enables innovative approaches in bioimaging, biosensors and therapeutic applications [4–6]. NPs expanding the scope of BLS by enabling specific tissue targeting or encapsulation of drug molecules. In the work of Yang et al., bioluminescence was used as an activator for photodynamic therapy with Rose Bengal loaded NPs to inhibit tumor growth [6]. Further, bioluminescent NPs offer a specific advantage over fluorescence techniques by circumventing the issues like autofluorescence and photobleaching, as they are inherently detectable without the need for external light [2, 7]. The immobilization of luciferase on NPs might be beneficial regarding effectiveness of BLS by yielding higher enzyme density or improving enzyme orientation [7, 8]. Currently, over 30 BLS can be employed for designing bioluminescent NPs [9, 10]. While many of these systems rely on cofactors, ATP, or coenzymes, BLS from marine organisms are particularly attractive as they require only oxygen for luciferin oxidation [11, 12]. NanoLuc, artificially generated from the deep-sea shrimp *Oplophorus gracilirostris*, is a small (19.1 kDa) luciferase emitting blue light upon furimazine oxidation [13]. In addition to its small size, which allows immobilization on the NP surface without notably increasing the NP dimensions, NanoLuc provides major advantages over conventional firefly luciferase (61 kDa). NanoLuc paired with furimazine exhibits glow-type kinetics, generating a prolonged and stable bioluminescent signal that is well suited for imaging in biological environments. In comparison to firefly luciferase, NanoLuc reveals a 150-fold higher luminescence signal intensity and is more stable in concerns of temperature and pH [13, 14]. All in all, NanoLuc is particular suitable for bioluminescence resonance energy transfer [15–18].

The integration of proteins into NPs is a critical step in designing functional BLS. Several strategies have been developed to achieve stable and efficient coupling. Non-covalent attachment by physical adsorption represents the easiest approach, relying on interaction between protein and NP. The resulting attachment is often weak, prone to desorption and leads to random protein orientation [19, 20]. In contrast, covalent conjugation provides robust linkage and greater control over the spatial orientation of the conjugated molecule. Covalent conjugation can be achieved by affinity-based coupling, exemplified by biotin-streptavidin and Strep-tag interactions, offering high specificity [21]. However, affinity-based coupling requires co-expression of complementary binding partner and may alter protein conformation, which can compromise enzymatic activity [22]. Targeting complementary reactive groups, such as maleimide-thiol reactions for cysteine-rich proteins, is the easiest way to accomplish covalent conjugation [20, 23, 24].

The goal of this study was to implement a bioluminescent polymeric core-shell NP by coupling NanoLuc via maleimide-thiol chemistry. Furthermore, special attention was given to assess the coupling efficiency and functional differences between native luciferase and its cysteine-enriched variant, prior coupling and surfaced-bound.

4.2 Material and Methods

4.2.1 Materials

Ultrapure water used for the experiments was treated with a Milli-Q EQ 7000 system (Merck, Darmstadt, Germany) equipped with Milli-Q Biopak filter (Merck, Darmstadt, Germany) and taken fresh every day. Hereinafter referred to as mQ water. Unless otherwise stated, all chemicals and reagents were obtained from Sigma-Aldrich (Taufkirchen, Germany) in analytical grade. *FastGene Plasmid mini kit*, *FastGene Gel/PCR Extraction kit* and Midori Green Advance deoxyribonucleic acid (DNA) stain were acquired from Nippon Genetics Europe GmbH (Dueren, Germany). 1 kb DNA ladder, 6x gel loading dye purple, NEBuilder ®HiFi DNA Assembly Master Mix, Q5 High-Fidelty DNA polymerase, competent bacteria cells (*E.coli* DH5α and *E.coli* BL21(DE3)) and super optimal broth with catabolite repression (SOC) medium were purchased from New England Biolabs (MA, USA). peqGOLD Protein Marker I was obtained from VWR International GmbH (Darmstadt, Germany). A 30 % (w/v) aqueous solution of acrylamide and N,N'-methylene bisacrylamide (Bis) (37.5:1 ratio), referred to as acrylamide mix, was purchased from SERVA Electrophoresis GmbH (Heidelberg, Germany). NanoBRET® Nano-Glo® Substrate was obtained from Promega GmbH (Walldorf, Germany). It is referred to as furimazine in the following. The primers were synthesized by Eurofins Genomics (Ebersberg, Germany). Lysogeny broth (LB) medium was prepared by dissolving Tryptone ($10\,\mathrm{g\,L^{-1}}$), Yeast Extract ($5\,\mathrm{g\,L^{-1}}$), and NaCl ($10\,\mathrm{g\,L^{-1}}$) in mQ water. The pH was adjusted to 7.0 using NaOH. Dulbecco's phosphate-buffered saline (DPBS) was prepared in-house according to the standard formulation, filtrated and autoclaved before use. The plasmid *pET-28a(+)::NL* was kindly provided by Andrew Millar (Addgene plasmid #141289; `http://n2t.net/addgene:141289`; RRID: Addgene_141289). Heterobifunctional t-Boc amine poly(ethylene glycol) hydroxyl with a molecular mass of $2000\,\mathrm{g\,mol^{-1}}$ (tBoc-NH-PEG$_{2k}$-OH) was purchased from Jenkem Technology USA, Inc. (Allen, TX, USA). Poly(ethylene glycol) methyl ether with a molecular mass of $2000\,\mathrm{g\,mol^{-1}}$ (mPEG$_{2k}$-OH) and N-Succinimidyl 3-Maleimidopropionate were bought from TCI (Eschborn, Germany). Resomer RG 502, poly(D,L-lactide-*co*-glycolide) (lactide:glycolide 50:50, ester terminated, M$_w$ 7000-17000 Da) (PLGA) and QuantiPro™BCA Assay Kit were obtained from Sigma-Aldrich (Taufkirchen, Germany). For cell disruption the Sonoplus HD 2070 UW 2070 Ultrasonic Homogenizer (Bandelin, Germany) was used. $\mathrm{Ni^{2+}}$−NTA agarose beads were purchased from Agarose Bead Technologies (Madrid, Spain). Sephadex™ G-25 M were obtained from Cytiva Europe GmbH (Germany). Nuclear magnetic resonance (NMR) spectra were recorded on a Bruker Avance-400 NMR spectrometer (Billerica, MA, USA). High-resolution mass spectrometry (HRMS) was performed on a Q-TOF 6540 ultrahigh definition(UHD) liquid chromatography/mass spectrometry (LC/MS) system (Agilent Technologies, Santa Clara, CA, USA) using an electrospray ionization (ESI) source. High-performance liquid chromatography (HPLC) analysis was performed with 1260 Infinity II from Agilent Technologies (Santa Clara, CA, USA) using a Kinetex EVO C18 column (100 Å, 2.6 µm, 150 mm x 4.6 mm, Phenomenex Ltd., Germany). Preparative HPLC analysis was performed with Prep 150 LC system from Waters (Eschborn, Germany) consisting of a 2545 binary gradient module, a 2489 UV/visible detector and a Waters Fraction Collector III. A Gemini-NX C18 column (110 Å, 5 µm, 250 mm × 21 mm, Phenomenex Ltd. Germany) was used. Size exclusion chromatography (SEC) was carried out with a custom-made device consisting of a HPLC pump 64 (Knauer, Germany) and an AF-10A XL fluorescence detector (Shimadzu Deutschland GmbH, Germany). Fractogel ®EMD BioSEC was used as column material. Data were recorded and processed using QtiPlot (Version 1.1.9, IONDEV SRL, Romania)

4.2.2 Frozen Stocks

E. coli BL21 DE Rossetta2 pLysS containing plasmid *pET-28a(+)::NL* were spread on LB agar plates containing kanamycin (50 µg $\mathrm{mL^{-1}}$) and chloramphenicol (25 µg $\mathrm{mL^{-1}}$) and incubated overnight at 37 °C. Two colonies were randomly picked and incubated overnight in 5 mL LB containing antibiotics at 37 °C and continuous shaking at 220 rpm. 500 µL of the overnight culture were mixed with 500 µL 50 % glycerol in a 2 mL screw top tube and frozen at −80 °C. The glycerol stock was stored at −80 °C.

4.2.3 NanoLuc: Plasmid Extraction

Plasmid extraction was performed using the *FastGene Plasmid Mini Kit. E.coli* cells harboring the plasmid *pET-28a(+)::NL* were recovered from frozen stocks in LB medium supplemented with kanamycin (50 µg $\mathrm{mL^{-1}}$) and chloramphenicol (25 µg $\mathrm{mL^{-1}}$), and incubated overnight at 37 °C with shaking at 220 rpm. Following incubation, 1.5 mL of the bacterial culture was centrifuged for 2 min at 13 300 rpm to pellet the cells. Plasmid isolation was carried out according to the manufacturer's protocol, with the exception that 50 µL mQ water was used for elution. Plasmid concentration was determined by UV/Vis spectrophotometry using a NanoDrop 2000 (Thermo Fisher Scientific, MA, USA).

4.2.4 Site-directed Mutagenesis

To incorporate the His-tag within the reading frame of the NanoLuc, which is sufficient for NanoLuc purification, site-directed mutagensis was performed to introduce two base pairs in the obtained plasmid *pET-28a(+)::NL*. Moreover, the open reading frame was extended by eliminating the stop codon of the 3' end of the NanoLuc sequence. In the case of Cys-NanoLuc, an additional cysteine residue was inserted at the C-terminus of NanoLuc and the amino acid sequence between NanoLuc and His-tag was shortened. For mutagenesis, two fragments were defined with primers overlapping within the origin of replication, ensuring that only the correctly assembled plasmid would replicate in *E. coli*. Mutation-specific primers were designed using SnapGene to introduce the desired point mutation within fragment 1. Additionally, the primers were designed with overlapping regions to allow seamless reassembly via Gibson. Sequences are provided in Table 4.1.

Table 4.1: Primer sequences used for amplification of NanoLuc and Cys-NanoLuc constructs. Forward and reverse primers are listed for each construct. Base pair changes introduced for shifting open-reading frame via site-directed mutagenesis are highlighted in red. The mutations for the introduction of a cysteine residue are highlighted in yellow.

Construct	Fragment	Direction	Sequence
NanoLuc	Fragment 1	forward	5'-GGT AAC CTT TTC GCC AGA ATG CGT TC-3'
		reverse	5'-TAG CAC CGC CTA CAT ACC TCG CTC TG-3'
	Fragment 2	forward	5'-CGA GGT ATG TAG GCG GTG CTA-3'
		reverse	5'-TCT GGC GAA AAG GTT ACC GGA TCC-3'
Cys-NanoLuc	Fragment 1	forward	5'- GCA TAA CCT TTT CGC CAG AAT GCG TTC GCA CA-3'
		reverse	5'-TAG CAC CGC CTA CAT ACC TCG CTC TG-3'
	Fragment 2	forward	5'-CGA GGT ATG TAG GCG GTG CTA-3'
		reverse	5'-CTG GCG AAA AGG TTA TGC AAG CTT GCG GCC GC-3'

PCR amplification was performed using manufacturer's instructions for Q5 High-Fidelty DNA polymerase. Each fragment was amplified separately in a 50 µL reaction containing: 50 ng DNA template , 2.5 µL of each primer (1 to 10 diluted in mQ water, final conc. 500 nM), 1 µL dNTPs (final conc. 200 µM), 10 µL Q5 buffer, 0.5 µL Q5 High-Fidelty DNA polymerase, 32.5 µL mQ water. PCR was performed using Bioer LifeECO (Bioer Technology, Zhejiang, China). The thermal cycling conditions are listed in Table 4.2 and Table 4.3. To verify successful amplification of the NanoLuc fragments, PCR products were analyzed by agarose gel electrophoresis. A 1 % agarose gel was prepared in 1× TAE buffer (40 mM Tris base, 20 mM acetic acid, 1 mM EDTA disodium salt dihydrate in mQ water) and supplemented with 4 µL Midori Green Advance DNA stain for DNA visualization. 5 µL of each PCR product was mixed with 1 µL of 6x gel loading dye purple and loaded into the gel wells. A 1 kb DNA ladder was used as a size reference. Electrophoresis was performed at 90 V for 60 min using ThermoEC MINICELL PRIMO EC 320 Electrophoretic gel system and Thermo EC250-90 (Thermo Fisher Scientific, MA, USA). DNA bands were visualized under UV light using the InGenius gel documentation system (Syngene, Cambridge, UK), allowing confirmation of successful amplification based on expected fragment sizes. Successfully amplified fragments were subsequently purified and assembled using Gibson Assembly.

Table 4.2: PCR conditions for amplification of fragment 1 NanoLuc / Cys-NanoLuc

Step	**Settings**	
	Temperature / [°C]	**Time** / [sec]
Initial denaturation	98	30
28 cycles	98	10
	65 / 72	30
	72	120
Final extension	72	120
Hold	4	

4.2.5 PCR Product Purification and Gibson Assembly

PCR products of Fragment 1 and Fragment 2 were combined and purified using the *FastGene Gel/PCR Extraction kit* according to the manufacturer's instructions. A total volume of 40 µL was processed, and DNA was eluted in 20 µL of mQ water. Purified PCR products were stored at −20 °C until further use.

To ligate both fragments, 5 µL of purified PCR product was mixed with 5 µL

Table 4.3: PCR conditions for amplification of fragment 2 NanoLuc / Cys-NanoLuc

Step	**Settings**	
	Temperature / [°C]	**Time** / [sec]
Initial denaturation	98	30
28 cycles	98	10
	70 / 69	30
	72	78
Final extension	72	120
Hold	4	

Gibson HiFi Master Mix and heated for 1 h at 50 °C. The ligation product was subsequently stored at −20 °C.

4.2.6 Plasmid Transformation for Replication, Isolation, Sequencing and Expression

Plasmid transformation was performed using the heat shock method, in which competent bacterial cells are briefly exposed to elevated temperatures to induce membrane permeability and allow plasmid DNA entry.

For replication, isolation, and sequencing, 5 µL of the ligation products and 50 µL of competent *E.coli* DH5α cells were mixed and incubated on ice for 30 min. Cells were heat shocked at 42 °C for 30 sec, returned to ice for 2 min and then supplemented with 500 µL of SOC medium. After 1 h of incubation at 37 °C with constant agitation at 150 rpm, 100 µL was plated on LB agar containing kanamycin (50 µg mL^{-1}). Plates were incubated overnight at 37 °C. Five colonies were randomly selected from each transformation and cultivated in 3 mL LB containing kanamycin (50 µg mL^{-1}). Plasmids were extracted using the *FastGene Plasmid mini kit* as described above. Concentrations (ng µL^{-1}) were measured via NanoDrop 2000. The plasmid sample with the highest concentration was selected for Sanger sequencing.

For expression, 1 µL of the plasmid DNA (*pET-28a(+)::His-NL* or *pET-28a(+)::Cys-NL*) was transformed into 50 µL of competent *E.coli* BL21(DE3) using the same heat shock protocol. After plating and overnight incubation on LB-kanamycin, one colony per construct was selected and cultured in 3 mL LB-kanamycin. Frozen stocks were prepared as previously described, using kanamycin (50 µg mL^{-1}) as the only antibiotic, and stored at −80 °C.

4.2.7 Expression and Purification

The NanoLuc and Cys-NanoLuc protein were overexpressed and purified from *E.coli* using the following protocol: To achieve sufficient cell density for the main-culture, a pre-culture was established by inoculating bacteria from frozen stock into 4 mL LB medium supplemented with kanamycin (50 µg mL^{-1}). Cells were grown overnight at 37 °C with orbital shaking at 220 rpm (ES-20, SIA Biosan, Latvia). Two milliliter of pre-culture were transferred into 100 mL LB medium containing kanamycin (50 µg mL^{-1}) in a 500 mL Erlenmeyer flask and incubated for 3 h at 37 °C with orbital shaking at 220 rpm (MAXQ 4450, Thermo Fisher Scientific, MA, USA) to promote exponential growth and prepare cells for induction. Protein expression was induced by adding isopropyl-β-D-thiogalactopyranosid (1 mmol), followed by overnight incubation at 30 °C with orbital shaking at 220 rpm.

Cells were harvested by centrifugation and lysed by sonication. The bacterial suspension was cooled on ice for 30 min, transferred into pre-cooled 50 mL tubes and centrifuged for 5 min at 4 °C, 6000 rcf. Pellets were resuspended in 5 mL lysis buffer (50 mM NaH_2PO_4, 300 mM NaCl, 10 mM imidazole, 10 mM mercaptoethanol, 1.5 mM phenylmethylsulfonyl fluoride, pH 8). The suspension was transferred into 10 mL tubes and kept on ice. Cell disruption was performed by sonication under the following conditions: duty cycle 50 %, power ~50 %, output control 5, eight cycles of 10 s on and 10 s off. The lysate was transferred into microcentrifuge tubes and centrifuged for 60 min at 13 300 rcf and 4 °C.

Protein purification was performed using Ni^{2+}−NTA affinity chromatography. A syringe was packed with Ni^{2+}−NTA agarose beads and equilibrated with equilibration buffer (50 mM NaH_2PO_4, 300 mM NaCl, 20 mM imidazole, pH 8) using five column volumes. The supernatant was loaded onto the column, and the flow-through was collected and reapplied to the column to maximize binding of the target protein. The column was then washed with washing buffer (50 mM NaH_2PO_4, 300 mM NaCl, 20 mM imidazole, 10 mM mercaptoethanol, pH 8) in three steps of 3 mL each. The NanoLuc protein was eluted with elution buffer (50 mM NaH_2PO_4, 300 mM NaCl, 200 mM imidazole, pH 8) in four steps of 3 mL each. 50 µL of the sample was collected after each step to perform a subsequent sodium dodecyl sulfate polyacrylamide gel electrophoresis (SDS-PAGE).

To enable coupling of NanoLuc to NPs, the buffer was exchanged by SEC. The eluted protein was transferred into Amicon® Ultra Centrifugal Filter with a molecular weight cut-off (MWCO) of 10 kDa and centrifuged at 6000 rcf and 4 °C until the sample volume was reduced to 2 mL. Buffer exchange was performed using a Sephadex™ G-25 M and 1X DPBS following the manufacturer's instructions.

4.2.8 SDS-PAGE and Protein Purity Analysis

The SDS-PAGE was performed using Peqlab PerfectBlue™Twin dual gel system (PEQLAB Biotechnologie GmbH, Erlangen, Germany) and Consort E844 (Consort, Turnhout, Belgium) as power supply. Protein samples were prepared by mixing 15 µL of sample solutions at different purification steps with 5 µL SDS sample buffer, resulting in a total volume of 20 µL. The SDS sample buffer consisted of 125 mg sodium dodecyl sulfate, 375 µL glycerol (prepared as 425 µL of 80 % glycerol), 25 µL bromophenol blue solution (0.8 % in Tris buffer, 175 mM, pH 6.8), and 115 mg dithiothreitol dissolved in 2.5 mL Tris buffer (175 mM, pH 6.8). A 12 % separation gel was prepared using the following components for one gel: 1.98 mL water, 1.5 mL Tris buffer (1.5 M, pH 8.8), 2.4 mL acrylamide mix, 60 µL SDS solution (10 %), 36 µL ammonium persulfate (APS) solution (10 %), and 3.6 µL N,N,N',N'-Tetramethylethane-1,2-diamine (TEMED). The gel was overlaid with water and allowed to polymerize for 20 min. The overlay was then discarded. A 4 % stacking gel was prepared using: 1.5 mL water, 625 µL Tris buffer (0.5 M, pH 6.8), 335 µL acrylamide mix, 25 µL SDS solution (10 %), 25 µL APS solution (10 %), and 2.5 µL TEMED. After pouring, a comb was inserted and the gel was allowed to polymerize for 20 min. The gel chamber was filled with laemmli electrophoresis running buffer (1× LRB Turbo), prepared by diluting the 10× stock (containing 30.3 g Tris, 142 g glycine, and 10 g SDS per L) in mQ water at a ratio of 1:10. Samples and protein marker (peqGOLD Protein Marker I, molecular weights: 14.4, 18.4, 25, 35, 45, 66.2, 116 kDa) were loaded and electrophoresis was performed at 30 mA for approximately 80 min. After electrophoresis, the gel was stained with Coomassie Brilliant Blue for 10 s, followed by washing with a solution containing 5 % methanol and 7.5 % glacial acetic acid for 5 min. The washing solution was then replaced, and the gel was incubated overnight with gentle shaking. Protein bands were visualized on the stained gels by eye and documented using a digital camera.

4.2.9 Protein Quantification

Protein concentration was determined using the QuantiPro™ BCA Protein Assay Kit according to the manufacturer's instructions. Briefly, 40 µL of each protein sample or standard (bovine serum albumin, BSA) was mixed with 40 µL of working reagent (prepared by mixing Reagent QA, Reagent QB and Reagent QC in a 25:25:1 ratio) in a transparent 384-well plate (Greiner Bio-One, Germany). The plate was sealed and incubated at 60 °C for 60 min. Absorbance was measured at 562 nm using a FLUOstar Omega microplate reader (BMG LABTECH GmbH, Germany). Protein concentrations were calculated based on a standard curve generated from serial dilutions of BSA ranging from 5 $\mu g\,mL^{-1}$ to 30 $\mu g\,mL^{-1}$. All measurements were performed in technical triplicates.

4.2.10 Luminescence Assay

All luminescence measurements were carried out using a FLUOstar Omega microplate reader with luminescence optics for 96-well plate.

Determination of NanoLuc Concentration

To determine a suitable concentration of NanoLuc exhibiting glow-type luminescence behavior, NanoLuc and Cys-NanoLuc were diluted to final concentrations of 80 nM, 8 nM, 800 pM, and 80 pM in DPBS + 1 mg mL^{-1} (0.1 %) BSA. Furimazine was diluted 1:1000 in DPBS. Measurements were conducted in a 96-well plate format by combining 50 µL of NanoLuc solution with 50 µL of diluted furimazine per well, immediately before luminescence recording. Luminescence signal stability was assessed by recording emission at 1 s intervals over a period of 5 min. For the concentrations 8 nM, 800 pM, and 80 pM, extended monitoring was performed at 20 s intervals for up to 100 min to evaluate long-term signal decay.

Determination of Michaelis-Menten Kinetics

Furimazine titration assays for determining the Michaelis constants (K$_m$) of NanoLuc and Cys-NanoLuc were performed using a final enzyme concentration of 40 pM, each diluted in DPBS supplemented with 1 mg mL^{-1} BSA. Variable dilutions of furimazine stock solution were prepared in DPBS to generate a concentration range suitable for kinetic analysis. Measurements were conducted in a 96-well plate format by mixing 25 µL of NanoLuc solution with 25 µL of diluted furimazine per well, immediately before luminescence recording. Luminescence was measured 3 min after the addition of furimazine. The data were fitted using Origin 2002b software (OriginLab Corporation, Northampton, MA, USA), according to the Michaelis-Menten Equation (4.1), where v is the initial reaction velocity, V_{max} is the maximum reaction velocity, and $[S]$ is the substrate concentration.

$$v = \frac{V_{max}[S]}{K_m + [S]} \tag{4.1}$$

Determination of Enzyme Stability

To assess the stability of NanoLuc and Cys-NanoLuc during storage at 4 °C, aliquots were taken at certain points and both enzymes were diluted to a concentration of 400 nM in DPBS supplemented with 1 mg mL^{-1} BSA, and subsequently stored at −80 °C. Before each objective, fresh mixtures containing 80 pM of the respective enzyme were prepared in DPBS supplemented with 1 mg mL^{-1} BSA. Furimazine was diluted 1:400 in DPBS and added to the enzyme solution at a 1:1 ratio directly prior to measurement. Luminescence was recorded 3 min after substrate addition. All samples up to day 42 were measured on the same day. All following samples were freshly prepared and analyzed on their respective storage day.

4.2.11 Polymer Synthesis

H_2N-PEG_{2k}-PLA_{10k} and $mPEG_{2k}$-PLA_{10k} block copolymers were synthesized according to Qian et al., with modifications previously reported by our group [25, 26]. Briefly, the heterobifunctional PEG polymer (1 equiv.), either tBoc-NH-PEG_{2k} or $mPEG_{2k}$, was used as a macroinitiator for the ring-opening polymerization of cyclic lactide (3,6-dimethyl-1,4-dioxane-2,5-dione, 70 equiv.). Both components were dissolved in anhydrous dichloromethane (DCM) and mixed with 1,8-diazabicyclo[5.4.0]-undec-7-ene (DBU, 3 equiv.) as catalyst. The reaction mixture was stirred at room temperature (RT) for exactly 1 h. Polymerization was quenched by the addition of benzoic acid (10 equiv.). The resulting product was precipitated in a 20-fold volume of ice-cold diethyl ether and centrifuged for 10 min at 6000 rcf and 0 °C. The polymer pellet was dried under a nitrogen stream overnight at RT. In the case of tert-butyloxycarbonyl (tBoc)-protected block copolymer, the protecting group was removed by treatment with trifluoroacetic acid (TFA) in a 1:1 (v/v) mixture with DCM for 30 min at RT. The product was precipitated with a 20-fold excess of ice-cold diethyl ether, centrifuged 10 min at 6000 rcf and 0 °C, and subsequently dried under vacuum at RT overnight. The purified polymers were characterized by ^{1}H-NMR spectroscopy.

4.2.12 Synthesis of PLA_{10k}-PEG_{2k}-maleimide

PLA_{10k}-PEG_{2k}-NH_2 was weighed (108 mg, 9.09 µmol) into a round-bottom flask and dried under vacuum at RT for 2 h. Subsequently, N-succinimidyl 3-maleimidopropionate (90.9 µmol) and triethylamine (90.9 µmol) were added to the flask. The reaction mixture was dissolved in 2 mL anhydrous acetonitrile (ACN) and was stirred at RT overnight. The product was precipitated with a 20-fold excess of ice-cold diethyl ether, followed by centrifugation for 10 min at 6000 rcf and 0 °C. The supernatant was decanted off and the polymer pellet was dried under nitrogen flow before being redissolved in ACN. This precipitation-centrifugation step was repeated twice to eliminate excess of N-succinimidyl 3-maleimidopropionate. The final product was dried under vacuum at RT overnight. The purified polymer was characterized by ^{1}H-NMR spectroscopy and coupling efficiency (CE) was determined (Supporting Information, Section S4.2.4)

4.2.13 Synthesis of Maleimide-functionalized 6-Aminofluorescein

6-Aminofluorescein (43.6 mg, 126 µmol, 1.00 equiv.) and N-succinimidyl-3-maleimidopropionate (53 mg, 199 µmol, 1.59 equiv.) were dissolved in 2.5 mL DMF. Subsequently, DIPEA (24.0 µL, 251 µmol, 2.00 equiv.) was added to the solution and stirred overnight at RT. The reaction was monitored using HPLC. A linear gradient elution was employed, starting from 95 % solvent A (mQ water with 0.05 % TFA) and 5 % solvent B (ACN with 0.05 % TFA), changing to a final ratio of 5 % solvent A / 95 % solvent B over 30 min. The high-organic phase was maintained for 10 min, after which the system was returned to the initial conditions (95 % A / 5 % B) for column re-equilibration (10 min). The flow rate was maintained at 1.0 mL min^{-1} and the temperature was set to 35 °C. Detection was carried out with a diode array detector (DAD) at 220 nm. The crude reaction product was purified via preparative HPLC. Again, a linear gradient elution was employed, starting from 95 % solvent A (mQ water with 0.1 % TFA) and 5 % solvent B (ACN), increasing to a final ratio of 5 % solvent A / 95 % solvent B over 30 min at a flow rate of 20 mL min^{-1}. Detection was performed at 220 nm. Fractions containing the desired product were collected, pooled, and lyophilized to yield the purified compound. Mass spectrometry and analytical HPLC were performed to confirm identity and purity.

4.2.14 Coupling of Fluorescent Dye to NanoLuc

NanoLuc and Cys-NanoLuc (1.00 equiv.) were treated with tris(2-carboxyethyl)-phosphine (TCEP) (10 equiv.) in mQ water for 30 min at RT under constant agitation at 800 rpm. Later on, maleimide-functionalized 6-aminofluorescein (10 equiv.) was added to the reaction mixture and incubated for 2 h at RT with shaking at 800 rpm. Excess unreacted dye was removed by SEC using Sephadex G-25 medium. Purification was performed according to the manufacturer's protocol. The coupling efficiency was determined by quantifying both the protein and the dye content. Protein concentration was measured using the BCA assay as described above. Dye content was assessed by UV-Vis absorption spectroscopy, based on the absorbance at the dye's characteristic wavelength ($\lambda_{ex,max} = 488\,\text{nm}$). A calibration curve for the dye was established using standard solutions ranging from 5 µM to 40 µM. The degree of labeling was calculated by comparing the molar concentration of the dye to that of the protein, allowing for an estimation of the labeling efficiency.

4.2.15 Spectral Characterization of Fluorescent Dye and NanoLuc

Absorption measurements were performed using a FLUOstar Omega plate reader or BioTek Synergy Neo2 (Agilent Technologies, Santa Clara, CA, USA). Therefore, 200 µL samples were transferred into quartz 96 well plate (Hellma GmbH & Co. KG, Müllheim, Germany). Luminescence and fluorescence spectra were obtained by BioTek Synergy Neo2 (Agilent Technologies, Santa Clara, CA, USA) using either white (luminescence) or black (fluorescence) well plate.

4.2.16 Bioluminescence Resonance Energy Transfer Fluorescent-labeled NanoLuc

Fluorescent-labeled NanoLuc was transferred into a white 96-well plate and mixed with a 1:1000 dilution of furimazine (1:1) immediately prior to measurement. Emission spectra were recorded from 380 nm to 600 nm using BioTek Synergy Neo2.

4.2.17 Nanoparticle Preparation and Characterization

Core-shell NPs with surface bound NanoLuc were manufactured by nanoprecipitation [27]. PLGA and the corresponding PLA-PEG copolymer were dissolved at a ratio of 30/70 (m/m) in ACN reaching a final concentration of $10\,\mathrm{mg\,mL^{-1}}$. Within the PEG-containing fraction, 10% was maleimide-functionalized PEG-PLA (PLA_{10k}-PEG_{2k}-maleimide), while the remaining 90% consisted of methoxy-terminated polymer chains (mPEG_{2k}-PLA_{10k}). The organic phase was added drop-by-drop into a 10-fold excess of 10 % DPBS under constant stirring at 900 rpm. The aqueous phase contained a 1.2-fold molar excess of NanoLuc or Cys-NanoLuc relative to maleimide groups. The mixture was stirred for 3 h at RT to remove the organic solvent. Subsequently, excess free NanoLuc was removed by filtration using Amicon®Ultra centrifugal filters with a MWCO of 100 kDa. The NP suspension was centrifuged at 6000 rcf and 4 °C for 5 min. Then, 2 mL of 10 % DPBS were added to the retentate, and the centrifugation step was repeated. This washing procedure was performed three times in total. Finally, the sample volume was adjusted to the original volume using 10 % DPBS. Complete removal of unbound NanoLuc was confirmed by SEC using DPBS as the mobile phase at a flow rate of $1\,\mathrm{mL\,min^{-1}}$. Control NPs were composed of mPEG_{2k}-PLA_{10k} and PLA_{10k}-PEG_{2k}-maleimide in the same ratio as the functionalized NPs. However, the aqueous phase used during nanoprecipitation did not contain NanoLuc.

NP tracking analysis (NTA) (NanoSight NS300, Malvern, United Kingdom) was used to determinate NP size (hydrodynamic diameter, d_h) and concentration. For

NTA measurements the NPs were diluted with mQ water to reach a particle concentration of 20-100 particles per frame. The polydispersity index (PDI) was calculated with the following equation.

$$PDI = (\frac{\sigma}{\mu})^2 \tag{4.2}$$

μ is defined by the mean particle size and σ is representing the standard deviation.

To evaluate the amount of NanoLuc conjugated to NPs, protein concentration was determined using the BCA assay as previously described. The coupling efficiency (CE) was calculated using the following equation:

$$CE[\%] = \frac{m_{NanoLuc,coupled}}{m_{NanoLuc,100\%}} * 100 \tag{4.3}$$

Here, $m_{NanoLuc,coupled}$ was determined by BCA assay, and $m_{NanoLuc,100\%}$, representing the complete coupling of NanoLuc to maleimide-PEG$_{2k}$-PLA$_{10k}$, was calculated. For further information see Supporting Information (Section S4.2.6).

The enzyme activity of NanoLuc@NP and Cys-NanoLuc@NP was tested by luminescence assay. Therefore, the NP preparations were diluted with DPBS + 0.01 % BSA to reach a final concentration of 80 pM NanoLuc, respectively, Cys-NanoLuc. Furimazine was diluted 1:400 in DPBS. Measurements were conducted in a 96-well plate format by combining 25 µL of NanoLuc@NP, respectively, Cys-NanoLuc@NP solution with 25 µL of diluted furimazine per well, immediately before luminescence recording. Luminescence signal stability was assessed by recording emission at 20 s intervals over a period of 5 min.

The prepared NP formulations were stored at 4 °C. The stability of mPEG-NP, NanoLuc@NP and Cys-NanoLuc@NP were investigated by size measurement via NTA. Prior to measurement the NP formulations were freshly diluted with mQ water. For NanoLuc@NP and Cys-NanoLuc@NP the enzyme activity over the storage time was evaluated by luminescence assays (Section 4.2.10). To prevent unintended concentration differences, samples containing 80 pM of NanoLuc variants, used for the initial enzyme activity measurements, were stored at 4 °C and reused for all subsequent analyses.

4.3 Results and Discussion

4.3.1 Expression of NanoLuc and Cys-NanoLuc

To enable coupling of NanoLuc to polymeric NPs via maleimide-thiol chemistry, the NanoLuc gene was genetically modified prior to expression. A His-tag was introduced into the open reading frame using site-directed mutagenesis to facilitate purification. In addition, a second cysteine residue was added at the C-terminus (Cys-NanoLuc) as we hypothesized that increasing the number of thiol groups would enhance coupling efficiency. Furthermore, conjugation through the native cysteine might interfere with the enzyme's function, whereas introducing an additional cysteine could mitigate this risk [22]. Amplification of the modified plasmid fragments was confirmed by agarose gel electrophoresis. Bands corresponding to the expected fragment sizes (3901 bp and 1921 bp for NanoLuc and 3905 bp and 1903 bp for Cys-NanoLuc) were observed, verifying successful mutagenesis (Figure 4.1).

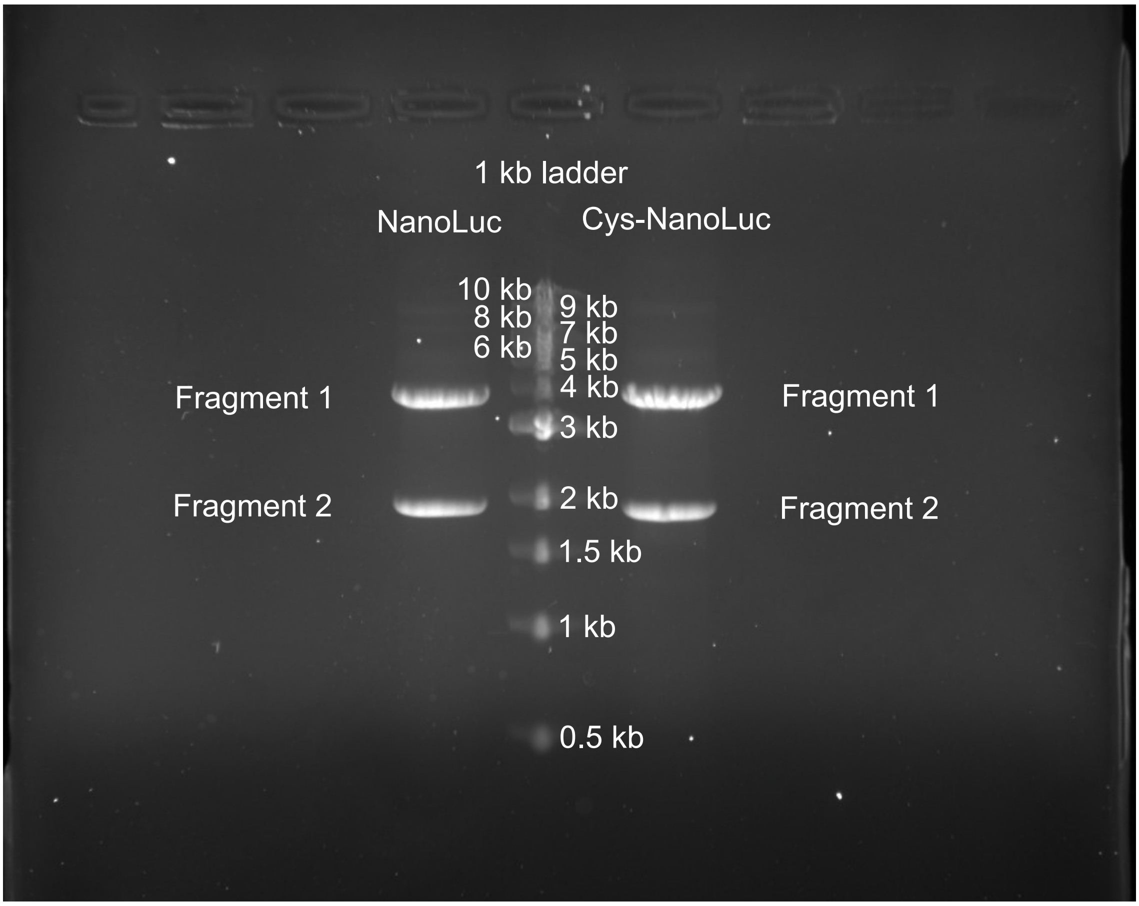

Figure 4.1: PCR products of site-directed mutagenesis of NanoLuc and Cys-NanoLuc plasmid consisted of two fragments: Fragment 1 contained the gene of interest (NanoLuc, 3901 bp; Cys-NanoLuc, 3905 bp), and Fragment 2 included the antibiotic resistance cassette and C-terminal His-tag sequence (NanoLuc, 1921 bp; Cys-NanoLuc, 1903 bp)

Successful reassembly of PCR fragements and transformation into *E.coli* DH5α was verified by Sanger sequencing of plasmids (Figure S4.1, Figure S4.2). Recombinant expression of NanoLuc and Cys-NanoLuc was confirmed by sodium dodecyl sulfate polyacrylamide gel electrophoresis (SDS-PAGE) analysis. A distinct band corresponding to the expected molecular weight of NanoLuc (21.9 kDa, Figure 4.2 A) and Cys-NanoLuc (21.1 kDa, Figure 4.2 B) was observed, indicating successful expression.

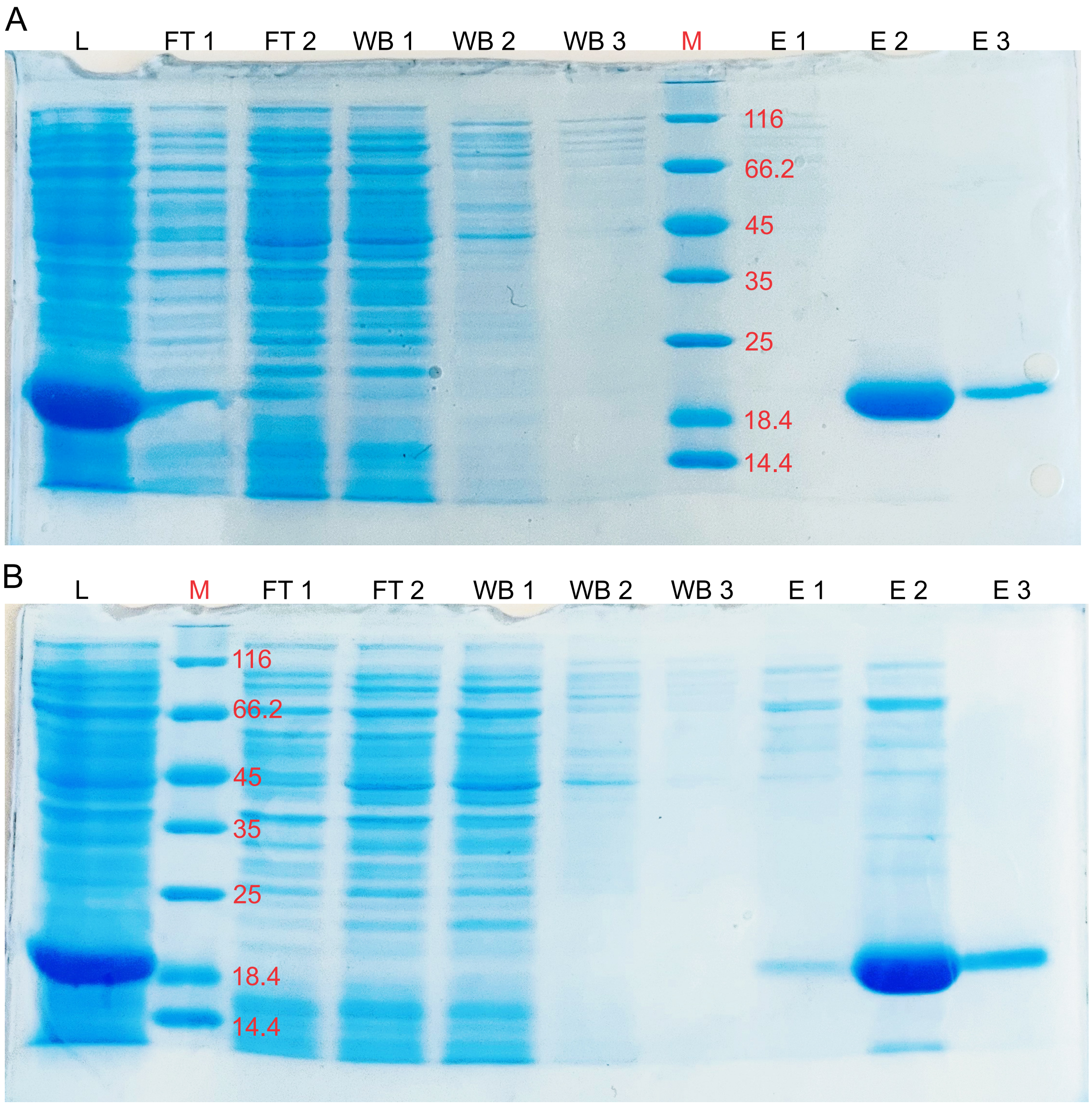

Figure 4.2: SDS-PAGE showing expression and purification steps of NanoLuc **A** and Cys-NanoLuc **B**. Lanes correspond to different fractions obtained during purification. Abbreviations: L, Lysate; FT, flow-through; WB, washing buffer; E, elution; M, molecular weight marker (kDa). Numbers indicate fraction counts. Proteins were separated on a 12 % polyacrylamide gel and stained with Coomassie Brilliant Blue.

4.3.2 Luminescence Assay

To evaluate the functionality of NanoLuc and Cys-NanoLuc coupled to NP (NanoLuc@NP, Cys-NanoLuc@NP) a luminescence assay was established. Key requirements included glow-type luminescence conditions, ensuring a stable and sustained signal over time, and the use of saturation concentration of substrate to guarantee full activation of all NanoLuc enzymes. Although NanoLuc is able to maintain a glow-type luminescent signal over a broad concentration range, signal half-life can decrease at high concentration of enzyme due to rapid substrate depletion. To identify conditions that support a stable and sustained signal different (Cys-)NanoLuc concentrations were screened at constant furimazine concentration (Figure 4.3 A, B). At a concentration of 40 pM NanoLuc, the luminescence signal remained stable during the 3-5 min interval, and this condition yielded the longest signal half-life, reaching approximately 40 min. At higher concentrations, the half-life decreased, indicating that substrate depletion limited signal stability. Comparable behavior was observed for Cys-NanoLuc. Therefore, 40 pM of NanoLuc variants and readout at 3 min were selected for subsequent kinetic studies. The Michaelis constant (K_m) of NanoLuc and furimazine has been reported to be approximately 10 µM [14]. For endpoint measurements a substrate concentration of at least 5-fold K_m is recommended [14]. As the concentration of NanoBRET® Nano-Glo® is not provided by the supplier, the K_m of both NanoLuc variants were determined as dilution of stock solution (stock $*$ dilution factor; Figure 4.3 C, D). Cys-NanoLuc ($K_M = 1.36 * 10^{-4} \pm 1.40 * 10^{-5} \hat{=} 1\,/\,7368 \pm 1\,/\,758$) shows higher affinity to furimazine than NanoLuc ($K_M = 1.78 * 10^{-4} \pm 1.84 * 10^{-5} \hat{=} 1\,/\,5600 \pm 1\,/\,584$), however, the maximal velocity (V_{max}) and the overall luminescence output is approximately half of NanoLuc. Nemergut et al., stated that allosteric site modulation has huge impact on NanoLuc kinetics [28]. Thus, modulation on C-terminus in Cys-NanoLuc could explain reduced luminescence output, as it might impact the conformation of NanoLuc protein. Furthermore, Krasiskaya et al. observed that C-terminal modifications led to an approximately 50 % reduction in activity [22].- The experiments conducted for establishment of luminescence assay led to the selection of a (Cys-)NanoLuc concentration of 40 pM and furimazine dilution of 1:800 for all subsequent experiments.

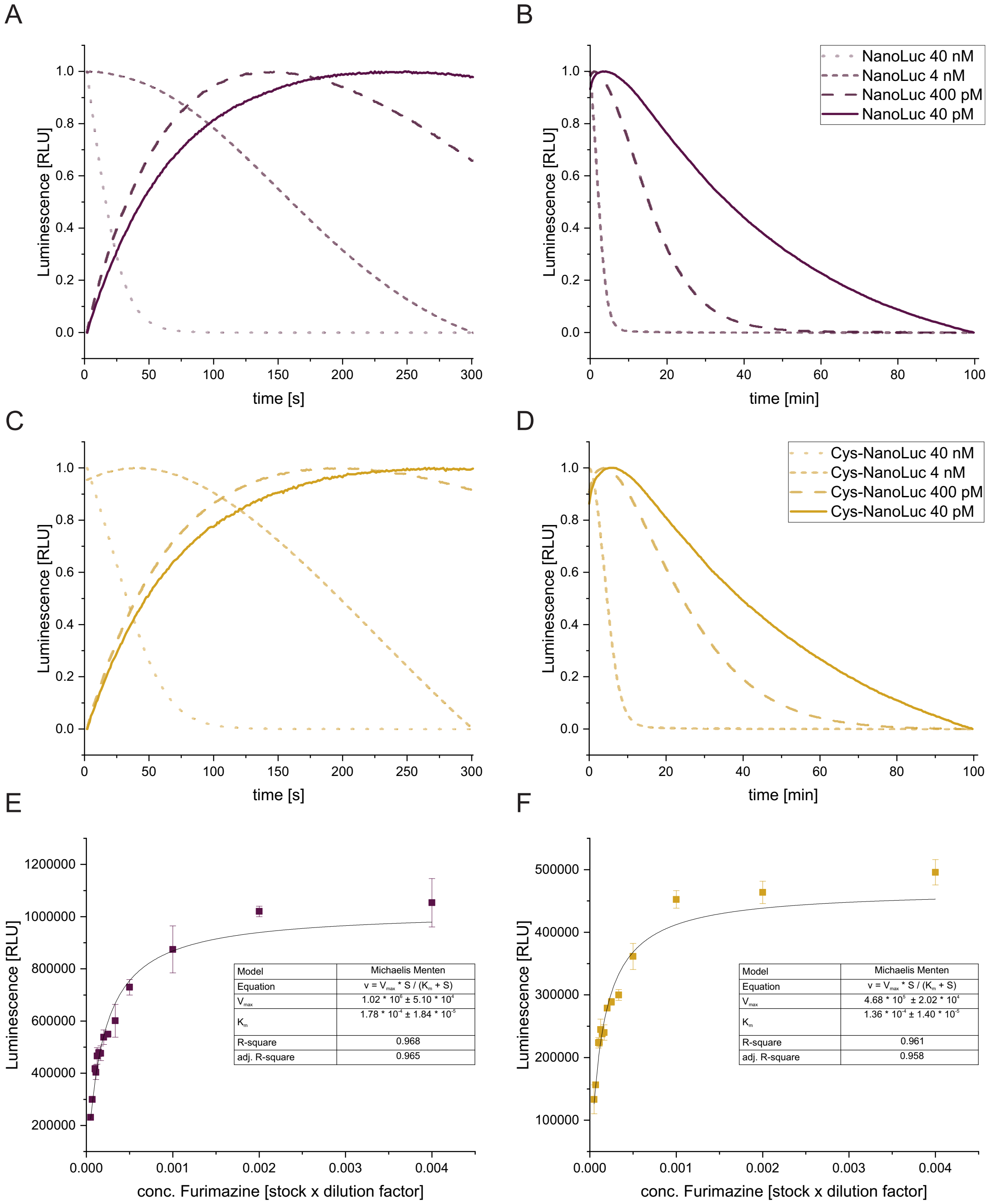

Model	Michaelis Menten
Equation	$v = V_{max} * S / (K_m + S)$
V_{max}	$1.02 * 10^6 \pm 5.10 * 10^4$
K_m	$1.78 * 10^{-4} \pm 1.84 * 10^{-5}$
R-square	0.968
adj. R-square	0.965

Model	Michaelis Menten
Equation	$v = V_{max} * S / (K_m + S)$
V_{max}	$4.68 * 10^5 \pm 2.02 * 10^4$
K_m	$1.36 * 10^{-4} \pm 1.40 * 10^{-5}$
R-square	0.961
adj. R-square	0.958

Figure 4.3: Luminescence measurements and Michaelis-Menten kinetics. Luminescence intensity of different NanoLuc and Cys-NanoLuc concentration is plotted for 300 s **A, C** and 100 min **B, D**. Individual luminescence intensities were normalized to their highest intensity to enable comparison between different concentrations. Michaelis-Menten analysis of NanoLuc (**E**) and Cys-NanoLuc (**F**). Furimazine concentration (dilution of stock solution) was plotted against luminescence intensity (defined as relative luminescence units, RLU) to determine kinetic parameters. The curve was fitted using nonlinear regression according to the Michaelis-Menten equation (v: reaction rate; S: substrate concentration; V_{max}: maximum velocity; K_m: Michaelis constant). Data points represent mean ± SD from technical triplicate.

4.3.3 Enzyme Stability

Both NanoLuc variants stored at 4 °C retained their enzymatic activity throughout the observation period (Figure 4.4). However, the signal intensity showed fluctuations. This spread can be attributed to the assay's high sensitivity to protein concentration. This sensitivity is advantageous, as it enables the detection of even minor losses in enzyme functionality. Yet, making it also prone to unintended concentration differences due to pipetting inaccuracies or protein adsorption to consumables during sample preparation. Stability evaluation of the stock solution employed for NanoLuc@NP and Cys-NanoLuc@NP synthesis required sampling and performing individual dilutions from stock solution at each time point. Despite efforts to standardize handling, minor variations in sample preparation were unavoidable and resulted in fluctuations in luminescence intensity. Importantly, the overall stability of NanoLuc variants ensures the preparation of bioluminescent NP without requiring freshly expressed protein prior to coupling.

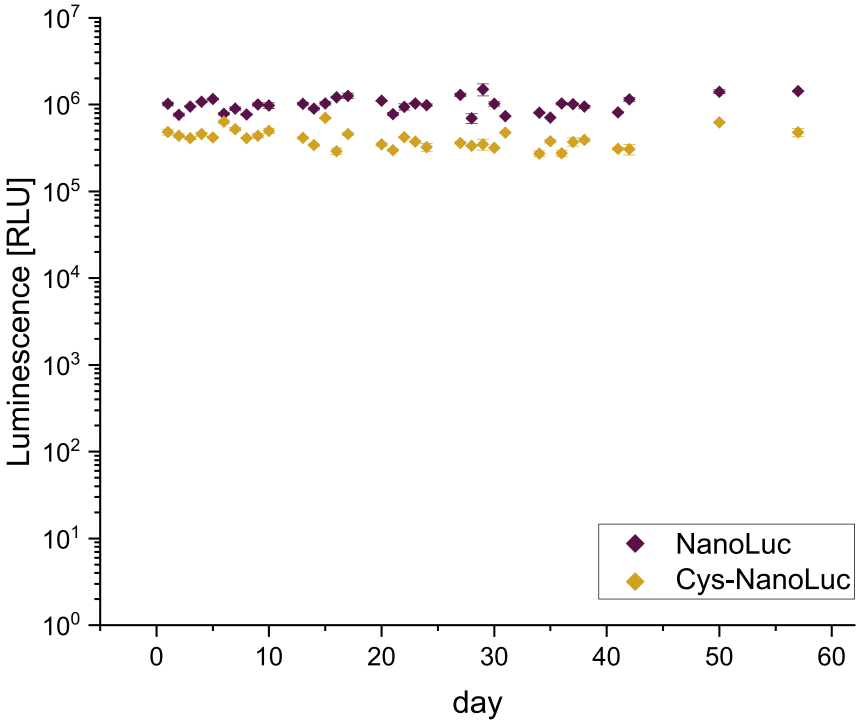

Figure 4.4: Stability of NanoLuc variants. Data points represent measured enzyme activity as luminescence intensity at each time point ± SD (n = 3). Relative Luminescence Units, RLU.

4.3.4 Fluorescent-labeled NanoLuc

To investigate the accessibility of cysteine residues for maleimide-thiol conjugation, NanoLuc and Cys-NanoLuc were incubated with maleimide-functionalized aminofluorescein. The spectral properties of aminofluorescein enable bioluminescence resonance energy transfer (BRET), due to the overlap of its absorption spectrum ($\lambda_{abs,max} = 448\ nm$) and the emission spectrum of NanoLuc ($\lambda_{em,max} = 456\ nm$) (Figure 4.5 A). BRET is only feasible when donor (NanoLuc) and acceptor (aminofluorescein) are in close proximity. This spatial requirement is fulfilled when the dye is covalently tethered to NanoLuc via maleimide-thiol conjugation. BRET, observed as a dye related emission peak following NanoLuc activation, confirmed the successful conjugation to both, NanoLuc and Cys-NanoLuc, variants (Figure 4.5). However, higher coupling efficiency for Cys-NanoLuc (50.6 ± 4.92 %) compared to NanoLuc (39.0 ± 4.07 %), indicated improved thiol accessibility in the engineered variant (Figure S4.4).

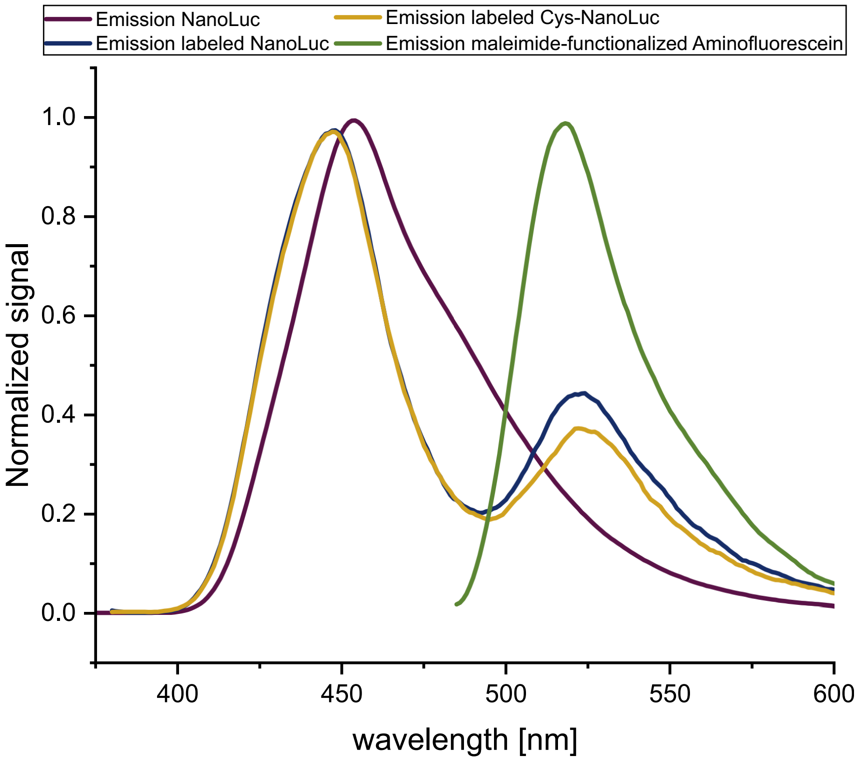

Figure 4.5: Spectral characterization of fluorescence dye, NanoLuc and labeled NanoLuc variants. The fluorescence emission spectrum of maleimide-functionalized aminofluorescein ($\lambda_{ex} = 488\ nm$) exhibits a peak at $\lambda_{em} = 518\ nm$. The luminescence emission spectrum of NanoLuc shows a peak at $\lambda_{em} = 456\ nm$. Emission spectra of labeled NanoLuc variants display two distinct peaks: the first peak corresponds to NanoLuc luminescence($\lambda_{em} = 447\ nm$) and the second to aminofluorescein fluorescence ($\lambda_{em} = 519\ nm$). Individual peaks were normalized to their highest peak intensity to enable comparison between spectra.

4.3.5 Synthesis and Characterization of Bioluminescent Nanoparticles

The model NPs chosen for this study were designed as core-shell NPs consisting of poly(D,L-lactide-*co*-glycolide) (PLGA) and poly(ethylene glycol)-*b*-poly(D,L-lactide) (PEG-PLA) block copolymer. PLA-PEG was functionalized with a maleimide linker (PLA_{10k}-PEG_{2k}-maleimide) to enable NanoLuc coupling. The coupling efficiency of PLA_{10k}-PEG_{2k}-maleimide was 89 % (Figure S4.5 and eq. (4.5)). Prior to analysis of the NanoLuc@NP and Cys-NanoLuc@NP conjugates, it was imperative to confirm the removal of unbound NanoLuc. SEC profiles (Figure 4.6) demonstrated complete separation of free protein from NP-bound NanoLuc, ensuring that subsequent measurements reflect only conjugated species.

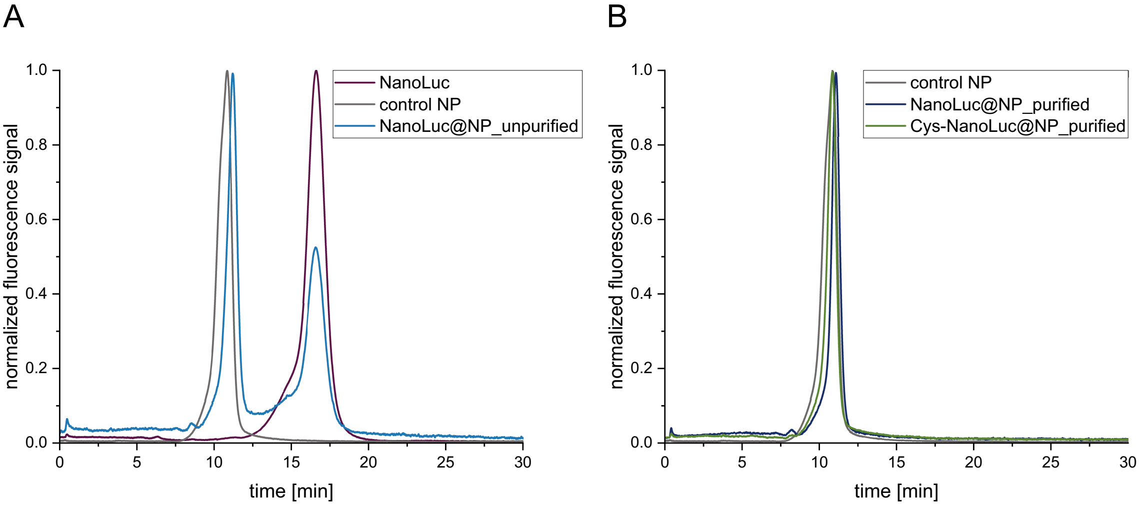

Figure 4.6: Size-exclusion chromatography profiles of NanoLuc, control NP, NanoLuc@NP and Cys-NanoLuc@NP conjugates. To enable comparison between chromatograms, individual peaks were normalized to their highest peak intensity. **A** Chromatogram of free NanoLuc ($t_R = 16.62\,\text{min}$), control NP ($t_R = 10.87\,\text{min}$) and unpurified NanoLuc@NP ($t_{R1} = 11.21\,\text{min}$, $t_{R2} = 16.62\,\text{min}$) sample, showing distinct peaks for free NanoLuc and NP-bound protein. **B** Chromatogram of purified NanoLuc@NP ($t_R = 11.05\,\text{min}$) and Cys-NanoLuc@NP ($t_R = 10.86\,\text{min}$) samples and control NP ($t_R = 10.87\,\text{min}$), demonstrating complete removal of unconjugated NanoLuc variants.

All NPs were compared in terms of size, size distribution and coupling efficiency. Comparison of coupling efficiencies between NanoLuc@NP and Cys-NanoLuc@NP confirmed the improved thiol accessibility in the engineered variant. While NanoLuc exhibited an average coupling efficiency of 12.5 %, Cys-NanoLuc showed significantly higher conjugation levels of 50.1 % (Figure 4.7).

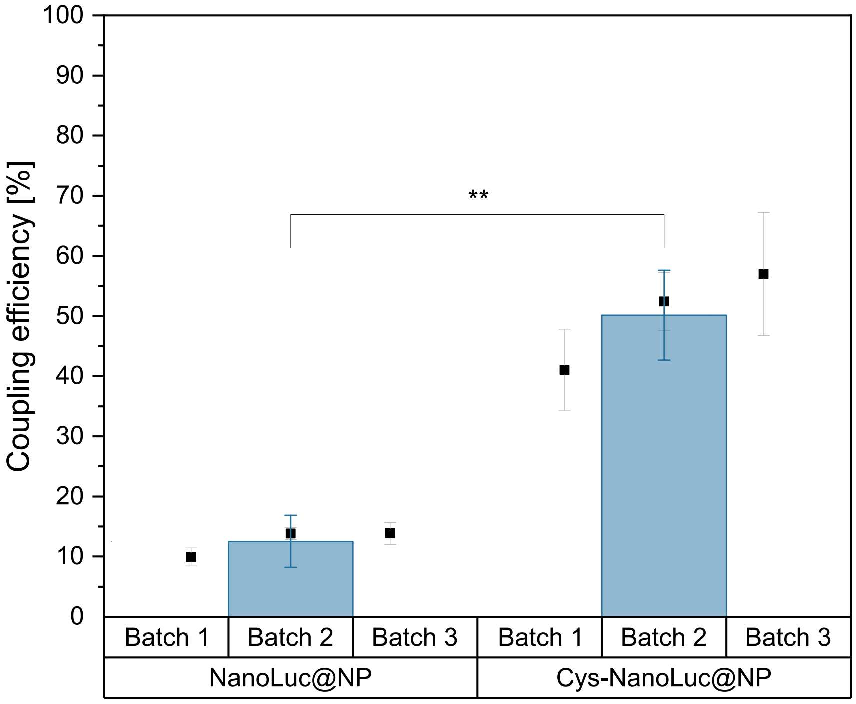

Figure 4.7: Coupling of NanoLuc and Cys-NanoLuc to NP. Coupling efficiency of the three NP preparations shown as individual data points ± SD (n = 3). The average of all preparations is represented by bars with pooled SD (N = 3). Statistical significance was assessed using an unpaired Student's t-test. Level of statistical significance is indicated as ns = not significant, * $p \leq 0.05$, ** $p \leq 0.01$, *** $p \leq 0.001$, **** $p \leq 0.0001$).

The violin plots (Figure 4.8) depict the distribution of NP sizes within the analyzed samples, highlighting the measures of central tendency (mean, median and mode), as well as the overall variability in size. A broader size distribution is observed for the NanoLuc-functionalized nanoparticles compared to control NPs, reflected by higher polydispersity index values (NanoLuc@NPs: 0.227; Cys-NanoLuc@NPs: 0.223; control NPs: 0.183). This lower uniformity suggests that NanoLuc is not equally distributed across the NP population. Regarding particle size, control NPs displayed a smaller mean hydrodynamic diameter (d_h; 82.7 nm) than NanoLuc@NP (109 nm) and Cys-NanoLuc@NP (110 nm). The increase in size of the functionalized NPs is consistent with surface-bound NanoLuc increasing NP solvation and thus their d_h. However, the observed differences in size were not significant.

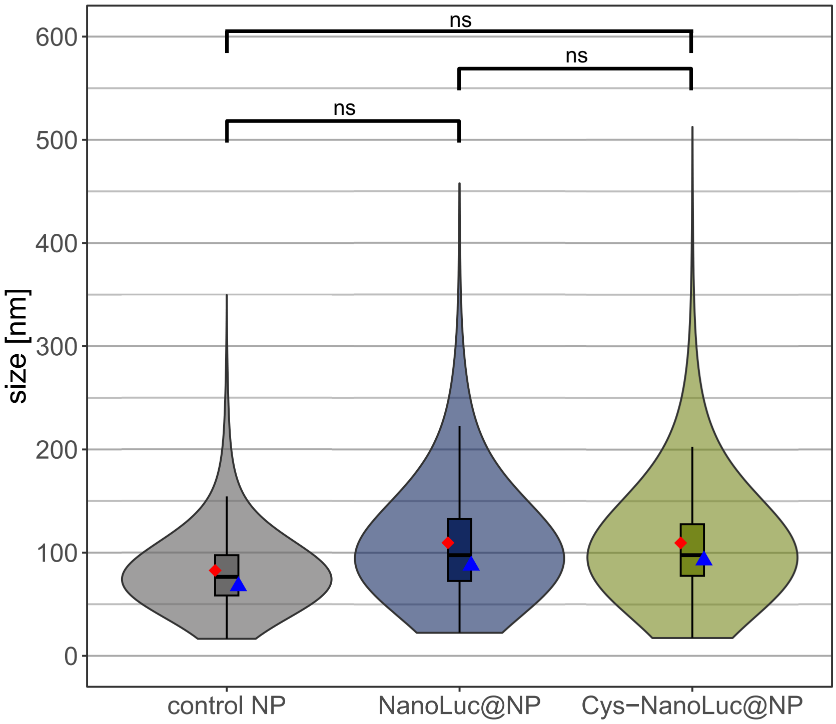

Figure 4.8: Violin plots represent size distribution of hydrodynamic diameters. Each violin illustrates the size distribution obtained from three independent measurements per batch across three NP batches (n = 3, N = 3). The median NP size is shown as horizontal line within the box, whose lower and upper edges represent the first (Q1) and third (Q3) quartiles, respectively. Whiskers indicate the most extreme data points within 1.5 times the interquartile range from the lower and upper quartiles. The mean is represented by a red rectangle and the mode is depicted by a blue triangle. Mean: control NP: 82.7 nm, NanoLuc@NP: 109 nm, Cys-NanoLuc: 110 nm; median: control NP: 76.5 nm, NanoLuc@NP: 97.5 nm, Cys-NanoLuc: 97.5 nm; mode: control NP: 67.5 nm, NanoLuc@NP: 87.5 nm, Cys-NanoLuc: 92.5 nm. Statistical significance on mean size was assessed using the Kruskal-Wallis test followed by Dunn's post hoc test with Bonferroni adjustment for multiple comparisons; no significant (ns) differences were observed between conjugates and control, confirming size stability upon conjugation of NanoLuc variants.

Luminescence experiments of bioluminescent NPs, revealed distinct differences in enzyme activity among NanoLuc variants (Figure 4.9). For free NanoLuc, the relative luminescence units (RLU) were $1.14 \times 10^6 \pm 9.50 \times 10^4$, whereas conjugation of NanoLuc to NP (NanoLuc@NP) resulted in a pronounced reduction to $1.46 \times 10^5 \pm 2.44 \times 10^4$ RLU, corresponding to approximately one-tenth of free NanoLuc activity. In contrast, the Cys-NanoLuc variant exhibited no significantly change in activity upon NP coupling, with luminescence values of $6.12 \times 10^5 \pm 9.52 \times 10^4$ RLU for free and $5.72 \times 10^5 \pm 2.04 \times 10^5$ RLU NP-bound forms.

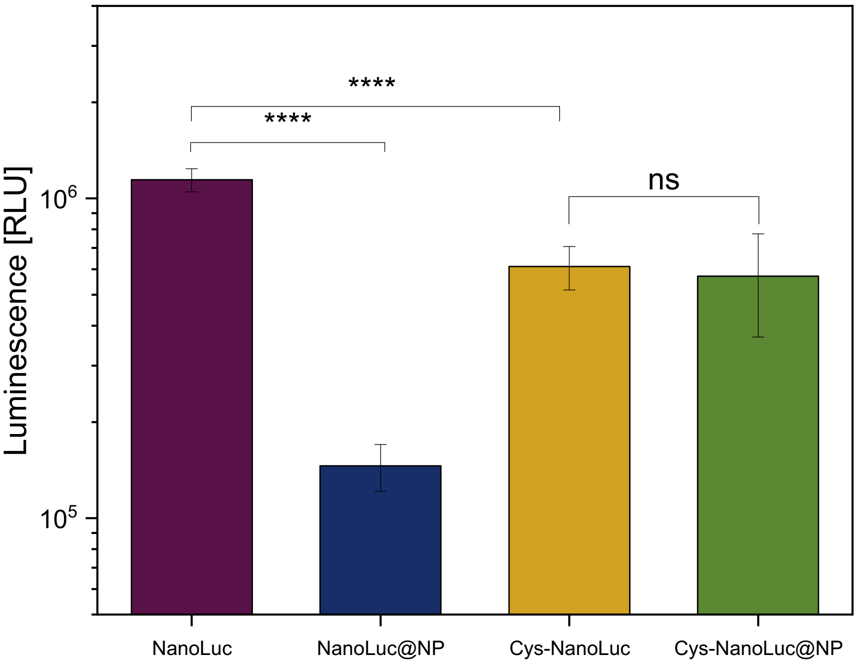

Figure 4.9: Luminescence intensity of free and NP-bound luciferase. Luminescence intensity is defined as relative luminescence units (RLU). Statistical significance on mean luminescence intensity was assessed using one-way ANOVA followed by Tukey's post hoc test. Data represent mean ± pooled SD (N = 3, level of statistical significance is indicated as ns = not significant, * $p \leq 0.05$, ** $p \leq 0.01$, *** $p \leq 0.001$, **** $p \leq 0.0001$).

These results diverge from previous reports that described enhanced activity of NP-bound NanoLuc. In those studies, NanoLuc was co-expressed with self-assembling protein. The increased activity was attributed to a favorable orientation of NanoLuc on the NP surface and a microenvironment conducive to efficient substrate turnover [7, 29]. However, the reduction of NanoLuc activity in our NP design is in line with results from Krasitskaya et al., which assumed loss of activity is associated with formation of covalent bond to native cysteine [22]. This suggests that Cys-NanoLuc was coupled exclusively via the additional cysteine residue to NP, as luminescence remained unchanged.

The particle size analysis of NP formulations stored at 4 °C revealed dimensional stability throughout the observation period (Figure 4.10 A, B). The initial d_h mean of mPEG-NP was 76.3 ± 2.95 nm, and the final measurement remained at 82.4 ± 1.88 nm, with no significant difference. NanoLuc@NP had an initial d_h mean of 111 ± 2.32 nm and final mean of 109 ± 1.65 nm with no significant difference. Also, no significant difference was detected in case of Cys-NanoLuc functionalized NPs with an initial d_h mean of 100 ± 2.90 nm and final mean of 100 ± 5.41 nm. These findings indicate the absence of aggregation or structural degradation under the applied storage conditions. Besides structural integrity of NPs, the enzyme activity was of high interest. Cys-NanoLuc@NP retained their enzyme activity for 5 weeks

(Figure 4.10 C). Also, the luminescence intensity of NanoLuc@NP at the end of stability test was in the same range as initial value. This observation supports the assumption that the protein is still linked to the NP in both cases, as unbound NanoLuc exhibited a higher luminescence intensity (Figure 4.9).

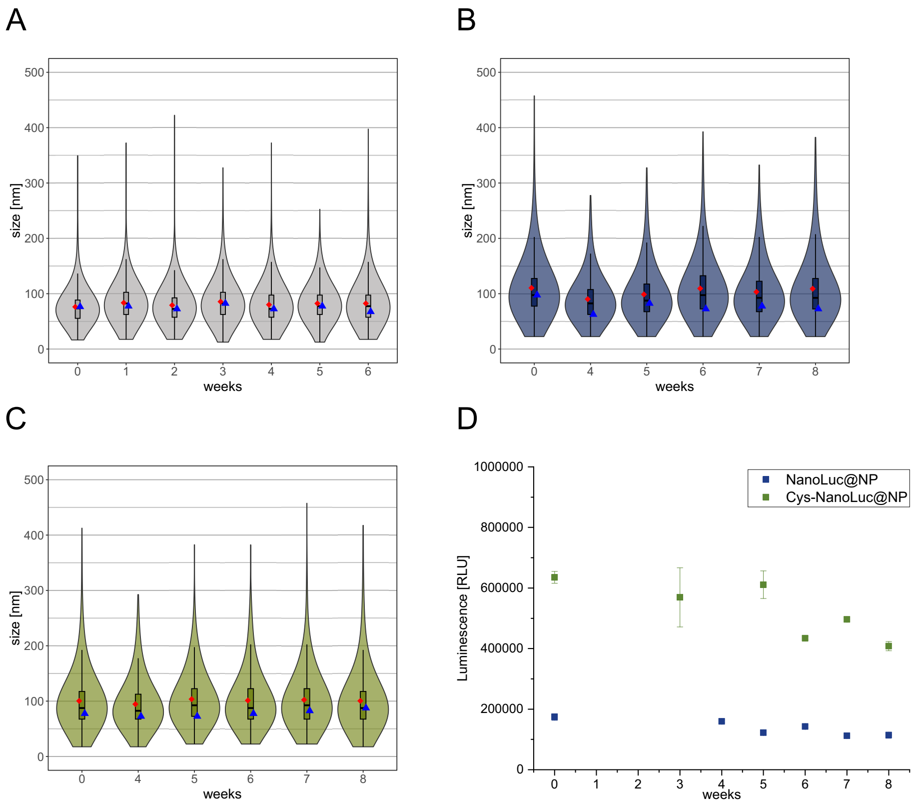

Figure 4.10: Size characterization and enzyme activity during storage. Size distribution and measures of central tendency of mPEG-NP **A**, NanoLuc@NP **B** and Cys-NanoLuc@NP **C** are plotted against storage time points. Each violin plot illustrates the size distribution obtained from technical triplicates of NPs (n=3). The median NP size is shown as horizontal line within the box, whose lower and upper edges represent the first (Q1) and third (Q3) quartiles, respectively. Whiskers indicate the most extreme data points within 1.5 times the interquartile range from the lower and upper quartiles. The mean is represented by a red rectangle and the mode is depicted by a blue triangle. The different time points are separated by semicolons. Mean size of control NP: 76.2 nm; 83.6 nm; 79.2 nm; 85.6 nm; 80.2 nm; 82.4 nm; 82.4 nm. Median size of control NP: 73.5 nm; 82.5 nm; 72.5 nm; 82.5 nm; 72.5 nm; 77.5 nm; 77.5 nm. Mode size of control NP: 76.5 nm; 77.5 nm; 72.5 nm; 82.5 nm; 72.5 nm; 77.5 nm; 67.5 nm. Mean size of NanoLuc@NP: 110 nm; 90.2 nm; 98.7 nm; 109 nm; 103 nm; 109 nm. Median size of NanoLuc@NP: 97.5 nm; 82.5 nm; 87.5 nm; 97.5 nm; 92.5 nm; 92.5 nm. Mode size of NanoLuc@NP: 97.5 nm; 62.5 nm; 82.5 nm; 72.5 nm; 77.5 nm; 72.5 nm. Mean size of Cys-NanoLuc@NP: 100 nm; 94.5 nm; 104 nm; 101 nm; 102 nm; 100 nm. Median size of Cys-NanoLuc@NP: 87.5 nm; 82.5 nm; 92.5 nm; 87.5 nm; 92.5 nm; 87.5 nm. Mode size of Cys-NanoLuc@NP: 77.5 nm; 72.5 nm; 72.5 nm; 77.5 nm; 82.5 nm; 87.5 nm. Statistical significance on mean size was assessed using the Kruskal-Wallis test followed by Dunn's post hoc test with Bonferroni adjustment for multiple comparisons; no significant differences were observed, confirming dimensional stability during storage. **D** Luminescence intensity of bioluminescent NPs is plotted against storage time points.

4.4 Conclusion

This study demonstrates, for the first time, the successful integration of NanoLuc variants into polymeric core-shell NPs. NanoLuc variants are stable under the applied storage condition for at least 5 weeks, enabling the preparation of bioluminescent NPs without the need to freshly express the luciferase prior to coupling. Although the insertion of an additional cysteine residue into the NanoLuc protein reduced the luminescence output of the free enzyme compared to unmodified NanoLuc in the first place, the modification was a huge benefit for the bioluminescent NP design as it significantly enhanced the coupling efficiency, enabling the immobilization of larger amount of NanoLuc on NP surface. Even more important, the enzymatic activity was preserved, whereas unmodified NanoLuc lost approximately 90 % of its activity.

References

[1] Sung-Bae Kim and Tadaomi Furuta. "Bioluminescence from the bright and dark sides". In: *Frontiers in Chemical Biology* 3 (2024). DOI: `10.3389/fchbi.2024.1459397`.

[2] Anna C. Love and Jennifer A. Prescher. "Seeing (and Using) the Light: Recent Developments in Bioluminescence Technology". In: *Cell chemical biology* 27.8 (2020), pp. 904–920. DOI: `10.1016/j.chembiol.2020.07.022`.

[3] Barbara Roda et al. "Shining light on biosensors: Chemiluminescence and bioluminescence in enabling technologies". In: *TrAC Trends in Analytical Chemistry* 180 (2024), p. 117975. ISSN: 01659936. DOI: `10.1016/j.trac.2024.117975`.

[4] Min-Kyung So et al. "Self-illuminating quantum dot conjugates for in vivo imaging". In: *Nature Biotechnology* 24.3 (2006), pp. 339–343. ISSN: 1546-1696. DOI: `10.1038/nbt1188`.

[5] Yusuke Ikeda et al. "Design of luciferase-displaying protein nanoparticles for use as highly sensitive immunoassay detection probes". In: *The Analyst* 141.24 (2016), pp. 6557–6563. DOI: `10.1039/c6an01253a`.

[6] Yingkun Yang et al. "Biodegradable Polymer Nanoparticles for Photodynamic Therapy by Bioluminescence Resonance Energy Transfer". In: *Biomacromolecules* 19.1 (2018), pp. 201–208. DOI: `10.1021/acs.biomac.7b01469`.

[7] Enya Li et al. "Macromolecular assembly of bioluminescent protein nanoparticles for enhanced imaging". In: *Materials today. Bio* 17 (2022), p. 100455. DOI: `10.1016/j.mtbio.2022.100455`.

[8] Shaowei Ding et al. "Increasing the activity of immobilized enzymes with nanoparticle conjugation". In: *Current opinion in biotechnology* 34 (2015), pp. 242–250. DOI: `10.1016/j.copbio.2015.04.005`.

[9] Jérôme Delroisse et al. "Leaving the Dark Side? Insights Into the Evolution of Luciferases". In: *Frontiers in Marine Science* 8 (2021). DOI: `10.3389/fmars.2021.673620`.

[10] Aisha J. Syed and James C. Anderson. “Applications of bioluminescence in biotechnology and beyond”. In: *Chemical Society reviews* 50.9 (2021), pp. 5668–5705. DOI: `10.1039/D0CS01492C`.

[11] Hsien-Wei Yeh and Hui-Wang Ai. “Development and Applications of Bioluminescent and Chemiluminescent Reporters and Biosensors”. In: *Annual review of analytical chemistry (Palo Alto, Calif.)* 12.1 (2019), pp. 129–150. DOI: `10.1146/annurev-anchem-061318-115027`.

[12] A. A. Kotlobay, Z. M. Kaskova, and I. V. Yampolsky. “Palette of Luciferases: Natural Biotools for New Applications in Biomedicine”. In: *Acta naturae* 12.2 (2020), pp. 15–27. ISSN: 2075-8251. DOI: `10.32607/actanaturae.10967`.

[13] Christopher G. England, Emily B. Ehlerding, and Weibo Cai. “NanoLuc: A Small Luciferase Is Brightening Up the Field of Bioluminescence”. In: *Bioconjugate Chemistry* 27.5 (2016), pp. 1175–1187. DOI: `10.1021/acs.bioconjchem.6b00112`.

[14] Mary P. Hall et al. “Engineered luciferase reporter from a deep sea shrimp utilizing a novel imidazopyrazinone substrate”. In: *ACS chemical biology* 7.11 (2012), pp. 1848–1857. DOI: `10.1021/cb3002478`.

[15] Leigh A. Stoddart, Laura E. Kilpatrick, and Stephen J. Hill. “NanoBRET Approaches to Study Ligand Binding to GPCRs and RTKs”. In: *Trends in pharmacological sciences* 39.2 (2018), pp. 136–147. DOI: `10.1016/j.tips.2017.10.006`.

[16] Thomas Machleidt et al. “NanoBRET–A Novel BRET Platform for the Analysis of Protein-Protein Interactions”. In: *ACS chemical biology* 10.8 (2015), pp. 1797–1804. DOI: `10.1021/acschembio.5b00143`.

[17] Natasha C. Dale et al. “NanoBRET: The Bright Future of Proximity-Based Assays”. In: *Frontiers in bioengineering and biotechnology* 7 (2019), p. 56. ISSN: 2296-4185. DOI: `10.3389/fbioe.2019.00056`.

[18] Jiho Kim and Regis Grailhe. “Nanoluciferase signal brightness using furimazine substrates opens bioluminescence resonance energy transfer to widefield microscopy”. In: *Cytometry. Part A : the journal of the International Society for Analytical Cytology* 89.8 (2016), pp. 742–746. DOI: `10.1002/cyto.a.22870`.

[19] Kim E. Sapsford et al. “Functionalizing nanoparticles with biological molecules: developing chemistries that facilitate nanotechnology”. In: *Chemical reviews* 113.3 (2013), pp. 1904–2074. DOI: `10.1021/cr300143v`.

[20] Sümeyra Vural Kaymaz et al. "Nanomaterial surface modification toolkit: Principles, components, recipes, and applications". In: *Advances in colloid and interface science* 322 (2023), p. 103035. DOI: `10.1016/j.cis.2023.103035`.

[21] Reinhard Schmidt et al. "Mechanism of photocleavage of (coumarin-4-yl)methyl esters". In: *The journal of physical chemistry. A* 111.26 (2007), pp. 5768–5774. DOI: `10.1021/jp071521c`.

[22] Vasilisa V. Krasitskaya, Maxim K. Efremov, and Ludmila A. Frank. "Luciferase NLuc Site-Specific Conjugation to Generate Reporters for In Vitro Assays". In: *Bioconjugate Chemistry* 34.7 (2023), pp. 1282–1289. DOI: `10.1021/acs.bioconjchem.3c00165`.

[23] Smita B. Gunnoo and Annemieke Madder. "Chemical Protein Modification through Cysteine". In: *Chembiochem : a European journal of chemical biology* 17.7 (2016), pp. 529–553. DOI: `10.1002/cbic.201500667`.

[24] Brandy J. Johnson et al. "Understanding enzymatic acceleration at nanoparticle interfaces: Approaches and challenges". In: *Nano Today* 9.1 (2014), pp. 102–131. ISSN: 17480132. DOI: `10.1016/j.nantod.2014.02.005`.

[25] Haitao Qian et al. "A Strategy for Control of "Random" Copolymerization of Lactide and Glycolide: Application to Synthesis of PEG-b-PLGA Block Polymers Having Narrow Dispersity". In: *Macromolecules* 44.18 (2011), pp. 7132–7140. ISSN: 0024-9297. DOI: `10.1021/ma201169z`.

[26] Kathrin Abstiens and Achim M. Goepferich. "Microfluidic manufacturing improves polydispersity of multicomponent polymeric nanoparticles". In: *Journal of Drug Delivery Science and Technology* 49 (2019), pp. 433–439. ISSN: 17732247. DOI: `10.1016/j.jddst.2018.12.009`.

[27] Christine Vauthier and Kawthar Bouchemal. "Methods for the preparation and manufacture of polymeric nanoparticles". In: *1573-904X* 26.5 (2009), pp. 1025–1058. ISSN: 1573-904X. DOI: `10.1007/s11095-008-9800-3`.

[28] Michal Nemergut et al. "Illuminating the mechanism and allosteric behavior of NanoLuc luciferase". In: *Nature communications* 14.1 (2023), p. 7864. DOI: `10.1038/s41467-023-43403-y`.

[29] Emily J. Hartzell et al. "Modular Hepatitis B Virus-like Particle Platform for Biosensing and Drug Delivery". In: *ACS nano* 14.10 (2020), pp. 12642–12651. DOI: `10.1021/acsnano.9b08756`.

Supporting Information Chapter 4

S4.1 NanoLuc

S4.1.1 Sequencing

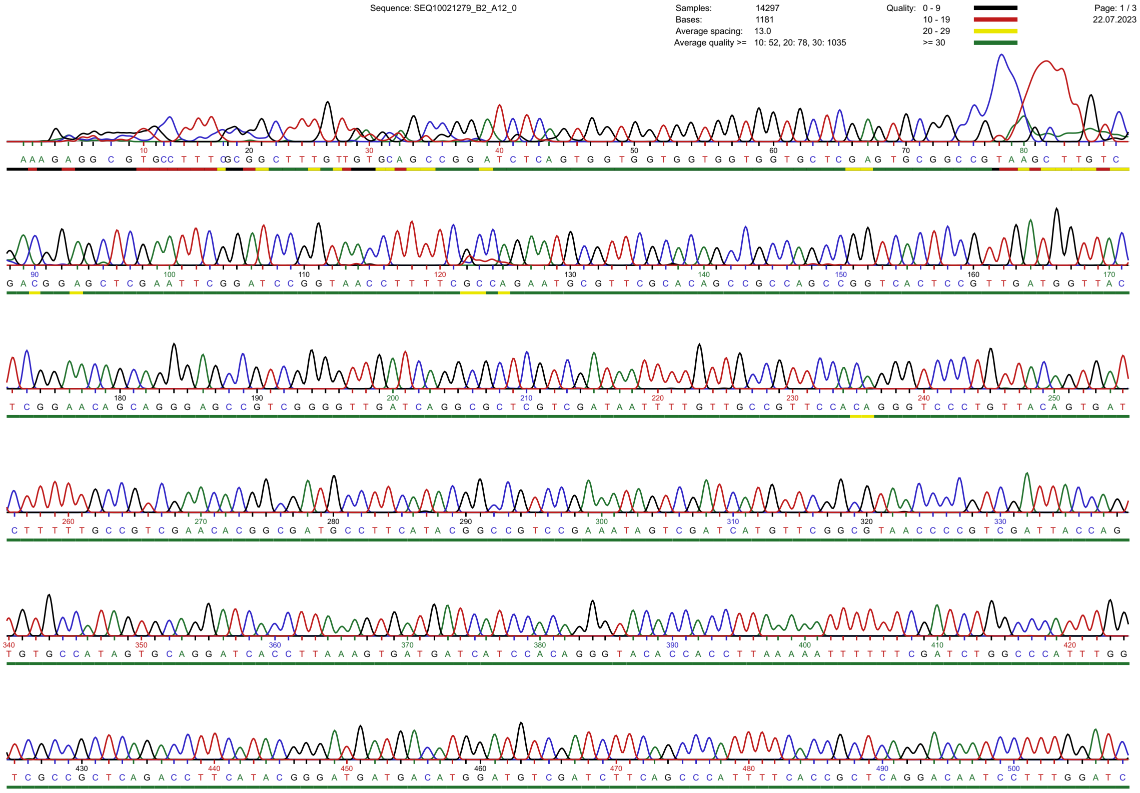

Figure S4.1: Sanger sequencing of *pET-28a(+)::His-NL* plasmid. The chromatogram shows the nucleotide sequence obtained from Sanger sequencing of *pET-28a(+)::His-NL* plasmid. From nucleotide position 42 onward, the sequence aligns with the complementary strand shown in Section S4.1.2.

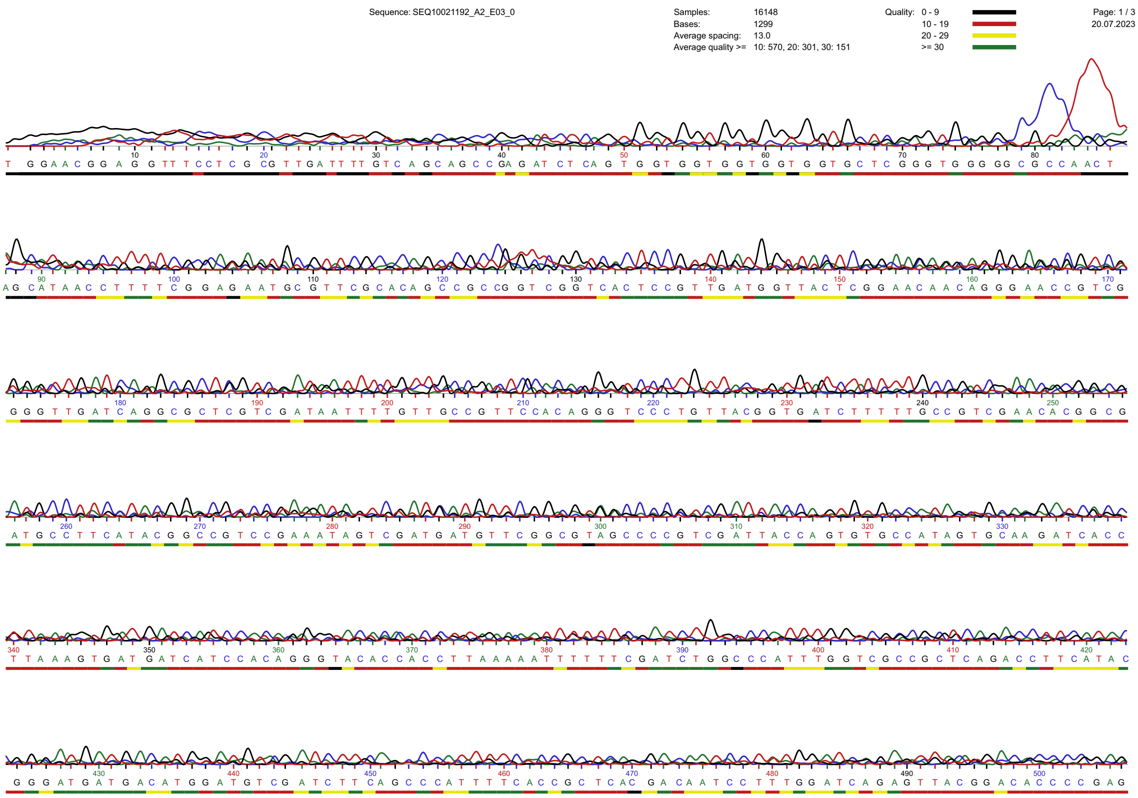

Figure S4.2: Sanger sequencing of *pET-28a(+)::Cys-NL* plasmid. The chromatogram shows the nucleotide sequence obtained from Sanger sequencing of *pET-28a(+)::Cys-NL* plasmid. From nucleotide position 46 onward, the sequence aligns with the complementary strand shown in Section S4.1.2.

S4.1.2 Open Reading Frame and Protein Sequence

The following sequence corresponds to the open reading frame (ORF) of the recombinant **NanoLuc** (*pET-28a(+)::His-NL* plasmid) expressed in *E.coli*, including an C-terminal His-tag.

```
5’-ATGGTCTTCACACTCGAAGATTTTCGTTGGGGACTGGCGACAGACAGCCGGCTACAACC
TGGACCAAGTCCTTGAACAGGGAGGTGTGTCCAGTTTGTTTCAGAATCTCGGGGTGTCCGTA
ACTCCGATCCAAAGGATTGTCCTGAGCGGTGAAAATGGGCTGAAGATCGACATCCATGTCAT
CATCCCGTATGAAGGTCTGAGCGGCGACCAAATGGGCCAGATCGAAAAAATTTTTAAGGTGG
TGTACCCTGTGGATGATCATCACTTTAAGGTGATCCTGCACTATGGCACACTGGTAATCGAC
GGGGTTACGCCGAACATGATCGACTATTTCCGGACGGCCGTATGAAGGCATCGCCGTGTTCG
ACGGCAAAAAGATCACTGTAACAGGGACCCTGTGGAACGGCAACAAAATTATCGACGAGCGC
CTGATCAACCCCGACGGCTCCCTGCTGTTCCGAGTAACCATCAACGGAGTGACCGGCTGGCG
GCTGTGCGAACGCATTCTGGCGAAAAGGTTACCGGATCCGAATTCGAGCTCCGTCGACAAGC
TTGCGGCCGCACTCGAGCACCACCACCACCACCACTGA-3’
```

The translated amino acid of **NanoLuc** is shown below.

MVFTLEDFVGDWRQTAGYNLDQVLEQGGVSSLFQNLGVSVTPIQRIVLSGENGLKIDIHVII
PYEGLSGDQMGQIEKIFKVVYPVDDHHFKVILHYGTLVIDGVTPNMIDYFGRPYEGIAVFDG
KKITVTGTLWNGNKIIDERLINPDGSLLFRVTINGVTGWRLCERILAKRLPDPNSSSVDKLA
AALE HHHHHH

The following sequence corresponds to the ORF of the recombinant **Cys-NanoLuc** (*pET-28a(+)::Cys-NL* plasmid) expressed in *E.coli*, including an C-terminal His-tag.

5'-ATGGTCTTCACACTCGAAGATTTTCGTTGGGGACTGGCGACAGACAGCCGGCTACAACC
TGGACCAAGTCCTTGAACAGGGAGGTGTGTCCAGTTTGTTTCAGAATCTCGGGGTGTCCGT
AACTCCGATCCAAAGGATTGTCCTGAGCGGTGAAAATGGGCTGAAGATCGACATCCATGTC
ATCATCCCGTATGAAGGTCTGAGCGGCGACCAAATGGGCCAGATCGAAAAAATTTTTAAGG
TGGTGTACCCTGTGGATGATCATCACTTTAAGGTGATCCTGCACTATGGCACACTGGTAAT
CGACGGGGTTACGCCGAACATGATCGACTATTTCCGGACGGCCGTATGAAGGCATCGCCGT
GTTCGACGGCAAAAAGATCACTGTAACAGGGACCCTGTGGAACGGCAACAAAATTATCGAC
GAGCGCCTGATCAACCCCGACGGCTCCCTGCTGTTCCGAGTAACCATCAACGGAGTGACCG
GCTGGCGGCTGTGCGAACGCATTCTGGCGAAAAGGTTATGCAAGCTTGCGCCGCACTCGAG
CACCACCACCACCACCAC TGA-3'

The translated amino acid of **Cys-NanoLuc** is shown below and additional cysteine residue is highlighted in red.

MVFTLEDFVGDWRQTAGYNLDQVLEQGGVSSLFQNLGVSVTPIQRIVLSGENGLKIDIHVI
IPYEGLSGDQMGQIEKIFKVVYPVDDHHFKVILHYGTLVIDGVTPNMIDYFGRPYEGIAVF
DGKKITVTGTLWNGNKIIDERLINPDGSLLFRVTINGVTGWRLCERILAKRLCKLAAALE
HHHHHH

S4.2 Synthesis and Characterization

S4.2.1 Synthesis and Characterization of Maleimide-functionalized 6-aminofluorescein

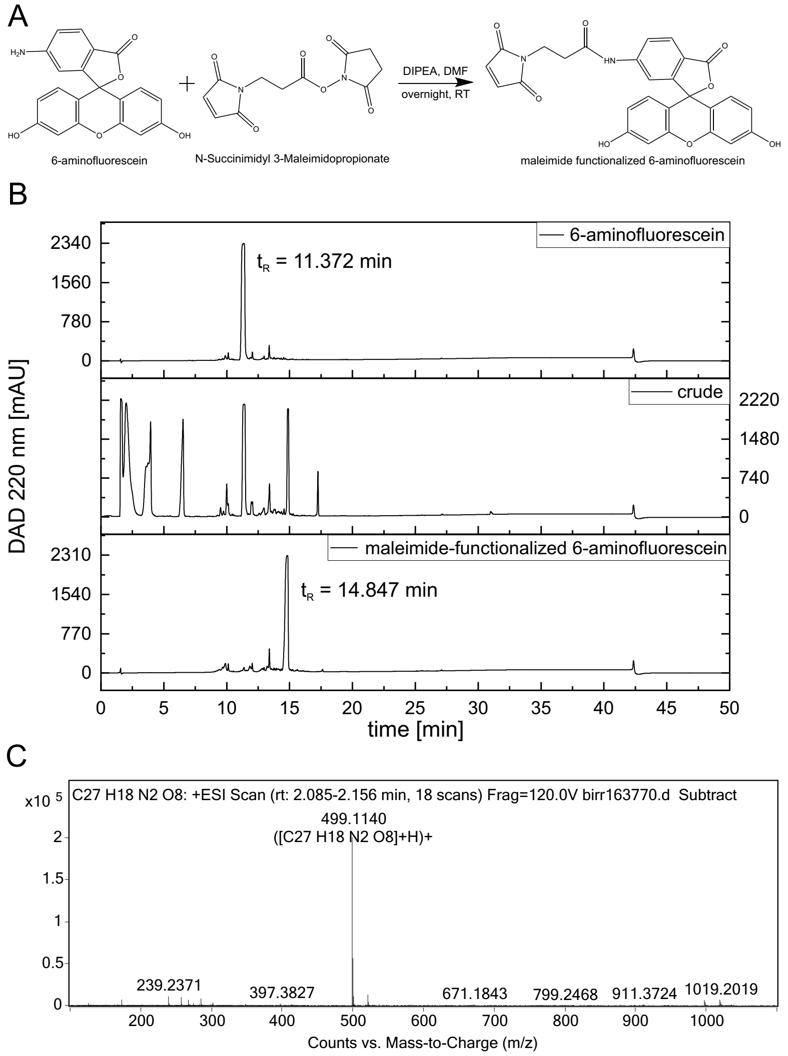

Figure S4.3: Synthesis and characterization of maleimide-functionalized 6-aminofluorescein. **A** Chemical equation for the synthesis of maleimide-functionalized 6-aminofluorescein. **B** RP-HPLC analysis of 6-aminofluorescein, crude reaction mixture and purified maleimide-functionalized 6-aminofluorescein. Retention time t_R: 6-aminofluorescein: 11.372 min; maleimide-functionalized 6-aminofluorescein: 14.847 min. **C** Mass spectrum of maleimide-functionalized 6-aminofluorescein.
HRMS (ESI) m/z calculated for $C_{27}H_{18}N_2O_8 + H^+$:499.1136
found: 499.1140.

S4.2.2 Fluorescence labeling of NanoLuc variants

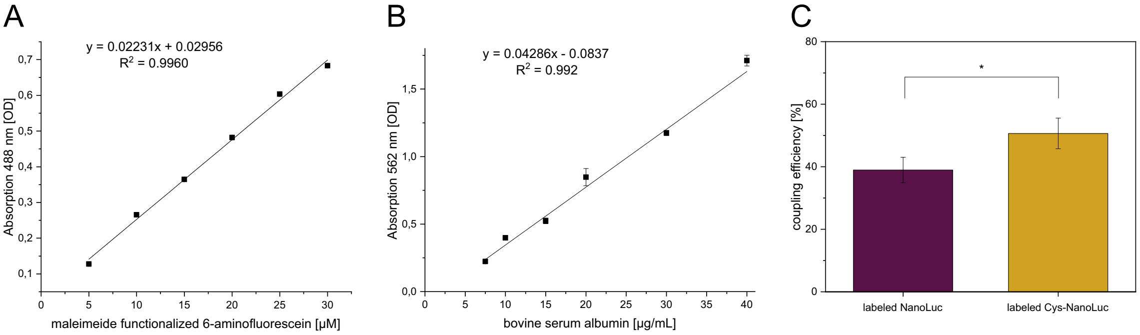

Figure S4.4: Determination of cysteine accessibility **A** Calibration curve of maleimide functionalized 6-aminofluorescein (5-30 µM) used to calculate the amount of coupled dye to NanoLuc variants. **B** BCA assay standard curve using bovine serum albumin (7.5-40 $\mu g\,mL^{-1}$) to quantify concentration of NanoLuc and Cys-NanoLuc. **C** Coupling efficiency of dye to NanoLuc variants. Data represent mean ± SD from technical triplicate. Statistical significance was assessed using an unpaired Student's t-test. Level of statistical significance is indicated as ns = not significant, * $p \leq 0.05$, ** $p \leq 0.01$, *** $p \leq 0.001$, **** $p \leq 0.0001$).

S4.2.3 Polymer Synthesis

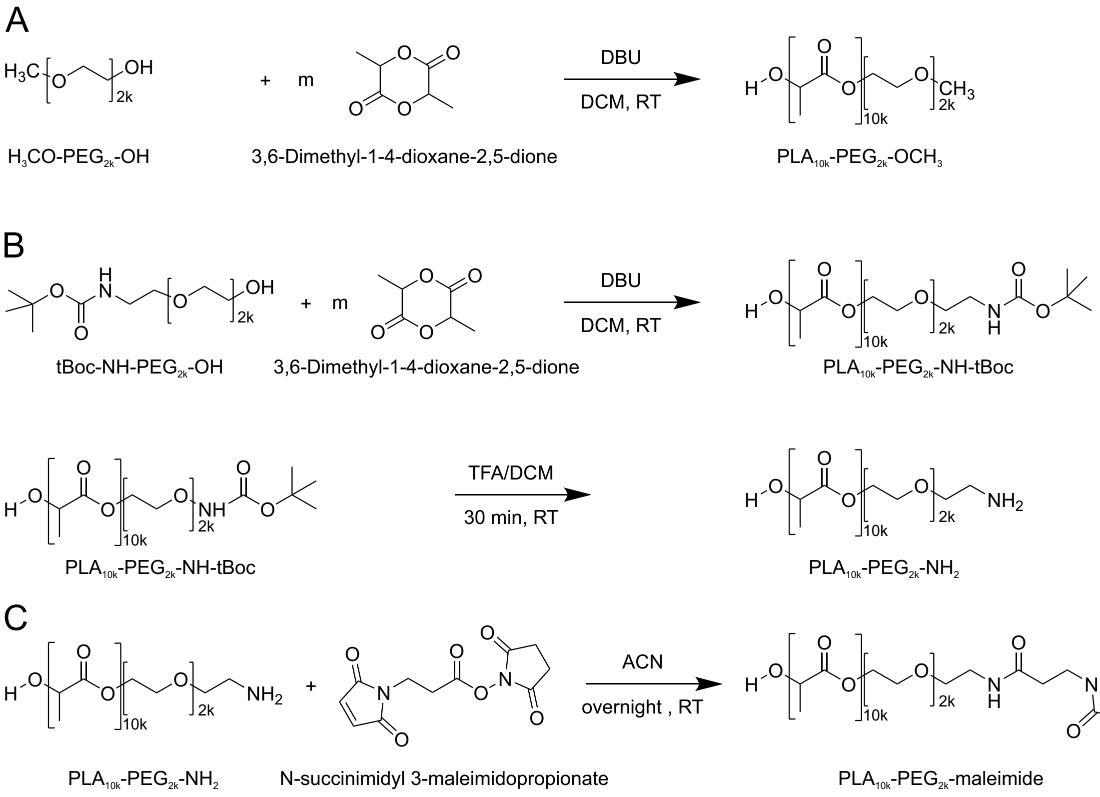

Scheme S4.1: Block copolymer synthesis. **A** Chemical equation for the synthesis of PLA_{10k}-$mPEG_{2k}$ block copolymer. **B** Chemical equations for the synthesis of PLA_{10k}-PEG_{2k}-NH_2 block copolymer. **C** Chemical equations for the synthesis of PLA_{10k}-PEG_{2k}-maleimide block copolymer.

S4.2.4 Polymer Characterization

The molar mass of the synthesized polymers was determined from the ^{1}H-NMR spectra as previously described by our group [1, 2] using the following equation:

$$M_{\text{PLA-polymer}} = \frac{\left(I_{\text{PLA,CH}_3} + I_{\text{PLA,CH}}\right) M_{\text{PLA,monomer}}}{I_{\text{PEG}}\, M_{\text{PEG,monomer}}} M_{\text{PEG-polymer}} \tag{4.4}$$

$M_{\text{PLA-polymer}}$ and $M_{\text{PEG-polymer}}$ are number-average molar masses of the PLA- and PEG-polymer block. $I_{\text{PLA,CH}_3}$ is the integral of protons from the lactic acid methyl group (-CH$_3$) and $I_{\text{PLA,CH}}$ is the integral of protons from the lactic acid methine group (-CH-). I_{PEG} is the integral of protons from the PEG repeating unit (-OCH$_2$CH$_2$-). $M_{\text{PLA,monomer}}$ and $M_{\text{PEG,monomer}}$ are molar masses of a single PLA and PEG unit.

The degree of functionalization (DOF) of maleimide-PEG$_{2k}$-PLA$_{10k}$ was determined by ^{1}H-NMR spectrum (Figure S4.5). If functionalization with maleimide is complete, the integral corresponding to the two vinylic protons of the maleimide moiety ($I_{maleimide,CHCH}$) at chemical shift δ: 6.67 ppm should equal 2. The DOF was calculated as followed:

$$DOF_{maleimide-PEG_{2k}-PLA_{10k}} = \frac{I_{maleimide,CHCH}}{2} * 100 \tag{4.5}$$

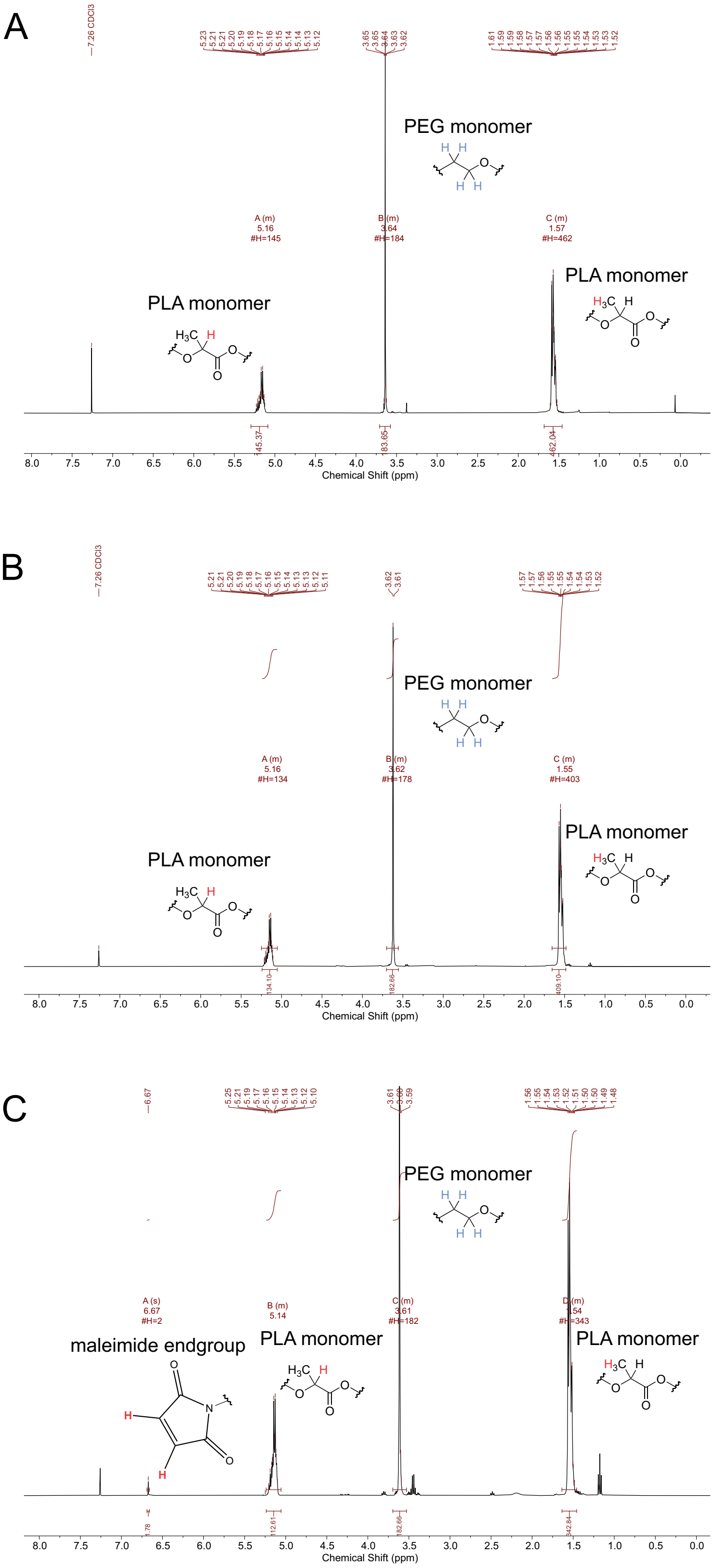

Figure S4.5: ^{1}H-NMR spectra of synthesized block copolymers (400 MHz, $CDCl_3$). **A** mPEG$_{2k}$-PLA$_{10k}$: δ (ppm): 5.16(m, PLA, CH_3), 3.64 (m, PEG), 1.57 (m, PLA, CH). **B** H_2N-PEG$_{2k}$-PLA$_{10k}$: δ (ppm): 5.16(m, PLA, CH_3), 3.62 (m, PEG), 1.55 (m, PLA, CH). **C** maleimide-PEG$_{2k}$-PLA$_{10k}$: δ (ppm): 6.67 (s, endgroup) 5.16(m, PLA, CH_3), 3.64 (m, PEG), 1.57 (m, PLA, CH).

S4.2.5 Nanoparticle Characterization

Figure S4.6 illustrates the size distributions of individual NP batches summarized in Figure 8. The minimal size variation observed between batches, combined with the absence of significant differences in mean diameter, demonstrates the high reproducibility of NP preparation method.

Figure S4.7 shows the cumulative hydrodynamic size distributions of NPs from batch two as a representative example. Percentile analysis shows modest broadening upon protein functionalization as D10, D50, and D90 values were consistently higher for NanoLuc@NP and Cys-NanoLuc@NP and span, which serves as an indicator of polydispersity proxy, slightly increased compared to control NPs. The span is defined according to Equation (4.6), with smaller values correspond to a narrower size distribution.

$$Span = \frac{(D90 - D10)}{D50} \tag{4.6}$$

D10, D50, and D90 represent the particle diameters at which the cumulative distribution reaches 10 %, 50 %, and 90 %, respectively

Span increased from 1.11 (control) to 1.23 (NanoLuc@NP) and 1.14 (Cys-NanoLuc@NP), driven primarily by higher D90 values (128 nm for control NP to 170 nm and 157 nm for NanoLuc@NP and Cys-NanoLuc@NP, respectively). Higher D90 values demonstrate a broader upper size tail and the presence of more large particles after protein coupling. Overall, functionalization broadens the NP size distribution without significantly altering colloidal uniformity and without shifting the central tendency (no significant differences in mean, Figure S4.6).

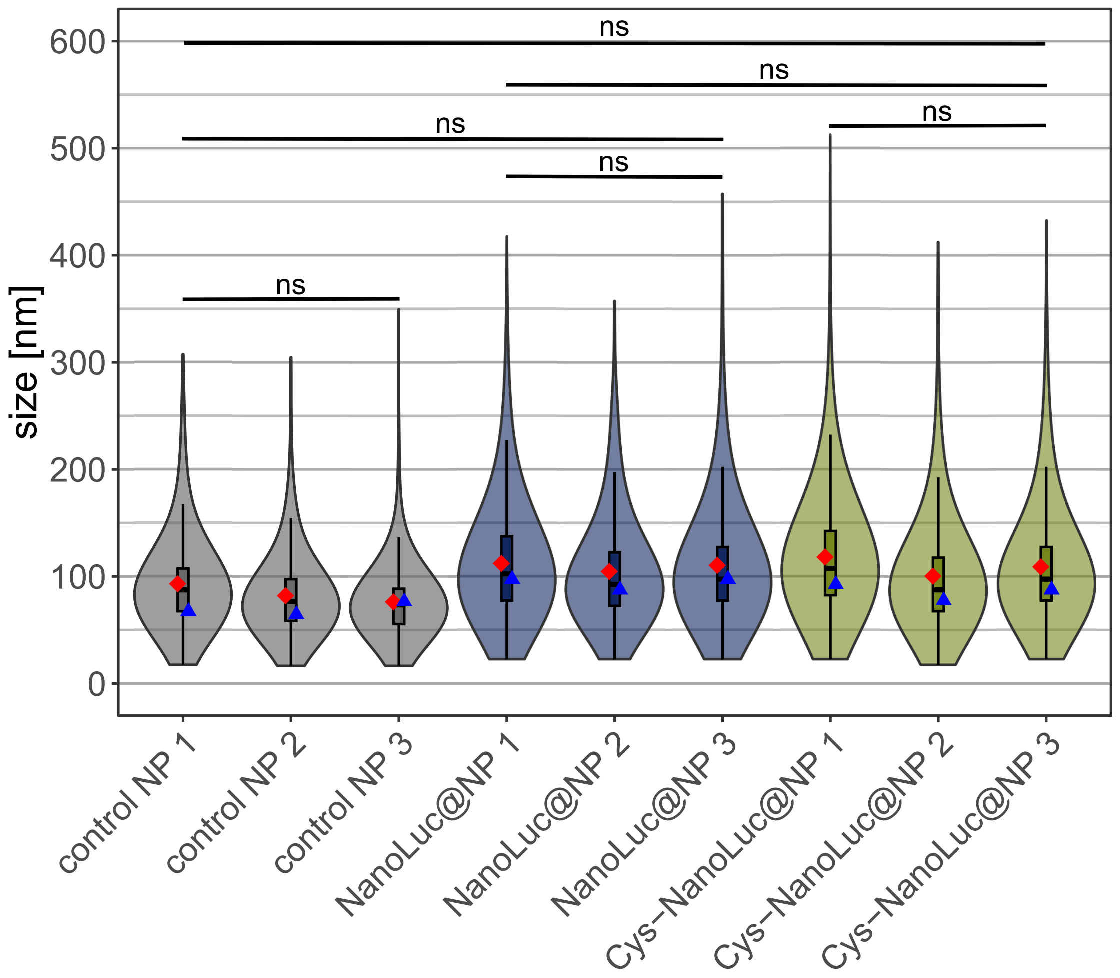

Figure S4.6: Size distribution and measures of central tendency of NPs. Violin plots represent size distribution of hydrodynamic diameters (n=3). The median NP size is shown as horizontal line within the box, whose lower and upper edges represent the first (Q1) and third (Q3) quartiles, respectively. Whiskers indicate the most extreme data points within 1.5 times the interquartile range from the lower and upper quartiles. The mean is represented by a red rectangle and the mode is depicted by a blue triangle. The different measure of central tendency are separated by commas in the following order mean, median and mode. Control NP 1: 93.2 nm, 87.5 nm, 67.5 nm; control NP 2: 82.1 nm, 76.5 nm, 64.5 nm; control NP 3: 76.2 nm, 73.5 nm, 76.5 nm; NanoLuc@NP 1: 112 nm, 103 nm, 97.5 nm; NanoLuc@NP 2: 105 nm, 92.5 nm, 87.5 nm; NanoLuc@NP 3: 110 nm, 97.5 nm, 97.5 nm; Cys-NanoLuc@NP 1: 118 nm, 108 nm, 92.5 nm; Cys-NanoLuc@NP 2: 100 nm, 87.5 nm, 77.5 nm; Cys-NanoLuc@NP 3: 109 nm, 97.5 nm, 87.5 nm. Statistical significance on mean size was assessed using the Kruskal-Wallis test followed by Dunn's post hoc test with Bonferroni adjustment for multiple comparisons; no significant (ns) differences were observed.

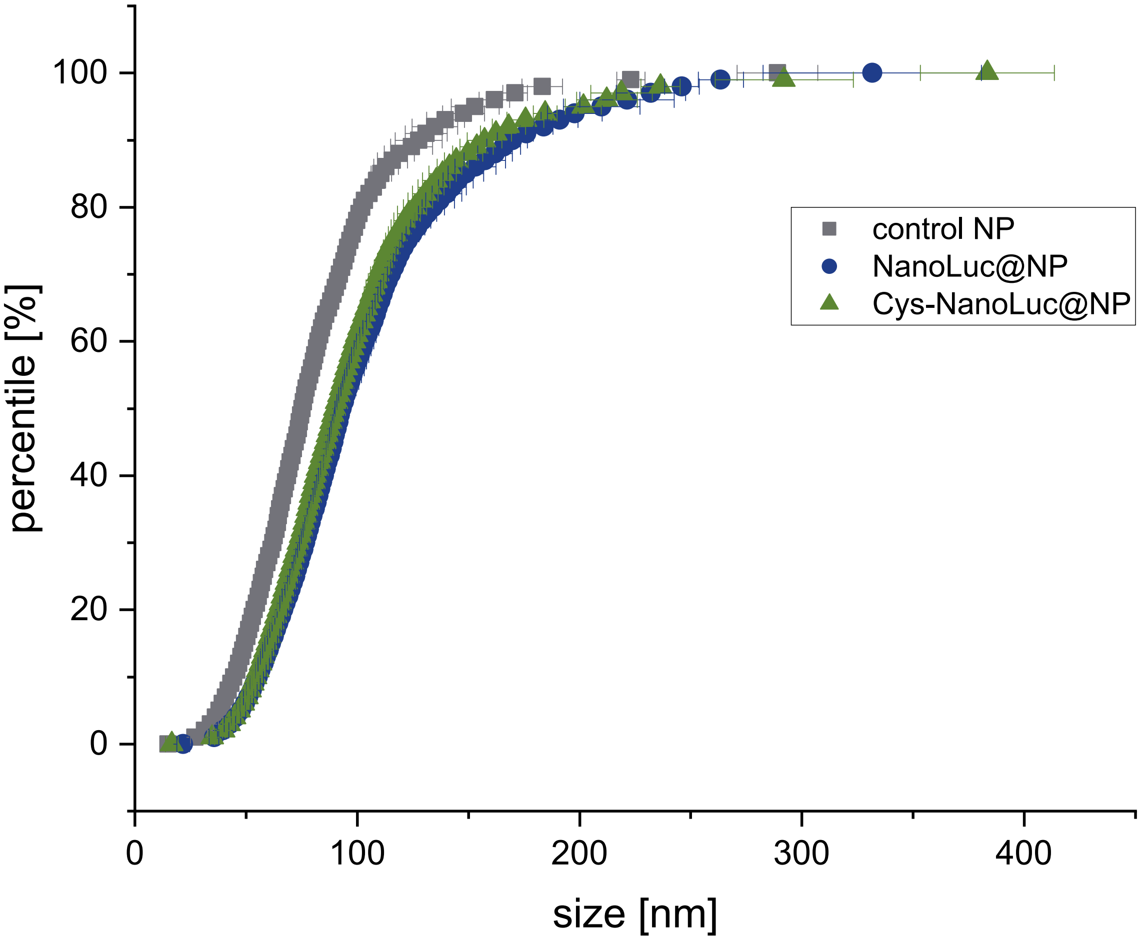

Figure S4.7: Cumulative hydrodynamic size distributions of control NP, NanoLuc@NP, and Cys-NanoLuc@NP (each batch 2) obtained from NTA measurements. Percentile diameters (D10/D50/D90) were 44.5/75.2/128 nm for control, 55.3/93.2/170 nm for NanoLuc@NP, and 54.3/90.0/157 nm for Cys-NanoLuc@NP.

S4.2.6 Coupling of NanoLuc Variants to NP

Coupling Efficiency

The amount of NanoLuc variants conjugated to NPs was calculated as following: The theoretical molar amount of maleimide-functionalized PEG-PLA is given by:

$$n_{PLA-PEG-maleimide} = \frac{V_{PLA-PEG-maleimide} * c_{PLA-PEG-maleimide}}{M_{PLA-PEG-maleimide}} \tag{4.7}$$

Assuming complete coupling, the corresponding molar amount of NanoLuc is:

$$n_{NanoLuc,100\%} = n_{PLA-PEG-maleimide} \tag{4.8}$$

The theoretical mass of NanoLuc at 100% coupling is:

$$m_{NanoLuc,100\%} = n_{NanoLuc,100\%} * M_{NanoLuc,100\%} \tag{4.9}$$

The actual mass of coupled NanoLuc, determined via BCA assay, is:

$$m_{NanoLuc,coupled} = c_{NanoLuc,BCA} * V_{NanoLuc@NP} \tag{4.10}$$

The coupling efficiency is calculated by Equation (4.3).

Amount of NanoLuc Variants per Nanoparticle

Using the geometrical model by Soloviev et al., we calculated the theoretical maximum number of proteins (NanoLuc; $\mathrm{N_{max}}$) that can assemble as a monolayer surrounding a spherical NP (eq. (4.11)) [3]. This equation is based on maximizing the number of equidistant points on a sphere, corresponding to the centers of neighboring proteins arranged in a near-hexagonal pattern. The authors assumed that the NP is a sphere with radius $\mathrm{R_1}$, and that the surrounding protein molecules can be approximated as identical spheres with radius $\mathrm{R_2} < \mathrm{R_1}$.

$$\mathrm{N_{max}} = \left[\frac{2\sqrt[2]{3}}{3}\,\pi\,\frac{1}{\alpha^2}\right] \tag{4.11}$$

Here, α is defined as half the angular distance between two neighboring spherical proteins on the NP surface.

The approximate protein radius (in nm) was estimated from its molar mass M_r ($\mathrm{g\,mol^{-1}}$) using Equation (4.12) , which models proteins as sphere characterized by a partial specific volume $\overline{v}$ ($\mathrm{cm^3\,g^{-1}}$) and a mass (g) given by quotient of molar mass and Avogadro's constant N_A (mol).

$$\mathrm{R_2} = \sqrt[3]{\frac{3\,\overline{v}\,M_r}{4\,\pi\,N_A}\,10^{21}} = 0.066\sqrt[3]{M_r} \tag{4.12}$$

Given the protein radius $\mathrm{R_2}$ and the NP radius $\mathrm{R_1}$ (with $\mathrm{r} = \mathrm{R_2}\ \mathrm{R_1}$), the value of $\sin\alpha$ can be calculated as follows:

$$\sin\alpha = \frac{\mathrm{R_2}}{\mathrm{R_1}+\mathrm{R_2}} = \frac{\mathrm{r}}{1+\mathrm{r}} \tag{4.13}$$

Based on the NP size (NanoLuc@NP: 109 nm; Cys-NanoLuc@NP: 110 nm), the maximum number of NanoLuc on NP for NanoLuc@NP is 3412 and for Cys-NanoLuc@NP is 3483.

The experimentally determined numbers of NanoLuc variants per NP were calculated by eq. (4.14). Individual batch results and their corresponding mean are shown in Figure S4.8.

$$\frac{NanoLuc}{Nanoparticle} = \frac{c_{NanoLuc}}{c_{Nanoparticle}} \tag{4.14}$$

Here, $c_{NanoLuc}$ represents the protein concentration quantified by the BCA assay and $c_{Nanoparticle}$ represent the concentration of NPs determined by NTA measurements. The uncertainties were estimated using error propagation.

Comparing the mean number of NanoLuc variants per NP, NanoLuc@NP contains less protein molecules (2381 ± 1625) than Cys-NanoLuc@NP (9274 ± 6400). The high uncertainties are due to the large error of NP quantification by NTA measurements.

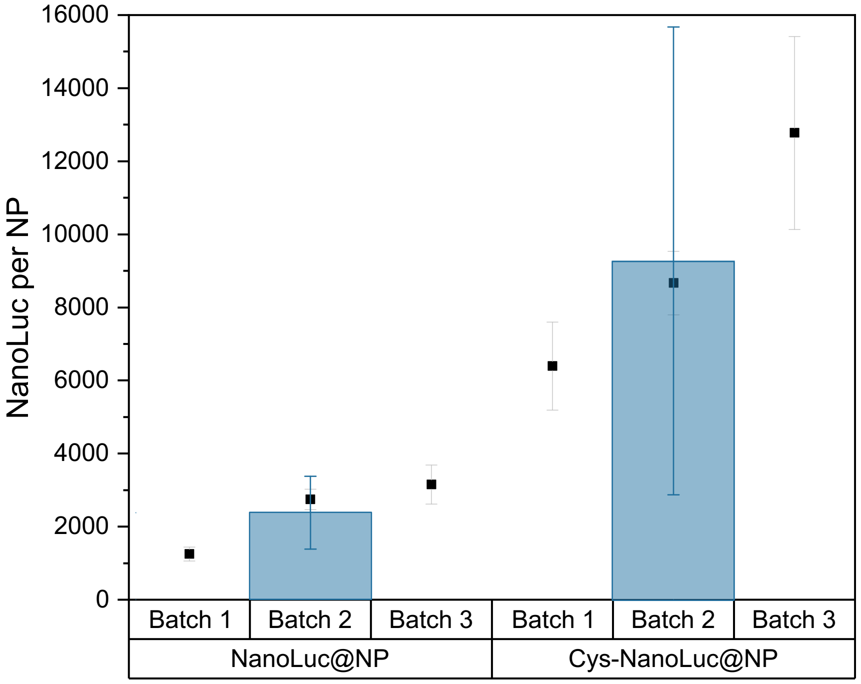

Figure S4.8: Coupling of NanoLuc and Cys-NanoLuc to NP. NanoLuc and Cys-Nanoluc per NP of the three NP preparations shown as individual data points ± SD (n=3; NanoLuc@NP: Batch 1: 1251 ± 191; Batch 2: 2745 ± 283; Batch 3: 3148 ± 533; Cys-NanoLuc@NP: Batch 1: 6390 ± 1205; Batch 2: 8661 ± 878; Batch 3: 12 772 ± 2643). The average of all preparations is represented by bars with pooled SD (N=3; Nanoluc@NP: 2381 ± 1625; Cys-NanoLuc@NP: 9274 ± 6400

.

The determined amount of Cys-NanoLuc per NP was larger than the theoretical maximum number in every batch. This higher experimentally determined protein amount per NP might be attributed to several factors: deviations from ideal spherical packing, flexibility of protein conformation and adsorption of protein causing multilayering. The latter point should have resulted in an increase in size. However, this was not observed for the Cys-NanoLuc@NP compared to NanoLuc@NP. In addition to these aspects, the methodology used to determine the amount of protein per NP must also be considered. Taking into account the uncertainty of protein concentration measurement via BCA assay and especially the uncertainty of NP concentration determination, the experimentally determined amount of protein per NP should be interpreted with caution. Nevertheless, the collected data suggest that a majority of NP surface is covered by protein.

References

[1] Oliver Zimmer and Achim Goepferich. “How clathrin-coated pits control nanoparticle avidity for cells”. In: *Nanoscale horizons* 8.2 (2023), pp. 256–269. DOI: `10.1039/d2nh00543c`.

[2] Kathrin Schorr et al. “The quantity of ligand-receptor interactions between nanoparticles and target cells”. In: *Nanoscale horizons* 10.4 (2025), pp. 803–823. DOI: `10.1039/D4NH00645C`.

[3] Mikhail Soloviev et al. “Modelling the adsorption of proteins to nanoparticles at the solid-liquid interface”. In: *Journal of colloid and interface science* 605 (2022), pp. 286–295. DOI: `10.1016/j.jcis.2021.07.072`.

Chapter 5

Bioluminescent-Responsive Nanoparticles: Beyond Brightness

Abstract

Nanoparticles (NPs) functionalized with photo-labile protecting groups (PPGs) can modulate intrinsic NP properties and thereby offer spatiotemporal control for targeting and drug delivery. However, activation of photo-responsive NPs is restricted by limited tissue penetration of light. Bioluminescence-responsive NPs may overcome this limitation by inducing cleavage of PPG through bioluminescence resonance energy transfer (BRET). A key requirement for efficient BRET is a sufficient spectral overlap between donor emission and acceptor absorption. To this end, we synthesized a red-shifted coumarin-derived PPG ($DEAC_{435}$) whose absorption spectrum is well matched to the emission of NanoLuc luciferase. Successful implementation of bioluminescence-responsive NPs requires two critical conditions: the PPG must effectively alter physicochemical and/or biological characteristics of NPs, and the donor-acceptor arrangement must support sufficient BRET to induce photocleavage. To enhance cell uptake of polymeric core-shell NPs composed of poly(D,L-lactide-*co*-glycolide) and a poly(ethylene glycol)-*b*-poly(D,L-lactide) block copolymer, we functionalized their shell with positively charged cell-penetrating peptides (CPPs). CPPs effectively promote membrane penetration but lack selectivity. To avoid nonspecific uptake, we incorporated $DEAC_{435}$ as a PPG into this NP design to temporarily camouflage the positive charge and restore CPP function only upon irradiation. However, $DEAC_{435}$ did not sufficiently mask the CPPs, as neither the NP surface charge nor the cellular interaction profile was altered, indicating that this PPG was inadequate for effective CPP masking. Nevertheless, we observed clear BRET-induced excitation of $DEAC_{435}$ on the NP surface, demonstrating that bioluminescence-driven activation is, in principle, feasible within this NP architecture.

5.1 Introduction

The incorporation of photo-labile protecting groups (PPGs) into nanoparticles (NPs) renders them photo-responsive, enabling high spatiotemporal control over activation processes and thereby offering opportunities for precisely regulated drug release and improved targeting [1–6]. However, most PPGs require ultraviolet or visible light, which is strongly scattered and absorbed by living tissue, resulting in poor penetration depth [7, 8]. Consequently, this limitation restricts the applicability of conventional PPGs to directly accessible tissues such as the vitreous of the eyes [9, 10]. Strategies to address this restriction involve red-shifting PPG absorption to the near-infrared region (NIR), thereby reducing tissue optical attenuation [7, 8, 11]. Complementary approaches include two-photon excitation, which requires high-intensity laser systems, or the use of upconverting NPs, which convert tissue-penetrating NIR light into higher-energy visible emission, to improve effective penetration depth [12–16].

In contrast to the aforementioned strategies, bioluminescence can function as an internal light source and thus represents a fundamentally different activation pathway. Bioluminescence arises from enzyme-catalyzed reactions yielding visible photons without an external excitation source [17]. It has become widely established in imaging and biosensing and more recently it has been exploited to drive the photocleavage of PPGs on small molecules [18–22]. In this photocleavage system, the energy required for bond cleavage is provided through bioluminescence resonance energy transfer (BRET), in which the emission of a luciferase substrate pair is funneled directly into the PPG. The feasibility of this energy transfer depends on the spectral overlap of donor (luciferase) and acceptor (PPG) and their proximity.

Chang et al. identified bioluminescence as an active biochemical effector and introduced the concept of "bioluminolysis", wherein bioluminescence drives photocleavage [20]. By tethering a coumarin-based PPG to a NanoLuc-HaloTag chimera, they achieved highly efficient energy transfer and rapid uncaging with kinetics comparable to light-emitting diode (LED) irradiation even in cellular assays.

In Chapter 3, we introduced photo-responsive NPs whose surface charge can be modulated by external light [23]. In this NP design, the positive cell-penetrating peptide (CPP) was masked by the incorporation of the coumarin-derived PPG (DEAC). Upon light irradiation, the PPG was cleaved, restoring the physicochemical and biological characteristics of CPP.

Building on this design and leveraging the bioluminescent NP platform established in the preceding chapter, our aim in the present work was to translate the bioluminolysis mechanism to a NP system (Figure 5.1 A).

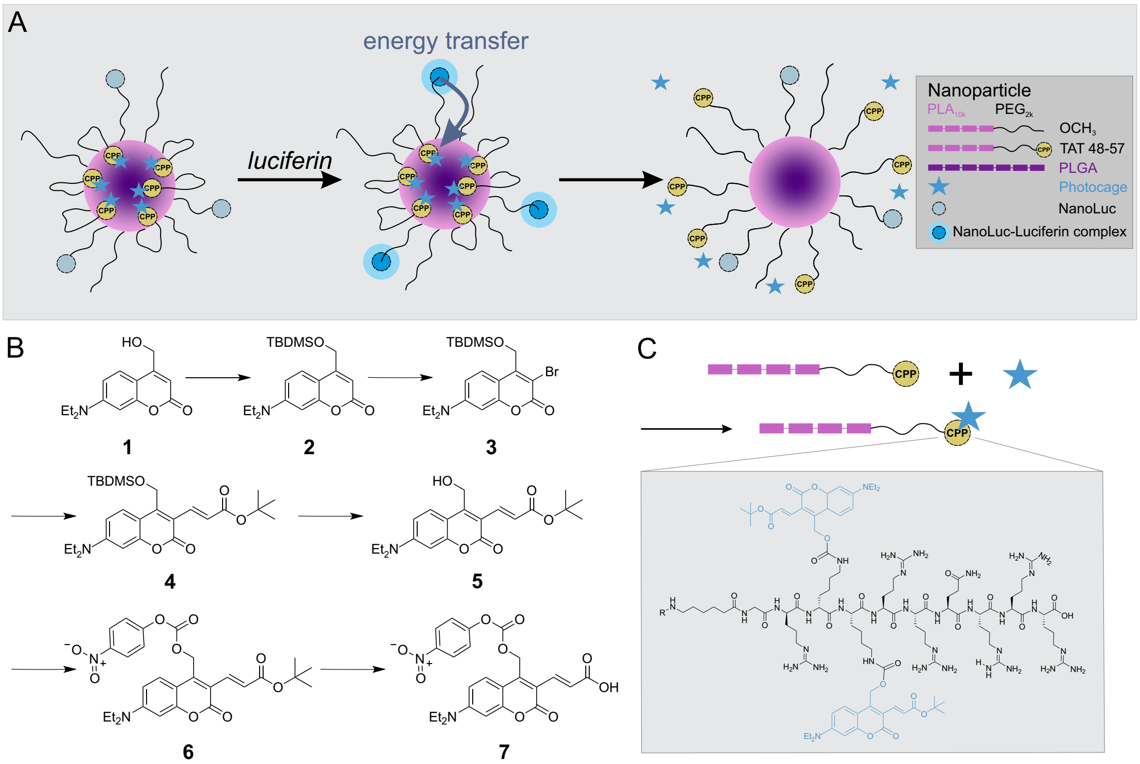

Figure 5.1: Schematic representation of bioluminescent-responsive NP and synthesis of red-shifted photo-labile protecting group (PPG). **A** Bioluminescent-responsive core-shell NP composed of poly(D,L-lactide-*co*-glycolide) (PLGA) and poly(ethylene glycol)-*b*-poly(D,L-lactide) (PEG-PLA) block copolymer, with its surface functionalized by photocaged CPP and NanoLuc. **B** Synthesis scheme of red-shifted coumarin-derived PPG (DEAC_{435}, **5**). TBDMS denotes for tert-butyldimethylsilyl protection of the hydroxyl group in the coumarin-based PPG. **C** Schematic synthesis of photocaged TAT-polymer. The amino acid sequence of TAT 48-57 (CPP) is depicted in the grey box. Red-shifted coumarin-derived PPG (blue) is attached to the lysine residues of TAT 48-57.

In this bioluminescence-responsive design, the NP itself must cleave the PPG via BRET. NanoLuc is particularly well suited luciferase for this purpose, as it provides exceptionally bright emission, high photon flux even at low concentrations, and a high quantum yield [24–27]. Beyond donor performance, the spectral characteristics of the PPG are equally critical, as its absorption profile must exhibit substantial overlap with NanoLuc emission. Further, the donor-acceptor pairs must remain in close proximity to enable efficient energy transfer [28]. However, the existing photo-responsive NPs exhibit deficient spectral alignment with NanoLuc, thereby limiting the probability of BRET-induced cleavage. To enhance energy-transfer efficiency within the NP system, it is imperative to implement a PPG that exhibits enhanced spectral overlap. Rather than introducing major changes to the established NP design, we opted to red-shift the existing DEAC PPG by extending its π-electron system, which resulted in DEAC_{435} (**5**, Figure 5.1). Its absorption scaffold is closely related to coumarin-derived PPG invented by the Ellis-Davies group used for photocaging of small molecules with uncaging quantum yield ranging from 0.18-0.78 [12, 29–31]. The suitability of NanoLuc-DEAC$_{435}$ as donor-acceptor pair for bioluminolysis has already been demonstrated in the literature, making DEAC$_{435}$ a promising candidate for a bioluminescent-responsive NP design [21].

To implement this bioluminescence-responsive strategy, we synthesized the red-shifted coumarin-derived PPG DEAC$_{435}$ and incorporated it into our NP platform. Based on the performance of the previously used PPG, we hypothesized that DEAC$_{435}$ would similarly mask the CPP characteristics. Moreover, its enhanced photochemical properties were expected to enable more efficient light-triggered uncaging. In parallel, we assessed whether the donor-acceptor arrangement provided sufficient BRET within the NP system. Together, these considerations guided the experimental work, which establishes the conceptual and experimental foundation for implementing bioluminolysis in NPs and highlights critical design parameters for future development.

5.2 Materials and Methods

5.2.1 Materials

Ultrapure water was obtained from a Milli-Q EQ 7000 system (Merck, Darmstadt, Germany) equipped with Milli-Q Biopak filter (Merck, Darmstadt, Germany) and was taken fresh every day. It is referred to as mQ water in the following. Heterobifunctional t-Boc amine poly(ethylene glycol) hydroxyl with a molecular mass of $2000\,\mathrm{g\,mol^{-1}}$ (tBoc-NH-PEG$_{2k}$-OH) and heterobifunctional poly(ethylene glycol)-carboxylic acid with a molecular mass of $2000\,\mathrm{g\,mol^{-1}}$ (COOH-PEG$_{2k}$-OH) were purchased from Jenkem Technology USA, Inc. (Allen, TX, USA). Poly(ethylene glycol) methyl ether with a molecular mass of $2000\,\mathrm{g\,mol^{-1}}$ (mPEG$_{2k}$-OH), N-Succinimidyl 3-Maleimidopropionate, 7-(diethylamino)-4-(hydroxy)methylcoumarin, tert-butyldimethylchlorosilane, N-Bromosuccinimide, anhydrous lithium chloride, tert-butyl acrylate (stabilized with 4-methoxyphenol), tetrabutylammonium fluoride (1 M in tetrahydrofuran, THF) and 1-Ethyl-3-(3-dimethylaminopropyl)carbodiimide (EDC) were purchased from TCI (Eschborn, Germany). Resomer RG 502, poly(D,L-lactide-*co*-glycolide) (lactide:glycolide 50:50, ester terminated, M$_w$ 7000-17000 Da) (PLGA) and QuantiPro™BCA Assay Kit were obtained from Sigma-Aldrich (Taufkirchen, Germany). N-Hydroxysuccinimide (NHS) was purchased from Carl Roth (Karlsruhe, Germany). 1-[Bis(dimethylamino)methylene]-1H-1,2,3-triazolo-[4,5-b]pyridinium 3-oxide hexafluorophosphate (HATU) was obtained from Fluorochem (Gadfield, United Kingdom). 4-Nitrophenylchloroformate and protected amino acids Fmoc-Arg(Pbf)-OH, Fmoc-Gln(Trt)-OH, Fmoc-D-Lys(Boc)-OH, Fmoc-Gly-OH and Fmoc-6-AHx-OH were obtained from BLDpharm (Karlsruhe, Germany). While Fmoc-Tyr(tBu)-OH was purchased from Iris Biotech (Marktredwitz, Germany). 2-Chlorotrityl chloride resin was sourced from Carbolution Chemicals (St. Ingbert, Germany). The cellulose dialysis membranes had a molecular weight cut-off (MWCO) of 6-8 kDa and were obtained from Spectrum Laboratories, Inc. (Rancho Domingues, CA, USA). The frits had a pore size of 35 µm and were sourced from Roland Vetter Laborbedarf (Ammerbuch, Germany). The infrared lamp was obtained from Medisana (Neuss, Germany), with a thermostat from PEARL GmbH (Buggingen, Germany). Syringes were purchased from Braun (Melsungen, Germany). All other chemicals and reagents used in this study were obtained from Sigma-Aldrich (Taufkirchen, Germany) in analytical grade. HeLa (CCL-2) cells were purchased from ATCC (Manassas, VA, USA). Fetal bovine serum (FBS) was purchased from Biowest (Nuaille, France). Eagle's minimum essential medium (EMEM), Leibovitz's L-15 medium (LM) and corning®-cell culture flasks with $75\,\mathrm{cm^2}$ area were purchased from Sigma Aldrich (Taufkirchen, Germany). Nuclear magnetic resonance (NMR) spectra were recorded on a Bruker Avance-400 or Avance-500 NMR spectrometer (Billerica, MA, USA). High-resolution mass spectrometry (HRMS) was performed on a Q-TOF 6540 ultrahigh definition(UHD) liquid chromatography/mass spectrometry (LC/MS) system (Agilent Technologies, Santa Clara, CA, USA) using an electrospray ionization (ESI) or atmospheric pressure chemical ionization (APCI) source. Silicia gel 60 (0.063-0.200 mm) was used for column chromatography. High-performance liquid chromatography (HPLC) analysis was performed with 1260 Infinity II from Agilent Technologies (Santa Clara, CA, USA) using a Kinetex EVO C18 column (100 Å, 2.6 µm, 150 mm x 4.6 mm, Phenomenex Ltd., Germany) or a XBridge ®BEH Shield RP18 column (130 Å, 3.5 µm, 3.0 mm x 50 mm, Waters, Eschborn, Germany). Preparative HPLC analysis was performed with Prep 150 LC system from Waters (Eschborn, Germany) consisting of a 2545 binary gradient module, a 2489 UV/visible detector and a Waters Fraction Collector III. A Gemini-NX C18 column (110 Å, 5 µm, 250 mm × 21 mm, Phenomenex Ltd., Germany) was used. Dulbecco's phosphate-buffered saline (DPBS) was prepared in-house according to the standard formulation, filtrated and autoclaved before use.

5.2.2 Synthesis of Cell-Penetrating Peptide

The TAT sequence was synthesized manually via solid-phase peptide synthesis employing a standard Fmoc protocol, as described in Chapter 3. Amino acids were coupled sequentially to 2-chlorotrityl chloride resin using HATU and collidine. Fmoc groups were removed with 20 % piperidine in N,N-dimethylformamide (DMF). After assembly, the peptide was cleaved from the resin with hexafluoroisopropanol(20 % in DMF), subsequently dried, and characterized by HPLC (Kinetex EVO C18) and mass spectrometry (see Supporting Information of Chapter 3 for details).

5.2.3 Synthesis of 7-diethylamino-4-hydroxymethylcoumarin (DEAC)

The PPG 7-diethylamino-4-hydroxymethylcoumarin (DEAC, **1**) was synthesized as previously described by Weinrich et al. with small modifications [32]. For detailed synthesis see Supporting Information of Chapter 3.

5.2.4 Synthesis of 7-(diethylamino)-(4-hydroxymethyl)-[(E)-3-(tert-butoxycarbonyl)prop-2-enyl]coumarin (DEAC$_{435}$)

The PPG 7-(diethylamino)-(4-hydroxymethyl)-[(E)-3-(tert-butoxycarbonyl)prop-2-enyl]coumarin (DEAC$_{435}$, **5**) was synthesized as previously described by Olson et al. with small modifications [12]. For detailed synthesis see Supporting Information.

5.2.5 Synthesis of Activated DEAC$_{435}$ (6)

For synthesis of caged TAT ([TAT]$_{435}$) the photocage DEAC$_{435}$ needed to be activated by transforming the hydroxy function into a reactive carbonate. DEAC$_{435}$ **5** (46.0 mg, 123 µmol, 1.00 equiv.) and 4-nitrophenylchloroformate (257 mg, 1.28 mmol, 10.3 equiv.) were dissolved in the least amount possible of anhydrous dichloromethane (DCM) and were cooled to 0 °C. N,N-diisopropylethylamine (DIPEA) (215 µL, 1.23 mmol, 10.0 equiv.) was added dropwise and stirred for 15 min. The reaction solution was then stirred for 6 h at room temperature (RT). Subsequently, the solvent was removed under reduced pressure. Purification of synthesis product was performed by preparative HPLC. The mobile phase consisted of solvent A (mQ water with 0.1 % trifluoroacetic acid, TFA) and solvent B (acetonitrile, ACN). The separation was initiated with an isocratic hold at 20 % B for 1 min, followed by a linear gradient from 20 % to 95 % B over 22 min at a flow rate of 20 mL/min. Detection was performed at 220 nm. Fractions containing the desired product were collected, pooled, and lyophilized to yield the purified compound **(6)**. The product was characterized by NMR spectroscopy and MS.

5.2.6 Synthesis of Activated DEAC$_{435acid}$ (7)

Activated DEAC$_{435}$ **(6)** (38.1 mg, 70.9 µmol, 1.00 equiv.) was dissolved in DCM (3.8 mL) followed by the addition of an equal volume of TFA. The mixture was stirred at RT for 30 min. The synthesis was monitored by HPLC (XBridge®BEH Shield RP18, see Supporting Information Section S5.1.3). Subsequently, the solvent was removed under reduced pressure. Purification of synthesis product was performed by preparative HPLC. The mobile phase consisted of solvent A (mQ water with 0.1 % TFA) and solvent B (ACN). The separation was initiated with an isocratic hold at 20 % B for 1 min, followed by a linear gradient from 20 % to 95 % B over 22 min at a flow rate of 20 mL/min. UV-detection was performed at 220 nm. Fractions containing the desired product were collected, pooled, and lyophilized to yield the purified compound **(6)**. The product was characterized by NMR spectroscopy and MS.

5.2.7 Polymer Synthesis

H_2N-PEG$_{2k}$-PLA$_{10k}$ and mPEG$_{2k}$-PLA$_{10k}$ block copolymers were synthesized according to Qian et al., with modifications previously reported by our group [33, 34]. Briefly, the heterobifunctional PEG polymer (1 equiv.), either tBoc-NH-PEG$_{2k}$ or mPEG$_{2k}$, was used as a macroinitiator for the ring-opening polymerization of cyclic lactide (3,6-dimethyl-1,4-dioxane-2,5-dione, 70 equiv.). Both components were dissolved in anhydrous DCM and mixed with 1,8-diazabicyclo[5.4.0]undec-7-ene (DBU, 3 equiv.) as catalyst. The reaction mixture was stirred at RT for exactly 1 h. Polymerization was quenched by the addition of benzoic acid (10 equiv.). The resulting product was precipitated in a 20-fold volume of ice-cold diethyl ether, centrifuged for 10 min at 6000 rcf and 0 °C and dried under a nitrogen stream overnight at RT. In the case of tert-butyloxycarbonyl (tBoc)-protected block copolymer, the protecting group was removed by treatment with TFA in a 1:1 (v/v) mixture with DCM for 30 min at RT. The product was precipitated with a 20-fold excess of ice-cold diethyl ether, centrifuged 10 min at 6000 rcf and 0 °C, and subsequently dried under vacuum at RT overnight. The purified polymers were characterized by ^{1}H-NMR spectroscopy (see Supporting Information of Chapter 4 for details).

5.2.8 Synthesis of PLA$_{10k}$-PEG$_{2k}$-maleimide

PLA$_{10k}$-PEG$_{2k}$-maleimide was synthesized as described in Chapter 4. Briefly, PLA$_{10k}$-PEG$_{2k}$-NH$_2$ was dried under vacuum at RT. N-succinimidyl 3-maleimidopropionate and triethylamine were added, and the mixture was dissolved in anhydrous ACN and stirred overnight at RT. The product was precipitated with a 20-fold excess of ice-cold diethyl ether, followed by centrifugation for 10 min at 6000 rcf and 0 °C. The polymer pellet was dried under nitrogen flow before being redissolved in ACN. This precipitation-centrifugation step was repeated twice to eliminate excess of N-succinimidyl 3-maleimidopropionate. The final product was dried under vacuum at RT overnight, and characterized by ^{1}H NMR spectroscopy (see Supporting Information of Chapter 4 for details).

5.2.9 TAT 48-57 Coupling to Polymer

TAT 48-57 coupling to the polymer was performed as described in Chapter 3. Briefly, COOH-PEG$_{2k}$-PLA$_{10k}$ was activated with EDC/NHS in anhydrous DMF and quenched with β-mercaptoethanol. Protected TAT 48-57 was added in the presence of DIPEA and reacted for 24 h at RT. The product was precipitated in ice-cold diethyl ether and dried under nitrogen overnight at RT. Subsequently, side-chain were deprotected in TFA, phenol, water, triisopropyl silane (88/5/5/2, v/v) and the product was precipitated and dried. Polymeric micelles of TAT-PEG$_{2k}$-PLA$_{10k}$ were produced by nanoprecipitation. The polymer solution was added dropwise into a 10-fold excess of vigorously stirring mQ water and the organic solvent was evaporated. Excess of TAT 48-57 and residual reagents were removed by dialysis (MWCO 6-8 kDa). The final product, TAT-PEG$_{2k}$-PLA$_{10k}$, was lyophilized, and coupling efficiency (CE) was determined by Fluram assay.

5.2.10 Fluram Assay

The CE of TAT48-57 coupling to polymer was determined by Fluorescamine assay as described in Chapter 3. Shortly, TAT-PEG$_{2k}$-PLA$_{10k}$ micelles (1 mg mL^{-1}) were produced by nanoprecipitation in mQ water. 10 µL of micelles or lysine hydrochoride (corresponding to 100 % CE) were incubated in 170 µL borate buffer (pH 8.5) for 5 min in 96-well plate while shaking at 150 rpm. 20 µL of freshly prepared fluorescamine reagent (0.3 mg mL^{-1} in aceton) was added to the mixuture and incubated at RT for 1 min. The fluorescence was measured at $\lambda_{em} = 485$ nm ($\lambda_{ex} = 380$ nm) on a FLUOstar Omega plate reader (BMG Labtech, Ortenberg, Germany). The coupling efficiency was determined by setting the measured value of TAT micelles in relation to the amount of lysine hydrochloride which corresponds to 100 % CE (see Chapter 3 Supporting Information Section S3.1.5 for details).

5.2.11 Synthesis of DEAC-NH-PEG$_{2k}$-PLA$_{10k}$

PLA$_{10k}$-PEG$_{2k}$-NH$_2$ (21.5 mg, 1.81 µmol, 1.00 equiv.) was dissolved in 200 µL DMF. Subsequently, DIPEA (2.00 µL, 11.5 µmol, 6.35 equiv.) and activated DEAC (13.0 mg mL^{-1} stock solution in DMF, 229 µL, 7.23 µmol, 4.00 equiv.) were added to the solution and stirred for four days at RT. The reaction product was first precipitated using a 20-fold excess of ice-cold diethyl ether, centrifuged for 10 min at 6000 rcf and 0 °C, and dried under a nitrogen flow overnight at RT. The dried product was subsequently dissolved in ACN, and the precipitation-centrifugation cycle with ice-cold diethyl ether was repeated twice. The coupling of DEAC to polymer was investigated by HPLC (Kinetex EVO C18, Figure S5.11). The mobile phase consisted of solvent A (mQ water with 0.05 % TFA) and solvent B (ACN with 0.05 % TFA). The flow rate was maintained at 1 mL/min. The chromatographic method initiated with an isocratic hold at 95 % A / 5 % B for 1 min, followed by a linear gradient to 5 % A / 95 % B over 15 min. The high-organic phase was maintained for 4 min, after which the system was returned to the initial conditions (95 % A / 5 % B) for column re-equilibration (5 min). Detection was carried out a diode array detector (DAD) at 220 nm and 400 nm.

5.2.12 Synthesis of Caged Polymer [TAT]$_{435}$-PEG$_{2k}$-PLA$_{10k}$

TAT-PEG$_{2k}$-PLA$_{10k}$ (49.0 mg, 3.62 µmol, 1.00 equiv.) was dissolved in the smallest possible amount of DMF. Subsequently, DIPEA (3.90 µL, 22.4 µmol, 6.18 equiv.) and activated DEAC$_{435}$ (11.5 mg, 21.38 µmol, 5.90 equiv.) were added to the solution and stirred for three days at RT. Subsequently, the reaction product was precipitated in 20-fold amount of ice-cold diethyl ether, centrifuged for 10 min at 6000 rcf and 0 °C and dried under nitrogen flow overnight at RT. The dried material was then dissolved in ACN, and the precipitation-centrifugation cycle was repeated twice. Finally, the polymer pellet was dried under vaccum at RT overnight. The coupling of $DEAC_{435}$ to polymer was proven by HPLC (XBridge ®BEH Shield RP18, Figure S5.12). The mobile phase consisted of solvent A (mQ water containing 0.05 % TFA) and solvent B (ACN containing 0.05 % TFA). The flow rate was set to $1\,\mathrm{mL\,min^{-1}}$. The chromatographic run began with an isocratic hold at 95 % A and 5 % B for 1 min, followed by a linear gradient to 5 % A and 95 % B over 5 min. This high-organic phase was maintained for 45 min, after which the system was returned to the initial conditions (95 % A and 5 % B) for column re-equilibration over 4 min. Detection was carried out with a fluorescence detector (FLD) with excitation at 400 nm and emission monitored at 500 nm

5.2.13 Synthesis of Caged Polymer $[TAT]_{435acid}$-PEG_{2k}-PLA_{10k}

TAT-PEG_{2k}-PLA_{10k} (62.7 mg, 4.66 µmol, 1.00 equiv.) was dissolved in the smallest possible amount of DMF. Subsequently, DIPEA (9.70 µL, 55.7 µmol, 12.0 equiv.) and activated $DEAC_{435acid}$ ($11.5\,\mathrm{mg\,mL^{-1}}$ stock solution in DMF/DMSO, 1.17 mL, 27.8 µmol, 6.00 equiv.) were added to the solution and stirred for three days at RT. Subsequently, purification of reaction product was achieved through three consecutive precipitation-centrifugation cycles. Finally, the polymer pellet was dried under vaccum at RT overnight. The coupling of $DEAC_{435acid}$ to polymer was investigated by HPLC (XBridge ®BEH Shield RP18, Figure S5.13). The same chromatographic method as used for $[TAT]_{435}$–PEG_{2k}–PLA_{10k} analysis was applied.

5.2.14 Spectral Characterization of DEAC and $DEAC_{435}$ Conjugates and NanoLuc

Absorption measurements were performed using a FLUOstar Omega plate reader. Therefore, 200 µL samples were transferred into quartz 96 well plate (Hellma GmbH & Co. KG, Müllheim, Germany). Emission spectrum of NanoLuc was recorded from from 380 nm to 650 nm using Cary Eclipse (Agilent Technologies, Santa Clara, CA, USA). NanoLuc (80 nM in Dulbecco's phosphate-buffered saline (DPBS) + 0.1 % bovine serum albumin (BSA) was transferred into a white 96-well plate and mixed with a 1:1000 dilution of furimazine (1:1) immediately prior to measurement.

5.2.15 Quantification of Caged Polymer

The coupling efficiency of DEAC_{435} to TAT polymer was determined by absorbance. DEAC_{435} was serially diluted in ACN to prepare equidistant concentrations ranging from $20\,\mu\text{g}\,\text{mL}^{-1}$ to $2.5\,\mu\text{g}\,\text{mL}^{-1}$. $[\text{TAT}]_{435}$-PEG_{2k}-PLA_{10k} was dissolved in ACN, reaching a final concentration of $200\,\mu\text{g}\,\text{mL}^{-1}$. Aliquots of 200 µL were transferred into a quartz 96-well plate for analysis. Absorbance was measured at $\lambda_{ex} = 433$ nm on a FLUOstar Omega plate reader. The absorption was used to calculate CE of DEAC_{435} to TAT polymer (see Supporting Information Section S5.1.7).

5.2.16 Photocleavage of DEAC and DEAC_{435}

For all uncaging experiments a light-emitting diode (LED, LED-TECH.DE optoelectronics GmbH, Moers, Germany) with $\lambda_{em} = 450$ nm and lens SM2F (Thorlabs Inc., NJ, USA) were used. The LED power was measured with FieldMax II Top laser power and energy meter (Coherent, Saxonburg, PA, USA). The samples were transferred into micro-UV-transparent cuvettes (Brand GmbH+Co KG, Wertheim, Germany) and irradiated with different powers and over different times.

The DEAC-NH-PEG_{2k}-PLA_{10k} polymer ($0.33\,\text{mg}\,\text{mL}^{-1}$, ACN) was irradiated at 100 mW for different time intervals to determine whether the limited overlap between DEAC absorption and LED emission could trigger DEAC cleavage from the polymer. The uncaging was monitored by HPLC (Kinetex EVO C18). The mobile phase consisted of solvent A (mQ water with 0.05 % TFA) and solvent B (ACN with 0.05 % TFA). The flow rate was maintained at 1 mL/min. The chromatographic method initiated with an isocratic hold at 50 % A / 50 % B for 1 min, followed by a linear gradient to 5 % A / 95 % B over 18 min. The high-organic phase was maintained for 4 min, after which the system was returned to the initial conditions (95 % A / 5 % B) for column re-equilibration. FLD with excitation at 375 nm and emission monitored at 480 nm was used for detection.

In order to determine irradiation time and energy required for photocleavage of DEAC_{435}, $[\text{TAT}]_{435}$-PEG_{2k}-PLA_{10k} was irradiated under various conditions. 15 µL of a $[\text{TAT}]_{435}$-PEG_{2k}-PLA_{10k} solution ($1\,\text{mg}\,\text{mL}^{-1}$, ACN) were used for irradiation and were diluted with 60 µL prior HPLC analysis. The uncaging was monitored by HPLC (Kinetex EVO C18) using the same chromatographic method as described above, with FLD settings adjusted to an excitation wavelength of 435 nm and emission monitored at 517 nm.

5.2.17 Nanoparticle Preparation and Characterization

Core-shell NPs were manufactured by nanoprecipitation [35]. PLGA and the corresponding poly(ethylene glycol)-*b*-poly(D,L-lactide) (PEG-PLA) copolymer were dissolved at a ratio of 30/70 (m/m) in ACN reaching a final concentration of 10 mg mL^{-1}. Within the PEG-containing fraction of photocaged DEAC$_{435}$-TAT-NP ([TAT]$_{435}$-NP), 50 % was DEAC$_{435}$-modified TAT-PEG$_{2k}$-PLA$_{10k}$ ([TAT]$_{435}$-PEG$_{2k}$-PLA$_{10k}$) while the remaining 50 % consisted of methoxy-terminated polymer chains (mPEG$_{2k}$-PLA$_{10k}$). NPs with methoxy-terminated polymer chains (mPEG-NP) served as a negative control, whereas NPs consisting of 50 % TAT-PEG$_{2k}$-PLA$_{10k}$ and 50 % mPEG$_{2k}$-PLA$_{10k}$ served as a positive control (TAT-NP). The organic phase was added dropwise into the 10-fold excess of stirring (900 rpm) 10 % DPBS. The mixture was stirred for 3 h at RT to remove the organic solvent.

Cys-NanoLuc was used for the preparation of bioluminescent and bioluminescent-responsive NP and is hereafter referred to as NanoLuc. Bioluminescent NP were composed of 10 % maleimide-functionalized PEG$_{2k}$-PLA$_{10k}$ (PLA$_{10k}$-PEG$_{2k}$-maleimide) and 90 % mPEG$_{2k}$-PLA$_{10k}$. Bioluminescent-responsive NPs were formulated with a fixed fraction of 50 % [TAT]$_{435}$-PEG$_{2k}$-PLA$_{10k}$. Maleimide-functionalized PEG$_{2k}$-PLA$_{10k}$ (PLA$_{10k}$-PEG$_{2k}$-maleimide) was used at either 2 % or 10 %, while the remaining polymer fraction was complemented with mPEG$_{2k}$-PLA$_{10k}$. The organic phase was added dropwise into a 10-fold excess of 10 % DPBS under constant stirring at 900 rpm. The aqueous phase contained a 1.2-fold molar excess of NanoLuc relative to maleimide groups. The mixture was stirred for 3 h at RT to remove the organic solvent. Subsequently, excess free NanoLuc was removed by ultrafiltration using Amicon®Ultra centrifugal filters with a MWCO of 100 kDa. The NP suspension was centrifuged at 6000 rcf and 4 °C for 5 min. Subsequently, 2 mL of 10 % DPBS was added to the retentate, and the centrifugation step was repeated. This washing procedure was performed three times in total. Finally, the sample volume was adjusted to the original volume using 10 % DPBS.

NP tracking analysis (NTA) (NanoSight NS300, Malvern, United Kingdom) was used to determinate NP size (hydrodynamic diameter, d_h) and concentration. For NTA measurements the NPs were diluted with mQ water to reach a particle concentration of 20-100 particles per frame. To evaluate the amount of NanoLuc conjugated to NPs, protein concentration was determined using the BCA assay. Zetapotential measurements were performed with Malvern Zetasizer Nano ZS (Malvern, United Kingdom). Therefore, NPs were diluted with 2 mM $NaCl_2$ by a factor of 20.

5.2.18 NanoLuc Quantification

Protein concentration was determined using the QuantiPro™BCA Protein Assay Kit according to the manufacturer's instructions. The 384-well plate was incubated at 60 °C for 60 min. Absorbance was measured at 562 nm using a FLUOstar Omega microplate reader (BMG LABTECH GmbH, Germany).

5.2.19 Stability of $[\mathrm{TAT}]_{435}$-PEG_{2k}-PLA_{10k} in the Presence of Water

HPLC (XBridge ®BEH Shield RP18) analysis was used to evaluate the integrity of $[\mathrm{TAT}]_{435}$-PEG_{2k}-PLA_{10k} in the presence of water. 15 µL polymer stock solution (40 mg mL^{-1} in ACN) was mixed with 15 µL mQ water. This mixture was, either stored under ambient light for 40 min or directly, diluted with 15 µL to dissolve any micelles that may have formed. 30 µL of three days old $[\mathrm{TAT}]_{435}$-NP were irradiated at 100 mW for 1 min and then dissolved with 30 µL ACN prior HPLC analysis. Also a non-irradiated sample of $[\mathrm{TAT}]_{435}$-NP was prepared. DEAC_{435} was used as reference (100 µg mL^{-1} in ACN). The same method as for photocleavage determination was used to analyze the samples.

5.2.20 Bioluminescence Resonance Energy Transfer on Nanoparticles

NanoLuc-NP was diluted with 10 % DPBS to a concentration corresponding to an amount equivalent to 80 nM of NanoLuc. $[\mathrm{TAT}]_{435}$-NanoLuc-NP was not diluted. 50 µL of each NP formulation was transferred in a white 96-well plate. Immediately before luminescence measurement, 50 µL of a 1:200 dilution of furimazine in DPBS was added. The spectrum was recorded from 380 nm to 650 nm. $[\mathrm{TAT}]_{435}$-NP was diluted 1:4 with 10 % DPBS and emission spectrum (460 nm to 650 nm) upon excitation at 435 nm was recorded. All emission spectra were normalized to 1. For $[\mathrm{TAT}]_{435}$-NanoLuc-NP, the peak corresponding to NanoLuc emission was set to 1. Signal smoothing was performed using the Savitzky-Golay filter (polynomial order: 2; window size: 20 points)

5.2.21 Cell Culture

HeLa cells were cultivated in Eagle's minimum essential medium (EMEM) and with 10 % fetal bovine serum (FBS).

5.2.22 Flow Cytometry

HeLa cells were seeded into 24-well plates at a concentration of 80 000 cells/well and incubated for 24 h at 37 °C and 5 % CO_2. NPs containing Cy5-PLGA were prepared and characterized. Leibovitz medium (LM) was used to adjust the NP concentration to 100 pM. The cell medium was discarded and 200 µL of NP formulation was added to each well. LM was used as cell blank. After incubation for 60 min at 37 °C, 5 % CO_2, the particle solutions were discarded, washed with 500 µL warm DPBS and the cells were harvested using 300 µL of 0.05 % trypsin/0.02 % EDTA solution. All subsequent work was done on ice. After complete cell detachment, trypsin was quenched by the addition of 400 µL EMEM + 10 % FBS and the cell suspension of each well was transferred into Eppendorf Tubes ®. After centrifugation for 5 min at 200 rcf at 4 °C, the supernatant was aspirated and the cell pellets were washed with 500 µL cold DPBS. Centrifugation step was repeated and the cell pellets were resuspended in 300 µL cold DPBS and stored on ice. Directly before the flow cytometry measurement, the cell suspension was transferred into flow cytometry tubes. The samples were analyzed using a FACS Canto II (Becton Dickinson, Franklin Lakes, NJ). NPs were excited at 633 nm, and the emission was recorded using a 661/16 nm bandpass filter. Data was analyzed using Flowing software 2.5.1 (Turku Centre for Biotechnology, Turku, Finland, with the support of Biocenter Finland).

5.3 Results and Discussion

5.3.1 Establishing a Photo-Responsive Nanoparticle System for Bioluminolysis

The greater the overlap between emission spectrum of donor and absorption spectrum of acceptor the higher are the chances for efficient BRET, which may lead to uncaging events. In this regard, the photo-responsive NPs from Chapter 3 offer unfavorable spectral characteristics in combination with NanoLuc (Figure 5.2 A). However, we evaluated whether the previously established photo-responsive NPs could be triggered by bioluminescent emission. To approximate the spectral characteristics of NanoLuc, we investigated the photocleavage of DEAC-NH-PEG$_{2k}$-PLA$_{10k}$ upon irradiation with an LED (λ_{em} = 450 nm) similar to NanoLuc emission (Figure 5.2 A). Even after irradiation for 20 min, 95 % of the polymer remained intact (Figure 5.2 B). This finding indicated that a spectrally better-matching photo-labile protecting group was required to increase the chances of BRET on the NP.

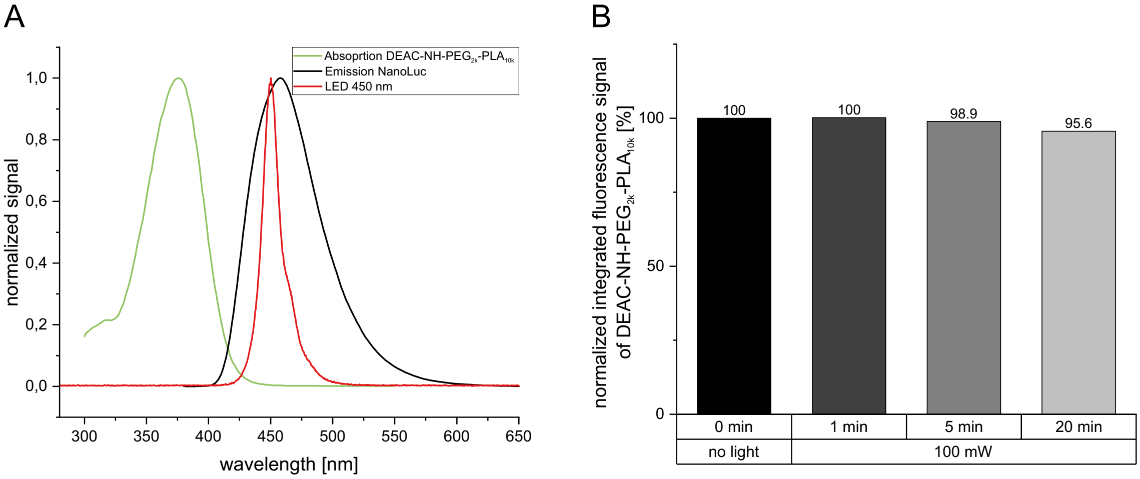

Figure 5.2: Spectral properties of DEAC-NH-PEG$_{2k}$-PLA$_{10k}$, NanoLuc and LED and photocleavage of DEAC from polymer. **A** Absorption spectrum of DEAC-NH-PEG$_{2k}$-PLA$_{10k}$ ($\lambda_{abs,max} = 376\ nm$) and emission spectrum of NanoLuc ($\lambda_{em,max} = 456\ nm$) and an LED ($\lambda_{em,max} = 450\ nm$). Individual peaks were normalized to their highest peak intensity to allow for comparison. **B** The integral of fluorescence detector (FLD) signal $\lambda_{ex} = 375\ nm$, $\lambda_{em} = 480\ nm$ at the retention time of DEAC-NH-PEG$_{2k}$-PLA$_{10k}$ as a function of different irradiation times. Irradiation experiments were performed using a LED with an emission wavelength λ_{em} = 450 nm and power of 100 mW.

5.3.2 Synthesis of DEAC$_{435}$ and Photocaged Polymer [TAT]$_{435}$-PEG$_{2k}$-PLA$_{10k}$ and Spectral Properties

In order to circumvent substantial modification of the prevailing photo-responsive NP design, the conjugation system of actual PPG DEAC was extended. Building on the synthetic strategy reported by Olson et al., we attempted to reproduce and adapt their approach [30]. Contrary to expectations, the allylation of the coumarin scaffold in step 3 proved challenging, yielding only 10 % compared to the reported 68 %. Extending the reaction time did not increase the yield. Instead, it promoted deprotection of the hydroxyl group, leading to the formation of side product **8** alongside the desired product DEAC$_{435}$ **5** (Figure S5.3). Consequently, multiple repetitions of this step were required to obtain the necessary amount of DEAC$_{435}$. All in all, we obtained 45 mg of DEAC$_{435}$ with a purity of 65 % (Figure S5.6). The activation of DEAC$_{435}$ achieved a yield of 70.5 % and a purity of 64 %. Coupling of DEAC$_{435}$ to TAT-PEG$_{2k}$-PLA$_{10k}$ proceeded with an efficiency of 64 %. The coupling efficiency (CE) was within the range reported for the previous NP design (56 %). Besides quantification of reaction yield, spectral properties of synthesized [TAT]$_{435}$-PEG$_{2k}$-PLA$_{10k}$ were measured. The absorption spectrum is depicted in Figure 5.3 A with $\lambda_{abs,max} = 433\ nm$ showing a great overlap with NanoLuc emission.

5.3.3 Photocleavage of DEAC$_{435}$

To evaluate the uncaging efficiency and assess the stability of [TAT]$_{435}$-PEG$_{2k}$-PLA$_{10k}$, a series of photolysis experiments were performed. Photocleavage of the DEAC$_{435}$ moiety from the polymer resulted in a measurable decrease in the integrated fluorescence signal of [TAT]$_{435}$-PEG$_{2k}$-PLA$_{10k}$ (Figure 5.3 B). Notably, a small fraction of DEAC$_{435}$ was already cleaved upon exposure to ambient laboratory light. This observation contrasts with the corresponding DEAC-caged polymer, which remained stable under identical conditions (Figure 3.3). Therefore, exposure to light should be minimized during handling, as complete exclusion of light is not feasible, particularly in the context of cell culture experiments. Consistent with previously reported uncaging behavior of DEAC, the uncaging yield of DEAC$_{435}$ increased with longer irradiation times and higher LED power. However, under identical irradiation conditions, DEAC$_{435}$ exhibited a notably higher degree of photocleavage compared to DEAC. This enhanced uncaging efficiency is in line with expectations and can be attributed to the higher molar absorption coefficient (ϵ_{max}: $4.3 \times 10^4\,\text{M}^{-1}\,\text{cm}^{-1}$ vs. $2.0 \times 10^4\,\text{M}^{-1}\,\text{cm}^{-1}$) and increased uncaging quantum yield (ϕ_u: 0.39 vs. 0.07) of DEAC$_{435}$ [29, 36].

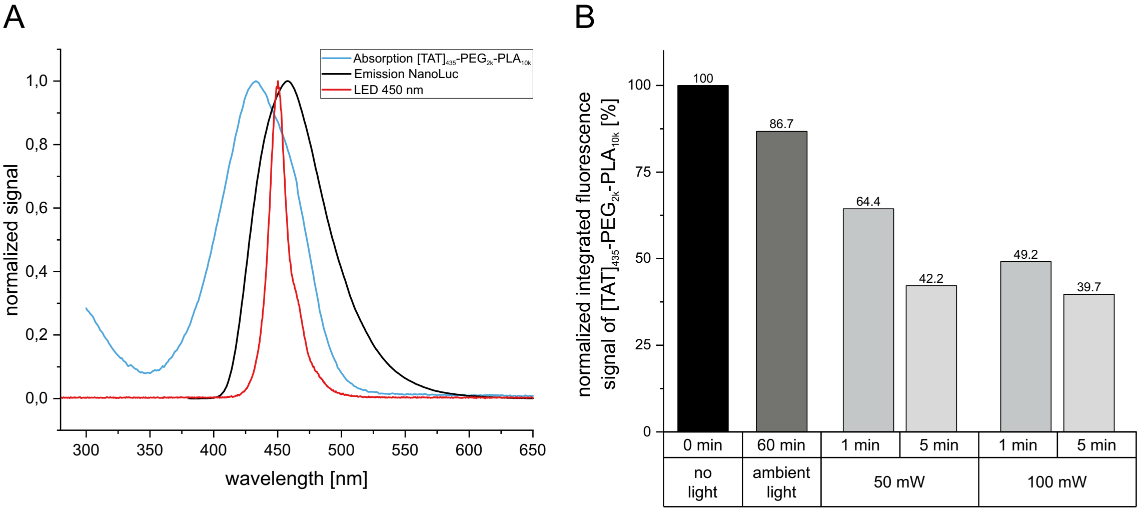

Figure 5.3: Spectral properties of $[TAT]_{435}$-PEG_{2k}-PLA_{10k}, NanoLuc and LED and photocleavage of $DEAC_{435}$ from $[TAT]_{435}$-PEG_{2k}-PLA_{10k}. **A** Absorption spectrum of $[TAT]_{435}$-PEG_{2k}-PLA_{10k} ($\lambda_{abs,max} = 433\ nm$) and emission spectrum of NanoLuc ($\lambda_{em,max} = 456\ nm$) and LED ($\lambda_{em,max} = 450\ nm$). Individual peaks were normalized to their highest peak intensity to enable comparison. **B** The integral of fluorescence detector (FLD) signal $\lambda_{ex} = 435\ nm$, $\lambda_{em} = 517\ nm$ at the retention time of $[TAT]_{435}$-PEG_{2k}-PLA_{10k} as a function of different irradiation times and LED powers. Irradiation experiments were performed using an LED with an emission wavelength $\lambda_{em} = 450\,\mathrm{nm}$.

5.3.4 $DEAC_{435}$ in Photo-Responsive Nanoparticle Design

Prior to the investigation of bioluminescent-responsive NPs, it was necessary to ascertain that the novel PPG is also capable of camouflaging the CPP characteristics of TAT-NPs. To this end, TAT-NP and $[TAT]_{435}$-NP with a degree of 50 % functionalization and methoxy-terminated polymer chain derived NP (mPEG-NP), as a control, were prepared. All NPs were characterized in terms of size and surface charge. To assess NP-cell interactions, the PLGA was labeled with the fluorescence dye Cy5. The control NP (73.1 nm) were smaller in size than TAT-NP (163 nm) and $[TAT]_{435}$-NP (148 nm), which can be explained by their composition (Figure 5.4 A). The positively charged amino acids within the TAT sequence are extensively solvated, which results in a larger hydrodynamic diameter (d_h). Although the mean d_h of the functionalized NP was significantly higher, transmission electron microscopy analysis presented in Chapter 3 revealed that the overall size distribution remained comparable to that of the control NP. Because the primary objective of this experiment was to assess whether the novel PPG could mask the NP surface charge, and since the DEAC-based photo-responsive system showed comparable size characteristics, we were not concerned about the size.

To evaluate the feasibility of $DEAC_{435}$ in the photo-responsive NP design, the surface charge was of particular interest, as it provides an accessible and informative first indication of whether the PPG can effectively mask the CPP characteristics. Based on the previous NP design, we expected the $[TAT]_{435}$-NP to exhibit a reduced positive surface charge, measured as zetapotential, relative to TAT-NP (18.0 mV). Contrary to this expectation, the $[TAT]_{435}$-NP had a positive zetapotential of 20.1 mV (Figure 5.4 B). It should be noted that zetapotential provides only an indirect indication of design feasibility and NPs may still exhibit altered behavior in cell-culture environment. Thus, the uptake respectively attachment of mPEG-, TAT- and $[TAT]_{435}$-NP to HeLa cells were studied by flow cytometry (Figure 5.4 C). Comparing the cell-associated fluorescence of non-functionalized and TAT functionalized NPs, functionalized NPs showed higher signals. Positively charged TAT-NP showed a 35-fold higher uptake in HeLa cells compared to TAT-free mPEG-NP. HeLa cells incubated with $[TAT]_{435}$-NP exhibited slightly lower cell-associated fluorescence than those treated with TAT-NP, although this difference was minimal. In contrast, DEAC-caged NPs in the previous study exhibited a significantly reduced interaction with HeLa cells, as demonstrated by a decrease in cell-associated fluorescence to approximately 50 % (Figure 3.5).

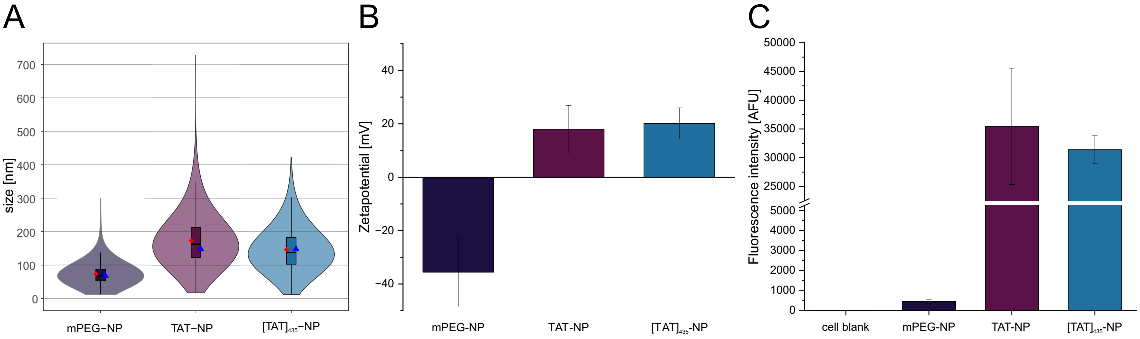

Figure 5.4: Characterization of NPs and cell-interaction study. **A** Violin plots represent size distribution of hydrodynamic diameter. The median NP size is shown as horizontal line within the box, whose lower and upper edges represent the first (Q1) and third (Q3) quartiles, respectively. Whiskers indicate the most extreme data points within 1.5 times the interquartile range from the lower and upper quartiles. The mean is represented by a red rectangle and the mode is depicted by a blue triangle. The measures of central tendency followed order mean, median and mode. mPEG-NP: 73.1 nm, 67.5 nm, 67.5 nm; TAT-NP: 173 nm, 163 nm, 148 nm; $[TAT]_{435}$-NP: 146 nm, 138 nm, 148 nm. **B** Zetapotenial. Data represent mean ± pooled SD of three measurements. **C** Results from flow cytometry experiment. Data represent mean ± SD (n = 3). AFU, arbitrary fluorescence units.

Taken together, the incorporation of $DEAC_{435}$ into our NP design did not alter its physicochemical or biological properties. Consequently, this novel PPG is not suitable for the development of a bioluminescent-responsive NP system.

A possible explanation for its failure as a PPG could be a loss of integrity of the caged polymer. The stability of $[TAT]_{435}$-PEG_{2k}-PLA_{10k} has been investigated in organic solvent. During NP preparation the polymer is exposed to water, which may compromise the integrity of the photocaged structure. This is consistent with literature reports demonstrating that water strongly influences coumarin-based photocleavage pathways [37, 38]. Upon photon absorption, the coumarin photocage bearing its leaving group (C-LG) is excited to [C-LG]* (Scheme 2). Deactivation through fluorescence and non-radiative processes, with rate constants k_{fl} and k_{nr}, compete with heterolytic bond cleavage, which generates the contact ion pair (CIP) [C^+ LG^-] with rate constant k_1. The resulting CIP intermediate can undergo two pathways. It can either recombine to form C-LG with rate constant k_{rec}, or it can dissociate into a solvent separated ion pair (not shown) followed by water trapping, which quenches the carbocation (C-OH), with rate constant k_2. The integrity of $[TAT]_{435}$-PEG_{2k}-PLA_{10k} was evaluated under aqueous conditions and after NP formulation (Figure 5.5). The caged polymer treated with mQ water and analyzed immediately served as a positive control, confirming the structural integrity of the protected polymer. In contrast, exposure of the caged polymer to mQ water under ambient light resulted in partial degradation. Analysis of the polymer recovered from the prepared TAT-NPs showed that most of the caged polymer remained stable during NP formulation in aqueous solution. Therefore, the failure of the PPG must originate from a different cause.

We hypothesized that the sterically demanding tert-butyl protecting group of $DEAC_{435}$ may hinder the orientation of $[TAT]_{435}$ towards the hydrophobic PLGA core. To address this potential limitation, we subsequently redesigned the PPG and removed the protecting group.

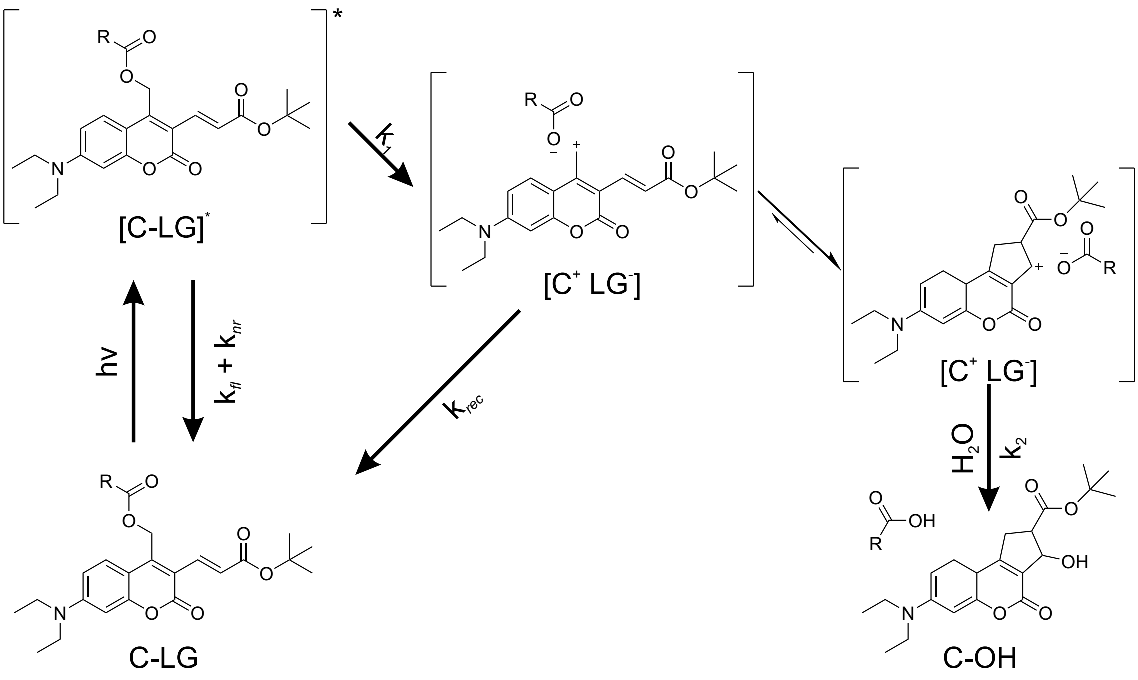

Scheme 2: Schematic representation of the coumarin photocleavage mechanism, adapted from the work of Schmidt et al. and Clotworthy et al. [38, 39].

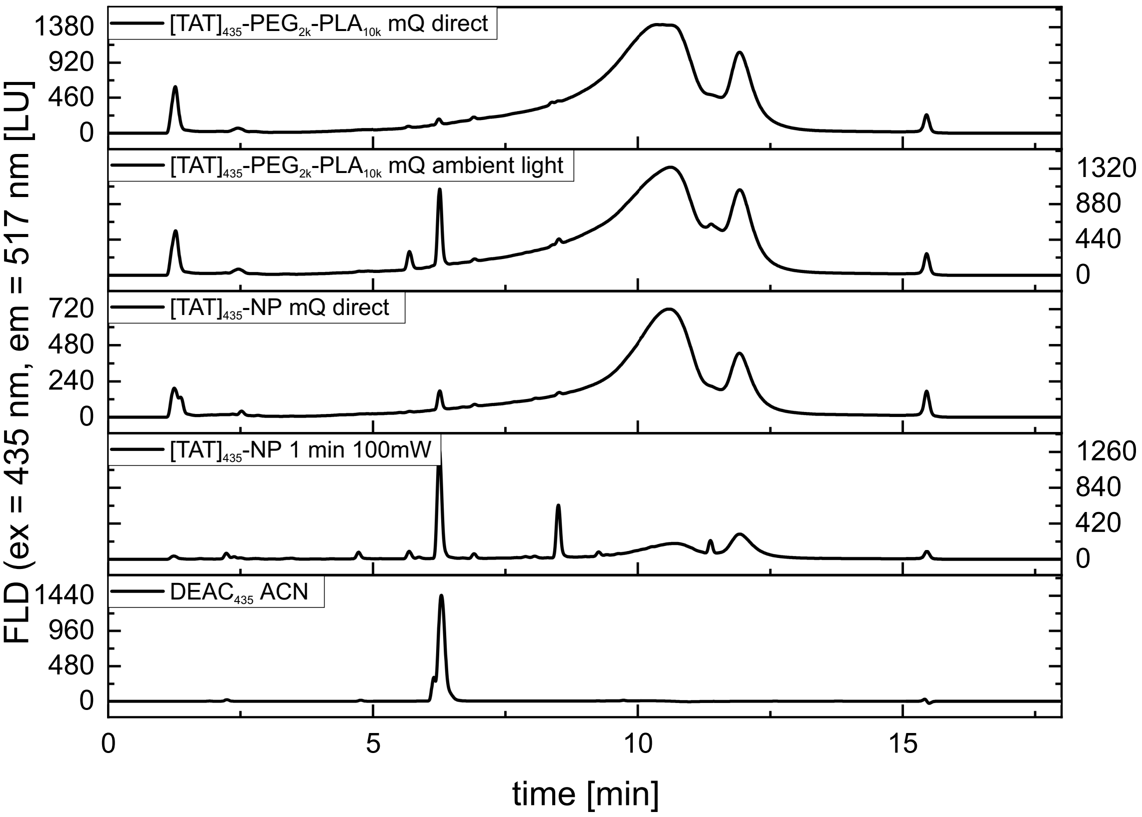

Figure 5.5: RP-HPLC analysis of $[TAT]_{435}$-PEG_{2k}-PLA_{10k} and $[TAT]_{435}$-NP under different conditions. $DEAC_{435}$ was included as a reference and $[TAT]_{435}$-NP (1 min, 100 mW) served as a control for photocleavage. $[TAT]_{435}$-NP analyzed immediately after preparation showed a small peak at the retention time of $DEAC_{435}$ indicating minor degree of photocleavage. However, the majority of $[TAT]_{435}$-PEG_{2k}-PLA_{10k} remained intact. Fluorescence detector, FLD; Luminescence units, LU.

5.3.5 Synthesis of $\mathrm{DEAC}_{435acid}$ and Coupling to TAT-PEG_{2k}-PLA_{10k}

In addition to the absence of the bulky protecting group, the newly exposed carboxylic acid may offer an advantage for masking the positive charge, as it is expected to exist in its deprotonated, negatively charged form in the vicinity of the basic amino acids within the TAT motif. $\mathrm{DEAC}_{435acid}$ was synthesized directly in its activated form for coupling by deprotecting the activated DEAC_{435}. The integrity of activated $\mathrm{DEAC}_{435acid}$ was confirmed by MS and ^{1}H-NMR (Figure S5.10). The coupling to TAT-PEG_{2k}-PLA_{10k} was insufficient (Figure S5.13). Thus, the suitability of $\mathrm{DEAC}_{435acid}$ as PPG for photo-responsive NP could not be evaluated.

5.3.6 Evaluation of BRET on NP

Hypothetically, if DEAC_{435} were to mask the charge as effectively as DEAC, the next logical step was to investigate its deprotection behavior. The photosensitivity of the photocage was demonstrated through external LED irradiation. In bioluminescent-responsive NPs, however, the energy for bond cleavage is provided by BRET. The resulting bioluminescent and photocaged NP, $[\mathrm{TAT}]_{435}$-NanoLuc-NP, displayed emission peaks corresponding to both NanoLuc and DEAC_{435} upon addition of luciferin (Figure 5.6 A), demonstrating the occurrence of BRET in this design. As described in Scheme 2, excitation of DEAC_{435} can result either in fluorescence (k_{fl}), as visible in the spectrum, or in bond cleavage. Given the high uncaging yield and the efficient photocleavage proven by LED irradiation, BRET-induced bond cleavage in this design is highly likely [21]. The actual amount of NanoLuc exposed on the surface of the NP could not be determined by BCA assay as the amino acid sequence of TAT interfered with the quantification. Therefore, we assumed a coupling efficiency of approximately 50 %, as evaluated for Cys-NanoLuc-NP in the previous chapter, resulting in $[\mathrm{TAT}]_{435}$-NanoLuc-NP formulations with 1 % or 5 % NanoLuc on the NP. The emission spectra of NPs were normalized to the NanoLuc emission peak. When comparing both $[\mathrm{TAT}]_{435}$-NanoLuc-NP formulations (Figure 5.6 A), the NP containing 1 % NanoLuc showed a weaker NanoLuc signal relative to DEAC_{435} emission than those containing up to 5 % NanoLuc. This could be misinterpreted as higher BRET efficiency in the NPs containing 1 % NanoLuc. However, the increased amount of NanoLuc merely produces a stronger luminescence signal. Therefore, the relative emission intensities do not provide information on BRET efficiency or on the number of DEAC_{435} molecules actually reached by the donor on the NP. To address this, the donor-acceptor distance on the NP must be evaluated.

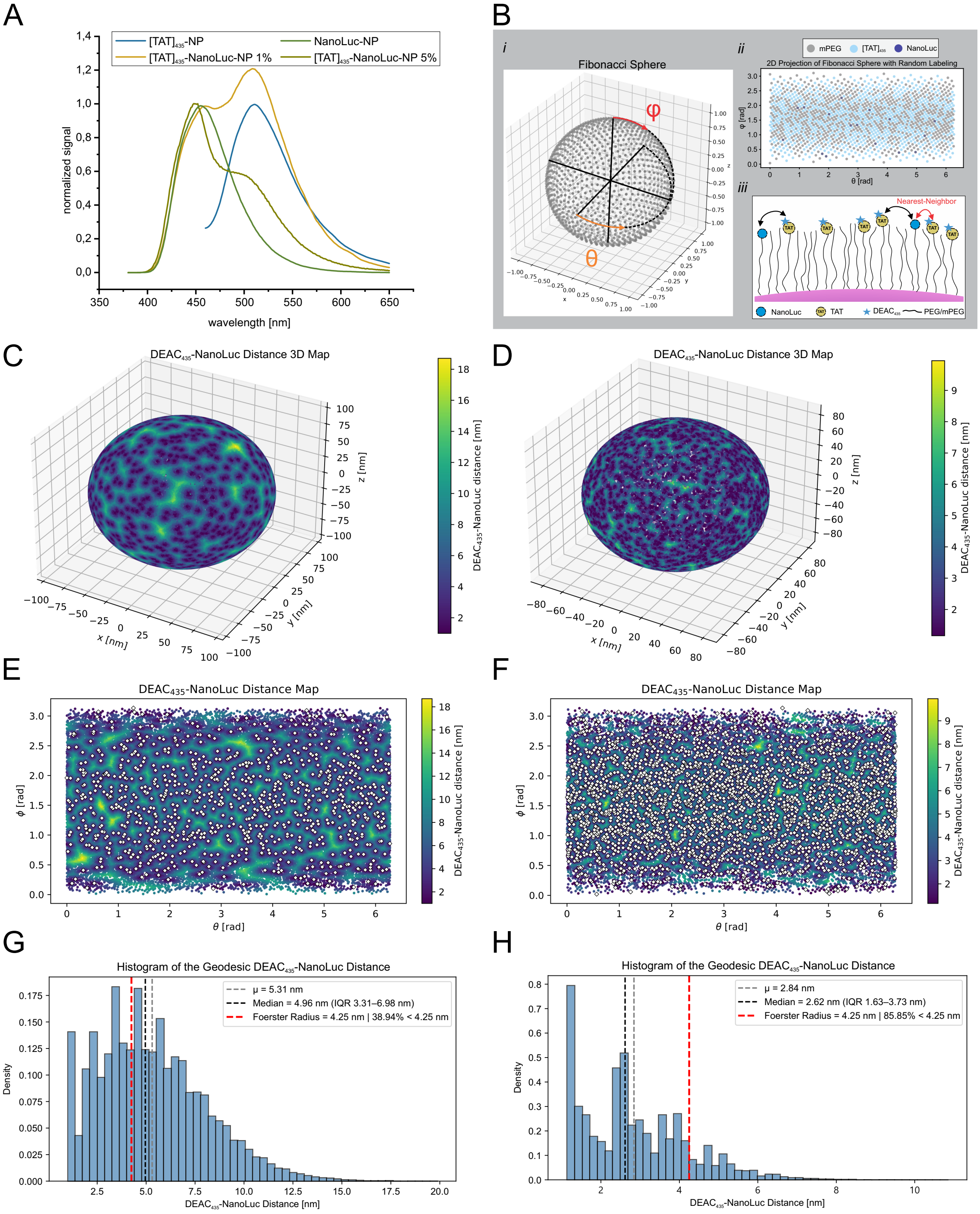

Figure 5.6: Characterization of BRET on [TAT]$_{435}$-NanoLuc-NP. **A** Spectral characterization of NPs. All NanoLuc containing NP were normalized to NanoLuc emission maximum ($\lambda_{em,max} = 456\ nm$). [TAT]$_{435}$-NP were normalized to DEAC$_{435}$ emission maximum ($\lambda_{em,max} = 511\ nm$). [TAT]$_{435}$-NanoLuc-NP formulations exhibit, in addition to the characteristic NanoLuc emission peak, a distinct DEAC$_{435}$ emission signal, demonstrating efficient BRET-mediated excitation of the DEAC$_{435}$ fluorophore.

B Schematic illustration of modeling BRET pair Nanoluc-DEAC$_{435}$ distance on NP surface. *i* Deterministic placement of evenly spaced PEG anchoring sites (gey dots on Fibonacci sphere). *ii* 2D Projection of Fibonacci sphere with Monte Carlo labeling. Random assignment of PEG endgroups, methoxy terminated (mPEG, grey), [TAT]$_{435}$ (light blue) and NanoLuc (marine blue) to fixed sites according to experimental fractions. *iii* Compute nearest-neighbor geodesic distances between [TAT]$_{435}$ and NanoLuc.**C, E, G** represent the modeling results for [TAT]$_{435}$-NanoLuc-NP containing 1 % NanoLuc, whereas **D, F, G** show the corresponding results for [TAT]$_{435}$-NanoLuc-NP containing 5 % NanoLuc. **C** and **D** show the three-dimensional reconstruction of the NP surface for a representative Monte Carlo simulation, generated from the Cartesian coordinates (x_i, y_i, z_i) of the [TAT]$_{435}$ ligands. Ligand positions were color-mapped according to their geodesic [TAT]$_{435}$→NanoLuc distance using a continuous distance-encoded scale. **E** and **F** show the two-dimensional surface projection of the same representative Monte Carlo simulation, obtained by mapping the angular coordinates (θ_i, ϕ_i) of the [TAT]$_{435}$ ligands. Each ligand is color-coded by its nearest-neighbor [TAT]$_{435}$→NanoLuc distance, with NanoLuc moieties marked as white diamonds. **G** and **H** represent the geodestic [TAT]$_{435}$→NanoLuc distance of all Monte Carlo simulations, visualized as a histogram. The mean nearest-neighbor distance is marked by a grey dotted line. The median nearest-neighbor distance is indicated by a black dotted line, and the interquartile range (IQR) is reported in the legend. The red dotted line indicates the Foerster radius (R_0) of the BRET pair Nanoluc-DEAC$_{435}$. The fraction of donor-acceptor pairs falling below R_0 threshold is reported in the legend.

5.3.7 Computational Assessment of BRET Donor-Acceptor Distances on Nanoparticle Surface

The donor-acceptor distance is the key determinant of BRET efficiency. The Foerster radius (R_0) represents the critical distance at which energy transfer reaches 50 %. At greater distances, efficiency decreases at a rate proportional to the inverse sixth power of the distance, thereby significantly reducing the probability of BRET. Calculation of R_0 for the NanoLuc-DEAC$_{435}$ donor-acceptor pair yielded a value of 4.25 nm (Section S5.2).

For the 1 % [TAT]$_{435}$-NanoLuc-NPs with d_h of 187 nm, the area occupied by a single PEG chain (S) was calculated as 1.11 nm^2, resulting in a PEG-PEG spacing of D = 1.19 nm (Supporting Information, Equations (5.8) and (5.9)). In the NP formulation containing 5 % NanoLuc (d_h = 162 nm), S increased to 1.51 nm^2, corresponding to a spacing of D = 1.39 nm. Although these values describe the average packing of PEG chains on the NP surface, they are not the decisive parameters for evaluating BRET efficiency. However, these values do confirm brush conformation of PEG chains on the NP surface, an important assumption for further modeling.

More relevant is the spatial separation between the randomly distributed NanoLuc donors and the [TAT]$_{435}$-functionalized PEG chains carrying DEAC$_{435}$ acceptors. To estimate the lateral proximity between NanoLuc and DEAC_{435}, the PEG anchoring sites on a spherical NP were generated by Fibonacci-sphere distribution and the different polymers were assigned corresponding to their experimental molar ratios using Monte Carlo sampling (Figure 5.6 B). Thereby, being able to calculate the geodesic distance between each $[\mathrm{TAT}]_{435} \rightarrow$NanoLuc. The resulting distance distributions allowed quantification of the fraction of NanoLuc positioned within the Foerster radius, which is required for efficient BRET. For further information on modeling and calculation see Section S5.3.2.

For the 1 % NanoLuc formulation, the calculated median donor-acceptor distance was approximately 4.96 nm, which is larger than R_0 and therefore indicative of limited BRET efficiency on average. Nevertheless, the heatmap (Figure 5.6 C, E) and distance distribution histogram (Figure 5.6 G) show that a substantial fraction (38.9 %) of donor-acceptor pairs, fall below R_0, demonstrating that localized BRET events remain likely despite the overall larger mean spacing. In contrast, the 5 % NanoLuc formulation exhibited a significantly shorter median donor-acceptor distance of 2.62 nm. Caused by the higher amount of NanoLuc, 85.9 % of DEAC_{435} acceptors had a NanoLuc donor within sub-foerster radius proximity, creating substantially more favorable conditions for efficient BRET across the entire NP surface.

The simulation provides an idealized estimate of donor-acceptor spacing and should be interpreted with caution. It assumes a perfectly spherical NP with homogeneous PEG packing, although real particles may exhibit local curvature and PEG heterogeneity due to mixed end groups. Geodesic distances also treat ligands as surface points and therefore do not account for the three-dimensional size of NanoLuc or the internal position of its active site. Although the use of the hydrodynamic radius partially mitigates this by approximating the outer shell of the NP. So, the true donor-acceptor separation is likely larger than the simulated distance. However, the simulation still provides a useful estimate for assessing whether the spatial separation is sufficiently small for NanoLuc to uncage all nearby $[\mathrm{TAT}]_{435}$ sites.

5.3.8 Conclusion

In this study, we synthesized a $DEAC_{435}$ with spectral properties favorable for BRET with NanoLuc and successfully conjugated it to TAT functionalized polymer. $DEAC_{435}$ exhibited improved photocleavage from polymer under external irradiation compared to DEAC, increasing the likelihood of bond cleavage upon BRET excitation. However, $DEAC_{435}$ photocaged NPs were unable to mask the TAT-properties of NPs, as indicated by comparable zetapotentials and cellular interaction relative to TAT-NP. These findings highlight that replacing a PPG is not as trivial as initially assumed. The intrinsic physicochemical properties of a PPG appear to strongly influence its functional performance, implying that the choice of PPG must be tailored to the specific application. For applications where the PPG merely inhibit the ligand receptor interaction, e.g. binding of cRGD to integrins, rather than masking charge, $DEAC_{435}$ might be a suitable candidate [40, 41]. Nevertheless, our results demonstrate that NanoLuc is capable of exciting $DEAC_{435}$ on the NP surface through BRET. This confirms the fundamental feasibility of a bioluminescent-triggered NP design and suggests that the overall concept remains valid.

References

[1] Mahdi Karimi et al. “Smart Nanostructures for Cargo Delivery: Uncaging and Activating by Light”. In: *Journal of the American Chemical Society* 139.13 (2017), pp. 4584–4610. DOI: `10.1021/jacs.6b08313`.

[2] Wei Zhao et al. “Remote Light-Responsive Nanocarriers for Controlled Drug Delivery: Advances and Perspectives”. In: *Small (Weinheim an der Bergstrasse, Germany)* 15.45 (2019), e1903060. DOI: `10.1002/smll.201903060`.

[3] Jinzhao Liu, Weirong Kang, and Weiping Wang. “Photocleavage-based Photoresponsive Drug Delivery”. In: *Photochemistry and photobiology* 98.2 (2022), pp. 288–302. DOI: `10.1111/php.13570`.

[4] Alina Y. Rwei, Weiping Wang, and Daniel S. Kohane. “Photoresponsive nanoparticles for drug delivery”. In: *Nano today* 10.4 (2015), pp. 451–467. ISSN: 1748-0132. DOI: `10.1016/j.nantod.2015.06.004`.

[5] Qian Liu et al. “Enhanced Precision of Nanoparticle Phototargeting in Vivo at a Safe Irradiance”. In: *Nano letters* 16.7 (2016), pp. 4516–4520. DOI: `10.1021/acs.nanolett.6b01730`.

[6] Kaiqi Long et al. “One-photon red light-triggered disassembly of small-molecule nanoparticles for drug delivery”. In: *Journal of nanobiotechnology* 19.1 (2021), p. 357. DOI: `10.1186/s12951-021-01103-z`.

[7] Caerwyn Ash et al. “Effect of wavelength and beam width on penetration in light-tissue interaction using computational methods”. In: *Lasers in medical science* 32.8 (2017), pp. 1909–1918. DOI: `10.1007/s10103-017-2317-4`.

[8] Louise Finlayson et al. “Depth Penetration of Light into Skin as a Function of Wavelength from 200 to 1000 nm”. In: *Photochemistry and photobiology* 98.4 (2022), pp. 974–981. DOI: `10.1111/php.13550`.

[9] Yanfei Wang et al. “Intravenous treatment of choroidal neovascularization by photo-targeted nanoparticles”. In: *Nature communications* 10.1 (2019), p. 804. DOI: `10.1038/s41467-019-08690-4`.

[10] Lorenzo Guidi, Maria Grazia Cascone, and Elisabetta Rosellini. “Light-responsive polymeric nanoparticles for retinal drug delivery: design cues, challenges and future perspectives”. In: *2405-8440* 10.5 (), e26616. ISSN: 2405-8440. DOI: `10.1016/j.heliyon.2024.e26616`.

[11] Hao Xiong et al. “Photo-controllable biochemistry: Exploiting the photocages in phototherapeutic window”. In: *Chem* 9.1 (2023), pp. 29–64. ISSN: 24519294. DOI: `10.1016/j.chempr.2022.11.007`.

[12] Jeremy P. Olson et al. “Spectral evolution of a photochemical protecting group for orthogonal two-color uncaging with visible light”. In: *Journal of the American Chemical Society* 135.42 (2013), pp. 15948–15954. DOI: `10.1021/ja408225k`.

[13] XiangYang Xie et al. “Photolabile-caged peptide-conjugated liposomes for siRNA delivery”. In: *Journal of drug targeting* 23.9 (2015), pp. 789–799. DOI: `10.3109/1061186X.2015.1009077`.

[14] Junhui Shi et al. “Ultralow-intensity NIR light triggered on-demand drug release by employing highly emissive UCNP and photocleavable linker with low bond dissociation energy”. In: *International journal of nanomedicine* 14 (2019), pp. 4017–4028. DOI: `10.2147/IJN.S201982`.

[15] Mengxue Zhou et al. “Light-Triggered PEGylation/dePEGylation of the Nanocarriers for Enhanced Tumor Penetration”. In: *Nano letters* 19.6 (2019), pp. 3671–3675. DOI: `10.1021/acs.nanolett.9b00737`.

[16] Yi-Hsin Chien et al. “Near-infrared light photocontrolled targeting, bioimaging, and chemotherapy with caged upconversion nanoparticles in vitro and in vivo”. In: *ACS nano* 7.10 (2013), pp. 8516–8528. DOI: `10.1021/nn402399m`.

[17] Sung-Bae Kim and Tadaomi Furuta. “Bioluminescence from the bright and dark sides”. In: *Frontiers in Chemical Biology* 3 (2024). DOI: `10.3389/fchbi.2024.1459397`.

[18] Anna C. Love and Jennifer A. Prescher. “Seeing (and Using) the Light: Recent Developments in Bioluminescence Technology”. In: *Cell chemical biology* 27.8 (2020), pp. 904–920. DOI: `10.1016/j.chembiol.2020.07.022`.

[19] Barbara Roda et al. “Shining light on biosensors: Chemiluminescence and bioluminescence in enabling technologies”. In: *TrAC Trends in Analytical Chemistry* 180 (2024), p. 117975. ISSN: 01659936. DOI: `10.1016/j.trac.2024.117975`.

[20] Dalu Chang et al. “Luciferase-Induced Photouncaging: Bioluminolysis”. In: *Angewandte Chemie (International ed. in English)* 58.45 (2019), pp. 16033–16037. DOI: `10.1002/anie.201907734`.

[21] Dalu Chang et al. "Luciferase Controlled Protein Interactions". In: *Journal of the American Chemical Society* 143.10 (2021), pp. 3665–3670. DOI: `10.1021/jacs.0c11016`.

[22] Eric Lindberg et al. "Luciferase-induced photoreductive uncaging of small-molecule effectors". In: *Nature communications* 9.1 (2018), p. 3539. DOI: `10.1038/s41467-018-05916-9`.

[23] Jan Birringer et al. "Coumarin-Caged Nanoparticle for Light-Driven Surface Modification". In: *ChemMedChem* 20.22 (2025), e202500636. DOI: `10.1002/cmdc.202500636`.

[24] Mary P. Hall et al. "Engineered luciferase reporter from a deep sea shrimp utilizing a novel imidazopyrazinone substrate". In: *ACS chemical biology* 7.11 (2012), pp. 1848–1857. DOI: `10.1021/cb3002478`.

[25] Christopher G. England, Emily B. Ehlerding, and Weibo Cai. "NanoLuc: A Small Luciferase Is Brightening Up the Field of Bioluminescence". In: *Bioconjugate Chemistry* 27.5 (2016), pp. 1175–1187. DOI: `10.1021/acs.bioconjchem.6b00112`.

[26] Mark A. Klein et al. "Luciferase Calibrants Enable Absolute Quantitation of Bioluminescence Power". In: *ACS measurement science au* 3.6 (2023), pp. 496–503. DOI: `10.1021/acsmeasuresciau.3c00036`.

[27] Francesco Russo, Beatrice Civili, and Nicolas Winssinger. "Bright Red Bioluminescence from Semisynthetic NanoLuc (sNLuc)". In: *ACS chemical biology* 19.5 (2024), pp. 1035–1039. DOI: `10.1021/acschembio.4c00033`.

[28] Th. Förster. "Zwischenmolekulare Energiewanderung und Fluoreszenz". In: *Annalen der Physik* 437.1-2 (1948), pp. 55–75. ISSN: 0003-3804. DOI: `10.1002/andp.19484370105`.

[29] Hitesh K. Agarwal et al. "Intracellular Uncaging of cGMP with Blue Light". In: *ACS chemical neuroscience* 8.10 (2017), pp. 2139–2144. DOI: `10.1021/acschemneuro.7b00237`.

[30] Jeremy P. Olson et al. "Optically selective two-photon uncaging of glutamate at 900 nm". In: *Journal of the American Chemical Society* 135.16 (2013), pp. 5954–5957. DOI: `10.1021/ja4019379`.

[31] Joseph M. Amatrudo et al. "Wavelength-selective one- and two-photon uncaging of GABA". In: *ACS chemical neuroscience* 5.1 (2014), pp. 64–70. DOI: `10.1021/cn400185r`.

[32] Timo Weinrich et al. “Synthesis of a Cytidine Phosphoramidite with Protected Nitroxide Spin Label for EPR Experiments with RNA”. In: *European Journal of Organic Chemistry* 2017.3 (2017), pp. 491–496. ISSN: 1434-193X. DOI: `10.1002/ejoc.201601174`.

[33] Haitao Qian et al. “A Strategy for Control of "Random" Copolymerization of Lactide and Glycolide: Application to Synthesis of PEG-b-PLGA Block Polymers Having Narrow Dispersity”. In: *Macromolecules* 44.18 (2011), pp. 7132–7140. ISSN: 0024-9297. DOI: `10.1021/ma201169z`.

[34] Kathrin Abstiens and Achim M. Goepferich. “Microfluidic manufacturing improves polydispersity of multicomponent polymeric nanoparticles”. In: *Journal of Drug Delivery Science and Technology* 49 (2019), pp. 433–439. ISSN: 17732247. DOI: `10.1016/j.jddst.2018.12.009`.

[35] Christine Vauthier and Kawthar Bouchemal. “Methods for the preparation and manufacture of polymeric nanoparticles”. In: *1573-904X* 26.5 (2009), pp. 1025–1058. ISSN: 1573-904X. DOI: `10.1007/s11095-008-9800-3`.

[36] Renjie Zhou et al. “Visible-light activatable coumarin-based phototriggers for fluorescence imaging with ultra-high photolysis efficiency”. In: *Physical chemistry chemical physics : PCCP* 25.16 (2023), pp. 11176–11184. DOI: `10.1039/D2CP05807C`.

[37] Albert M. Schulte et al. “Strategy for Engineering High Photolysis Efficiency of Photocleavable Protecting Groups through Cation Stabilization”. In: *Journal of the American Chemical Society* 144.27 (2022), pp. 12421–12430. DOI: `10.1021/jacs.2c04262`.

[38] Reinhard Schmidt et al. “Mechanism of photocleavage of (coumarin-4-yl)methyl esters”. In: *The journal of physical chemistry. A* 111.26 (2007), pp. 5768–5774. DOI: `10.1021/jp071521c`.

[39] Megan R. Clotworthy et al. “Coumarin-Derived Caging Groups in the Spotlight: Tailoring Physiochemical and Photophysical Properties”. In: *ChemPlusChem* 89.10 (2024), e202400377. DOI: `10.1002/cplu.202400377`.

[40] Weiping Wang et al. “Efficient Triplet-Triplet Annihilation-Based Upconversion for Nanoparticle Phototargeting”. In: *Nano letters* 15.10 (2015), pp. 6332–6338. DOI: `10.1021/acs.nanolett.5b01325`.

[41] Albert Gandioso et al. “A Green Light-Triggerable RGD Peptide for Photocontrolled Targeted Drug Delivery: Synthesis and Photolysis Studies”. In: *The Journal of organic chemistry* 81.23 (2016), pp. 11556–11564. DOI: `10.1021/acs.joc.6b02415`.

Supporting Information
Chapter 5

S5.1 Synthesis and Characterization

S5.1.1 Synthesis of 7-(diethylamino)-(4-hydroxymethyl)-[(E)-3-(tert-butoxycarbonyl)prop-2-enyl]coumarin (DEAC$_{435}$)

7-(diethylamino)-4-(((tert-butyldimethylsilyl)oxy)methyl)coumarin (2)

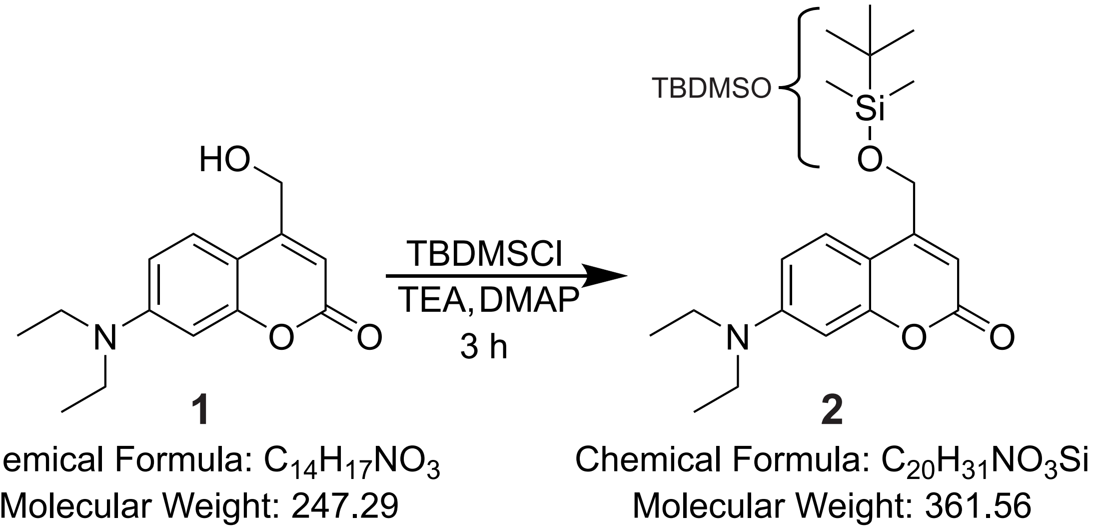

Scheme S5.1: Reaction equation for synthesis of 7-(diethylamino)-4-(((tert-butyldimethylsilyl)oxy)methyl)coumarin (**2**)

7-(diethylamino)-4-(hydroxymethyl)coumarin (**1**) (200 mg, 809 µmol, 1.00 equiv.) was dissolved in anhydrous dichlormethane (DCM; 8 mL). Tert-butyldimethylchlorosilane (TBDMSCl; 181.5 mg, 1.20 mmol, 1.49 equiv.) was also dissolved in DCM (2 mL) and was added to **(1)**. Subsequently, triethylamine (TEA; 169.2 µL, 1.21 mmol, 1.50 equiv.) and dimethylaminopyridine (DMAP; 5.2 mg, 4.26 µmol, 0.05 equiv.) were added to the reaction mixture and stirred for 3 h at RT. The reaction was quenched by addition of saturated NH_4Cl (6 mL) and extracted into ethyl acetate (3x 10 mL). Organic layers were combined, silica (2 g) was added and solvent was removed under reduced pressure. The crude material was then purified by column chromatography (90:10, hexane:ethyl acetate) to obtain (**2**) as an off-white solid.

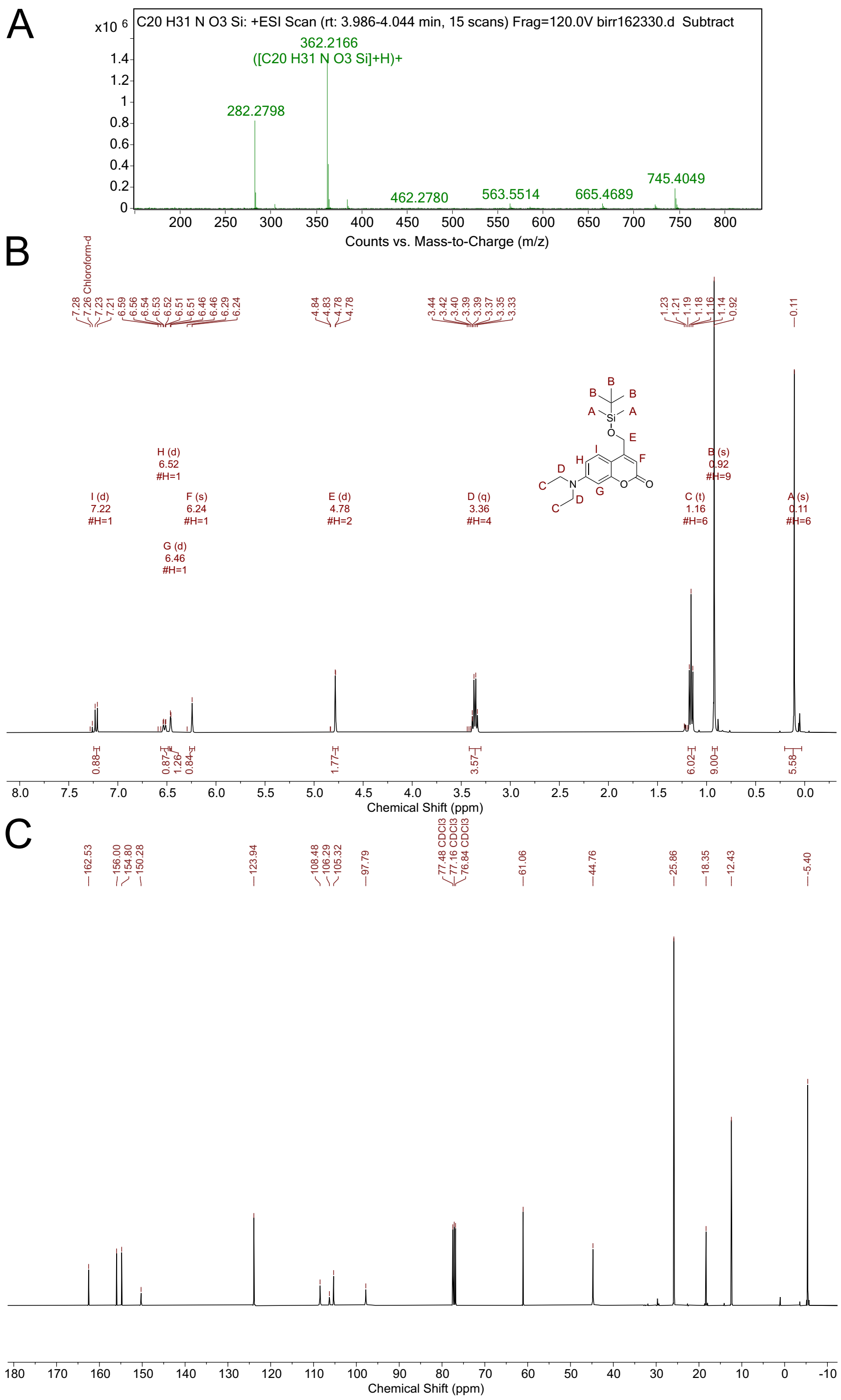

Figure S5.1: Mass spectrum and NMR spectra of 7-(diethylamino)-4-(((tert-butyldimethylsilyl)oxy)methyl)coumarin (**2**).

A MS (ESI) m/z calculated for $C_{20}H_{31}NO_3Si + H^+$: 362.21, found: 362.2166.

B ^{1}H-NMR (400 MHz, $CDCl_3$) δ(ppm) 7.22 (d, J = 9.0 Hz, 1H), 6.52 (d, J = 11.1 Hz, 1H), 6.46 (d, J = 2.3 Hz, 1H), 6.24 (s, 1H), 4.78 (d, J = 1.4 Hz, 2H), 3.36 (q, J = 7.1 Hz, 4H), 1.16 (t, J = 7.1 Hz, 6H), 0.92 (s, 9H), 0.11 (s, 6H).

C ^{13}C-NMR (101 MHz, $CDCl_3$) δ(ppm) 162.53, 156.00, 154.80, 150.28, 123.94, 108.48, 106.29, 105.32, 97.79, 77.48, 77.16, 76.84, 61.06, 44.76, 25.86, 18.35, 12.43, -5.40.

3-bromo-7-(diethylamino)-4-(((tert-butyldimethylsilyl)oxy)methyl)coumarin (**3**)

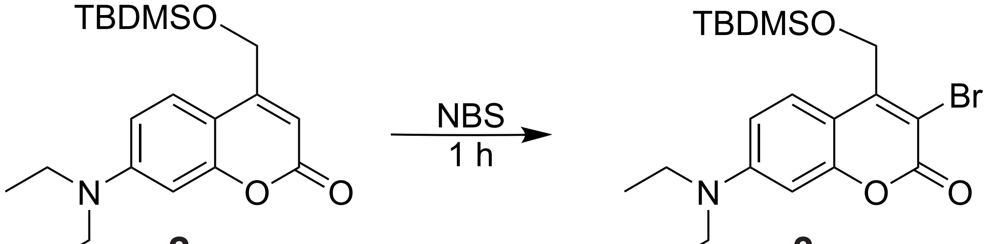

2

3

Chemical Formula: $C_{20}H_{31}NO_3Si$
Molecular Weight: 361.56

Chemical Formula: $C_{20}H_{30}BrNO_3Si$
Molecular Weight: 440.45

Scheme S5.2: Reaction equation for synthesis of 3-bromo-7-(diethylamino)-4-((-(tert-butyldimethylsilyl)oxy)methyl)coumarin (**3**)

To a solution of 7-(diethylamino)-4-(((tert-butyldimethylsilyl)oxy)methyl)coumarin (**2**) (245 mg, 678 µmol, 1.00 equiv.) in acetonitrile (ACN; 4 mL), N-Bromosuccinimide (NBS; 133 mg, 747 µmol, 1.10 equiv.) was added. Then, ammonium acetate (5.3 mg, 6.78 µmol, 0.10 equiv.) was added and the reaction was stirred for 1 h at RT. The reaction was then stopped by the addition of water (10 mL). The aqueous phase was extracted with ethyl acetate (3x 20 mL). Organic layers were combined, silica (2 g) was added and solvent was removed under reduced pressure. Purification by silica gel chromatography (80:20, hexane:ethyl acetate) gave title compound (**3**) as a yellow solid.

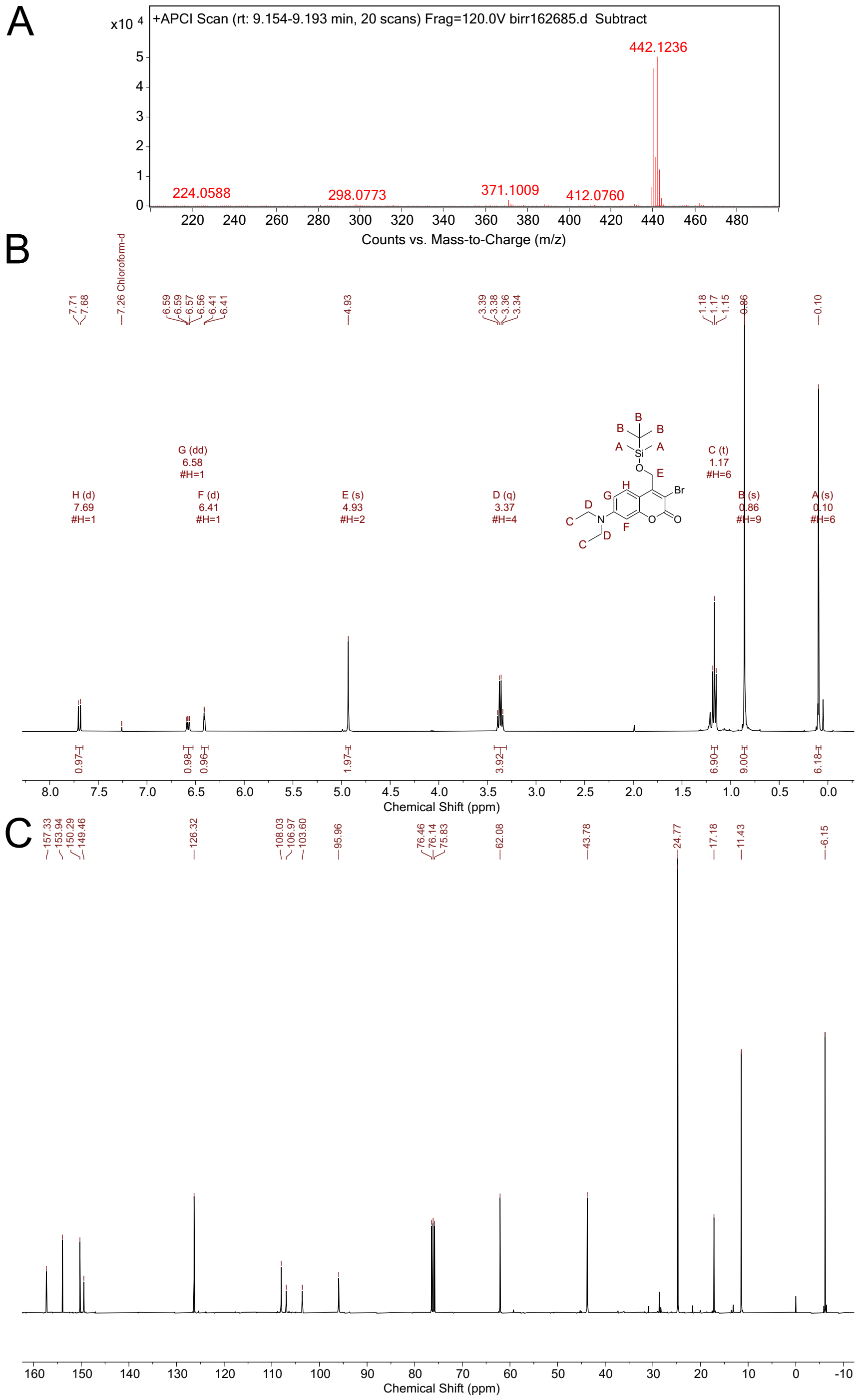

Figure S5.2: Mass spectrum and NMR spectra of 3-bromo-7-(diethylamino)-4-(((tert-butyldimethylsilyl)oxy)methyl)coumarin (**3**).

A MS (APCI) m/z calculated for $C_{20}H_{31}BrNO_3Si + H^+$: 442.12, found: 442.1236.

B ^{1}H-NMR (400 MHz, $CDCl_3$) δ(ppm) 7.69 (d, $J = 9.2$ Hz, 1H), 6.58 (dd, $J = 9.2$, 2.5 Hz, 1H), 6.41 (d, $J = 2.5$ Hz, 1H), 4.93 (s, 2H), 3.37 (q, $J = 7.1$ Hz, 4H), 1.17 (t, $J = 7.1$ Hz, 6H), 0.86 (s, 9H), 0.10 (s, 6H).

C ^{13}C-NMR (101 MHz, $CDCl_3$) δ(ppm) 157.33, 153.94, 150.29, 149.46, 126.32, 108.03, 106.97, 103.60, 95.96, 76.46, 76.14, 75.83, 62.08, 43.78, 24.77, 17.18, 11.43, -6.15.

7-(diethylamino)-4-(((tert-butyldimethylsilyl)oxy)methyl)-[(E)-3-(tert-butoxycarbonyl)prop-2-enyl]coumarin (4)

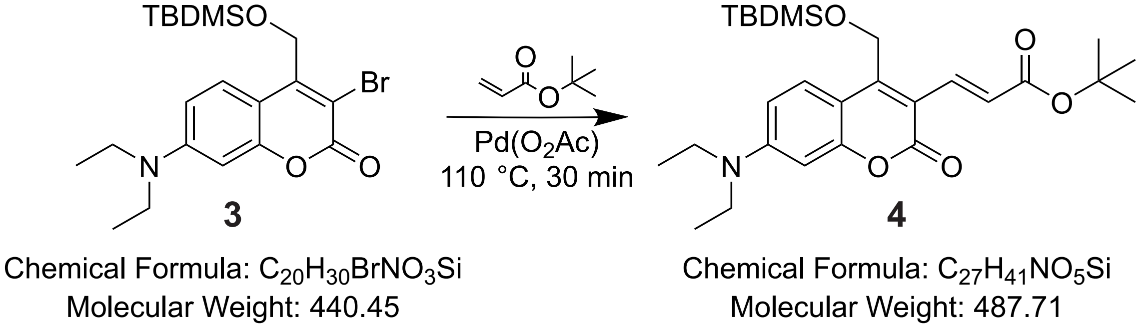

Scheme S5.3: Reaction equation for synthesis of 7-(diethylamino)-4-(((tert-butyldimethylsilyl)oxy)methyl)-[(E)-3-(tert-butoxycarbonyl)prop-2-enyl]coumarin (**4**)

3-bromo-7-(diethylamino)-4-(((tert-butyldimethylsilyl)oxy)methyl)coumarin (**3**) (310 mg, 704 µmol, 1.00 equiv.) and tert-butyl acrylate (308 µL, 2.11 mmol, 3.00 equiv.) were dissolved in dimethylformamide (6 mL) and degassed for 10 min with nitrogen. Lithium chloride (50.7 mg, 1.20 mmol, 1.70 equiv.), sodiumhydogencarbonate (177 mg, 2.11 mmol, 3.00 equiv.) and tetrabutylammonium chloride (215 mg, 774 µmol, 1.10 equiv.) were added to reaction mixture and degassed for 5 min. Subsequently, the reaction mixture was treated with palladium acetate (Pd(O_2Ac); 7.90 mg, 3.52 µmol, 5 mol % equiv.) and heated to 110 °C for 30 min under nitrogen flow and continuous stirring. The reaction was then cooled to RT and quenched by addition of water (10 mL). The aqueous phase was extracted with ethyl acetate (6x 10 mL). Organic layers were combined, silica (3 g) was added and solvent was removed under reduced pressure. The crude material was then purified by column chromatography (90:10, hexane:ethyl acetate) to obtain (**4**) as a yellow solid.

As the reaction yield was very low (~10 %), the reaction time was prolonged and after different time points samples were taken and analyzed by HPLC. During the reaction, the protecting group on the hydroxy function was cleaved, giving rise to two additional peaks. The peak at a retention time of 7.40 min corresponds to the final photocage product (5), whereas the peak at 3.74 min represents the deprotected educt (**8**). The mobile phase consisted of solvent A (mQ water with 0.05 % trifluoroacetic acid, TFA) and solvent B (ACN with 0.05 % TFA). The flow rate was maintained at 1 mL/min. The chromatographic run was initiated at 55 % A / 45 % B and linearly adjusted to 5 % A / 95 % B within 15 min. This high-organic composition was maintained for 10 min. The system was returned to the initial conditions (55 % A / 45 % B) for column re-equilibration (10 min). Detection was carried out with a diode array detector (DAD) at 400 nm.

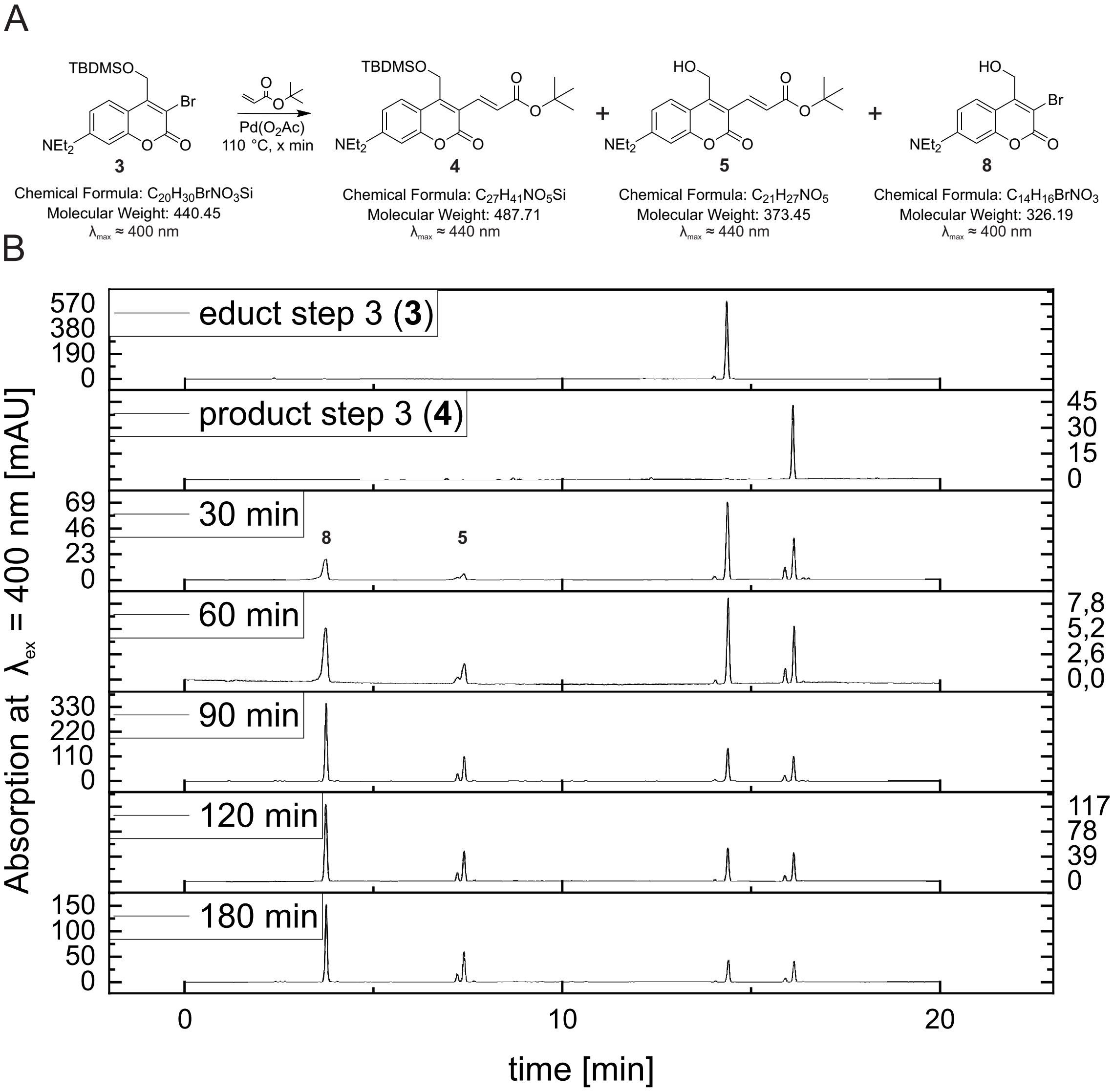

Figure S5.3: Reaction control of 7-(diethylamino)-4-(((tert-butyldimethylsilyl)-oxy)methyl)-[(E)-3-(tert-butoxycarbonyl)prop-2-enyl]coumarin (**4**) synthesis. **A** Reaction equation with possible side products. **B** RP-HPLC chromatograms corresponding to the 0-20 min section of the 35 min runtime were recorded at selected reaction time points. Chromatograms of the educt and the purified product were included as reference traces for comparison. milli Absorbance Units, mAU.

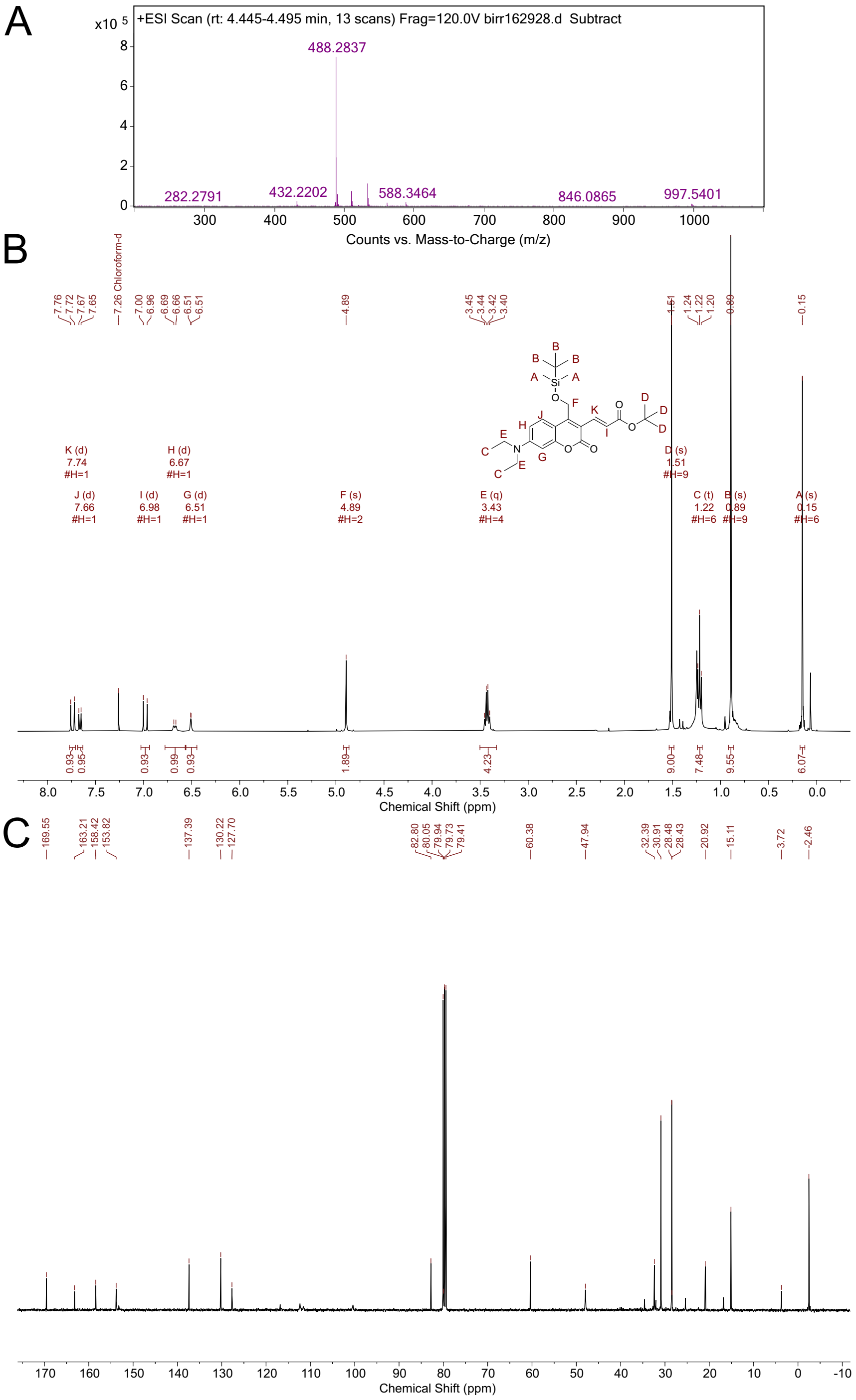

Figure S5.4: Mass spectrum and NMR spectra of 7-(diethylamino)-4-(((tert-butyldimethylsilyl)oxy)methyl)-[(E)-3-(tert-butoxycarbonyl)prop-2-enyl]coumarin (**4**).

A MS (ESI) m/z calculated for $C_{27}H_{41}NO_5Si + H^+$: 488.28, found: 488.2837.

B ^{1}H-NMR (400 MHz, $CDCl_3$) δ(ppm) 7.74 (d, J = 15.7 Hz, 1H), 7.66 (d, J = 9.2 Hz, 1H), 6.98 (d, J = 15.7 Hz, 1H), 6.67 (d, J = 8.5 Hz, 1H), 6.51 (d, J = 1.8 Hz, 1H), 4.89 (s, 2H), 3.43 (q, J = 7.1 Hz, 4H), 1.51 (s, 9H), 1.22 (t, J = 7.1 Hz, 6H), 0.89 (s, 9H), 0.15 (s, 6H).

C ^{13}C-NMR (101 MHz, $CDCl_3$) δ(ppm) 169.55, 163.21, 158.42, 153.82, 137.39, 130.22, 127.70, 82.80, 80.05, 79.94, 79.73, 79.41, 60.38, 47.94, 32.39, 30.91, 28.48, 28.43, 20.92, 15.11, 3.72, -2.46.

7-(diethylamino)-(4-hydroxymethyl)-[(E)-3-(tert-butoxycarbonyl)prop-2-enyl]coumarin (5)

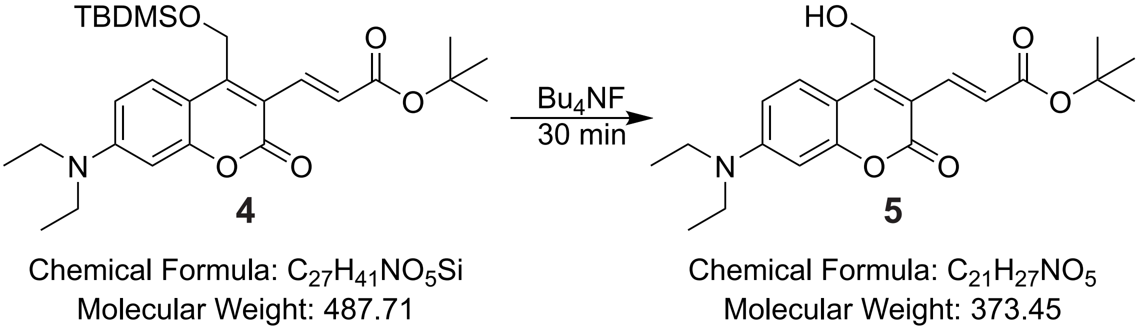

Scheme S5.4: Reaction equation for synthesis of 7-(diethylamino)-(4-hydroxymethyl)-[(E)-3-(tert-butoxycarbonyl)prop-2-enyl]coumarin (**5**)

To a solution of 7-(diethylamino)-4-(((tert-butyldimethylsilyl)oxy)methyl)-[(E)-3-(tert-butoxycarbonyl)prop-2-enyl]coumarin (**4**) (64 mg, 131 µmol, 1.00 equiv) in tetrahydrofuran (THF; 3 mL), tetrabutylammonium fluoride (Bu_4NF; 1 M in THF; 281 µL, 281 µmol, 2.14 equiv) was added and stirred for 30 min. The reaction was quenched by addition of saturated NH_4Cl (6 mL). The aqueous phase was extracted with ethyl acetate (3x 10 mL). Organic layers were combined and solvent was removed under reduced pressure. The crude material was purified by preparative HPLC. The mobile phase consisted of solvent A (mQ water with 0.1 % TFA) and solvent B (ACN). A linear gradient from 45 % to 95 % B over 15 min at a flow rate of 20 mL/min was applied. Detection was performed at 220 nm. Fractions containing the desired product were collected, pooled, and lyophilized to yield the purified compound (**5**).

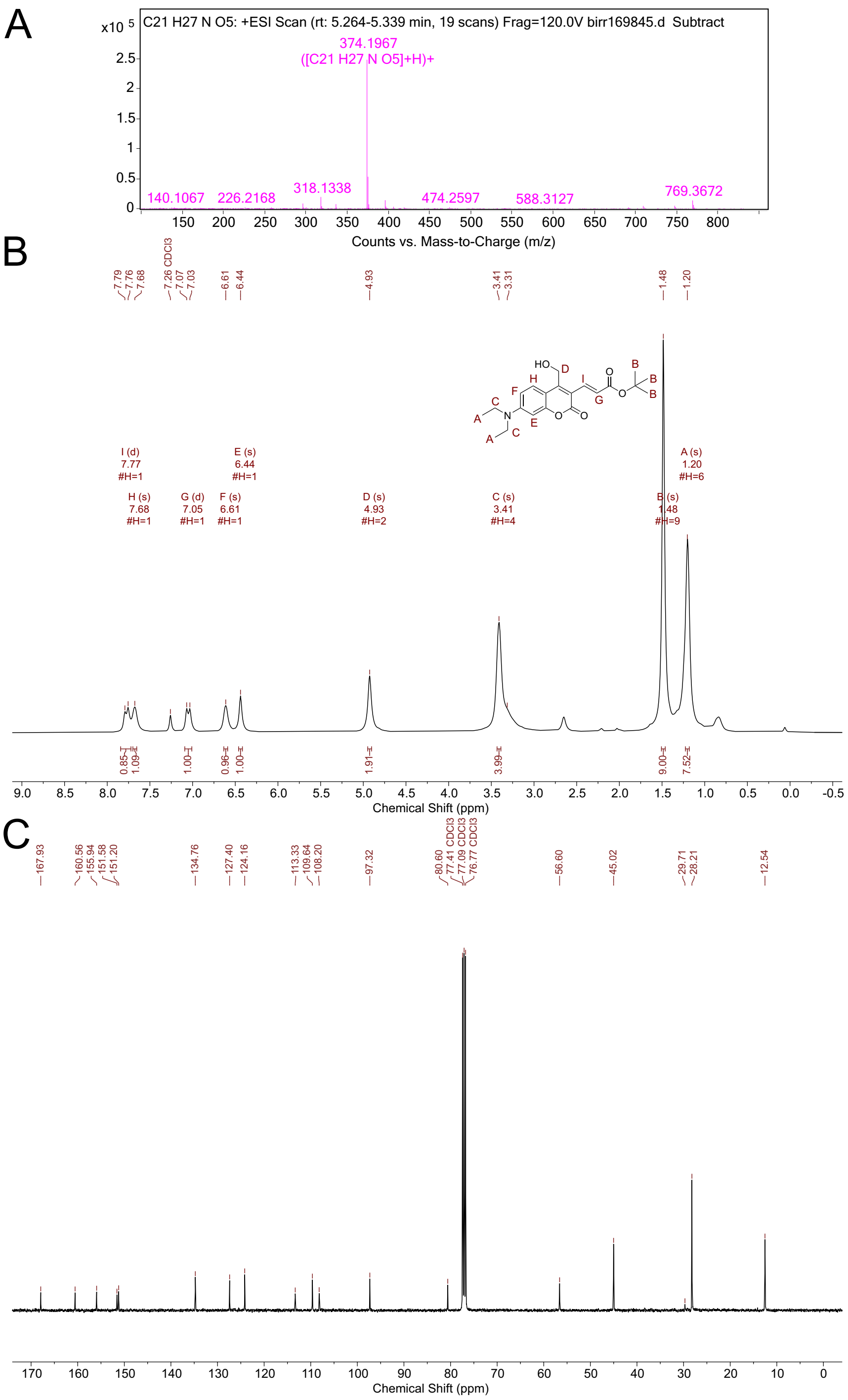

Figure S5.5: Mass spectrum and NMR spectra of 7-(diethylamino)-4-(((tert-butyldimethylsilyl)oxy)methyl)-[(E)-3-(tert-butoxycarbonyl)prop-2-enyl]coumarin (**5**).

A MS (ESI) m/z calculated for $C_{21}H_{27}NO_5 + H^+$: 374.19, found: 374.1967.

B ^{1}H-NMR (400 MHz, $CDCl_3$) δ(ppm) 7.77 (d, J = 15.2 Hz, 1H), 7.68 (s, 1H), 7.05 (d, J = 15.1 Hz, 1H), 6.61 (s, 1H), 6.44 (s, 1H), 4.93 (s, 2H), 3.41 (s, 4H), 1.48 (s, 9H), 1.20 (s, 6H).

C ^{13}C-NMR (101 MHz, $CDCl_3$) δ(ppm) 167.93, 160.56, 155.94, 151.58, 151.20, 134.76, 127.40, 124.16, 113.33, 109.64, 108.20, 97.32, 80.60, 77.41, 77.09, 76.77, 56.60, 45.02, 29.71, 28.21, 12.54.

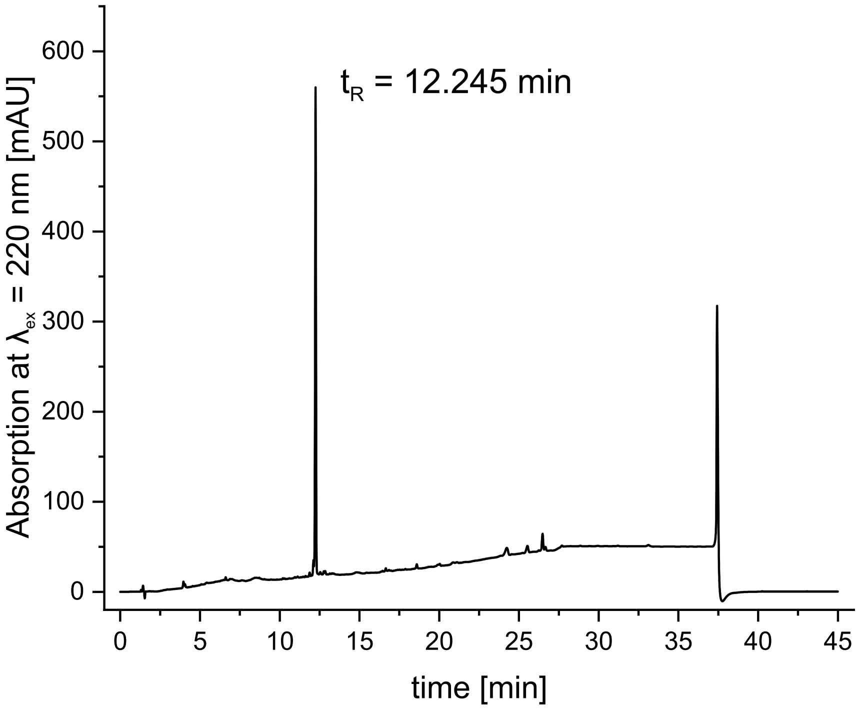

Figure S5.6: RP-HPLC analysis of $DEAC_{435}$. The mobile phase consisted of solvent A (mQ water with 0.05 % TFA) and solvent B (ACN with 0.05 % TFA). The flow rate was maintained at 1 mL/min. The chromatographic run was initiated at 75 % A / 25 % B and linearly adjusted to 40 % A / 60 % B within 10 min. Subsequently, the gradient was further shifted to 5 % A / 95 % B over 10 min, and this high-organic composition was maintained for 10 min. The system was returned to the initial conditions (95 % A / 5 % B) for column re-equilibration (10 min). Detection was carried out with a diode array detector (DAD) at 220 nm. Retention time t_R: 12.245 min. Purity of 65 %. milli Absorbance Units, mAU.

S5.1.2 Synthesis of Activated $DEAC_{435}$

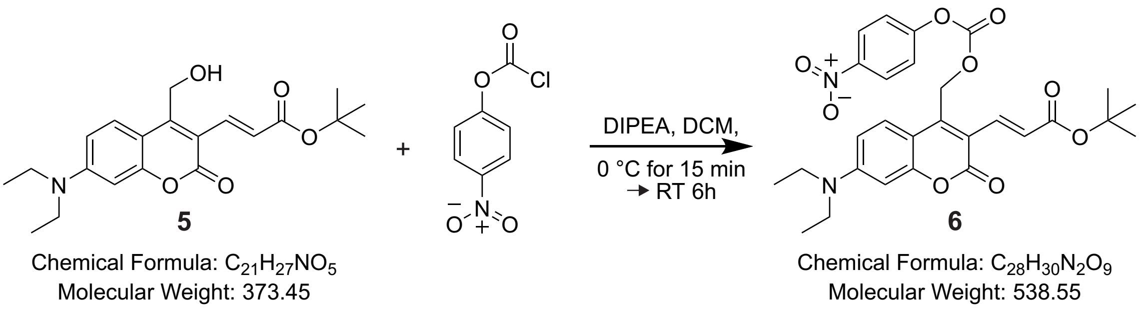

Chemical Formula: $C_{21}H_{27}NO_5$
Molecular Weight: 373.45

Chemical Formula: $C_{28}H_{30}N_2O_9$
Molecular Weight: 538.55

Scheme S5.5: Reaction equation for synthesis of tert-butyl (E)-3-(7-(diethylamino)-4-((((4-nitrophenoxy)carbonyl)oxy)methyl)-2-oxo-2H-chromen-3-yl)acrylate (**6**)

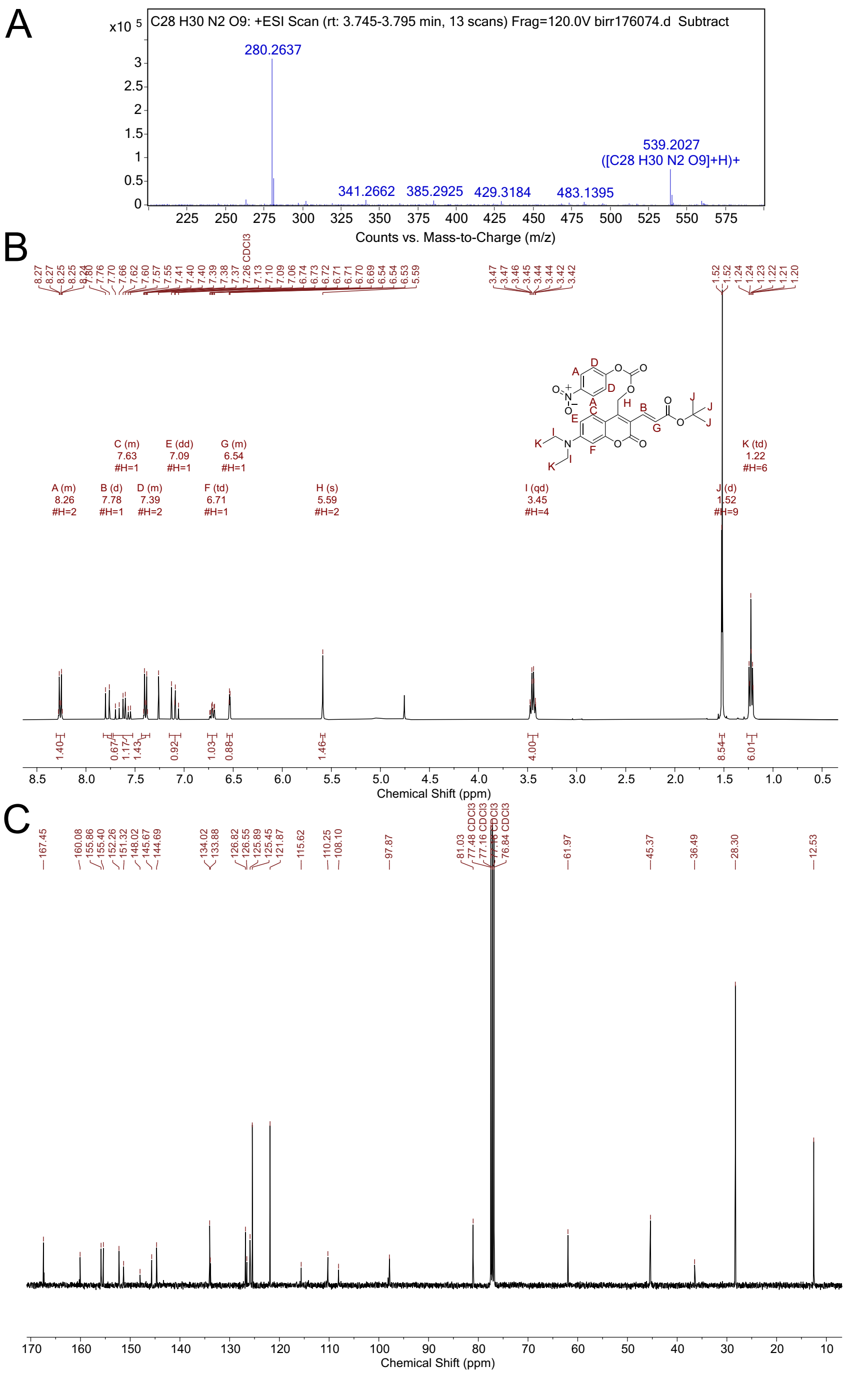

Figure S5.7: Mass spectrum and NMR spectra of tert-butyl (E)-3-(7-(diethylamino)-4-((((4-nitrophenoxy)carbonyl)oxy)methyl)-2-oxo-2H-chromen-3-yl)acrylate (**6**).

A MS (ESI) m/z calculated for $C_{28}H_{30}N_2O_9 + H^+$: 539.20, found: 539.2027.

B ^{1}H NMR (400 MHz, $CDCl_3$) δ(ppm) 8.30-8.22 (m, 2H), 7.78 (d, J = 15.6 Hz, 1H), 7.72-7.52 (m, 1H), 7.43-7.35 (m, 2H), 7.09 (dd, J = 15.6, 13.2 Hz, 1H), 6.71 (td, J = 9.3, 8.5, 2.6 Hz, 1H), 6.56-6.51 (m, 1H), 5.59 (s, 2H), 3.45 (qd, J = 7.2, 1.2 Hz, 4H), 1.52 (d, J = 2.4 Hz, 9H), 1.22 (td, J = 7.1, 1.8 Hz, 6H).

C ^{13}C NMR (101 MHz, $CDCl_3$) δ(ppm) 167.45, 160.08, 155.86, 155.40, 152.26, 151.32, 148.02, 145.67, 144.69, 134.02, 133.88, 126.82, 126.55, 125.89, 125.45, 121.87, 115.62, 110.25, 108.10, 97.87, 81.03, 77.48, 77.16, 76.84, 61.97, 45.37, 36.49, 28.30, 12.53.

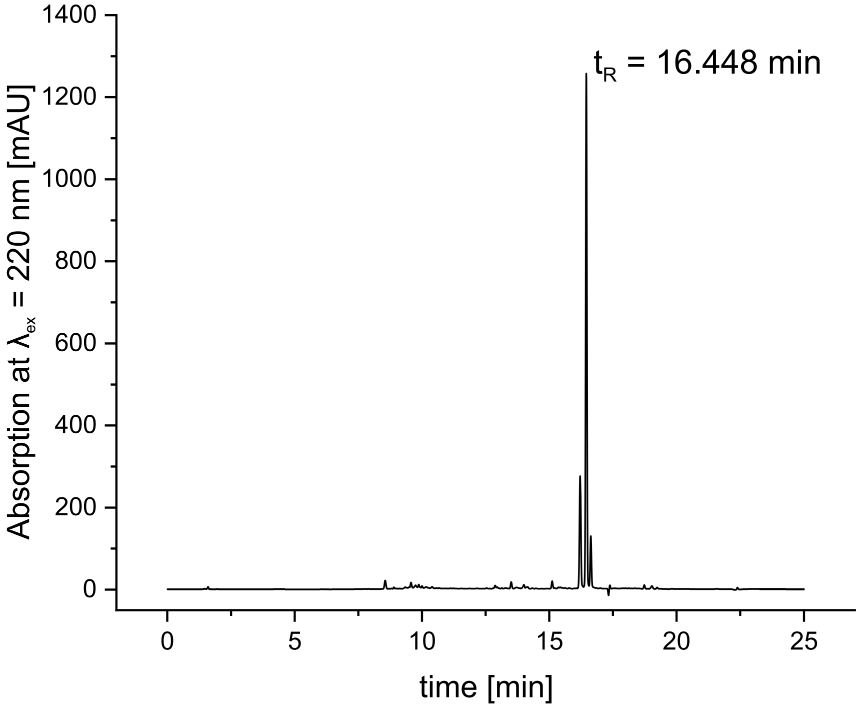

Figure S5.8: RP-HPLC analysis of activated DEAC$_{435}$. The mobile phase consisted of solvent A (mQ water with 0.05 % TFA) and solvent B (ACN with 0.05 % TFA). The flow rate was maintained at 1 mL/min. The chromatographic method initiated with an isocratic hold at 95 % A / 5 % B for 1 min, followed by a linear gradient to 5 % A / 95 % B over 15 min. The high-organic phase was maintained for 4 min, after which the system was returned to the initial conditions (95 % A / 5 % B) for column re-equilibration (5 min). Detection was carried out a diode array detector (DAD) at 220 nm. Retention time t_R: 16.448 min. Purity of 64 %. milli Absorbance Units, mAU.

S5.1.3 Synthesis of Activated DEAC$_{435acid}$

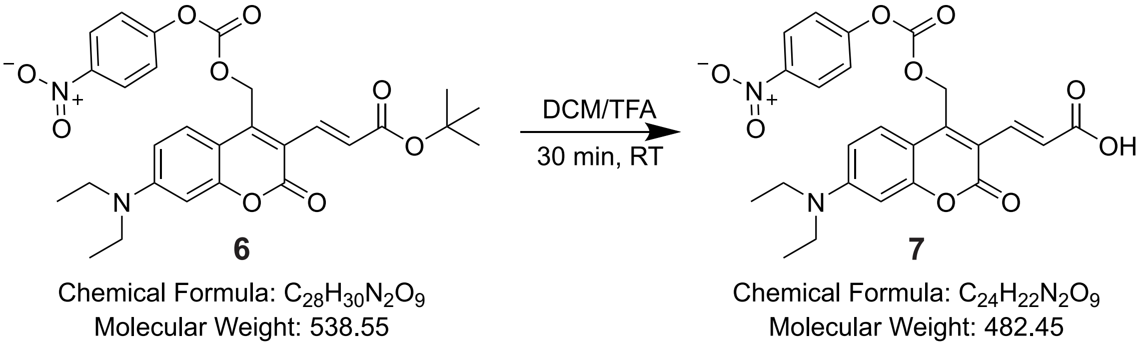

Scheme S5.6: Reaction equation for synthesis of (E)-3-(7-(diethylamino)-4-((((4-nitrophenoxy)carbonyl)oxy)methyl)-2-oxo-2H-chromen-3-yl)acrylic acid (**7**), DEAC$_{435acid}$

A reaction time of 30 min was sufficient to convert all educt (6). The reactive carbonate is not stable under the deprotection conditions, as DEAC$_{435}$ (5) is a by-product of the reaction. Shortening the reaction time would lead to incomplete conversion of educt. The mobile phase consisted of solvent A (mQ water with 0.05 % TFA) and solvent B (ACN with 0.05 % TFA). The flow rate was maintained at 1 mL/min. The chromatographic method initiated with an isocratic hold at 95 % A / 5 % B for 1 min, followed by a linear gradient to 5 % A / 95 % B over 15 min. The high-organic phase was maintained for 4 min, after which the system was returned to the initial conditions (95 % A / 5 % B) for column re-equilibration (5 min). Detection was carried out with a diode array detector at 435 nm.

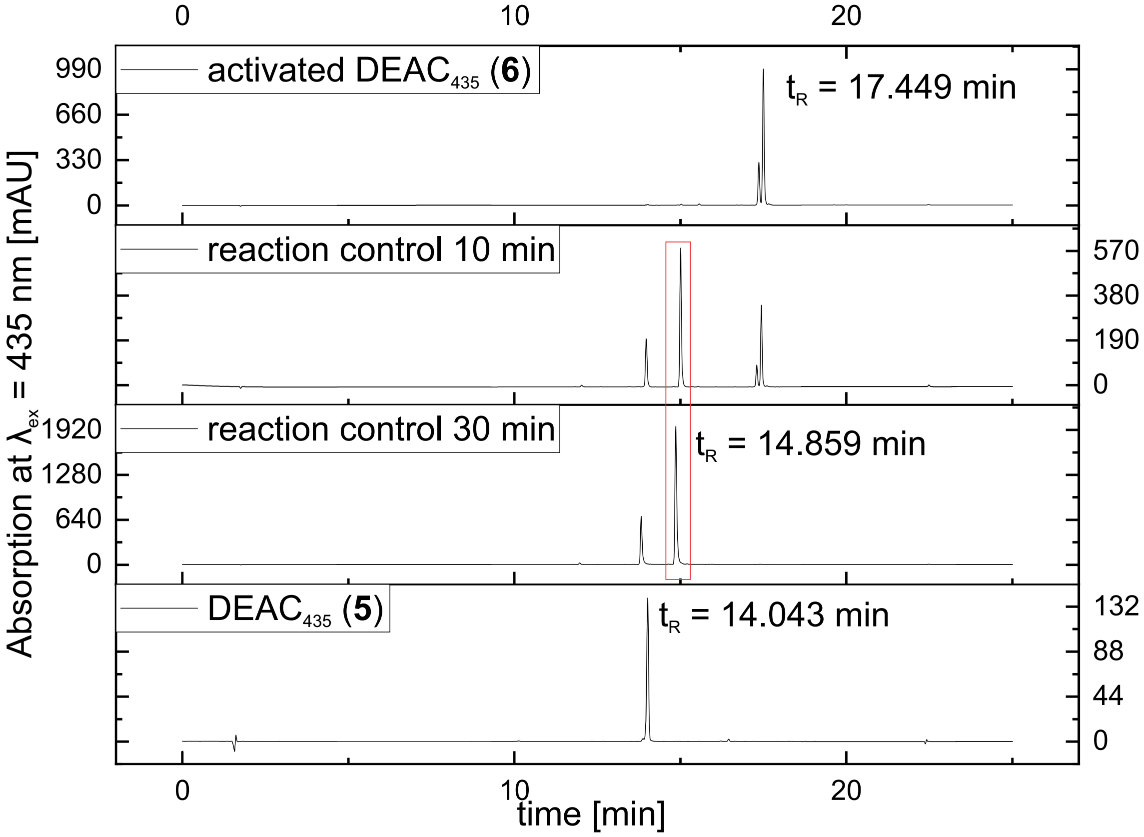

Figure S5.9: RP-HPLC chromatograms of activated DEAC$_{435acid}$ synthesis and references. The desired activated DEAC$_{435acid}$ (**7**) is indicated in the red rectangle. milli Absorbance Units, mAU.

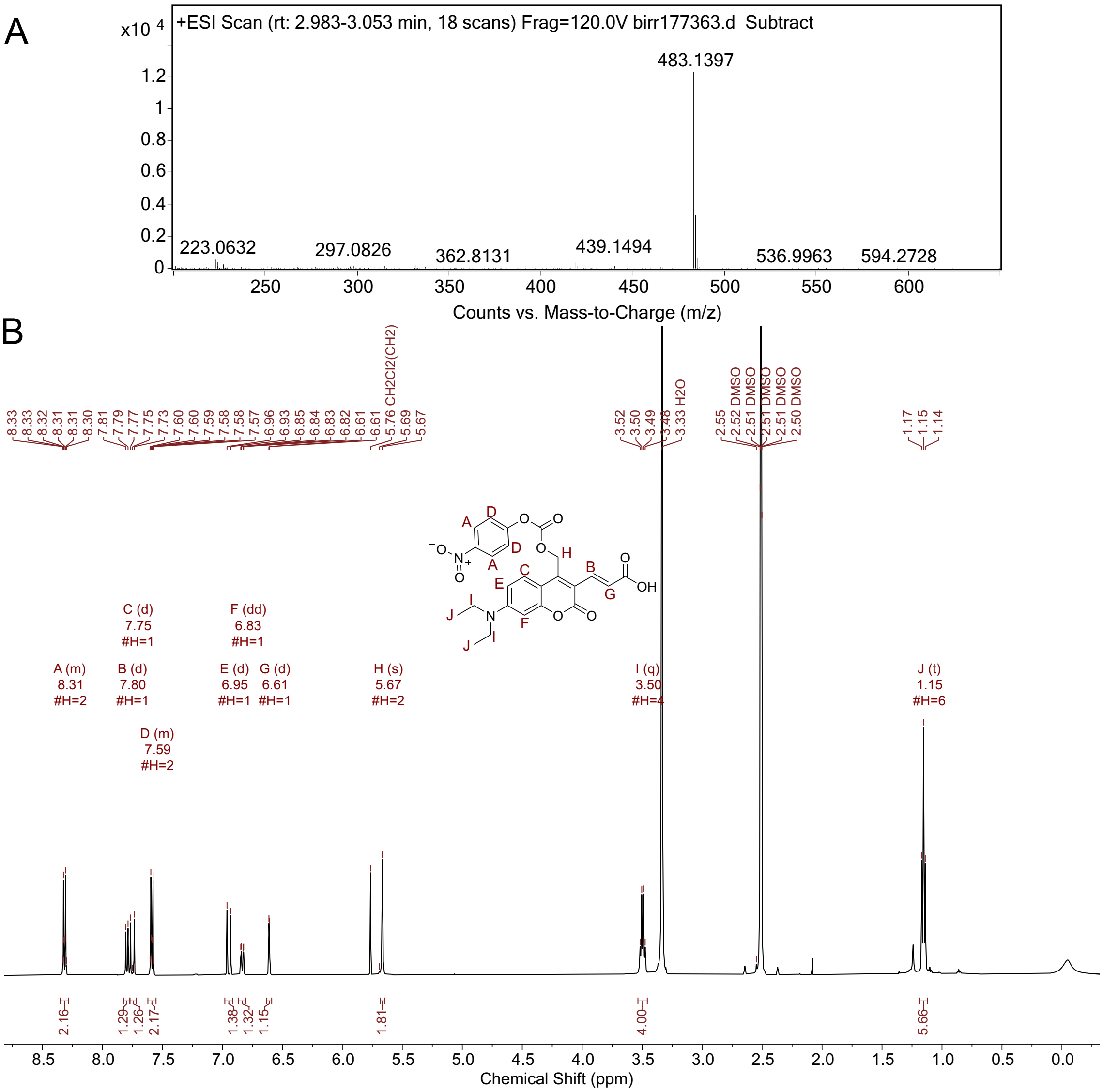

Figure S5.10: Mass spectrum and NMR spectra of (E)-3-(7-(diethylamino)-4-(((-(4-nitrophenoxy)carbonyl)oxy)methyl)-2-oxo-2H-chromen-3-yl)acrylic acid (**7**).
A MS (ESI) m/z calculated for $C_{28}H_{30}N_2O_9 + H^+$: 483.13, found: 483.1397.
B ^{1}H NMR (500 MHz, DMSO) δ(ppm) 8.35-8.28 (m, 2H), 7.80 (d, J = 9.3 Hz, 1H), 7.75 (d, J = 15.5 Hz, 1H), 7.62-7.55 (m, 2H), 6.95 (d, J = 15.5 Hz, 1H), 6.83 (dd, J = 9.3, 2.6 Hz, 1H), 6.61 (d, J = 2.5 Hz, 1H), 5.67 (s, 2H), 3.50 (q, J = 7.0 Hz, 4H), 1.15 (t, J = 7.0 Hz, 6H).

S5.1.4 Synthesis of DEAC-NH-PEG$_{2k}$-PLA$_{10k}$

The sufficient coupling of DEAC to NH$_2$-PEG$_{2k}$-PLA$_{10k}$ was proven by RP-HPLC. The chromatogram recorded at λ_{ex} = 220 nm shows the eluation of the NH$_2$-PEG$_{2k}$-PLA$_{10k}$ polymer between 17 min and 18 min (Figure S5.11 A), whereas no NH$_2$-PEG$_{2k}$-PLA$_{10k}$ is traceable at λ_{ex} = 400 nm. The chromatogram of DEAC-NH-PEG$_{2k}$-PLA$_{10k}$ at λ_{ex} = 400 nm depicts a peak at the retention time of the polymer (t$_R$ = 17.543 min), proofing the coupling of DEAC to the polymer (Figure S5.11 B).

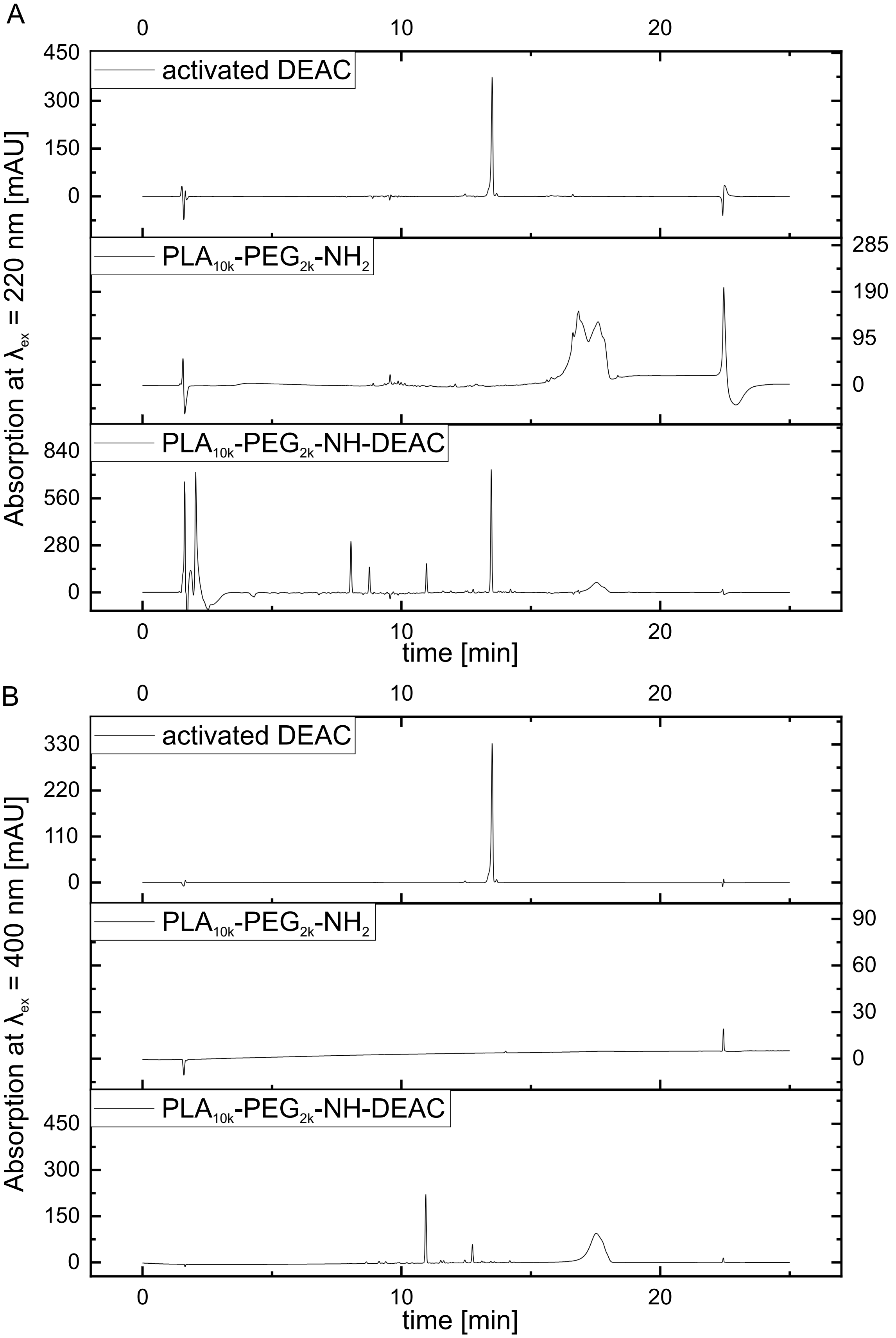

Figure S5.11: RP-HPLC analysis of DEAC-NH-PEG$_{2k}$-PLA$_{10k}$ synthesis.
A HPLC traces recorded at $\lambda_{ex} = 220\,\text{nm}$. **B** HPLC traces recorded at $\lambda_{ex} = 400\,\text{nm}$. milli Absorbance Units, mAU.

S5.1.5 Synthesis of Caged Polymer $[\mathrm{TAT}]_{435}$-PEG_{2k}-PLA_{10k}

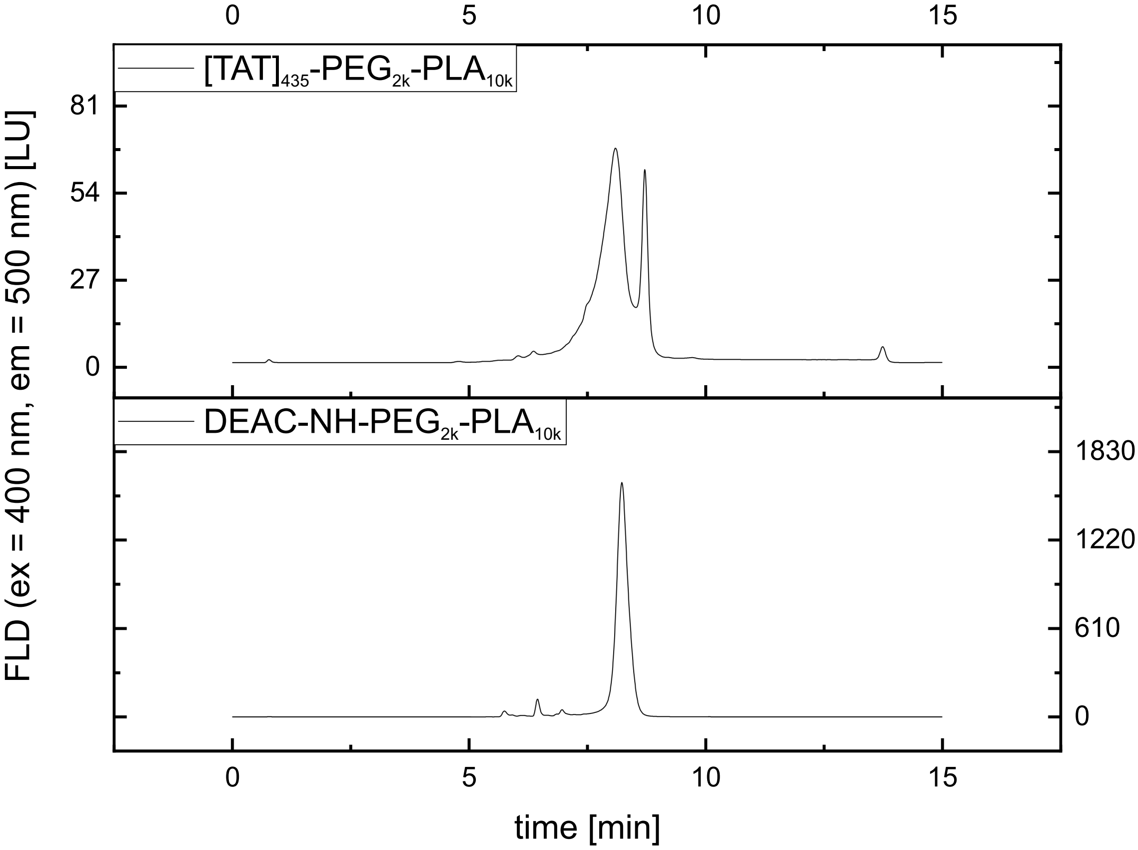

Figure S5.12: RP-HPLC analysis of $[\mathrm{TAT}]_{435}$-PEG_{2k}-PLA_{10k} and DEAC-NH-PEG_{2k}-PLA_{10k}. DEAC-NH-PEG_{2k}-PLA_{10k} was used as a reference. Both traces show a peak at approximately 8 min. Fluorescence detector, FLD; Luminescence units, LU.

S5.1.6 Synthesis of Caged Polymer $[\mathrm{TAT}]_{435acid}$-PEG$_{2k}$-PLA$_{10k}$

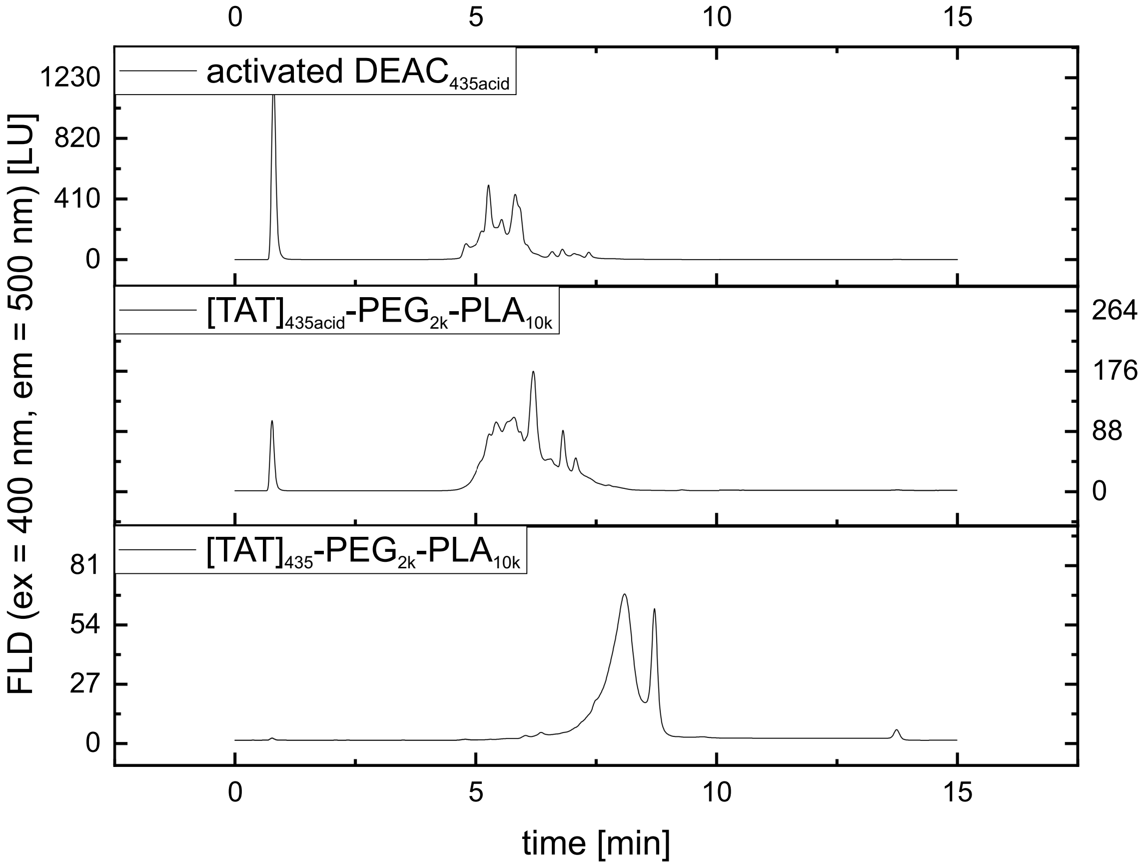

Figure S5.13: RP-HPLC analysis of activated DEAC$_{435acid}$, $[\mathrm{TAT}]_{435acid}$-PEG$_{2k}$-PLA$_{10k}$ and $[\mathrm{TAT}]_{435}$-PEG$_{2k}$-PLA$_{10k}$. $[\mathrm{TAT}]_{435}$-PEG$_{2k}$-PLA$_{10k}$ was used as a reference. Chromatogram of $[\mathrm{TAT}]_{435acid}$-PEG$_{2k}$-PLA$_{10k}$ shows no polymer peak at approximately 8 min, indicating that photocage DEAC$_{435acid}$ is not coupled to TAT-PEG$_{2k}$-PLA$_{10k}$. Fluorescence detector, FLD; Luminescence units, LU.

S5.1.7 Quantification of DEAC_{435} Coupling to TAT-PEG_{2k}-PLA_{10k}

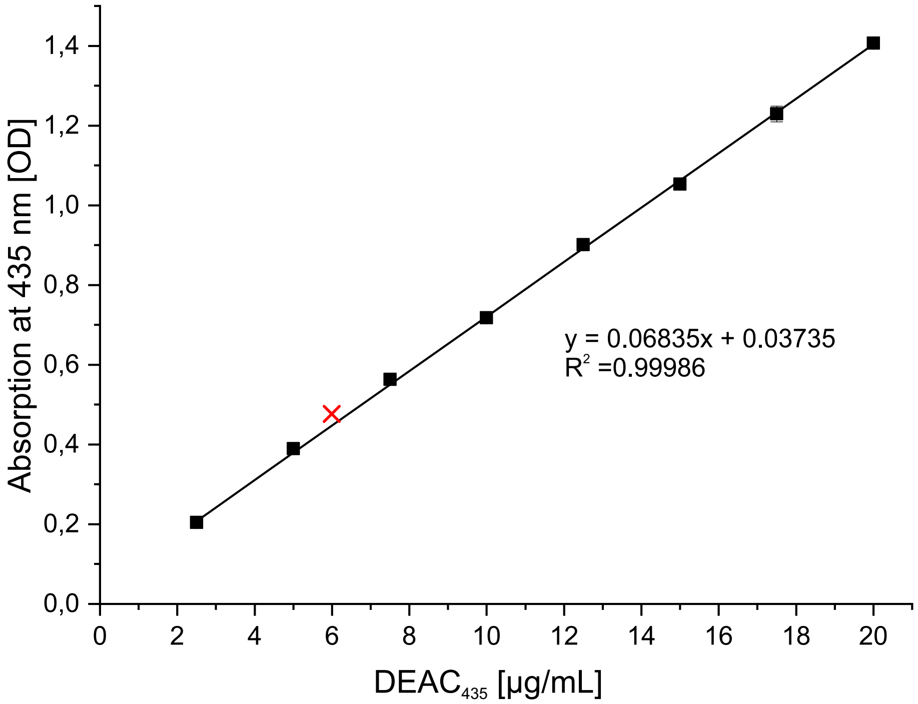

Figure S5.14: Coupling efficiency of DEAC_{435} to TAT-polymer. Plotting a calibration curve for quantification of DEAC_{435} coupling to TAT-Polymer. Absorption is plotted against DEAC_{435} concentration. The amount of DEAC_{435} in $[\text{TAT}]_{435}$-PEG_{2k}-PLA_{10k} was $5.99\,\mu\text{g}\,\text{mL}^{-1}$. The value is marked as a red cross on the calibration line. Data points represent mean ± SD (n = 3).

Assuming a complete reaction, two DEAC_{435} molecules couple to TAT-PEG_{2k}-PLA_{10k}. The efficiency is calculated:

$$c_{\text{DEAC}_{435}} = \frac{\beta_{\text{DEAC}_{435}}}{\text{M}_{\text{DEAC}_{435}}} \tag{5.1}$$

$\beta_{[\text{TAT}]_{435}-\text{PEG}_{2\text{k}}-\text{PLA}_{10\text{k}}\text{Polymer}}$ is the mass concentration of DEAC_{435} coupled to TAT-PEG_{2k}-PLA_{10k} determined by absorption measurement.

$$c_{[\text{TAT}]_{435}-\text{PEG}_{2\text{k}}-\text{PLA}_{10\text{k}}\text{Polymer}} = \frac{\beta_{[\text{TAT}]_{435}-\text{PEG}_{2\text{k}}-\text{PLA}_{10\text{k}}\text{Polymer}}}{\text{M}_{[\text{TAT}]_{435}-\text{PEG}_{2\text{k}}-\text{PLA}_{10\text{k}}\text{Polymer}}} \tag{5.2}$$

$\text{M}_{[\text{TAT}]_{435}-\text{PEG}_{2\text{k}}-\text{PLA}_{10\text{k}}\text{Polymer}}$ was calculated as followed:

$$\begin{aligned}\text{M}_{[\text{TAT}]_{435}-\text{PEG}_{2\text{k}}-\text{PLA}_{10\text{k}}\text{Polymer}} = {} & \text{M}_{\text{TAT}-\text{PEG}_{2\text{k}}-\text{PLA}_{10\text{k}}\text{Polymer}} - 2 \\ & + 2\Big(\text{M}_{\text{DEAC}_{435}} - 2 + \text{M}_\text{C} + \text{M}_\text{O}\Big)\end{aligned} \tag{5.3}$$

$$\mathrm{CE}_{[\mathrm{TAT}]_{435}-\mathrm{PEG}_{2\mathrm{k}}-\mathrm{PLA}_{10\mathrm{k}}\mathrm{Polymer}}[\%] = \frac{\frac{c_{\mathrm{DEAC}_{435}}}{c_{[\mathrm{TAT}]_{435}-\mathrm{PEG}_{2\mathrm{k}}-\mathrm{PLA}_{10\mathrm{k}}\mathrm{Polymer}}}}{2} * 100 \tag{5.4}$$

S5.2 Calculation on Foerster Radius

The Foerster Radius (R_0) was calculated with Equation (5.5)

$$R_0 = 0.211 * \sqrt[6]{\kappa^2 n^{-4} Q_D J(\lambda)} \tag{5.5}$$

where κ^2 is the orientation factor, n is the refractive index, Q_D is the quantum yield of the donor and $J(\lambda)$ is the overlap integral calculated separately by Equation (5.6) [1].

$$J(\lambda) = \frac{\int\limits_0^\infty F_D(\lambda)\varepsilon_A(\lambda)\lambda^4\, d\lambda}{\int\limits_0^\infty F_D(\lambda)\, d\lambda} \tag{5.6}$$

$\varepsilon_A(\lambda)$ is the extinction coefficient of the acceptor fluorophore at a defined wavelength, F_D is the fluorescence spectrum of the donor. For the calculation of Foerster radius for the BRET pair NanoLuc-DEAC$_{435}$, κ^2 was assumed 2/3. The excitation coefficient (ϵ_{max}) of DEAC$_{435}$ was taken from literature as $4.3 \times 10^4\,\mathrm{M}^{-1}\,\mathrm{cm}^{-1}$ and Q_D of NanoLuc was obtained from literature with a value of 0.45 [2, 3]. R_0 was calculated to be 42.5 Å or 4.25 nm respectively.

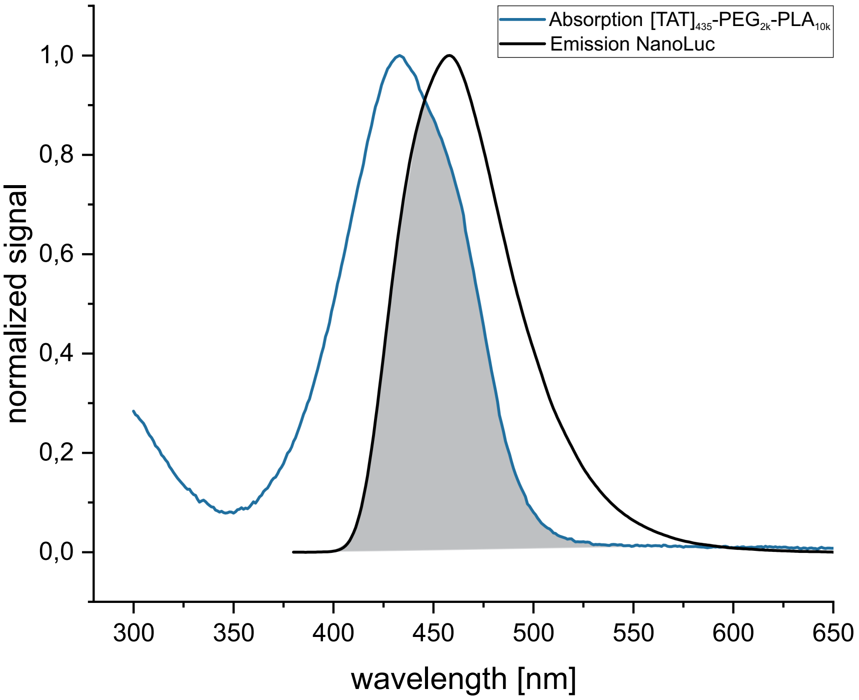

Figure S5.15: Absorption spectrum of [TAT]$_{435}$-PEG$_{2k}$-PLA$_{10k}$ and emission spectrum of NanoLuc. Individual peaks were normalized to their highest peak intensity to enable comparison. Overlap J(λ) is indicated as grey area.

S5.3 Characterization of PEG Conformation and Modeling of Ligand Distributions on NP Surface

S5.3.1 Characterization of PEG Conformation and Estimation of PEG Grafting Distance

Assuming that the hydrophobic PLA segment embeds into and anchors the PLA-PEG copolymer within the nanoparticle core, while the hydrophilic PEG segment orients outward to form a surface PEG shell, the resulting PEG chain conformation on the nanoparticle surface can be described based on theoretical models [4]. NPs were approximated as perfect sphere with a homogeneous distribution of polymer. Further, the surface area occupied by each PEG chain (S) was assumed to be a circular area. The conformation of PEG chains within the core-shell NP design is described by the quotients of Flory Radius (R_F) and the distance of two grafting PEG chains (D), which was previously described by our group and others [5, 6]. A value of $R_F/D < 1$ is linked to mushroom conformation and $R_F/D > 1$ is referred as brush conformation, which can be further characterized as dense brush with a $R_F/D > 2.8$ [6].

The Flory radius R_F is defined by Equation (5.7), where α denotes the length of a PEG monomer (0.35 nm) and N is the number of monomers in PEG chain calculated by dividing the molecular weight of the PEG chain ($2000\,\mathrm{g\,mol^{-1}}$) by the monomer molecular weight ($44\,\mathrm{g\,mol^{-1}}$).

$$R_F = \alpha * N^{\frac{3}{5}} \tag{5.7}$$

R_F was calculated to be 3.46 nm for the PEG_{2k}-PLA_{10k} block copolymer used in our NP design. The grafting distance (D) between two polymer chains on a particle surface is calculated by Equation (5.8), where S corresponds to the surface occupied by a single PEG chain [4].

$$D = 2 * \sqrt[2]{\frac{S}{\pi}} \tag{5.8}$$

S is given by:

$$S = \frac{6 * M_{PEG}}{d_h * N_A * f * \rho_{NP}} \tag{5.9}$$

where, M_{PEG} is the molecular weight of the PEG chain, d_h is the hydrodynamic diameter of the NP, N_A is the Avogadro number, f is the mass fraction of PEG in the blends of the PEG_{2k}-PLA_{10k} block copolymer and ρ_{NP} is the density of the NP. The density of $1.25\,\mathrm{g\,cm^{-2}}$ for NP was estimated corresponding to the density of NP composed of PLA-g-PEG blends [7]. For $[\mathrm{TAT}]_{435}$-NanoLuc-NP 1 % the distance between two PEG chains was calculated to be 1.11 nm, resulting in a value for $R_F/D = 2.91$. The PEG spacing for $[\mathrm{TAT}]_{435}$-NanoLuc-NP 5 % was determined 1.28 nm resulting in a value for $R_F/D = 2.71$.

Thus, it can be assumed that the polymer chains in both NP formulations arrange themselves in a brush conformation, and in the case of $[\mathrm{TAT}]_{435}$-NanoLuc-NP 1 %, even in a dense brush.

S5.3.2 Computational Modeling of Ligand Distributions on Nanoparticle Surface and Calculation of Geodesic Distance of BRET-pair NanoLuc-DEAC$_{435}$

The lateral arrangement of PEG chains anchored at the surface on spherical nanoparticles was simulated. The nanoparticles were represented as ideal spheres with hydrodynamic diameter d_h and radius $r = d_h/2$. Given the area occupied by each PEG chain (S) and the total surface area of an ideal sphere (A) defined in Equation (5.10),

$$A = 4\pi r^2, \tag{5.10}$$

the number of possible PEG anchoring sites on the particle was estimated as

$$N \approx \frac{A}{S} \tag{5.11}$$

Each lattice site corresponds to the terminal end of one PEG chain and can host [TAT], NanoLuc or methyl endgroup.

Fibonacci Lattice and Monte Carlo Simulation

A deterministic Fibonacci-sphere algorithm was used to generate a quasi-uniform distribution of N surface sites on a spherical nanoparticle. This method distributes points over a sphere with minimal clustering and without the stochastic irregularities characteristic of purely random sampling. It relies on the golden ratio ($\varphi = (1+\sqrt{5})/2$), whose irrational value ensures that each point is placed with a non-repeating angular shift, producing a smooth and nearly uniform coverage of the sphere [8, 9]. For each index $i = 0, \ldots, N-1$, the azimuthal angle θ_i and polar angle ϕ_i were computed as

$$\theta_i = \left(\frac{2\pi i}{\varphi}\right) \bmod 2\pi, \tag{5.12}$$

$$\phi_i = \arccos\left(1 - 2\frac{i+0.5}{N}\right). \tag{5.13}$$

θ_i and ϕ_i uniquely define a quasi-uniformly distributed point on the sphere. The corresponding Cartesian coordinates (x_i, y_i, z_i) on the NP surface were obtained using standard Spherical-to-Cartesian transformations:

$$(x_i, y_i, z_i) = \Big(r\sin\phi_i\cos\theta_i,\ r\sin\phi_i\sin\theta_i,\ r\cos\phi_i\Big) \tag{5.14}$$

For a given choice of N and r, this procedure yields a fixed, deterministic distribution of PEG anchoring sites on the nanoparticle surface. This spatial arrangement was kept constant across all simulation replicates so that stochastic variation arose exclusively from the reassignment of PEG endgroup identities.

Each surface site was assigned one of three PEG endgroup types, denoted A, B and C, using predefined probabilities (fractions) that reflect the experimental molar ratios of the different PEG-PLA in the nanoparticle formulation. In the reference implementation, type A corresponds to the acceptor-functionalized PEG ($[\text{TAT}]_{435}$), type B to the donor-functionalized PEG (NanoLuc), and type C to methoxy terminated PEG chains.

A series of 20 independent Monte Carlo simulations were performed. In each simulation, PEG endgroup identities were resampled stochastically for all N sites using the specified probability distribution, while the underlying spatial coordinates remained unchanged. For the $[\text{TAT}]_{435}$-NanoLuc-NP with 1 % NanoLuc fraction, the probabilities were A = 0.5, B = 0.01, C = 0.49. For $[\mathrm{TAT}]_{435}$-NanoLuc-NP with 5 % NanoLuc fraction, the probabilities were A = 0.5, B = 0.05, C = 0.45.

Geodesic Distance

The geodesic distance, defined as the arc length along the spherical surface, between $[\mathrm{TAT}]_{435}$ and NanoLuc on the spherical surface was calculated, to quantify the proximity between the BRET pair [10]. For a given $[\mathrm{TAT}]_{435}$ at position vector $\mathbf{a}$ and a set of NanoLuc at positions $\{\mathbf{b}_j\}$, the geodesic distance is given by

$$d_{\mathrm{geo}}(\mathbf{a}, \mathbf{b}_j) = r \arccos\left(\frac{\mathbf{a} \cdot \mathbf{b}_j}{r^2}\right), \tag{5.15}$$

where the dot product encodes the central angle between the corresponding vectors. For each $[\mathrm{TAT}]_{435}$, the minimum of $d_{\mathrm{geo}}(\mathbf{a}, \mathbf{b}_j)$ over all NanoLuc sites was recorded as its nearest-neighbor $[\mathrm{TAT}]_{435}$→NanoLuc distance.

All $[\mathrm{TAT}]_{435}$→NanoLuc distances from all simulations were pooled to obtain a distribution characterizing the typical donor-acceptor separation on the NP surface. To estimate the fraction of donor ligands residing within a functionally relevant interaction range of at least one acceptor ligand, the Foerster threshold distance $R_0 = 4.25\,\mathrm{nm}$ was applied (Section S5.2). For each simulation, the number of $[\mathrm{TAT}]_{435}$ with at least one NanoLuc at $d_{\mathrm{geo}} < R_0$ was counted, and the corresponding fraction with respect to all $[\mathrm{TAT}]_{435}$ was determined. These fractions were then aggregated across simulations to obtain a statistical description of the proportion of NanoLuc within the R_0 distance of a $[\mathrm{TAT}]_{435}$ moiety.

Taken together, the analytical estimates of grafting distance and the computational simulations of PEG endgroup distributions provide a consistent framework to relate polymer brush architecture to the statistical distribution of donor-acceptor distances on the nanoparticle surface.

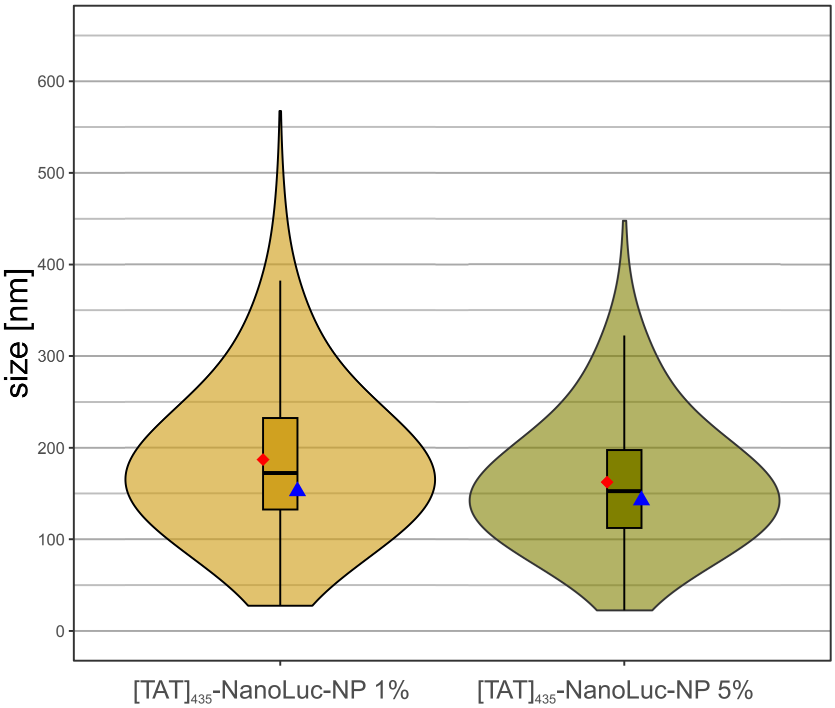

Figure S5.16: Size distribution and measures of central tendency of $[TAT]_{435}$-NanoLuc-NP 1 % and $[TAT]_{435}$-NanoLuc-NP 5 %. Violin plots represent size distribution of hydrodynamic diameters (n=3). The median NP size is shown as horizontal line within the box, whose lower and upper edges represent the first (Q1) and third (Q3) quartiles, respectively. Whiskers indicate the most extreme data points within 1.5 times the interquartile range from the lower and upper quartiles. The mean is represented by a red rectangle, and the mode is depicted by a blue triangle. The different measures of central tendency are separated by commas in the following order mean, median and mode. $[TAT]_{435}$-NanoLuc-NP 1 %: 187 nm, 173 nm, 153 nm; $[TAT]_{435}$-NanoLuc-NP 5 %: 162 nm, 153 nm, 143 nm

References

[1] P. Wu and L. Brand. "Resonance energy transfer: methods and applications". In: *Analytical biochemistry* 218.1 (1994), pp. 1–13. ISSN: 0003-2697. DOI: `10.1006/abio.1994.1134`.

[2] Hitesh K. Agarwal et al. "Intracellular Uncaging of cGMP with Blue Light". In: *ACS chemical neuroscience* 8.10 (2017), pp. 2139–2144. DOI: `10.1021/acschemneuro.7b00237`.

[3] Francesco Russo, Beatrice Civili, and Nicolas Winssinger. "Bright Red Bioluminescence from Semisynthetic NanoLuc (sNLuc)". In: *ACS chemical biology* 19.5 (2024), pp. 1035–1039. DOI: `10.1021/acschembio.4c00033`.

[4] R. Gref et al. "'Stealth' corona-core nanoparticles surface modified by polyethylene glycol (PEG): influences of the corona (PEG chain length and surface density) and of the core composition on phagocytic uptake and plasma protein adsorption". In: *Colloids and Surfaces B: Biointerfaces* 18.3-4 (2000), pp. 301–313. ISSN: 09277765. DOI: `10.1016/S0927-7765(99)00156-3`.

[5] Kathrin Schorr et al. "The quantity of ligand-receptor interactions between nanoparticles and target cells". In: *Nanoscale horizons* 10.4 (2025), pp. 803–823. DOI: `10.1039/D4NH00645C`.

[6] Qi Yang and Samuel K. Lai. "Engineering Well-Characterized PEG-Coated Nanoparticles for Elucidating Biological Barriers to Drug Delivery". In: *Methods in molecular biology (Clifton, N.J.)* 1530 (2017), pp. 125–137. DOI: `10.1007/978-1-4939-6646-2_8`.

[7] Jean-Michel Rabanel et al. "Effect of the Polymer Architecture on the Structural and Biophysical Properties of PEG-PLA Nanoparticles". In: *ACS applied materials & interfaces* 7.19 (2015), pp. 10374–10385. DOI: `10.1021/acsami.5b01423`.

[8] Álvaro González. "Measurement of Areas on a Sphere Using Fibonacci and Latitude–Longitude Lattices". In: *Mathematical Geosciences* 42.1 (2010), pp. 49–64. ISSN: 1874-8961. DOI: `10.1007/s11004-009-9257-x`.

[9] Benjamin Keinert et al. “Spherical fibonacci mapping”. In: *ACM Transactions on Graphics* 34.6 (2015), pp. 1–7. ISSN: 0730-0301. DOI: `10.1145/2816795.2818131`.

[10] Michael Spivak. *A comprehensive introduction to differential geometry*. 3. edition with correections. Vol. 1. Houston, Texas: Publish or Perish, 2005. ISBN: 0914098705.

Chapter 6

Summary and Conclusion

Summary

The application of highly potent therapeutic agents often fails in conventional treatment approaches because these drugs exhibit unfavorable biodistribution. Moreover, rapid systemic clearance can further hinder drugs from achieving therapeutically relevant concentrations at the target site. Nanoparticle-mediated delivery offers several fundamental advantages to address these challenges [1]. By encapsulating the active pharmaceutical ingredient (API), nanoparticles can compensate for the API's unfavorable intrinsic drug properties by transferring their own advantageous physicochemical characteristics and thereby prolonging systemic circulation and improving bioavailability [1, 2]. Furthermore, functionalization with biorecognition molecules enables active targeting of diseased tissue, thereby improving therapeutic efficacy [3]. Despite these advantages, unwanted off-target delivery still remains a major limitation as more than 90 % of the administered nanoparticles fail to reach their intended target site [4]. The effective accumulation of nanoparticles in target tissue is constrained by rapid opsonization and clearance via the mononuclear phagocyte system [5]. Furthermore, the limited specificity of targeting ligands can result in off-target delivery, especially when these ligands bind to receptors that are ubiquitously expressed throughout the body [6, 7]. To address this drawback, nanoparticles responsive to endogenous (pH, enzymes, redox) and/or exogenous (light, magnetism, temperature) stimuli have been developed [8–10]. Among these stimuli, light is particularly promising, because it is non-invasive and orthogonal to the biochemical environment and enables precise spatiotemporal control. However, light faces the limitation of shallow penetration depth within biological tissues. Tissue associated chromophores cause the absorption of wavelengths below 650 nm, whereas wavelengths above 900 nm are predominantly absorbed by water [11]. **Chapter 1** outlines the approaches to overcome this limitation and introduces the conceptual frameworks and mechanisms of light-controlled drug targeting.

In **Chapter 3** we developed a photo-responsive nanoparticle system with switchable surface charge [12]. To achieve this, core-shell nanoparticles composed of poly(D,L-lactide-*co*-glycolide) PLGA and poly(ethylene glycol)-*b*-poly(D,L-lactide)-(PEG-PLA) block copolymer were modified with positively charged cell-penetrating peptide (CPP). As CPP we used the transactivator of transcription peptide (TAT) from the human immunodeficiency virus, which contains two lysine and six arginine residues and therefore carries a strongly positive net charge. Elevated levels of positive charge enhance unspecific cellular uptake and may facilitate endosomal escape [13, 14]. However, increased positive charge is also associated with enhanced protein adsorption leading to accelerated clearance [15–17]. The coumarin-derived photo-labile protecting group (PPG) DEAC was attached to the lysine residues of the TAT sequence. This modification anchors the TAT motif within the nanoparticle core, thereby masking the surface charge as reflected by the reduced zetapotential of caged nanoparticles. In addition to these physicochemical alterations, the biological properties of the particles were also significantly affected. While the particles carrying the CPP are genuinely internalized by cells, conjugation of DEAC effectively camouflaged the TAT motif and consequently reduced cellular uptake. Upon light irradiation, photolysis of DEAC revealed the TAT motifs on the nanoparticle surface, generating a highly positive surface charge and restoring the CPP's penetration enhancing properties. In the future, such nanoparticles have the potential to facilitate enhanced spatiotemporal targeting of cells within a diseased tissue. Moreover, these nanoparticles could be used to allow for spatiotemporal drug transfer into target cells.

Photocleavage of DEAC requires UV-light ($\lambda_{em,max} = 365\,\text{nm}$), which is limited by its low penetration depth in biological tissues. To overcome this constraint, we aimed to improve the photo-responsive design by employing bioluminescence as an endogenous energy source. **Chapter 4** addresses the implementation of bioluminescent nanoparticles that provides the foundation for enhanced photo-responsive design. NanoLuc, a luciferase originating from the deep-sea shrimp *Oplophorus gracilirostris*, was selected due to its small size and remarkable stability under acidic conditions and elevated temperatures [18]. Upon oxidation of its substrate furimazine, NanoLuc emits intense blue light with a high quantum yield and operates without the need for additional cofactors or coenzymes [19]. To incorporate NanoLuc in polymeric core-shell nanoparticles, the PLA-PEG block copolymer was modified with a maleimide group to enable covalent immobilization of NanoLuc within the shell via its native cysteine residue. The introduction of an additional cysteine residue in the protein significantly enhanced coupling efficiency. Furthermore, the modified NanoLuc variant retained its enzymatic activity after immobilization, whereas native NanoLuc lost approximately 90 % of its activity.

Building on the concepts of photo-responsive and bioluminescent nanoparticles, **Chapter 5** focuses on establishing a bioluminescent-responsive nanoparticle system. In this study, the objective was to translate the well-established bioluminolysis mechanism, in which bioluminescence resonance energy transfer (BRET) thrives photocleavage, to a nanoparticle system [20, 21]. The efficiency of BRET is determined by the extent of spectral overlap between the donor (luciferase) and the acceptor (PPG), as well as their proximity. The establishment of a bioluminescent-responsive nanoparticle system with the previously used PPG DEAC was not promising, as it demonstrated no photosensitivity upon irradiation with a light-emitting diode corresponding to the NanoLuc spectrum. This finding rendered bioluminolysis highly unfeasible and highlights the need for a better spectrally matched PPG. To address this, the PPG $DEAC_{435}$, whose absorption aligns with NanoLuc emission, was implemented into the TAT-modified nanoparticles. However, $DEAC_{435}$ incorporation did not alter the physicochemical or biological properties of the photocaged nanoparticles. Nonetheless, implementing $DEAC_{435}$ and NanoLuc in nanoparticle design demonstrated that $DEAC_{435}$ is excited upon luciferin addition. This indicates efficient BRET on the nanoparticle surface, confirming the fundamental feasibility of a bioluminescent-responsive nanoparticle design.

Conclusion

The goal of this dissertation was to develop a photo-responsive nanoparticle system and to establish a bioluminescent-responsive nanoparticle system capable of overcoming the limited penetration depth of light in biological tissues. We engineered a photo-responsive nanoparticle with switchable surface charge by photocaging TAT motifs with coumarin-derived PPG (DEAC). This design enables light-controlled presentation of TAT and thus regulating cellular uptake. To circumvent the limited penetration depth of external light for this switchable nanoparticle design, we introduced bioluminescent nanoparticles as an endogenous energy source and explored their potential for activating photo-responsive systems via BRET. While DEAC proved unsuitable for bioluminolysis due to poor spectral overlap with NanoLuc, implementation of $DEAC_{435}$ enabled excitation of PPG via BRET on nanoparticles. However, $DEAC_{435}$ failed to provide effective caging and therefore did not enable the intended functional control of TAT properties. This highlights that replacing a PPG is not trivial and the choice of PPG must be tailored to the specific application. Future work may explore whether $DEAC_{435}$ is capable of inhibiting ligand-receptor interactions, such as the binding of cRGD to integrins [22, 23]. The successful demonstration of BRET on the nanoparticle surface confirms the conceptual feasibility of a bioluminescence-responsive nanoparticle system and opens new opportunities for deep-tissue activation.

References

[1] Elvin Blanco, Haifa Shen, and Mauro Ferrari. “Principles of nanoparticle design for overcoming biological barriers to drug delivery”. In: *Nature biotechnology* 33.9 (2015), pp. 941–951. DOI: `10.1038/nbt.3330`.

[2] Maximilian A. Beach et al. “Polymeric Nanoparticles for Drug Delivery”. In: *Chemical reviews* 124.9 (2024), pp. 5505–5616. DOI: `10.1021/acs.chemrev.3c00705`.

[3] Amanda K. Pearce and Rachel K. O’Reilly. “Insights into Active Targeting of Nanoparticles in Drug Delivery: Advances in Clinical Studies and Design Considerations for Cancer Nanomedicine”. In: *Bioconjugate Chemistry* 30.9 (2019), pp. 2300–2311. DOI: `10.1021/acs.bioconjchem.9b00456`.

[4] Stefan Wilhelm et al. “Analysis of nanoparticle delivery to tumours”. In: *Nature Reviews Materials* 1.5 (2016). DOI: `10.1038/natrevmats.2016.14`.

[5] Zahid Hussain et al. “PEGylation: a promising strategy to overcome challenges to cancer-targeted nanomedicines: a review of challenges to clinical transition and promising resolution”. In: *Drug Delivery and Translational Research* 9.3 (2019), pp. 721–734. ISSN: 2190-3948. DOI: `10.1007/s13346-019-00631-4`.

[6] Maria Marti-Solano et al. “Combinatorial expression of GPCR isoforms affects signalling and drug responses”. In: *Nature* 587.7835 (2020), pp. 650–656. DOI: `10.1038/s41586-020-2888-2`.

[7] Ying Shen et al. “Transferrin receptor 1 in cancer: a new sight for cancer therapy”. In: *American journal of cancer research* 8.6 (2018), pp. 916–931. ISSN: 2156-6976.

[8] Nikolitsa Nomikou, Hamzah Masood, and Shiv Patel. “Stimulus-Responsive Nanoparticles for Drug Delivery”. In: *Fundamentals of Pharmaceutical Nanoscience*. Ed. by Ijeoma F. Uchegbu et al. Cham: Springer Nature Switzerland, 2024, pp. 389–422. ISBN: 978-3-031-59477-9. DOI: `10.1007/978-3-031-59478-6_15`.

[9] Alan Clavelland Ochioni, Italo Rennan Sousa Vieira, and Carlos Adam Conte-Junior. “Advances in stimuli-responsive nanoparticles for cancer therapy: Mechanisms, functional materials, and emerging technologies”. In: *Journal of Drug Delivery Science and Technology* 114 (2025), p. 107519. ISSN: 17732247. DOI: `10.1016/j.jddst.2025.107519`.

[10] Simona Mura, Julien Nicolas, and Patrick Couvreur. “Stimuli-responsive nanocarriers for drug delivery”. In: *Nature materials* 12.11 (2013), pp. 991–1003. DOI: `10.1038/nmat3776`.

[11] R. Weissleder. “A clearer vision for in vivo imaging”. In: *Nature biotechnology* 19.4 (2001), pp. 316–317. DOI: `10.1038/86684`. URL: `https://www.nature.com/articles/nbt0401_316`.

[12] Jan Birringer et al. “Coumarin-Caged Nanoparticle for Light-Driven Surface Modification”. In: *ChemMedChem* 20.22 (2025), e202500636. DOI: `10.1002/cmdc.202500636`.

[13] Slavko Kralj et al. “Effect of surface charge on the cellular uptake of fluorescent magnetic nanoparticles”. In: *Journal of Nanoparticle Research* 14.10 (2012). ISSN: 1388-0764. DOI: `10.1007/s11051-012-1151-7`.

[14] Dehua Pei and Marina Buyanova. “Overcoming Endosomal Entrapment in Drug Delivery”. In: *Bioconjugate Chemistry* 30.2 (2019), pp. 273–283. DOI: `10.1021/acs.bioconjchem.8b00778`.

[15] Qiuju Dai et al. “Enzyme-Responsive Modular Peptides Enhance Tumor Penetration of Quantum Dots via Charge Reversal Strategy”. In: *ACS applied materials & interfaces* 16.5 (2024), pp. 6208–6220. DOI: `10.1021/acsami.3c11500`.

[16] Hana Cho et al. “Beyond Nanoparticle-Based Intracellular Drug Delivery: Cytosol/Organelle-Targeted Drug Release and Therapeutic Synergism”. In: *Macromolecular bioscience* 24.7 (2024), e2300590. DOI: `10.1002/mabi.202300590`.

[17] Xiao-Ru Shao et al. “Independent effect of polymeric nanoparticle zeta potential/surface charge, on their cytotoxicity and affinity to cells”. In: *Cell proliferation* 48.4 (2015), pp. 465–474. DOI: `10.1111/cpr.12192`.

[18] Mary P. Hall et al. “Engineered luciferase reporter from a deep sea shrimp utilizing a novel imidazopyrazinone substrate”. In: *ACS chemical biology* 7.11 (2012), pp. 1848–1857. DOI: `10.1021/cb3002478`.

[19] Christopher G. England, Emily B. Ehlerding, and Weibo Cai. “NanoLuc: A Small Luciferase Is Brightening Up the Field of Bioluminescence”. In: *Bioconjugate Chemistry* 27.5 (2016), pp. 1175–1187. DOI: `10.1021/acs.bioconjchem.6b00112`.

[20] Dalu Chang et al. “Luciferase-Induced Photouncaging: Bioluminolysis”. In: *Angewandte Chemie (International ed. in English)* 58.45 (2019), pp. 16033–16037. DOI: `10.1002/anie.201907734`.

[21] Dalu Chang et al. “Luciferase Controlled Protein Interactions”. In: *Journal of the American Chemical Society* 143.10 (2021), pp. 3665–3670. DOI: `10.1021/jacs.0c11016`.

[22] Weiping Wang et al. “Efficient Triplet-Triplet Annihilation-Based Upconversion for Nanoparticle Phototargeting”. In: *Nano letters* 15.10 (2015), pp. 6332–6338. DOI: `10.1021/acs.nanolett.5b01325`.

[23] Albert Gandioso et al. “A Green Light-Triggerable RGD Peptide for Photocontrolled Targeted Drug Delivery: Synthesis and Photolysis Studies”. In: *The Journal of organic chemistry* 81.23 (2016), pp. 11556–11564. DOI: `10.1021/acs.joc.6b02415`.

Appendix

List of Abbreviations

ACN acetonitrile.

AHx aminohexanoic acid.

ANOVA analysis of variance.

APCI atmospheric pressure chemical ionization.

API active pharmaceutical ingredient.

APS ammonium persulfate.

BCA bicinchoninic acid.

BLS bioluminescent system.

Boc/tBoc tert-butyl carbamate.

BODIPY *meso*-methyl boron dipyrromethene.

BRET bioluminescence resonance energy transfer.

BSA bovine serum albumin.

Cb chlorambucil.

CE coupling efficiency.

CIP contact ion pair.

CLSM confocal light scanning microscopy.

CPP cell-penetrating peptide.

CRET chemiluminescence resonance energy transfer.

cRGD cyclo(-Arg-Gly-Asp).

Cy5 Cyanine5 fluorophore.

$\mathbf{d}_h$ hydrodynamic diameter.

DAD diode array detector.

DAPI 4’,6’-diamidine-2’-phenylindole dihydrochloride.

DBU 1,8-Diazabicyclo(5.4.0)undec-7-ene.

DCM dichloromethane.

DEAC 7-(diethylamino)-4-(hydroxymethyl)coumarin.

$\mathbf{DEAC}_{435acid}$ (E)-4-(7-(diethylamino)-4-(hydroxymethyl)-2-oxo-2H-chromen-3-yl)but-2-enoic acid.

$\mathbf{DEAC}_{435}$ 7-(diethylamino)-(4-hydroxymethyl)-[(E)-3-(tert-butoxycarbonyl)prop-2-enyl]coumarin.

$\mathbf{DEAC}_{450}$ (E)-(3-(7-(diethylamino)-4-(hydroxymethyl)-2-oxo-2H-chromen-3-yl)acryloyl)aspartic acid.

DEACM [7-(diethylamino)coumarin-4-yl]methyl.

DIPEA N,N-diisopropylethylamine, N-ethyl-N-(propan-2-yl)propan-2-amine.

DMAP 4-(dimethylamino)pyridine.

DMF N,N-dimethylformamide.

DMF-DMA N,N-diemthylformaidediemthylacetal.

DMNB 4,5-dimethoxy-2-nitrobenzyl.

DMSO dimethyl sulfoxide.

DNA deoxyribonucleic acid.

DOF degree of functionalization.

DPBS dulbecco’s phosphate buffered saline.

EDC 1-Ethyl-3-(3-dimethylaminopropyl)-carbodiimide.

EDTA ethylenediamine tetraacetic acid.

EMEM Eagle’s minimum essential medium.

EPR enhance permeability and retention.

ESI electrospray ionization.

FACS fluorescence activated cell sorting.

FBS fetal bovine serum.

FLD fluorescence detector.

Fmoc fluorenemethanol carbamate.

FRET fluorescence resonance energy transfer.

HaloTag self-labeling protein tag derived from bacterial haloalkane dehalogenase.

HATU 1-[Bis(dimethylamino)methylene]-1H-1,2,3-triazolo[4,5-b]pyridinium 3-oxide hexafluorophosphate.

HBTU 2-(1H-Benzotriazol-1-yl)-1,1,3,3-tetramethyluronium-hexafluorophosphat.

HeLA chlorambucil.

HFIP hexafluoroisopropanol.

HIV human immunodeficiency virus.

HPLC high-performance liquid chromatography.

HRMS high-resolution mass spectrometry.

HUVEC human umbilical vein endothelial cells.

iRGD internalizing RGD.

LB lysogeny broth.

LC liquid chromatography.

LED light-emitting diode.

MS mass spectrometry.

MWCO molecular weight cut-off.

NanoLuc engineered luciferase originating from the deep-sea shrimp *Oplophorus gracilirostris*.

Nbz 2-nitrobenzyl.

NIR	near-infrared.
NLS	nucleus localization sequence.
NMR	nuclear magnetic resonance.
NP	nanoparticle.
NTA	nanoparticle tracking analysis.
NVOC	6-nitroveratryloxycarbonyl.
ORF	open reading frame.
PAE	poly(β-amino ester).
Pbf	2,2,4,6,7-pentamethyl-dihydrobenzofuran-5-sulfonyl.
PCR	polymerase chain reaction.
PDI	polydispersity index.
PDT	photodynamic therapy.
PEG	poly(ethylene glycol).
PFA	paraformaldehyde.
PFV	polyfluorene vinylene).
PLA	poly(D,L-lactide).
PLGA	poly(D,L-lactide-*co*-glycolide.
PPG	photo-labile protecting group.
ROS	reactive oxygen species.
rpm	revolutions per minute.
RT	room temperature.
SD	standard deviation.
SDS-PAGE	sodium dodecyl sulfate polyacrylamide gel electrophoresis.
SEC	size exclusion chromatography.
SOC	super optimal broth with catabolite repression.

TAT transactivator of transcription protein from HIV.

TBDMS tert-butyldimethylsilyl.

TBDMSCl tert-butyldimethylchlorosilane.

tBu tert-butyl.

TCEP tris(2-carboxyethyl)phosphine.

TEM Transmission Electron Microscopy.

TEMED N,N,N’,N’-Tetramethylethane-1,2-diamine.

TFA trifluoroacetic acid.

THF tetrahydrofuran.

Trt triphenylmethyl.

UV ultraviolet.

Curriculum Vitae

List of Publications

Peer-reviewed publications:

1. Birringer, J., Konrad, J., Melchner, S., Remmert, M., & Goepferich, A. (2025). Coumarin-Caged Nanoparticle for Light-Driven Surface Modification. *ChemMedChem*, *20*(22), e202500636. (**Chapter 3**)
2. Remmert, M., Konrad, J., Birringer, J., & Goepferich, A. (2025). Interferon gamma modifies nanoparticle tropism and cell uptake. *Journal of Drug Delivery Science and Technology*, 107301.
3. Schorr, K., Konrad, J., Birringer, J., Damm, C., Breunig, M., & Goepferich, A. (2026). A refined coadministration regime to mitigate immunological clearance of biomedical nanoparticles. *European Journal of Pharmaceutics and Biopharmaceutics*, 114989.

Submitted to peer-reviewed journal:

1. Melchner, S., Jungblut, M., Birringer, J., Erl, J., Lächelt, U., Wegener, J., Beliu, G., Goepferich, A., & Breunig, M. (2026). Clickable Turn-On Nanoparticles for Target-Specific Intracellular Activation

Conference Abstracts:

1. Birringer, J., & Goepferich, A. (2024). Light-controlled Targeting of Nanoparticles Using Coumarin-derived Photocage. CRS Germany Local Chapter, Bad Dürkheim, Germany
2. Birringer, J., & Goepferich, A. (2025). Increasing Tissue-selectivity of CCP-functionalized Nanoparticles by Coumarin-derived Photocaging. CRS DeChAt Local Chapter, Bern, Switzerland

Acknowledgments

First and foremost, I would like to express my sincerest gratitude to Prof. Dr. Achim Goepferich for giving me the opportunity to join his research group. I am deeply thankful for the trust he placed in me and for the freedom he allowed in planning and conducting my research. His enthusiastic and supportive guidance, along with the many inspiring scientific discussions, created an atmosphere that greatly contributed to the successful completion of this work and to my personal as well as professional growth. For this, I am truly grateful.

I would also like to extend my special thanks to Prof. Dr. Miriam Breunig for her valuable scientific advice and insightful discussions. Her expertise and constructive feedback significantly improved the overall quality of this dissertation.

Furthermore, I would like to thank my former and current colleagues and fellow researchers in the Department of Pharmaceutical Technology in Regensburg for their support and creating a enjoyable working environment. In particular, I wish to express my appreciation to:

- Johannes Konrad and Marius Remmert, my lab colleagues, for the many engaging conversations, both scientific and personal and being part of the "Kammer des Schreckens" since day one. Thank you, JK, for your remarkable patience and your readiness to help - whether it was with equipment issues or conceptual ideas. And thank you, Marius, for your constant support and for always being there to listen to. I am thankful to both of you for the wonderfully diverse music selection from Hildegard von Bingen to Bayern 3.
- Stephan Melchner, for his support within the scientific work and for the many kilometers spent cycling and running together in pursuit of personal bests and new challenges. I am grateful for the countless scientific discussions that enriched my work, but above all for his openness, emotional support, and for continuously pushing limits. Thank you, Stephan.
- Carsten Damm, for your help with the LaTeX issues, for your support in resolving HPLC errors, and for completing the "Keller-WG" together with the aforementioned colleagues.
- Felix Hauswirth, for enjoyable conversations during lunch breaks and while cycling.
- Andreas Schreiber, for being the driving force behind the daily “Schafkopf” rounds during lunch breaks.

- Felix Baumann, for his valuable scientific advice and support, especially during my first year, as well as for the endless supply of snacks.
- Dr. Johannes Lang, for the many enjoyable football nights and the long runs we shared.
- Dr. Melanie Bresinsky, for our cheerful chats during LAF box cleaning and always being "the" contact person.
- Dr. Kathrin Schorr, for her helpful scientific advice and the great sunny coffee breaks. Thanks, Kathrin. It was always fun to chat with you, and it was just nice having someone from Rheinland-Pfalz on the team.

I am grateful for the excellent technical assistance I received during my time at the university. In particular, I would like to thank Grace Faltermeier for her assistance with polymer synthesis, and Renate Liebl for her excellent support in cell culture. Furthermore, I would like to express my gratitude to Eva Wrobel for her assistance with organizational and administrative matters.

I would like to thank the Department of Pharmaceutical and Medicinal Chemistry I and II for access to the HPLC-MS, the freeze-dryer, and the preparative HPLC, as well as for their support with synthesis. In particular, I would like to thank Prof. Dr. Steffen Pockes, Jonas Daschner, Alexander Hubmann, Bernadette Vallaster and Beate Hoffelner for their support.

I would also like to express my gratitude to the Department of Physical Chemistry I for providing LEDs and equipment for photocleavage experiments, and in particular Sebastian Boesl-Bichlmeier for his support in this regard.

I want to extend my thanks to the Institute of Analytical Chemistry, Chemo- and Biosensor Technology, particularly Prof. Dr. Joachim Wegener's group, for providing me with the opportunity to express NanoLuc. I would also like to acknowledge the invaluable support of Anne-Kathrin Grimm in this regard.

Microsoft Copilot was used during the writing process for linguistic improvements such as rephrasing, grammar correction, and spell-checking. The conceptual contributions, scientific analyses, and final interpretations presented in this dissertation originate solely from the author.

A very special thanks goes to my mother, uncle and beloved friends who encouraged me in every part of my life. Your unwavering support has made this progress possible, and I am deeply grateful for it!

Finally, I would like to thank Nina for cheering me up, always supporting me, for her patience, and for being a constant source of strength.

Declaration in Lieu of an Oath

I hereby declare that I have completed the dissertation presented without the impermissible help of third parties, without the use of resources other than those indicated, and that any data and concepts stemming directly or indirectly from other sources are indicated with citations to the literature.

No further persons were involved with the creation of the contents of the dissertation presented. In particular, I have not made use of the assistance of a doctoral consultant or other person in return for payment. No-one has received payment in kind either directly or indirectly for work which is associated with the content of the dissertation submitted.

The dissertation has not been submitted in the same or similar form to another examining authority, neither in Germany nor abroad.

Regensburg, 28.04.2026

Jan Birringer

In loving memory of my late father.